SAND2024-01999R

FY23 Status of Engineered Barrier Systems Work Package

Spent Fuel and Waste Disposition

Prepared for US Department of Energy
Spent Fuel and Waste Science and Technology

E.N. Matteo, T. Hadgu, N. Bell, J. Greathouse,
J. N. Kruichak, A. Taylor, and P. Weck
Sandia National Laboratories

F. Caporuscio, A. E. Zanadel, M. Rock, and A. J. McKanna
Los Alamos National Laboratories

L. Zheng, S. Borglin, P. Zarzycki, C. Chang,
P. Fox, S. Yoon, W. Dong, P. Nico,
C. Tournassat, C. Chou, C. Steefel, L. Peruzzo,
S. Farrell, B. Gilbert, and Y. Wu
Lawrence Berkeley National Laboratories

L. Brown, C. Gruber, and D. Kosson
Vanderbilt University

November 3, 2023
M2SF-24SN010308052
SAND2024-01999R

DISCLAIMER

This information was prepared as an account of work sponsored by an agency of the U.S. Government. Neither the U.S. Government nor any agency thereof, nor any of their employees, makes any warranty, expressed or implied, or assumes any legal liability or responsibility for the accuracy, completeness, or usefulness, of any information, apparatus, product, or process disclosed, or represents that its use would not infringe privately owned rights. References herein to any specific commercial product, process, or service by trade name, trademark, manufacturer, or otherwise, does not necessarily constitute or imply its endorsement, recommendation, or favoring by the U.S. Government or any agency thereof. The views and opinions of authors expressed herein do not necessarily state or reflect those of the U.S. Government or any agency thereof.

Sandia National Laboratories

U.S. DEPARTMENT OF ENERGY

National Nuclear Security Administration

Sandia National Laboratories is a multi-mission laboratory managed and operated by National Technology & Engineering Solutions of Sandia, LLC., a wholly owned subsidiary of Honeywell International, Inc., for the U.S. Department of Energy's National Nuclear Security Administration under contract DE-NA00035.

Revision 6
10/7/2019

APPENDIX E
NFCSC DOCUMENT COVER SHEET [1]

Name/Title of Deliverable/Milestone/Revision No.	FY23 Status of the Engineered Barrier Systems Work Package/ M2SF-24SN010308052
Work Package Title and Number	Engineered Barrier System R&D – SNL / SF-23SN01030805
Work Package WBS Number	1.08.01.03.08
Responsible Work Package Manager	Edward N. Matteo / (Name/Signature)
Date Submitted	

Quality Rigor Level for Deliverable/Milestone[2]	☐ QRL-1 ☐ Nuclear Data	☐ QRL-2	☒ QRL-3	☐ QRL-4 Lab QA Program[3]

This deliverable was prepared in accordance with Sandia National Laboratories
(Participant/National Laboratory Name)

QA program which meets the requirements of

☒ DOE Order 414.1 ☐ NQA-1 ☐ Other

This Deliverable was subjected to:

☒ Technical Review ☐ Peer Review

Technical Review (TR)
Review Documentation Provided

☐ Signed TR Report or,
☐ Signed TR Concurrence Sheet or,
☒ Signature of TR Reviewer(s) below

Peer Review (PR)
Review Documentation Provided

☐ Signed PR Report or,
☐ Signed PR Concurrence Sheet or,
☐ Signature of PR Reviewer(s) below

Name and Signature of Reviewers

Carlos Miguel Lopez

Carlos M Lopez

NOTE 1: *Appendix E should be filled out and submitted with the deliverable. Or, if the PICS:NE system permits, completely enter all applicable information in the PICS:NE Deliverable Form. The requirement is to ensure that all applicable information is entered either in the PICS:NE system or by using the NTRD Document Cover Sheet.*

- *In some cases there may be a milestone where an item is being fabricated, maintenance is being performed on a facility, or a document is being issued through a formal document control process where it specifically calls out a formal review of the document. In these cases, documentation (e.g., inspection report, maintenance request, work planning package documentation or the documented review of the issued document through the document control process) of the completion of the activity, along with the Document Cover Sheet, is sufficient to demonstrate achieving the milestone.*

This page is intentionally left blank.

SUMMARY

This report describes research and development (R&D) activities conducted during Fiscal Year 2023 (FY23) specifically related to the Engineered Barrier System (EBS) R&D Work Package in the Spent Fuel Waste Science and Technology (SFWST) Campaign supported by the United States (U.S.) Department of Energy (DOE). The R&D activities focus on understanding EBS component evolution and interactions within the EBS, as well as interactions between the host media and the EBS. The R&D team represented in this report consists of individuals from Sandia National Laboratories, Lawrence Berkeley National Laboratory (LBNL), Los Alamos National Laboratory (LANL), and Vanderbilt University. EBS R&D work also leverages international collaborations to ensure that the DOE program is active and abreast of the latest advances in nuclear waste disposal.

High-level Purpose of this work: A primary goal of the EBS work package is to advance the development of process models that can be implemented directly within the Generic Disposal System Analysis (GDSA) platform. Improved process models can contribute to the safety case in several ways, such as:

- building confidence and improving the robustness of the performance assessment,
- providing further insight into the processes being modeled, establishing better constraints on parameters critical to repository performance, and
- assessing technical readiness of EBS design components.

A major focus of this work is to understand the processes that will impact and control the permeability and/or transport in the EBS. Permeability evolution in the geotechnical seal system is typically a major driver of repository performance, or otherwise an important scenario that needs to be evaluated in self-sealing host media. The interfaces of the EBS components, including the disturbed rock zone (DRZ), play a critical role in the near-field environment, where complex processes have a significant impact on overall transport and fate of radionuclides.

Improved understanding of these interfaces requires capabilities to characterize, test, and model the EBS, in such a way that relevant complex phenomena are captured and represented. EBS processes are often coupled, e.g., thermal- hydrologic-mechanical-chemical (THMC), multi-scale (from molecular to continuum scale), and nonlinear (e.g., multi-phase flow).

The FY23 EBS report includes results from modeling, analysis, and experimental work and is focused on several key themes:

- Improved understanding and model representation of coupled processes, e.g., thermal-hydrologic-mechanical-chemical (THMC), in EBS materials, with a particular focus on swelling behavior and high temperature effects on bentonite buffer materials.
- Investigation and characterization at multiple length scales – from molecular to mesoscale to continuum scale - to understand near-field process models for radionuclide retention and transport through the EBS and disturbed rock zone.
- Field scale testing and analysis to validate and improve process modelling tools and overall conceptual understanding of complex processes in the *in situ* setting.

These themes are investigated in various ways within the EBS work package, with projects ranging from molecular dynamic simulations to bench-scale testing and characterization, and all the way up to the drift-scale testing and demonstration in underground research laboratories.

FY23 Accomplishments: Overall, significant progress has been made in FY23 towards developing the modeling and analysis tools and experimental and characterization capabilities needed to investigate the performance of EBS materials and the associated interactions in the drift and the surrounding near-field environment under a variety of conditions, including high temperature regimes. This includes the follwing accomplishments from the FY23 EBS work package:

- Particpation in the the planning, implementation, and design of the HotBENT Field Test at the Grimsel Test Site in Switzerland. *The heaters were initated in FY23*.
- Continued development of a state-of-the-art micro-oedometric experimental capability that utilizes the Advanced Light Source to study the role of groundwater chemistry on the structure and swelling behavior of smectitite clay minerals, e.g. bentonite buffer.
- Development of a computational pipeline to generate synthetic datasets, train AI/ML models for molecular scale modeling of radionuclide retention by bentonites – this, in turn, can used to parametrize meso- and macroscopic models of radionuclide migration in a bentonite barrier to develop a robust safety assessment model.
- Development of an improved model for diffusion in bentonite clays via bench-scale experiments to better understand diffusion-dominated transport as a function of clay interlayer cation composition and groundwater
- Modeling and completion of bench-scale testing of a bentonite clay column in support of the HotBENT Field Test
- Validation of THMC modelling capabilities for bentonite via validation against international URL field tests
- Completion of a series of hydrothermal experiments to study EBS materials interactions (e.g., waste package materials, host, buffer materials) and the associated characterization and analysis.
- Modelling validation exercise and reporting as participants in the DECOVALEX2023, Task C
- Development of novel, state-of-the-art workflow for analysis and characterization of chemo-mechanical process at EBS/host rock interfaces

FY24 Priorities:

- Continued particpation in HotBENT testing support, modelling, and analysis
- Continued activity on mutli-scale bentonite studies on THMC representation, diffusion, and molecular-scale investigations
- Finalize DECOVALEX2023 deliverables, begin transition to next phase DECOVALEX and/or other internaional activities based on EBS work package priorities and integration with GDSA modelling needs
- Utilize chemo-mechanical characterization workflow to study argillite host rock material interfaces

This page is intentionally left blank.

ACKNOWLEDGEMENTS

This work was supported by the U.S. Department of Energy Office of Nuclear Energy, through the Office of Spent Fuel and Waste Science and Technology (SFWST) Research and Development Campaign (DOE NE-81) within the Office of Spent Fuel and Waste Disposition.

The authors acknowledge contributions in the form of discussions on technical and integration issues from the following people from Sandia National Laboratories: R. Chris Camphouse, Emily Stein, Ernie Hardin(retired), Carlos Jové-Colón, Yifeng Wang, and David Sassasni. In addition, the authors thank Jorge Monroe-Rammsy (DOE NE-81), Prasad Nair (DOE NE-81), Tim Gunter (DOE NE-81) and William Boyle (DOE NE-81) for their discussions, oversight, and guidance on topics covered in this report.

The authors thank Deborah Phipps for assistance with formatting and proofing of this document.

Lastly, the authors thank Carlos Miguel Lopez (Sandia) for providing a careful and thorough technical review of this document.

This page is intentionally left blank.

TABLE OF CONTENTS

SUMMARY iv

ACKNOWLEDGEMENTS vii

TABLE OF CONTENTS ix

LIST OF FIGURES xiii

LIST OF TABLES xxiii

ACRONYMS xxv

1. INTRODUCTION 1

2. Chemical Controls On Montmorillonite Structure And Swelling Pressure (LBNL) 6
   - 2.1 Introduction 6
   - 2.2 Materials and Methods 6
     - 2.2.1 Clay Sample and Characterization 6
     - 2.2.2 Chemical Solutions 7
     - 2.2.3 Clay Swelling Pressure Measurement Experiment 7
     - 2.2.4 X-Ray Scattering Measurement Experiment 8
   - 2.3 Results and Discussion 9
     - 2.3.1 Measurement of Cation Exchange Capacity (CEC) 9
     - 2.3.2 Influence of Na^+/K^+ Ratios on Clay Swelling Pressure 9
     - 2.3.3 Influence of Ionic Strength on Clay Swelling Pressure 11
     - 2.3.4 Influence of Ionic Strength on Clay Microstructure 13
     - 2.3.5 Influence of Cation Type on Clay Microstructure 16
   - 2.4 Summary and Future Work 17

3. Molecular modeling of Radionuclide Retention by Bentonites 20
   - 3.1 Introduction 20
   - 3.2 Molecular and Thermodynamic Modeling of Radionuclides Sorption to Mineral Surfaces 21
     - 3.2.1 Surface Complexation Modeling 21
     - 3.2.2 Machine Learning / Artificial Intelligence Model Construction 25
     - 3.2.3 Results 26
     - 3.2.4 Future Directions 28

4. Experimental Investigations on Bentonite and other clay-based Materials 30
   - 4.1 Introduction 30
   - 4.2 Experimental Materials and Methods 31
     - 4.2.1 Filter Diffusion Measurements 31
     - 4.2.2 Clay Samples 32
     - 4.2.3 Se Sorption 32
     - 4.2.4 Se(IV) Diffusion Experiments 33
   - 4.3 Experimental Results and Discussion 34
     - 4.3.1 Filter Diffusion Properties 34

4.3.2 Se Sorption....35
4.3.3 Selenite and ^{3}H Diffusion through Compacted Montmorillonite....35
4.4 CrunchEase Graphical User Interface for Interpretation of Diffusion Results....37
4.4.1 Effect of Filters....38
4.4.2 CrunchEase Quick Tutorial....39
4.5 Summary and Future Work....44

5. Coupled Microbial Abiotic Processes in EBS and Host Rock Materials....46
5.1 Introduction....46
5.2 Methods....46
5.3 Data Interpretation....51
5.4 Summary and Future Work....60

6. Heating and Hydration Column Test on Bentonite....62
6.1 Introduction....62
6.2 Analysis of HotBENT Lab #1 and #2 Dismantled Samples....64
6.2.1 Characterization and Monitoring....64
6.3 Preliminary Results....67
6.3.1 X-ray CT....67
6.3.2 Electrical Resistivity Tomography (ERT)....82
6.3.3 Postmortem Sampling....88
6.4 Summary and Future Work....90

7. MODELING THE CONCRETE/BENTONITE INTERFACE: TASK 12 IN SKB EBS TASK FORCE Introduction....92
7.1 Introduction....92
7.2 Description of Task 12....92
7.3 Model Development....94
7.3.1 Initial Conditions....94
7.3.2 Thermodynamic and Kinetic Data....100
7.3.3 Model Setup....103
7.4 Model Results....103
7.4.1 Subtask A1....103
7.4.2 Subtask A3....108
7.5 Summary and Future Work....113

8. Understanding the THMC Evolution of Bentionite Using Large Scale Field Experiments: Hotbent....116
8.1 Introduction....116
8.2 HotBENT Project....117
8.2.1 Field Test Updates....117
8.2.2 Modeling Platform....121
8.3 Model for the Field Test....123
8.3.1 Model Set Up....123
8.3.2 Model Results....125
8.4 Summary and Future Work....130

9. HYDROTHERMAL ALTERATION OF EBS INTERFACES 132
9.1 Background 132
9.1.1 EBS Concepts in Crystalline Rock 132
9.2 Methods 137
9.2.1 Hydrothermal Experiments 137
9.2.2 Materials 139
9.3 Results 141
9.3.1 Aqueous Geochemistry 141
9.3.2 Quantitative X-ray Diffraction (QXRD) 147
9.3.3 Clay XRD 150
9.3.4 X-Ray Fluorescence (XRF) 153
9.3.5 Microprobe 154
9.3.6 Scanning Electron Microscope (SEM)/EDS 154
9.4 Discussion 155
9.4.1 Hydrothermal interaction of Wyoming Bentonite, Grimsel Granodiorite, and Groundwater Solution 155
9.4.2 Steel-Bentonite Interface 156
9.4.3 Effects of Cement on EBS Alteration (IEBS-6 and -8 through -10) 158
9.5 Conclusions 166
9.5.1 Research Concepts Developed in FY23: 167
9.5.2 Research Avenues to be Emphasized in FY24: 168

10. Hydrothermal Testing to Support the Hotbent Field Test 169
10.1 Introduction 169
10.2 Methods 171
10.2.1 Hydrothermal Experiments 171
10.2.2 Materials 173
10.3 Results 173
10.3.1 Aqueous Geochemistry 173
10.3.2 XRD 177
10.3.3 XRF 183
10.3.4 Electron Microprobe Analysis 185
10.3.5 SEM / EDS 185
10.4 Discussion 186
10.4.1 Previous FY experiments 186
10.4.2 FY23 Experiments 188
10.5 Conclusions 190

11. Calibrated Simulations of a Full-Scale Heater Experiment in Opalinus Clay 193
11.1 Introduction 193
11.2 Step 1c Modeling 193
11.2.1 Step 1c Model Geometry 193
11.2.2 Simulation Model Setup 195
11.3 Step 1c Simulation Results 196
11.3.1 Results in the Bentonite 197
11.4 Summary and Future Work 203

12. Synthesis, Characterization, and Evaluation of Modified Boehmite Materials as Anion Sorbent Additive in EBS Design 205
12.1 Introduction 205
12.2 Structural and Spectroscopic Properties of Glycoboehmite from Molecular Modeling 205
12.3 Experimental Evaluation of Glycoboehmite Materials for Anion Sorption 208
12.4 Summary and Future Work 209

13. Chemo-Mechanical Characterization of Cement-Rock Interfaces 211
13.1 Overview 211
13.2 Objectives 211
13.3 Methods 211
13.3.1 Workflows 211
13.3.2 Sample Casting/Aging 213
13.3.3 MicroCT 214
13.3.4 Sample Preparation – Sectioning 214
13.3.5 Sample Preparation – Polishing 214
13.3.6 SEM-EDS 214
13.3.7 Micro/Nano-indentation 214
13.3.8 LA-ICP-MS & MicroXRF 215
13.3.9 Image Segmentation & Analysis Programs 215
13.4 Results and Discussion 215
13.4.1 Oil Shale-OPC Paste Interface 215
13.4.2 Other Rock-Cement Interfaces 218
13.5 Experimental Comparison to Models 218
13.6 Summary and Future Work 219

References 221

LIST OF FIGURES

Figure 2-1 AFM image of Kunipia-F 7

Figure 2-2. Photograph of the clay swelling experimental setup, including (a) Harvard syringe pump to introduce chemical solutions, (b) μ-oedometer including a black PEEK cell to hold the clay sample (red small circle) and the force sensor on the cell (red small rectangle) to monitor the cell force changes, (c) a displacement sensor display (left) and a force sensor display (right), (d) an automatic fraction collector to collect the effluent for chemical analysis, and (e) a computer with software to digitally record the time-resolved force and displacement changes. 8

Figure 2-3. Chemical- and time-resolved swelling pressure change as a function of Na+/K+ ratios at a constant ionic strength = 1.0 M 10

Figure 2-4. Time-resolved cation concentrations from the effluents corresponding to Figure 2-2. 11

Figure 2-5. Clay swelling pressure change as a function of ionic strength and cation type (Na^+/K^+ 12

Figure 2-6. Time-resolved cation concentrations from the effluents corresponding to Figure 2-5. 13

Figure 2-7. Original SAXS spectra of compacted montmorillonite as a function of ionic strength. 14

Figure 2-8. SAXS spectra (background corrected) of compacted montmorillonite as a function of ionic strength (0.001 M, 0.01 M, 0.1 M, 1.0 M, 5.0 M NaCl). 15

Figure 2-9. SAXS spectra of compacted montmorillonite saturated with 1.0 M KCl vs. 1.0 M NaCl 17

Figure 3-1. (a) Schematic diagram of hypothetical leakage of spent nuclear fuel from geological storage, showing migration upward, mobilization of uranium (U) oxidizing subsurface conditions, and retention by sorption to oxides minerals, (b) Schematic of the 2-pK TLM of the oxide/U-containing solution interface, (c) Traditional, numerical approach to predict thermodynamic properties of the mineral/electrolyte interface and the extent of ion sorption, and (d) a schematic pipeline of machine learning. Taken from Li et al. (2023) 20

Figure 3-2. Multioutput regressor as an SCM surrogate. The architecture consists of 12 random forests (estimators), each trained to predict a single target value (output) based on a complete input vector. The input consists of a description of the oxide surface (surface area, site density), the SCM parameter values, such as affinity constants ($\log K_i$) capacitances, and a description of solution composition (12 values). The output consists of charge densities and electrostatic potential in each layer and concentrations of surface complexes (12 values) (Li et al., 2023). 24

Figure 3-3. Surrogate model prediction vs. numerical SCM-based ground truth. The red solid line represents the ideal prediction, where prediction equals to ground truth value. R^2 score represents the goodness of fit of surrogate predictions to corresponding ground truth values. MSE stands for the mean squared error between prediction and target. See reference (Li et al., 2023) for details. 25

Figure 3-4 Importance of selected features (input values) in predicting target values (output values). See reference (Li et al., 2023) for details. 26

Figure 3-5 Correlation analysis on input features. (a) A dendrogram of input features. It divided features into different groups based on their relevance. The lower the height, the stronger the correlation. (b) Pair correlation between different input features. 27

Figure 4-1. Custom-built diffusion cells for measuring diffusion properties of filters. 32

Figure 4-2. Example plot of NaCl mass (mol) in the "low" reservoir over time. The linear regression equation is also shown. 34

Figure 4-3 Normalized ^{3}H flux in three diffusion cells. Each cell received two pulses of ^{3}H, and data for both are shown. The autosampler missed several samples during the first pulse for the Ca cell. 36

Figure 4-4. Schematic of an (a) ideal and (b) actual through-diffusion experimental setup with the goal of achieving constant boundary conditions (*i.e.*, with a constant concentration gradient across the diffusion cell at steady state). (c) 1D diffusion geometry, and (d) €: 2D- axisymmetric cylindrical geometries. Tracer cannot diffuse through the plain O-ring of the filter support (d), making the diffusional path 2D. The cross-sectional area available for diffusion in the filters is equal to $\boldsymbol{dfilter22dsample22}$ of the cross-sectional area of the sample. 38

Figure 4-5. Comparison of diffusion breakthrough curves calculated in CrunchEase/CrunchClay in the absence (full lines) and presence (dashed lines) of filters, as a function of sample length (L_{sample} = 5 mm vs. 10 mm) and K_D value (from 0 to 2 L kg^{-1}). 39

Figure 4-6 Screenshot of the CrunchEase install directory. 40

Figure 4-7. Screenshot of the main window of the CrunchEase interface. 40

Figure 4-8. Screenshot of the Diffusion window of the CrunchEase interface. 40

Figure 4-9. Screenshot of the 1D- Through-Diffusion window of the CrunchEase interface. Follow numbered instructions to run your first simulation. 41

Figure 4-10. Screenshot of the 1D- Through-Diffusion window of the CrunchEase interface after calculation 41

Figure 4-11. Screenshot of the Tutorial directory after calculation. 42

Figure 4-12. Screenshot of the simulation directory (named after your Experiment Title) after calculation. 42

Figure 4-13. Screenshot of the 1D- Through-Diffusion window of the CrunchEase interface with options and parameters selected to model Br diffusion data from Tinnacher et al. (2016). 44

Figure 5-1. Locations of bentonite samples in original FEBEX experiment: (a) Longitudinal cross-section along FEBEX tunnel, and (b) cross-sections B-D-48 and B-D-69 (modified from Villar, 2017) Samples were taken from B-D-59-10 (T-ambient), B-D-48-4 (T-35), B-D-48-5 (T-50), and B-D-48-6 (T-90). 47

Figure 5-2. Percent H2, CO2, and O2 for Experiment 2. Experiments were re-gassed with hydrogen at 150 days. 50

Figure 5-3. Relative abundance of phylum from DNA sequencing results for Experiment 2. Although in this figure the high heat samples shows higher diversity, due to low DNA recovery this data is probably due to noise. 51

Figure 5-4. Alpha diversity from DNA sequencing shows the heated clays have reduced microbial diversity. 52

Figure 5-5. For the non-heated (T-ambient) samples different rates of H_2 consumption were observed. Analysis here shows alpha diversity is higher in samples with higher H_2 consumption. 52

Figure 5-6. Percent H_2, CO_2, and O_2 for Experiment 3. 55

Figure 5-7. Percent H_2, CO_2, and O_2 for Experiment 4 after O_2 was reduced at 120 days. 56

Figure 5-8. DNA sequencing results for Experiment 4. 57

Figure 5-9. Alpha diversity index for Experiment 4, showing as before in Experiment 2 that heating reduces microbial diversity. 58

Figure 6-1. Relationship between measured gravimetric density of calibration samples and CT number from X-ray CT images. The equation derived from the data-fitting was then used to compute bentonite bulk wet density from X-ray CT scans during the experiment. 65

Figure 6-2. The metal coupons used in the heated and non-heated columns. The color bars in the figure bound the surface roughness, varying from 0 to 2276 um in the top right figure due to the induced dent, and 0-287 µm in the bottom right figure without dent. 66

Figure 6-3. Cross-sectional CT images of the two compacted columns that are used for a heating and hydration experiments. The blue curve presents the dry density profile calculated from the bulk CT density and the water content. 67

Figure 6-4. 3-D CT images showing the initial density distribution in the non-heated (a) and heated (b) columns. (c) and (d) present key instrumentations—heater and heater shaft, thermocouples, tracer particles, metal coupons, ERT and sensor wires 68

Figure 6-5. The 3-D clay density maps showing the spatial and temporal variations of clay density in the HotBENT Lab #2 non-heated column for 426 days. The sub-image at t=0 shows the initial condition after packing, with the low-density packing cavities. (b) Comparison of the 2-D images at 0 and 10 days when clogging of water flow path happened. The white arrows in (b) mark the invasion of swelling bentonite into the surrounding sand layer and water flow pathway. The yellow dotted box in (a) represents the axial location of the selected 2-D images in (b). 69

Figure 6-6. HotBENT Lab #2 non-heated column: (a) the radially averaged density map and changes with time for the non-heated column subject to hydration for 426 days, (b) the average density vs. radial distance from the center shaft along the white dotted line #1 in (a), and (c) the average density vs. radial distance from the center shaft along the white dotted line #2 in (a). 70

Figure 6-7. HotBENT Lab #2 temperature variations as a function of time and radial distance from the heater shaft in the heated column for 500 days (left) and for 13 days (right) 71

Figure 6-8. The 3-D clay density map and temporal variations in the heated column. The sub-image at T=0 day shows the initial condition after packing column packing and sensors installation. 72

Figure 6-9. (a) The radially averaged density map and changes with time for the heated column subject to heating and hydration for 129 days. (b) The average density vs. radial distance from the center shaft along the white dotted line in (a).....73

Figure 6-10. Comparison of the changes of radially averaged density vs. radial distance from the heater shaft in the two sets of heated columns in HotBENT Lab #1 and #2.....74

Figure 6-11. Photograph and CT image of the bentonite clay used for HotBENT Lab #2 test. 75

Figure 6-12. HotBENT Lab #2 non-heated column (a) Selected time-lapse 2-D CT images showing the displacement of the selected tracer particle and temporal density distributions in the non-heated column. (b) The magnified images showing the displacement of the tracer particle relative to its initial location marked by the crossing of the white dotted lines. (c) Variations of displacement as a function of time for the selected tracer particles in (a), and another two selected in the low-density segment. The white dotted boxes in (a) bound the magnified images in (b), and the particles selected in (c) at 59 and 40 mm away from the central shaft and at 1.68 g/cm^3 initial bentonite density. 76

Figure 6-13. HotBENT Lab #2 heated column (a) Selected time-lapse 2-D CT images showing the displacement of the selected tracer particles and temporal density distributions in the heated column. (b) The magnified images showing the displacement of the tracer particle relative to its initial location marked by the crossing of the white dotted lines. (c) Variations of displacement as a function of time for the selected tracer particles. The white dotted boxes in (a) bound the magnified images in (b).....77

Figure 6-14. HotBENT Lab #2 plane locations of emplaced tracer particles along the axial direction of the column.....78

Figure 6-15. The radial strain vs. time in the HotBENT Lab #2 non-heated column measured by the tracer particles emplaced in different radial and axial locations. 79

Figure 6-16. The axial z-displacement in the HotBENT Lab #2 non-heated column measured by the tracer particles emplaced in different radial and axial locations. 80

Figure 6-17. The radial strain vs. time in the HotBENT Lab #2 heated column measured by the tracer particles emplaced in different radial and axial locations. 81

Figure 6-18. The axial z-displacement in the HotBENT Lab #2 heated column measured by the tracer particles emplaced in different radial and axial locations. 82

Figure 6-19. Apparent resistivity of the (a) heated and (b) non-heated column post data processing. The points mark the median apparent resistivity value from each data acquisition (i.e., time point), and the error bars show the log-scaled interquartile range of resistivity values.....83

Figure 6-20. Time-lapse ERT of the non-heated column.....84

Figure 6-21. Time series of ERT resistivity of the non-heated column: averaged resistivity of (a) the entire column and (b) in the high and low dry bulk density layers. The shaded regions represent one standard deviation from the mean value. 84

Figure 6-22. Time-lapse ERT of the heated column. The dashed line separated the reference color bars for visualization. 85

Figure 6-23. Time-lapse 2D temperature distribution of the heated column. The dashed line separated the reference color bars for visualization. 85

Figure 6-24. Time-lapse temperature corrected ERT of the heated column. 86

Figure 6-25. Time series of averaged ERT resistivity of the entire heated column (a) without and (b) with temperature correction. 86

Figure 6-26. Non-heated column. (a) Petrophysical fitting result between column saturation degree and resistivity using a simplified Archie Law. Radial profiles of (b) depth-averaged ERT resistivity [Ωm] and (c) calibrated saturation degree [m^3 m^{-3}]. Each curve represents one data acquisition with the corresponding day labeled on the color bar. 87

Figure 6-27. Heated column. (a) Petrophysical fitting result between column saturation degree and resistivity using a simplified Archie Law. Radial profiles of (b) depth-averaged, temperature-corrected ERT resistivity [Ωm] and (c) calibrated saturation degree [m^3 m^{-3}]. Each curve represents one data acquisition with the corresponding day labeled on the color bar. 88

Figure 6-28. Images from dismantling of the HotBENT Lab #2 experiment. Clockwise from top left, (a) images of ring placement and map of sample removals, (b) sample removed for analysis, (c) residual central layer preserved for future analysis, and (d) bulk sample. 89

Figure 6-29. Water content, dry density, and degree of saturation measured from samples removed from the non-heated column. 90

Figure 6-30. Water content, dry density, and degree of saturation measured from samples removed from the heated column. 90

Figure 7-1. A benchmark model for Subtask A. 93

Figure 7-2. Schematic diagram of the HLW disposal cells for HLW waste packages (ANDRA, 2005) 93

Figure 7-3. Schematic diagram of two-clay buffer layer EBS (Zheng et al., 2014) 94

Figure 7-4. The schematic design of subtask C (Zheng et al., 2014). 94

Figure 7-5. The concentration profiles of Cl, pH, C, and S at different times. The interface is located at a distance of 0.5m. 105

Figure 7-6 The concentration profiles of K, Na, Ca, and Mg at several times. The interface is located at a distance of 0.5m. 106

Figure 7-7 The concentration profiles of Si and Al at different times. The interface is located at a distance of 0.5m. 106

Figure 7-8. The volume fraction of portlandite, C2AH6, monocarboaluminate and CSH at several times. 107

Figure 7-9. The volume fraction of ettringite and hydrotalcite at several times. 107

Figure 7-10. The volume fraction of gypsum and calcite at several times. 108

Figure 7-11. The volume fraction of montmorillonite and illite at several times. 108

Figure 7-12 The concentration profiles at several times for Cl, pH, C, and S. The interface is located at a distance of 0.5m. 110

Figure 7-13 The concentration profiles at several times for K, Na, Ca, and Mg. The interface is located at a distance of 0.5m. 111

Figure 7-14 The concentration profiles at several times for Si and Al. The interface is located at a distance of 0.5m. 111
Figure 7-15 The volume fraction of portlandite, C2AH6, monocarboaluminate and CSH at several times. 112
Figure 7-16. The volume fraction of ettringite and hydrotalcite at several times. 112
Figure 7-17. The volume fraction of gypsum and calcite at several times. 113
Figure 7-18. The volume fraction of montmorillonite and illite at several times. 113
Figure 8-1. Planned timeline for HotBENT experiment (Kober & Schneeberger, 2022). 118
Figure 8-2. Location of the FEBEX Drift at the Grimsel Test Site (NAGRA, 2017). 118
Figure 8-3. Final HotBENT design with individual modules and key construction milestones (Kober et al., 2022). 118
Figure 8-4. The heating procedure at HotBENT (Kober & Schneeberger, 2022). 119
Figure 8-5. Sensor layout around Heater 1. 119
Figure 8-6. Graphs of temperature measured at S4 (the middle of H1) (Kober, 2022). 120
Figure 8-7. Graphs of thermal conductivity measured at S16, S8, S21, S23 (Kober, 2022). 120
Figure 8-8. Graphs of relative humidity measured at S21, Heater 4 (Kober, 2022). 121
Figure 8-9. Graphs of pore pressure measured at S4 (Kober, 2022). 121
Figure 8-10. Structure of HotBENT modeling platform (Kober, 2022) 122
Figure 8-11 Numerical grid used in 2-D TH model (y-z cross section. 123
Figure 8-12. Time-series results of temperature in the buffer. 126
Figure 8-13. Time-series in the host rock. 127
Figure 8-14 Time-series results for temperature (thermal conductivity of Bentonite (dry/wet) – 0.1/0.9 W/m /°C). 128
Figure 8-15. Time series results of liquid saturation. 129
Figure 8-16. Time series results of relative humidity. 130
Figure 10-1 Possible scenario for bentonite-colloid facilitated transport of radionuclides away from a corroded waste package. Waste package breach coincides with fracture formation in the bentonite buffer and the formation of bentonite colloids at the buffer-host rock interface. Radionuclides sorbed to colloids are transported away from the EBS via fractures in the host rock. Figure from Missana & Geckeis (2006) 132
Figure 10-3. Conceptual diagram of high-temperature alteration products at a stainless steel-bentonite interface (modified from Cheshire et al., 2018). 136
Figure 10-4. SEM-EDS characterization of unreacted ESD cement: (a) Backscatter (BSE) image of ESD cement, showing relative areas of high-calcium ("calcite") and high-silica (SiO2) regions at a mm scale; (b) EDS map of calcium abundance; (c) EDS map of carbon abundance; (d) EDS map of Si abundance; and (e) EDS map of O abundance. Note co-occurrence of relative abundances of calcium with carbon, and of silica with oxygen 139

Figure 10-5. pH of the sampled fluids as measured at bench conditions. 141
Figure 10-6. Concentration in mg L^{-1} of calcium in the sampled fluids. 142
Figure 10-7. Concentration in mg L^{-1} of sodium in the sampled fluids. 143
Figure 10-8. Concentration in mg L^{-1} of potassium in the sampled fluids. 143
Figure 10-9. Concentration in mg L^{-1} of silica in the sampled fluids. 144
Figure 10-10. Concentration in mg L^{-1} of aluminum in the sampled fluids. 145
Figure 10-11. Concentration in mg L^{-1} of chloride in the filtered reaction fluids. 146
Figure 10-12. Concentration in mg L^{-1} of sulfate in the filtered reaction fluids. 147
Figure 10-13. QXRD patterns of reacted bentonite and granodiorite from IEBS-0, -6, -8, -9, and -10 compared to unreacted bentonite and granodiorite. Peaks correspond to smectite (Sme), mica, clinoptilolite-heulandite (Cpt-Heu), albite (Ab), corundum (Crn), feldspar (Fsp), quartz (Qtz), pyrite (Py), magnetite (Mag), and smectite-feldspar (Sme-Fsp) 148
Figure 10-14. QXRD patterns of reacted cement from IEBS-6 and -8 compared to unreacted OPC. Peaks correspond to smectite (Sme), zeolite (Zeo), clinoptilolite (Cpt), portlandite (Por), albite (Ab), calcite (Cal), brownmillerite (Bmlr), heulandite (Hul), and larnite (Lrn). 149
Figure 10-15. QXRD patterns of reacted cement from IEBS-9 and -10 compared to unreacted experimental low-pH cement. Peaks correspond to smectite (Sme), brownmillerite (Bmlr), wollastonite (Wo), calcite (Cal), and quartz (Qtz). 149
Figure 10-16. QXRD patterns of reacted cement from the CEM series experiments compared to unreacted ESD cement. Peaks correspond to tobermorite (Tbm), silica (SiO_2), and calcite (Cal). 150
Figure 10-17. XRD patterns of the oriented, ethylene glycol-saturated, <2 µm fraction from IEBS-6, -8, -9, and -10 compared to that of unreacted WY bentonite. Presented values are d-spacings for major glycolated smectite (GS) peaks. 151
Figure 10-18. SEM micrographs of ESD cement chips reacted in CEM-1 and CEM-3. (a). BSE images of the surface of a ESD cement chip reacted at 100 °C, with inset showing the morphology of secondary phases at the cement surface. EDS analyses showed these phases are chemically consistent with calcium carbonate species (calcite, aragonite). (b). SE images of the surface of a cement chip reacted at 200 °C showing the morphology of secondary phases at the cement surfaces. The phases were identified as CSH by morphology and EDS analysis. 155
Figure 10-20. Zeolite formation in experiments that reacted OPC. (a). Zeolites (Na-Ca bearing analcime) formed in the clay groundmass reacted in IEBS-8, along with collocated garronite. (b). Na-Ca bearing zeolite noted as analcime/wairakite, identified in the bentonite groundmass reacted in IEBS-6. 159
Figure 10-21. VU cement reacted in IEBS-9. Substantial deterioration of the cement product is visible at the macroscale. 161
Figure 10-22. BSE images unreacted ESD cement and of the reaction rims at formed at three different temperatures, as viewed from cross-sections formed from the ESD cement cylinders. (a). BSE image of unreacted ESD cement; (b). ESD cement reacted at 100 ºC in CEM-1; BSE image of unreacted ESD cement; (c). ESD

cement reacted at 150 ºC in CEM-2; BSE image of unreacted ESD cement; (d). ESD cement reacted at 200 ºC in CEM-3 162

Figure 10-23. Ca and Si solubility with respect to select minerals of interest at the conditions of the initial GW solution. Each curve represents a concentration where the saturation index (SI)=0 in the GW solution over temperature. The area above a curve then indicates oversaturation and thermodynamic pressure toward precipitation, while the area below a curve indicates undersaturation and tendency toward dissolution. The symbols mark the concentration of Ca or Si in each experiment as analyzed in the penultimate sample collected before experiment termination. a. Geochemical stability with respect to Ca-bearing minerals portlandite, anhydrite, tobermorite, and calcite. b. Geochemical stability with respect to SiO_2-bearing minerals quartz, analcime, and tobermorite. 164

Figure 10-24. Comparison of K and Na concentrations from three selected experiments: IEBS-0 (bentonite and GW at 250 ºC), IEBS-9 (bentonite, GW, and VU cement at 200 ºC), and CEM-3 (ESD cement and GW at 200 ºC). 166

Figure 11-1 Schematic of the HotBENT heater test. Heaters are depicted in brown with the temperature indicated. BCV, Czech bentonite (figure adapted from AMBERG, 2019). 169

Figure 11-2. Concentration in mg L^{-1} of pH, SiO_2, Fe, and Al in HBT-1 through -5. 175

Figure 11-3. Concentration in mg L^{-1} of Na, K, Ca, and Mg in HBT-1 through -5. 176

Figure 11-4. Concentration in mg L^{-1} of Cl and SO_4 in HBT-1 through -5. 177

Figure 11-5. QXRD patterns of reacted bentonite from HBT-1 and -5 compared to unreacted FE bentonite. Peaks correspond to smectite (Sme), mica, kaolinite (Kln), quartz (Qtz), corundum (Crn), albite (Ab), and calcite (Cal). 178

Figure 11-6 QXRD patterns of reacted bentonite from HBT-2 and -4 compared to unreacted BCV bentonite. Peaks correspond to smectite (Sme), mica, kaolinite (Kln), quartz (Qtz), feldspars (Fsp), corundum (Crn), albite (Ab), and calcite (Cal) 179

Figure 11-7. QXRD patterns of reacted bentonite from HBT-3 compared to the unreacted FE-BCV mixture. Peaks correspond to smectite (Sme), quartz (Qtz), corundum (Crn), albite (Ab), and calcite (Cal). 179

Figure 11-8. QXRD patterns of reacted ESD cement from HBT-5 compared to unreacted ESD cement. Peaks correspond to felspar (Fsp), silica (SiO_2), halite (Hal), and calcite (Cal). 180

Figure 11-9. XRD patterns of the oriented, ethylene glycol-saturated, <2 µm fraction from HBT-1 through -5 compared to that of unreacted bentonite. Presented values are d-spacings for major glycolated smectite (GS) peaks. 181

Figure 11-10. Images from BSE analysis of ESD cement reacted in HBT-5, in contact with FE-bentonite. A reaction rim was observed at the cement surface as well as isolated sections of adhered smectite. 186

Figure 11-11. ESD cement round post-reaction in HBT-5. (a). BSE image of the cement mount in cross section, showing an area mapped for chemical analysis in the inset box. (b). EDS map of Si counts mapped in the area of the inset box. (c). EDS map of Al counts from the same area. (Fig 35) 189

Figure 11-12. K and Na concentrations from CEM-3, that reacted ESD cement with synthetic Grimsel groundwater at 200 ºC; and HBT-5, that reacted the same ESD cement with FE bentonite in synthetic Grimsel groundwater. 190
Figure 12-1. The FE experiment at the Mont Terri underground laboratory 193
Figure 12-2. Schematic diagram of model geometry for Step 1 simulations. 194
Figure 12-3. Model geometry for Step 0 (cross-section view of tunnel). 194
Figure 12-4. Geometry and meshing used for Step 1c simulations. 194
Figure 12-5. Representation of shotcrete used for Step 1c simulations. 195
Figure 12-6. Representation of the experimental tunnel, Step 1c simulations. 195
Figure 12-7. Prediction of temperature distribution at 1800 days. 197
Figure 12-8. Location of observation points in the granular bentonite near Heater 2 (Points 2, 3) and, 20 cm away from Heater 2 (Points 6, 7 and 9) 198
Figure 12-9. Model temperature prediction at early time at selected observation points in the granular bentonite 199
Figure 12-10. Model gas saturation prediction at early time at selected observation points in the granular bentonite 199
Figure 12-11. Temperature comparison at observation point 7 (Model and Experimental). 200
Figure 12-12. Relative humidity comparison at observation point 7 (Model and Experimental). 200
Figure 12-13. Temperature comparison at observation point 7, effect of shotcrete thermal conductivity. 201
Figure 12-14. Location of observation point 2 in the opalinus clay, close to the experimental tunnel. 201
Figure 12-15. Pressure comparison at observation point 2 in the opalinus clay (Model and Experimental) 202
Figure 12-16. Temperature comparison at observation point 2 in the opalinus clay (Model and Experimental). 202
Figure 12-17. Comparison of pressure predictions at observation point 2 in the opalinus clay, effect of shotcrete permeability. 203
Figure 13-1. Results from MD simulations showing average layer spacing of glycoboehmite as a function of butanediol loading. Results from DFT calculations measurements and XRD (Inoue et al., 1989) are shown for comparison. 205
Figure 13-2. Snapshot of GB from CMD simulations at a) 0.5 diols/u.c and b) 2.0 diols/u.c.; corresponding DFT-optimized structures c) 0.5 diols/u.c and d) 2.0 diols/u.c. (Al=purple, O_boehmite=red, C=gray, H=white, O_alcohol=blue). 206
Figure 13-3. Results from CMD simulations of GB showing the layer spacing as a function of temperature for loadings of 1.0 and 2.0 diols/u.c. Error bars are shown as lines. 207
Figure 13-4. Radial distribution functions, g(r), as functions of pair separation distance (Å) for various atom pairs in the (a) AIMD and (b) CMD simulations at 573 K of the chemisorbed GB models corresponding to low loading (1.0 diols/u.c.). 207

Figure 13-5. Average value and standard deviation of glycoboehmite zeta potential as a function of pH. 208

Figure 13-6. ICP-OES results from GB cation exchange experiments showing uptake of Mg^{2+}, Ca^{2+}, and Ni^{2+} along with release of K^{+} 209

Figure 13-7. Results from batch sorption experiments showing I^{-} adsorption coefficient (kD) for (left) as-synthesized and cation-exchanged GB at natural pH of the material (5.8–6.0), and (right) as-synthesized and Ni-exchanged GB while adjusting the pH to 7.0. 209

Figure 14-1. Project workflow combining a variety of characterization equipment; outlines how simulation results can be compared to experimental data. 212

Figure 14-2. AIVIA software segmentation workflow, with final layer segments within the cement shown on the far right. 216

Figure 14-3. Previously reported nanoindentation results are shown on the left, with the updated results that include an additional region are shown on the right. 217

Figure 14-4. Comparison of the cement phases on indented hydrates in cement Zones A B and C. 217

Figure 14-5. Comparison of the reduced modulus values to the Si/Ca ratio of indents on hydrates in Zone A 218

Figure 14-6. Model carbonation front predictions (from Gruber et. al. 2022). 219

LIST OF TABLES

Table 2-1. Measurement of cations exchange capacity and relative contributions of cations to CEC. 9

Table 2-2. Summary of clay swelling pressure (P) affected by Na^+/K^+ ratios....10

Table 2-3. Summary of clay swelling pressure (P) affected by ionic strength. 12

Table 2-4. Measurement of interlayer hydration state (basal spacing) and osmotic swelling of montmorillonite (Kunipia-F) as a function of ionic strength and cation types by using SAXS (d values are obtained from d = 2π/q)....16

Table 4-1. Diffusion parameters for diffusion of NaCl though PEEK filters. 35

Table 4-2. Results of Se(IV) and Se(VI) batch sorption experiments with 10 g/L montmorillonite in 0.1 M NaCl at pH 6. The starting Se concentration was 100 μM. 35

Table 4-3 Summary of measured diffusion parameters, including dry bulk density, porosity, and normalized mass flux (J_N). 36

Table 5-1. Experimental descriptions. 48

Table 5-2. Groundwater media used for Experiment 4....59

Table 5-3. Cation and anion data for Experiment 4. BDL = below detection limit. GW = artificial groundwater, st = sterilized sample 59

Table 6-1 Differences in design between the two HotBENT experiments....63

Table 6-2. Differences in water chemistry in HotBENT Lab #1 and HotBENT Lab #2. For HotBent Lab #1 we used an artificial groundwater and HotBENT Lab #2 we used simulated Grimsel water. 64

Table 6-3. List of analysis to be completed on the clay removed from the HotBENT experimental column. 91

Table 7-1 Initial mineral and exchanger composition of MX-80 (Idiat et al., 2020)....95

Table 7-2 Mineral composition of oven-dried MX-80 (Bradbury & Baeyens, 2003)....95

Table 7-3 Initial mineral and exchanger composition of MX-80 (Idiat et al., 2020)....96

Table 7-4. Calculated initial porewater composition for MX-80 by SKB and LBNL 97

Table 7-5. Suggested mineralogical phase assemblage and exchanger composition of the OPC concrete (Rasmusson, 2022)....98

Table 7-6. Calculated initial porewater composition for OPC (Rasmusson, 2022)....98

Table 7-7. Suggested mineralogical phase assemblage and exchanger compositions of the low pH OPC concrete (Rasmusson, 2022). 99

Table 7-8. Calculated initial porewater composition for OPC (Rasmusson, 2022)....99

Table 7-9. The kinetic rate for the primary and secondary minerals in OPC. 101

Table 7-10. The kinetic rate for the primary and secondary minerals in MX-80. 102

Table 7-11. The kinetic rate for the primary and secondary minerals in LPC....103

Table 7-12. The saturation index (log (Q/K) for the initial pore water of OPC and MX-80....104

Table 7-13. The initial pore water composition for OPC in Subtasks A1 and A3. 109
Table 8-1. Description of tasks of the model platform in the HotBENT project.....122
Table 8-2. Thermal and hydrodynamic material properties.....124
Table 8-3. Initial liquid saturation of materials. 125
Table 10-1 Parameters for experiments completed in FY23 and experiments from previous years that had new analytical results collected in FY23. Detailed information on reactants is included in Section 10.2.2 below. All values are mass (g) except where otherwise noted. 138
Table 10-2. Major element chemistry of the experimental and make-up fluids. 140
Table 10-3. Glycolated smectite (GS) peak positions for the < 2 µm clay fraction separated from the Wyoming bentonite. Expandability and percent illite (%I) were calculated based on the difference in position of the 002 and 003 glycolated smectite peaks. 152
Table 10-4. X-Ray fluorescence (XRF) analyses of the starting materials and solid reactants from IEBS-0, -6, -8, -9, & -10. 153
Table 11-1 Summary of the expected temperature gradient for the 200 ºC heater scenario of the HotBENT long-term (5-20 year) experiments (AMBERG, 2019).....169
Table 11-2. Parameters for the HBT experiment completed in FY23 as well as those completed in FY21 and FY22. Detailed information on reactants is included in Section 11.2.2 below. All values are mass (g) except where otherwise noted. 172
Table 11-3. Glycolated smectite (GS) peak positions for the < 2 µm clay fraction separated from the FE and BCV bentonites. Expandability and percent illite (%I) were calculated based on the difference in position of the 002 and 003 glycolated smectite peaks. 182
Table 11-4. Weight percent oxides in unreacted and reacted solid materials. 184
Table 12-1. Heating schedule for the three heaters (Task C Specifications).....196
Table 12-2. Calibrated properties. 197
Table 14-1. Characterization Summary 213
Table 14-2. Layer Property Summary 216
Table 14-3. Result Summary – Modeling vs. Experimental. 219

ACRONYMS

1D	one-dimensional
2D	two-dimensional
3D	three-dimensional
AI	artificial intelligence
AIMD	ab initio molecular dynamics
ALS	advanced light source
BCV	Czech bentonite
BSE	backscatter
C(A)SH	calcium alumino silicate hydrate
CEC	cation exchange capacity
CMD	classical molecular dynamics
CSH	calcium silicate hydrate
CT	computed tomography
cryoET	Cryo-electron tomography
DFT	density functional theory
DNA	deoxyribonucleic acid
DOE	U.S. Department of Energy
DPC	dual-purpose canister
EBS	engineered barrier system
EDS	energy dispersive spectroscopy
EDZ	excavation damage zone
EMP	Electron Microprobe
EOS	equation of state
ERT	Electrical Resistivity Tomography
ESDRED	Engineering Studies and Demonstrations of Repository Designs
ESEM	environmental scanning electron microscope
FE	Wyoming bentonite
FEBEX	Full-scale Engineered Barrier EXperiment
FY	fiscal year
GB	glycoboehmite
GBM	granulated bentonite material
GC	gas chromatograph
GCMC	grand canonical Monte Carlo
GW	groundwater
HLW	high-level waste
HotBENT	High Temperature Effects on Bentonite)
ICP-MS	Inductively Coupled Plasma – Mass Spectrometer
IEBS	International Engineered Barrier Systems project
IEP	isoelectric point
KMMT	Potassium Montmorillonite
LBNL	Lawrence Berkley National Laboratory
LCS	low carbon steel
LOI	loss on ignition

MMT	Montmorillonites
ML	machine learning
MSE	mean square error
MSM	minimal salts media
MTU	Metric Tons of Uranium
NAGRA	National Cooperative for the Disposal of Radioactive Waste (Switzerland)
NaMMT	sodium montmorillonite
NFST	Nuclear Fuels Storage and Transportation Planning Project
NRC	Nuclear Regulatory Commission
OD	outer diameter
OPC	Ordinary Portland Cement
PCR	Polymerase Chain Reaction
PVP	polyvinylpyrrolidone
PZC	Point of Zero Charge
QXRD	quantitative X-ray diffraction
R&D	research & development
SAXS	Small angel X-ray scattering
SCM	surface complexation model
SEM	scanning electron microscopy
SFWD	spent fuel and waste disposition
SFWST	spent fuel waste science and technology
SKB	Swedish Nuclear Fuel and Waste Management Company
SNL	Sandia National Laboratory
SWRC	soil water retention curves
THMC	thermal, hydrological, mechanical, and chemical
TLM	Triple Layer Model
UNF-ST&DARDS	Used Nuclear Fuel – Storage, Transportation & Disposal Analysis Resource and Data Systems
URL	underground research laboratory
VU	Vanderbilt University
WHAM	weighted histogram analysis method
WRR	water:rock ratio
XRD	X-ray diffraction
XRF	X-Ray fluorescence

SPENT FUEL AND WASTE DISPOSITION EVALUATION OF ENGINEERED BARRIER SYSTEMS FY23 REPORT

1. INTRODUCTION

This report describes research and development (R&D) activities conducted during Fiscal Year 2023 (FY23) specifically related to the Engineered Barrier System (EBS) R&D Work Package in the Spent Fuel Waste Science and Technology (SFWST) Campaign supported by the United States (U.S.) Department of Energy (DOE). This report fulfills the SFWST Campaign deliverable M2SF-23SN010308051.

The R&D activities focus on understanding EBS component evolution and interactions within the EBS, as well as interactions between the host media and the EBS. The R&D team represented in this report consists of individuals from Sandia National Laboratories, Lawrence Berkeley National Laboratory (LBNL), Los Alamos National Laboratory (LANL), and Vanderbilt University. EBS R&D work also leverages international collaborations to ensure that the DOE program is active and abreast of the latest advances in nuclear waste disposal.

High-level Purpose of this work: A primary goal of the EBS work package is to advance the development of process models that can be implemented directly within the Generic Disposal System Analysis (GDSA) platform. Improved process models can contribute to the safety case in several ways, such as:

- building confidence and improving the robustness of the performance assessment,
- providing further insight into the processes being modeled, establishing better constraints on parameters critical to repository performance, and
- assessing technical readiness of EBS designs and/or components.

A major focus of this work is to understand the processes that will impact and control the permeability and/or transport in the EBS. Permeability evolution in the geotechnical seal system is typically a major driver of repository performance, or otherwise an important scenario that needs to be evaluated in self-sealing host media. The interfaces of the EBS components, including those with the disturbed rock zone (DRZ), play a critical role in the near-field environment, where complex processes have a significant impact on overall transport and fate of radionuclides.
Improved understanding of these interfaces requires capabilities to characterize, test, and model the EBS, in such a way that relevant complex phenomena are captured and represented. EBS process are often coupled, e.g., thermal- hydrologic-mechanical-chemical (THMC), multi-scale (from molecular to continuum scale), and nonlinear (e.g., multi-phase flow).
The FY23 EBS report includes results from modeling, analysis, and experimental work and is focused on several key themes:

- Improved understanding and model representation of coupled processes, e.g., thermal-hydrologic-mechanical-chemical (THMC), in EBS materials, with a particular focus on swelling behavior and high temperature effects on bentonite buffer materials.
- Investigation and characterization at multiple length scales – from molecular to mesoscale to continuum scale - to understand near-field process models for radionuclide retention and transport through the EBS and disturbed rock zone.
- Field scale testing and analysis to validate and improve process modelling tools and overall conceptual understanding of complex processes in the *in situ* setting.

These themes are investigated in various ways within the EBS work package, with projects ranging from molecular dynamic simulations, to bench-scale testing and characterization, and all the way up to the drift-scale testing and demonstration in underground research laboratories.
The contents of this reports are summarized in detail below:

- **Chemical Controls of Montmorillonite Structure and Swelling Pressure (Section 2)**

Section 2 presents the progress of research activity combining microscopic experimental and simulation studies to address the mechanical-chemical coupling in bentonite. The previous work focused on modeling the effect of exchangeable cations on the swelling stress of pure smectite using molecular dynamic models and developing an experimental apparatus that can measure the swelling pressure of compacted clay, as well as key aspects of the clay microstructure using synchrotron X-ray methods and specialized oedometer. In FY23 we conducted a series of experiments to assess the influence of ionic strength and type of cations on clay swelling pressure and microstructure via adjusting the type of solutions (NaCl vs KCl solutions) and the K+/Na+ ratios in NaCl + KCl mixtures.the K^+/Na^+ ratios in NaCl+KCl mixtures on clay swelling pressure and microstructure.

- **Molecular Modeling of Radionuclide Retention by Bentonite (Section 3)**

Section 3 presents an effort to improve the parametrization and performance of meso- and macroscopic models (such as surface complexation model, SCM) of radionuclide migration in the bentonite barrier via molecular modeling and Artificial Intelligence/Machine Learning methods. In FY23, we developed a computational pipeline to generate synthetic datasets, train AI/ML models, and used these trained models as the SCM surrogate for the case of uranium sorption to oxides at varying environmental conditions.

- **Experimental Investigations of Bentonite nd Other Clay-based Materials (Section 4)**

Section 4 presents the results of experimental and modeling studies of the diffusion and adsorption of Se. After finishing the 3H and Se(VI) through-diffusion experiments using a well-characterized, purified montmorillonite source clay (SWy-2) and the preliminary modeling of these experiments FY22, the work accomplished in FY23 includes (1) diffusion experiments conducted on the filters, which will allow better modeling interpretation of the diffusion data for 3H and Se(VI) in the through-diffusion experiments; (2) a new set of ongoing diffusion experiments conducted with Se(IV) under the same conditions as the experiment with Se(VI) and Se batch adsorption experiments on montmorillonite; and (3) a newly released graphical user interface, CrunchEase, which is based on the reactive transport code CrunchClay and can be used to simulate diffusion processes in an explicit and user-friendly manner.

- **Coupled Microbial-Abiotic Processes in EBS and Host Rock Materials (Section 5)**

Section 5 presents the study of microbial-abiotic processes in EBS and host rock materials. Experiments on potential microbial activity in materials collected from the FEBEX experiment were conducted to understand the change of microbial activity for samples after long-term heating and hydration. Samples were incubated in non-enriched minimal conditions and experiments were designed to determine if these materials possess microbial communities with the ability to metabolize H2 or other substrates, and to assess how the FEBEX test impacted those capabilities. The findings indicate that there is still a considerable metabolic potential within the microbial communities, underscoring the significant role of microbial metabolism in long-term nuclear waste disposal repositories employing clay as a barrier material.

- **Heating and Hydration Column Test on Bentonite (Section 6)**

Section 6 presents the benchtop-scale high-temperature column experiments, HotBENT-Lab, in support of the HotBENT field tests. In FY22, the first set of columns, HotBENT-Lab #1, was completed and extensive data sets were collected during the test and after the column dismantling. In FY23, we conducted the HotBENT-Lab #2 test, which differed from the HotBENT-Lab #1 in the following features: (1) bentonite type, (2) initial bentonite density and water content, (3) water chemistry, and (4) hydration pressure. After observing HotBENT-Lab #2 for over one year, it was found that a steady state was reached under conditions of no changes of temperature and hydration, the columns were then dismantled to measure chemical and physical changes within the column materials. Section 6 includes the monitoring results and a preliminary analysis of data obtained after the column dismantling.

- **Modeling the Concrete/Bentonite Interface: Task 12 in the SKB EBS Task Force (Section 7)**

Section 7 presents a modeling effort as part of the Task 12 of SKB EBS Task Force to simulate the bentonite/concrete interaction. The overall goal of of all modeling teams invovled in this task is to collaboratively simulate long-term reactions occurring at cement-bentonite interfacial regions taking into account mineralogical, chemical, and textural changes. In this section, we document the results of FY23 LBNL's activities focused on simulations of the benchmark problem identified in Task 12 of the SKB EBS task force.

- **Understanding the THMC Evolution of Bentonite using Large-scale Field Experiments: HotBENT (Section 8)**

Section 8 presents the endeavor of using the large-scale field experiment HotBENT to understand the THMC evolution of bentonite under high temperature. This section contains two parts. In the first part, we give an update on the current status of the HotBENT field test. In the second part, we present the preliminary model of the HotBENT field test.

- **Hydrothermal Alteration of EBS Interfaces (Section 9)**

Section 9 summarizes hydrothermal experiments reacting EBS materials in an analogue crystalline host rock environment, specifically through experiments that include combinations of Wyoming bentonite + Grimsel granodiorite + Grimsel granodiorite synthetic groundwater ± stainless/low carbon steel ± OPC or low-pH cement. Results from these experiments include: 1) SEM images and EDS data, 2) QXRD data, 3) clay mineral XRD data, 4) electron microprobe data for major mineral phases, and 5) aqueous geochemistry data.

- **Hydrothermal Testing to Support the HOTBENT Field Test (Section 10)**

Section 10 presents hydrothermal experiments were designed to understand geochemical and mineralogical changes that may occur in the EBS at the HotBENT conditions. Experiments completed in FY23 included different combinations of the two bentonites (FE and BCV) plus cement with groundwater (synthetic Grimsel granodiorite groundwater). In FY22, an experiment was completed that included Grimsel granodiorite wall rock as a reactant in addition to BCV bentonite and LCS.

- **Calibrated Simulations of a Full-scale Heater Experiment in Opalinus Clay (Section 11)**

Section 11 presents preliminary thermal-hydrologic simulations of Task C, Step 1 were conducted using PFLOTRAN numerical code and a 3-D geometry. The simulations included blind predictions using parameter values developed in Step 0 of Task C, as well as calibration predictions with varied parameter values. Temperature evolution results at selected observation points were close to experimental data. Blind predictions of opalinus clay pressure values were much lower than experimental. Predicted pressure evolution at selected observation points for the calibration runs were very close to experimental data.

- **Synthesis, Characterization, and Evaluation of Modified Boehmite as Anion Sorbent Additive in EBS Design (Section 12)**

Section 12 presents investigations into development of anionic sorbent material that could be used as an additive to bentonite buffer or as part of the plugging/sealing systems in the EBS. Anionic species (e.g., Iodine -129) typically drive repository performance, as transport of these species is not impeded as efficiently (relative to cationic species) by traditional EBS components. This effort is focused on modifying layered AlOOH (boehmite) to develop hybrid materials whose internal and external surfaces can be altered for high selectivity for specific radionuclides.. Molecular modeling was used to evaluate glycoboehmite (GB) structural and spectroscopic properties as a function of butanediol loading, and batch sorption experiments were used to evaluate iodide uptake capacity of ion-exchanged GB.

- **Chemo-Mechanical Characterization of Cement-Rock Interfaces (Section 13)**

Section 13 presents research that: (i) characterizes chemical and mechanical changes within the alteration zones of both the cements and the minerals after controlled aging processes; (ii) identifies structural and chemical features that affect the fate of radionuclides at the interface of dissimilar materials; and (iii) provides a basis to verify predicted changes in major mineral phase composition and distribution that affect the diffusion-controlled transport of tracer constituents using reactive transport modeling.

The above activities are integrated with the SFWST 2019 Roadmap. Please see Appendix A for an evaluation of progress towards addressing EBS-related SFWST Roadmap priorities.

This page is intentionally left blank.

2. CHEMICAL CONTROLS ON MONTMORILLONITE STRUCTURE AND SWELLING PRESSURE (LBNL)

2.1 Introduction

The long-term performance of bentonite buffer in Engineered Barrier Systems (EBS) hinges on its ability to maintain sufficient swelling pressure, mechanical stability, and retardation capacity when EBS bentonite goes through the coupled thermal, hydrological, mechanical, and chemical (THMC) processes. Among all the complex coupled processes, mechanical and chemical couplings have been a focal point of LBNL studies (Zheng et al., 2014; 2015a; 2017b) because of their importance for the long-term evolution of bentonite. In the large-scale models (e.g., Zheng et al., 2015a), the effect of chemical changes on the swelling of bentonite has been formulated by empirical relationships and implemented in the numerical codes. However, more mechanistic understanding of such an effect is needed for better parameterization and more accurate representation in the large-scale model.

Zheng et al. (2015a) identified three types of chemical changes that affect the swelling of bentonite: changes in the composition of exchangeable cation, changes of pore water ionic strength, and changes in the abundance of swelling clay minerals (smectite). In the last couple of years, LBNL scientists have attempted to measure the change of swelling stress as a function of exchangeable cations and pore water ionic strength and model such processes with molecular dynamic models. Bentonite is composed of smectite, illite, and other non-clay minerals, and swelling pressure is strongly affected by the content of smectite. In order to clearly delineate effect of chemical conditions on swelling, in the past two years the studies have focused on pure smectites (or montmorillonites (MMT) – a common type of smectite clay mineral) and the effect of exchangeable cations on swelling stress. In FY20 (Zheng et al., 2020a), we reported a series of simulations on smectite swelling free energy in dilute aqueous solution and on layer-state mixing energetics. Our work in FY21 expanded these simulations to include swelling free energy calculations in different solution compositions, high ionic strength electrolytes, as well as a thermodynamic study of coupled ion exchange and water uptake for a fixed swelling state. In FY22, we constructed the X-ray transparent micro-oedometer system for measurements of montmorillonite swelling pressure and microstructure as a function of dry bulk density and aqueous solution composition. The modified system can provide time- and chemically resolved measurements on clay swelling pressure and the potential structure changes. In FY23 we conducted a series of experiments to assess the influence of ionic strength and type of cations on clay swelling pressure and microstructure via adjusting the type of solution (NaCl vs KCl solutions) and the K^+/Na^+ ratios in NaCl + KCl mixtures. We present the latest experimental results in this section of the FY23 report.

2.2 Materials and Methods

2.2.1 Clay Sample and Characterization

The clay material used in this work was montmorillonite (Kunipia-F) obtained from the Tsukinuno mine in Yamagata prefecture, Japan (Kunimine Industry Co. Ltd.). Kunipia-F is a purified montmorillonite sample via hydraulic alteration without using any chemical substances. It has been well characterized and widely used in many applications (Morodome & Kawamura, 2011; Takahashi et al., 2015). Its chemical formula is $Na_{0.42}Ca_{0.068}K_{0.008}(Al_{1.56}Mg_{0.31})Fe(III)_{0.09}Fe(II)_{0.01}(OH)_2(Si_{3.91}Al_{0.09})O_{10}$. A unit crystal of Kunipia-F montmorillonite is a very thin (flat) plate that is about 1 nm thick and about 100 to 1,000 nm wide (Figure 2-1). The layer charge of this high-charge montmorillonite was estimated to be 0.564 e^- per formula unit with a cation exchange capacity (CEC) of 116 meq/100g (Morodome & Kawamura, 2011).

In order to measure the exchangeable cations associated with Kunipia-F, we applied a $BaCl_2$ compulsive exchange method (Ross & Ketterings, 1986) for determination of its CEC and the exchangeable cations including Na^+, K^+, Mg^{2+}, Ca^{2+} and Sr^{2+} by ICP- MS analysis.

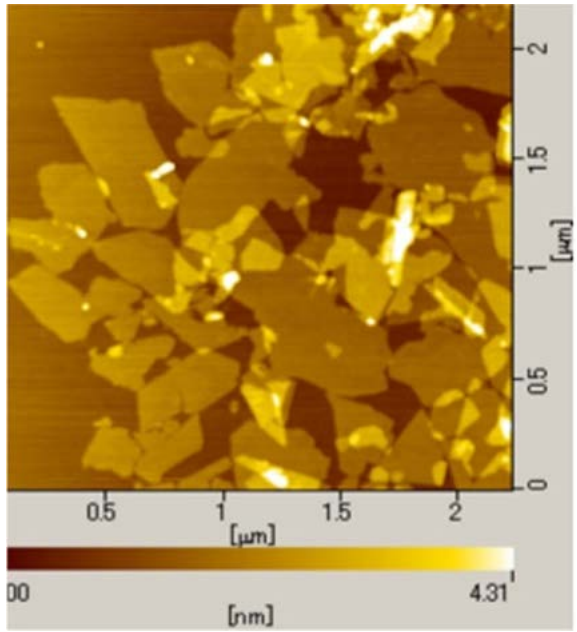

Figure 2-1 AFM image of Kunipia-F

2.2.2 Chemical Solutions

Chemical solutions with variable ionic strength and Na^+/K^+ ratios were prepared to evaluate their influence on clay swelling pressure and microstructure change. Ionic strength solutions included 0.001 M, 0.01 M, 0.1 M, 1.0 M and 5.0 M NaCl. The variable Na^+/K^+ solutions with a constant ionic strength (1 M) include1.0 M NaCl, 0.75 M NaCl + 0.25 M KCl, 0.5 M NaCl + 0.5 M KCl, 0.25 M NaCl + 0.75 M and 1.0 M KCl. All solutions were prepared with MQ-water (18.2 MΩ·cm) and degassed before use. All chemicals used are ACS analytical grade or above.

2.2.3 Clay Swelling Pressure Measurement Experiment

Measurements of swelling pressure were designed to obtain a time- and chemically resolved swelling pressure curve. We determined the swelling pressure as a function of aqueous ionic strength (0.001 M – 5.0 M NaCl) and variable Na^+/K^+ ratios at a constant bulk clay density. Measurements were conducted using our modified µ-oedometer system (Figure 2-2). Briefly, a syringe pump (Figure 2-2(a)) introduces chemical solutions into a small black PEEK clay cell through the bottom inlet to top outlet. The cell is fixed on the µ-oedometer cell holder (labeled with a red circle in Figure 2-2(b). Details about the cell size and holders were provided in our EBS FY20 progress report. The cell was packed with dry clay sample and bounded on either side by permeable membrane filters and metal frits. The clay was confined by a displaceable piston. Miniscule displacements on the piston generated a force measurement (labeled with small red rectangle in Figure 2-2(b), which was displayed on the displacement sensor meter (left in Figure 2-2(c)) and the force sensor meter (right in Figure 2-2(c)). Simultaneously, the measurements of force and displacement were recorded digitally into a datalogging Excel macro (Figure 2-2(e)), which enables us to measure the time-resolved swelling pressure. The automatic fraction collector (Figure 2-2(d)) was used to collect the effluent for chemical analysis, particularly to monitor time-resolved cation exchange reaction of K^+/Na^+.

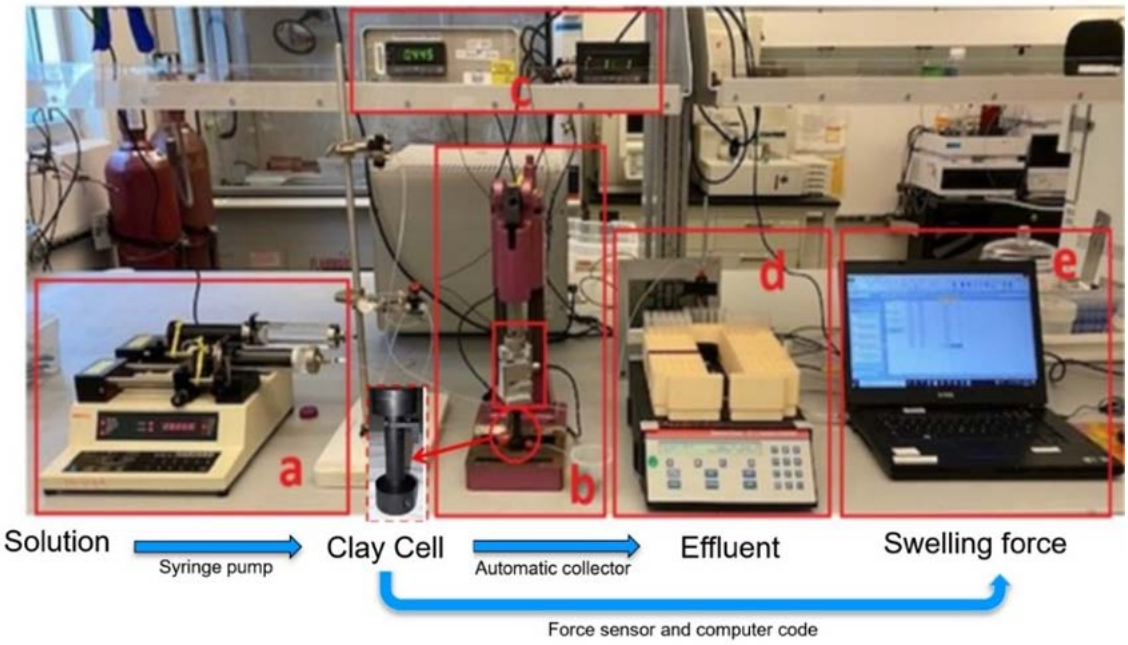

Figure 2-2. Photograph of the clay swelling experimental setup, including (a) Harvard syringe pump to introduce chemical solutions, (b) μ-oedometer including a black PEEK cell to hold the clay sample (red small circle) and the force sensor on the cell (red small rectangle) to monitor the cell force changes, (c) a displacement sensor display (left) and a force sensor display (right), (d) an automatic fraction collector to collect the effluent for chemical analysis, and (e) a computer with software to digitally record the time-resolved force and displacement changes.

With the modified experimental setup, we packed cells (5 mm inner diameter, 9 mm height) with a designed dry bulk clay density (d=~1.3 g/cm^3). We used the same clay cell to run all ionic strength solutions by switching syringes without concerning about the potential variability of cell packing. Another identical clay cell was used to run all K^+/Na^+ chemical solutions. The syringe pump (Harvard Apparatus, Pump 33 or Chemyx Inc, Fusion 200.) and the precision glass syringes with PTFE tipped plunger and dispenser (50 mL, 25 mL, 10 mL, SGE Analytical Science) were able to deliver the accurate flow rate (100 or 50 μL/hr in this work) and solution volume and allowed for continuous flow to ensure constant composition boundary conditions in the cell. In addition, the use of the syringes also prevents the exposure of the degassed solutions from the atmosphere, which could potentially affect the clay pore space.

Prior to injecting solutions, the dry clay packed cells were purged with research grade CO_2 to remove trapped air and to allow full saturation of the sample. Effluent samples were collected to analyze the concentrations of Na^+, K^+, Ca^{2+}, Mg^{2+}, Sr^{2+} and Ba^{2+} for determination of cation exchange reactions and for interpreting the clay swelling/collapse mechanisms. In order to measure the swelling force under a constant temperature (25°C), the μ-oedometer and clay cell were placed in a temperature-controlled chamber.

2.2.4 X-Ray Scattering Measurement Experiment

Small angel X-ray scattering (SAXS) measurements were conducted at the X-ray scattering beamline 7.3.3 at the Advanced Light Source (ALS) to investigate the microstructural changes of clay as a function of aqueous chemistry using the micro-oedometer cells described in the previous section. The cells were constructed with relatively X-ray transparent PEEK material (TECAPEEK CF30, Ensinger Plastics),

which is more transparent to X-rays than hydrated clay. SAXS data was collected on a charged coupled device detector with sample-detector distances of 1983.36 mm. The wavelength of radiation was set to 1.2398 Å and X-ray energy was 10 keV. We targeted a scattering vector q-range of 0.009 – 0.7 $Å^{-1}$, corresponding to real space distances between 700 - 9 nm to cover multi-scale nature of montmorillonite swelling. The SAXS data was analyzed with the program Igro Pro 9.

The SAXS samples were prepared in three steps: (1) carefully packed dry clay sample into the PEEK cells (inner diameter 3.00 mm, height 8.52 mm) for a consistent density (~1.3 g/cm^{-3}), (2) purged thoroughly with research grade CO_2 to remove trapped air after the sample saturation, and (3) introduced chemical solutions (100 or 50 µL/hr) into the clay cells to reach an "equilibrium" using the experimental setup (Figure 2-2), then sealed tightly (steps 1-3 were conducted in our geochemistry lab space) and transported to ALS Beamline 7.3.3 for SAXS measurements.

2.3 Results and Discussion

2.3.1 Measurement of Cation Exchange Capacity (CEC)

The CEC of Kunipia-F montmorillonite and the relative contribution of each cation to CEC were determined and are provided in Table 2-1. The average value from the two replicate CEC measurements is 113.4 meg/100g, which agrees with literature reported measurements at CEC = 116 meq/100g (Morodome & Kawamura, 2011). The major exchangeable cations are Na^+ (85%) and Ca^{2+} (11%) with remaining minor cations of K^+ (2.6%), Mg^{2+} (1.1%) and Sr^{2+} (0.2%).

Table 2-1. Measurement of cations exchange capacity and relative contributions of cations to CEC.

Kunipia-F	CEC*	CEC**	Relative contribution (%) of cations to CEC				
	meq/100g	meq/100g	Na^+	K^+	Mg^{2+}	Ca^{2+}	Sr^{2+}
Rep-1	112.9	111.9	84.8	2.6	1.1	11.3	0.2
Rep-2	113.9	112.0	85.2	2.7	1.1	10.8	0.2
Average	113.4	112.0	85.0	2.6	1.1	11.0	0.2
Stdev	0.50	0.10	0.2	0.1	0.01	0.3	0.0

* $BaCl_2$ Compulsive Exchange Method. **Ba^{2+} exchangeable cations analyzed by ICP- MS.

2.3.2 Influence of Na^+/K^+ Ratios on Clay Swelling Pressure

Figure 2-3 shows the time- and chemically-resolved swelling pressure curves as a function of $Na^{+/}K^+$ ratios under a constant ionic strength 1.0 M (i.e., Na^+/K^+ = 1:0 (1 M NaCl), 3:1 (0.75 M NaCl + 0.25 M KCl), 1:1 (0.5 M NaCl + 0.5 M KCl), 1:3 (0.25 M NaCl + 0.75 M KCl) and 0:1 (1 M KCl)). It is apparent the swelling pressure decreases with deceasing Na^+/K^+ ratio, indicating that presence of K^+ tends to reduce clay swelling promoted by Na^+. This result is consistent with the observation by Wakim et al. (2009) and Abdullah et al. (1999).

Figure 2-3 also shows that the swelling pressure increased quickly within the first few hours after injection of 1.0 M NaCl, then reached a steady state of pressure of 2.12 MPa within 0.5 day and remained constant, with no change, to day 4.7. When switched to the mixed solution of 0.75 M NaCl + 0.25 M KCl, the pressure started to decrease to 1.85 MPa at 10.5 days. As time progressed, the pressure continuously decreased to 1.74 MPa with the injection of 0.5 M KCl + 0.5 M NaCl at day 13.7, 1.65 MPa with 0.25 M

KCl + 0.75 M NaCl at day 17.7, and 1.59 MPa with 1.0 M KCl until day 20.7. A steady state of pressure (equilibrium) seems not to have been achieved within 3-6 days of saturation when K^+ is introduced, suggesting K^+/Na^+ exchange reaction is a slow process.

In order to determine the injection pressure by syringe pump, we purposely stopped and released pump syringe pressure for ~ 22 hours after day 4.7 (Figure 2-2). The pressure immediately dropped ~ 0.1 MPa, and then stabilized, suggesting the injection pressure = ~ 0.1 MPa. Table 2-2 provides a summary of the swelling pressure, flow duration time, and injection pressure at our designed Na^+/K^+ ratios.

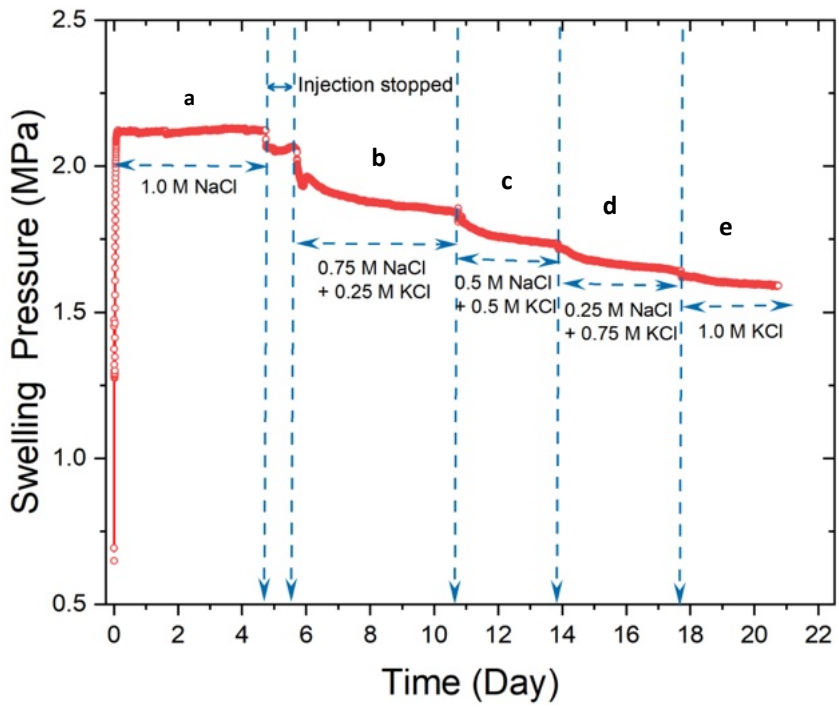

Figure 2-3. Chemical- and time-resolved swelling pressure change as a function of Na+/K+ ratios at a constant ionic strength = 1.0 M

Table 2-2. Summary of clay swelling pressure (P) affected by Na^+/K^+ ratios.

Na^+/K^+	Injecting solution	Injection pressure (MPa)	Flow duration (day)	Swelling P (MPa)
1:0	1 M NaCl	0.1	4.7	2.12
3:1	0.75 M NaCl + 0.25 M KCl	0.1	6	1.85
1:1	0.5 M NaCl + 0.5 M KCl	0.1	3	1.74
1:3	0.25 M NaCl + 0.75 M KCl	0.1	4	1.65
0:1	1 M KCl	0.1	3	1.59

Figure 2-4 provides the time-resolved cation concentrations of the effluents corresponding to Figure 2-2. The change of the effluent Na^+ and K^+ concentrations is consistent with initially injected concentrations, but their concentrations are relatively higher than initially injected. This is likely due to the water

evaporation during collecting effluent drops. Figure 2-3 also shows that other exchangeable cations of Ca^{2+}, Mg^{2+}, Sr^{2+} and Ba^{2+} were released via exchange reactions with Na^{+} and K^{+}

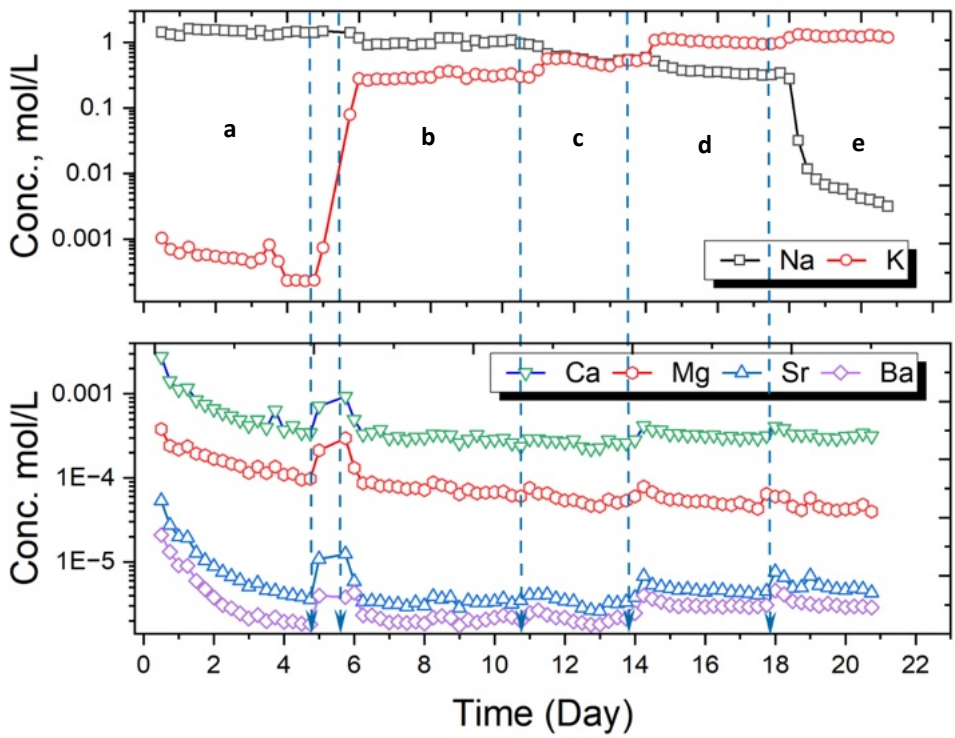

Figure 2-4. Time-resolved cation concentrations from the effluents corresponding to Figure 2-2.

2.3.3 Influence of Ionic Strength on Clay Swelling Pressure

Figure 2-5 shows the time- and chemical-resolved swelling pressure curves as a function of aqueous ionic strength (i.e., 5.0 M, 1.0 M, 0.1 M, 0.001 M NaCl and 1.0 M KCl). It indicates that the swelling pressure increases with the decrease of ionic strength and changes with cation type (Na^{+} vs. K^{+}). This observation is in good agreement with those observed by Castellanos et al. (2008) and Wakim et al. (2009).

Specifically, Figure 2-5shows that when 5.0 M NaCl was injected, the swelling pressure increased quickly within the first 10 hours, reached a maximum at ~ day 1, then decreased slightly during days 1 to 2, and finally reached a steady state of pressure 1.49 MPa between days 3 and 4. After switching to 1.0 M NaCl, only minor pressure changes were observed with a pressure = 1.51 MPa at days 4 to 7. Then, when the injection solution was switched to 0.1 M NaCl, the pressure increased quickly from 1.51 MPa to 2.51 MPa at days 7 to 10. The pressure increased sharply up to 3.50 MPa once switched over to 0.001 M NaCl, then decreased slightly and reached a steady state of 3.40 MPa at days 10 to14.6. In order to determine the injection pressure by the syringe pump, we stopped and released syringe pump pressure overnight from day 14 to day 14.6. The pressure immediately dropped ~ 0.1 MPa unit and then stabilized at 3.30 MPa. This suggests that the injection pressure was ~ 0.1 MPa. When the injection solution was switched to 1.0 M KCl, the pressure dropped immediately from 3.30 MPa to 1.80 MPa at day 15, then reduced slowly to 1.68 MPa until day 19.5. Note that the injection time does not seem to be sufficient to reach a steady state with 0.1 M NaCl and 1.0 M KCl. The time required to obtain a steady state of swelling pressure (equilibrium) is highly dependent on the solution chemistry under a constant clay density. The swelling pressure at “steady state” with each chemical condition are summarized in Table 2-3.

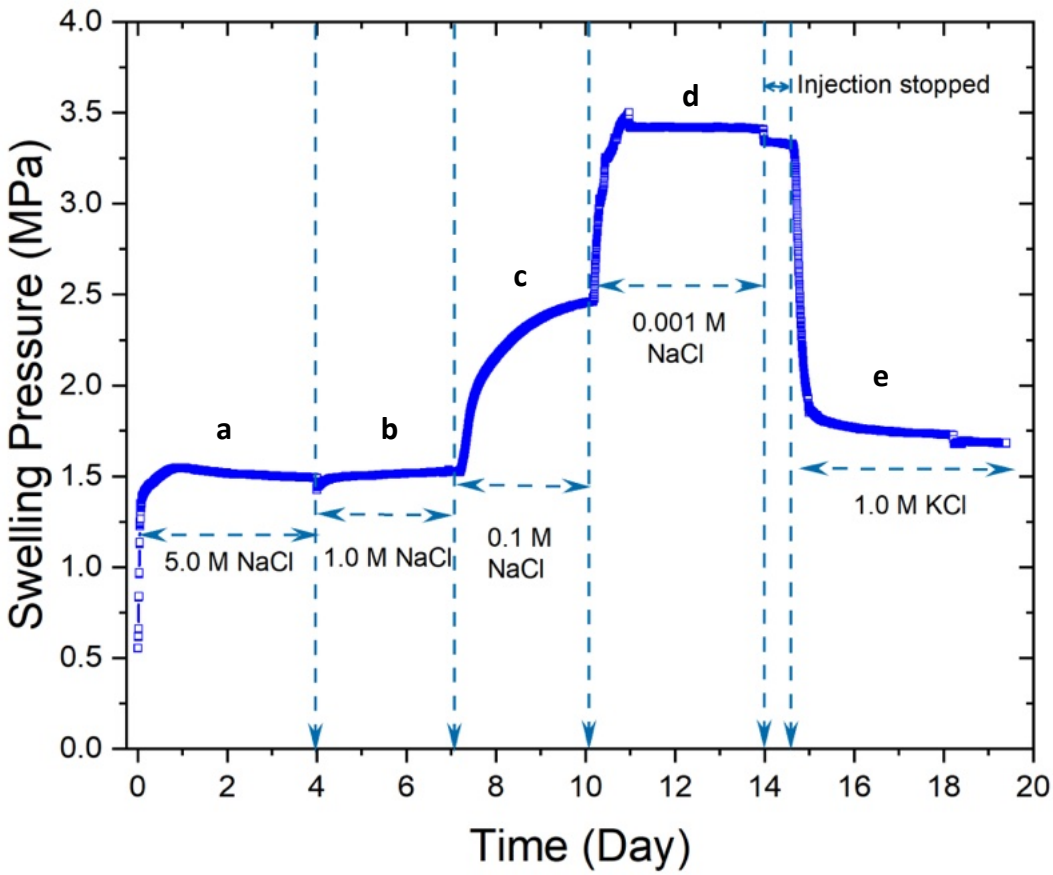

Figure 2-5. Clay swelling pressure change as a function of ionic strength and cation type (Na^+/K^+

Table 2-3. Summary of clay swelling pressure (P) affected by ionic strength.

Injecting solution	Injection pressure (MPa)	Flow duration (days)	Swelling P (MPa)
5.0 M NaCl	0.1	4	1.49
1.0 M NaCl	0.1	3	1.51
0.1 M NaCl	0.1	3	2.51
0.001 M NaCl	0.1	4.5	3.40
1.0 M KCl	0.1	4	1.68

Figure 2-6 provides the time resolved cation concentrations of the effluents corresponding to Figure 2-5. The pattern of effluent Na+ concentrations are consistent with initially injected concentrations, but analyzed concentrations from effluents are relatively higher than initially injected due to the water evaporation during collecting the effluent drops by the automatic fraction collector. Figure 2-3 also shows that other exchangeable cations (e.g., K^+, Ca^{2+}, and Mg^{2+}) were released via exchange reactions with injected Na^+ or K^+.

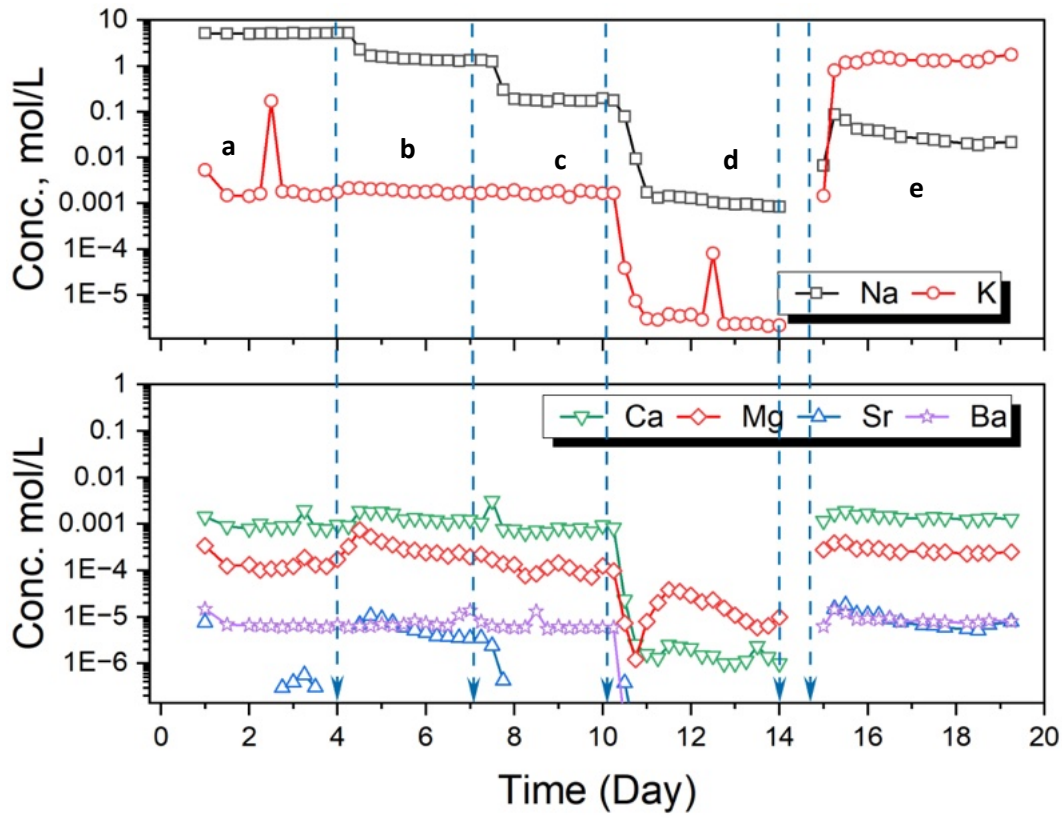

Figure 2-6. Time-resolved cation concentrations from the effluents corresponding to Figure 2-5.

The swelling pressure and swelling trend affected by ionic strength measured in this work are comparable to those reported in literature (Castellanos et al, 2008; Liu, 2013; Takahashi et al., 2015; Wakim et al., 2009). For example, Takahashi et al. (2015) used the same Kunipia-F montmorillonite, and measured the swelling pressure in deionized water, which was 3.29 MPa and 1.58 MPa with a dry density of 1.43 g/cm^3 and 1.23 g/cm^3, respectively. Our values are 2.51 MPa and 3.40 MPa in 0.1 M and 0.001 M NaCl solutions with a density of 1.3 g/cm^3. The swelling pressure obtained by Castellanos et al. (2008) was 4.0 MPa using a FEBEX bentonite with a higher clay density of 1.65 g/cm^3.

An interesting observation is that the different swelling pressures observed using the same 1.0 M NaCl in Figure 2-2 and Figure 2-4 (i.e., 2.12 MPa in Figure 2-2 and 1.51 MPa in Figure 2-4). We repeated the 5.0 M and 1.0 M NaCl measurement in Figure 2-4 and obtained the similar results. This suggests that the swelling pressure is also dependent on different solution composition. This observation is inconsistent with those reported by Wakim et al. (2009) who reported the swelling is fully independent of the order in which different solution chemistries, and that the swelling/shrinkage is completely reversible with respect to Na+, K+ and Ca2+. This difference in the observations is likely due to use of different clay minerals. Our clay is a pure montmorillonite (Kunipia-F), while Wakim et al. (2009) used a Tournemire shale sample with a mixed mineral composition of illite, kaolinite, quarts, and calcite. Further study is needed to explore this important process.

2.3.4 Influence of Ionic Strength on Clay Microstructure

Clay swelling occurs in two regimes, crystalline and osmotic, depending on the d spacing of the clay particles. The d spacing is defined for clay particles as the sum of the interlayer distance and the thickness of one clay layer. Crystalline swelling occurs when the d spacing increases from 10 to 22 Å, and osmotic swelling occurs when the d spacing swells beyond 22 Å (Rao et al., 2013; Chen et al., 2022). SAXS

technique has become a very useful tool to characterize the microstructural and swelling properties of montmorillonite in aqueous dispersions (Segad et al., 2012a; Segad et al., 2012b). Its application in compacted montmorillonite has so far been limited.

Figure 2-7 shows our original SAXS measurement curves as a function of ionic strength, including the data from the montmorillonite cell samples saturated with the solutions of 0.001 M, 0.01 M, 0.1 M, 1.0 M and 5.0 M NaCl and a background cell sample. The background sample contained the same NaCl concentration solution as in the clay cell, but without clay. The SAXS profile in Figure 2-7 is not background corrected, but it still shows the presence of diffraction peaks at q = ~ 0.40 $Å^{-1}$ (15.7 Å) and ~ 0.33 $Å^{-1}$ (19.0Å), which are characteristic of 2- and 3-water layer crystalline hydrates, respectively. The broad peaks at q = ~ 0.18 $Å^{-1}$ (35.7 Å) at 0.01 M NaCl and ~ 0.16 $Å^{-1}$ (40.3Å) at 0.001 M NaCl are characteristic of osmotic swelling space.

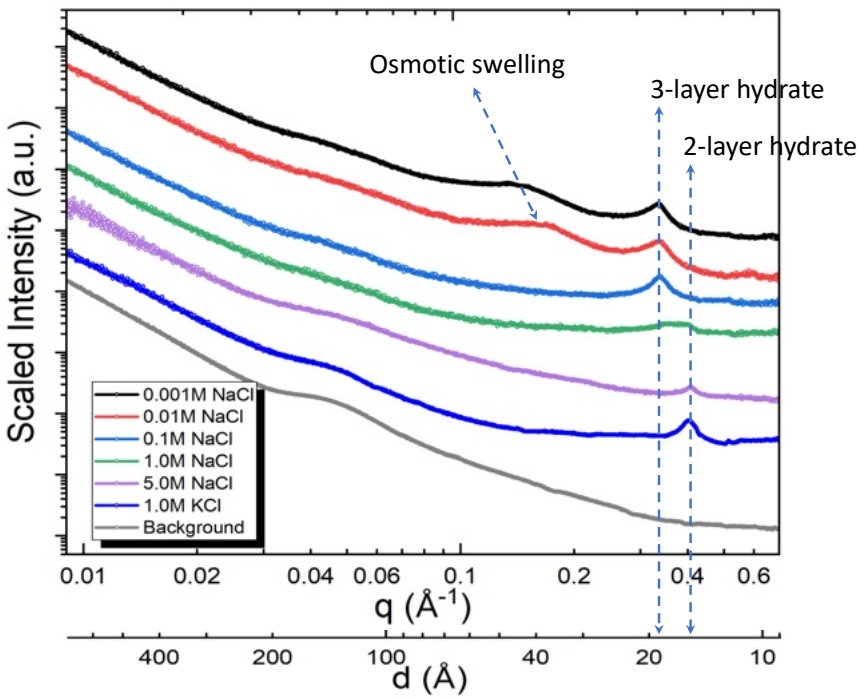

Figure 2-7. Original SAXS spectra of compacted montmorillonite as a function of ionic strength.

The background correction for clay aqueous dispersions was performed by subtracting the background solution data from the clay-containing samples (Segad et al., 2012a; Segad et al., 2012b). With our compacted clay cell samples, the subtraction resulted in negative values. Therefore, we performed the background correction by dividing the clay SAXS intensities (cell + clay + solution) with the same background solution SAXS intensities (cell + solution), and the results are shown in Figure 2-8.

Figure 2-8 shows the SAXS profile after background correction, which provides more microstructural information, including the peaks from 1-layer, 2-layer, 3-layer hydrates and the osmotic swelling, and a wide peak at low q = ~ 0.03 $Å^{-1}$ (210Å). A summary of the interlayer hydration state, osmotic swelling space and the broad peak at low q = ~ 0.03 $Å^{-1}$ (210Å) is provided in Table 2-4. As expected, both interlayer crystalline and osmotic swelling space increase with decreasing ionic strength, which is in good agreement with our chemically-resolved swelling pressure measurement where the swelling pressure increases with decreasing ionic strength (5.0 M to 0.001 M NaCl).

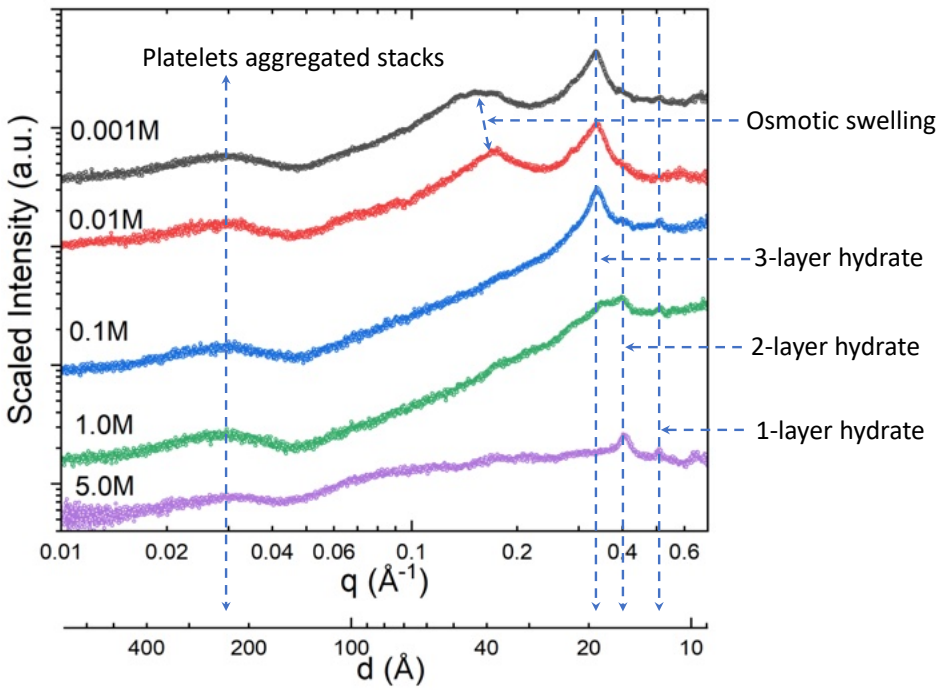

Figure 2-8. SAXS spectra (background corrected) of compacted montmorillonite as a function of ionic strength (0.001 M, 0.01 M, 0.1 M, 1.0 M, 5.0 M NaCl).

The clay interlayer basal spacing increases from 15.7 Å to 18.8 Å with decreasing ionic strength in response to the interlayer hydration state changing from 2-layer hydrate dominated at 5.0 M NaCl, to a transient mixture of 2- and 3-layer hydrates at 1.0 M NaCl, and 3-layer hydrate dominated at 0.1 M, 0.01 M and 0.001 M NaCl. A small peak occurred at ~ 12.3 Å at all ionic strengths, which is attributed primarily to the presence of a 1-layer hydrate.

A more interesting result is that we experimentally observed the osmotic swelling peaks with a medium d spacing = 35.7 Å at 0.01 M NaCl and 40.3 Å at 0.001 M NaCl (Table 2-4), an observation unique to compacted clay systems using the SAXS technique. This observation was measured in a relatively low dry clay density (1.3 g/cm^3). We will investigate this at higher clay density in future work.

We also observed a wide peak with a medium peak d spacing = 210 Å, which could be attributed primarily to the clay platelets aggregated stacks in compacted montmorillonite. The single montmorillonite molecule is of a lamellar shape (a platelet but is not necessarily flat) with the size of approximately100 nm width and 1 nm thickness, and several platelets are gathered in a group, forming a stack (Takahashi et al., 2015). The stacks are similar to the tactoid formation in aqueous dispersions (Segad et al., 2012a; Segad et al., 2012b).

The peak positions of 2-layer and 3-layer hydrates shifted slightly to higher d spacing with the decrease of ionic strength (Figure 2-7 and Table 2-4). The 2-layer's d spacing increased from 15.6 Å at 5.0 M NaCl to 16.2 Å at 0.001 M NaCl. The 3-layer's d spacing increased from 18.1 Å at 1.0 M NaCl to 18.8 Å at 0.001 M NaCl. Takahashi et al. (2015) used the same montmorillonite Kunipia-F sample and obtained a basal d spacing = 16.3 Å for 2-layer hydrate and 19.5 Å for 3-layer hydrate using deionized water (Table 2-4). These results suggest that the 2- and 3-layer's d spacing as well as the osmotic swelling spacing also depend on aqueous ionic strength or aqueous chemistry.

Takahashi et al. (2015) also measured 1-layer hydrate with a d spacing = 13.1 Å using the same Kunipia-F montmorillonite and X-ray diffraction (XRD) method. Chen et al. (2022) performed the molecular

dynamic simulation and obtained d spacing = 12.57 Å for 1-layer hydrate and 15.03 Å for 2-layer hydrate. These studies concluded that crystalline swelling occurs when the d spacing increases from 10 to 22 Å, and osmotic swelling occurs when the d spacing swells beyond 22 Å (Rao et al., 2013; Chen et al., 2022).

Table 2-4. Measurement of interlayer hydration state (basal spacing) and osmotic swelling of montmorillonite (Kunipia-F) as a function of ionic strength and cation types by using SAXS (d values are obtained from d = 2π/q).

Chemical	Interlayer hydration state and osmotic swelling								Platelets aggregated stacks	
	1-layer hydrate		2-layer hydrate		3-layer hydrate		Osmotic swelling			
	q (Å^{-1})	d (Å)	q (Å^{-1})	d (Å)	q (Å^{-1})	d (Å)	q (Å^{-1})	d (Å)	q (Å^{-1})	d (Å)
0.001 M NaCl*	0.51	12.3	0.389	16.2	0.334	18.8	0.156	40.3	0.03	210
0.01 M NaCl*	0.51	12.3	0.394	16.0	0.337	18.6	0.176	35.7	0.03	210
0.1 M NaCl*	0.51	12.3	0.396	15.9	0.338	18.6	-	-	0.03	210
1 M NaCl*	0.51	12.3	0.397	15.8	0.347	18.1	-	-	0.03	210
5 M NaCl*	0.51	12.3	0.401	15.7	-	-	-	-	0.03	210
1 M KCl*	0.51	12.3	0.403	15.6	-	-	-	-	0.03	210
Deionized water**	-	13.1	-	16.3	-	19.5	-	-	-	-

* This work; ** Takahashi et al. (2015)

2.3.5 Influence of Cation Type on Clay Microstructure

Figure 2-9 shows a comparison of SAXS spectra between 1.0 M KCl and 1.0 M NaCl. The difference is clear that 1.0 M K^+ saturated clay has a strong 2-layer hydrate peak (d spacing = 15.6 Å), while 1.0 M Na^+ shows a broad mixed transient peak of 2- and 3-layer hydrates (d spacing = 15.8 Å - 18.1 Å). These results explain the influence of Na^+/K^+ ratios on swelling pressure in Figure 2-2 and Table 2-2 where the swelling pressure decreased with decreasing Na^+/K^+ ratios because 1.0 M K^+ tends to form 2-layer hydrate only, and Na^+ tends to form both 2- and 3-layer hydrates.

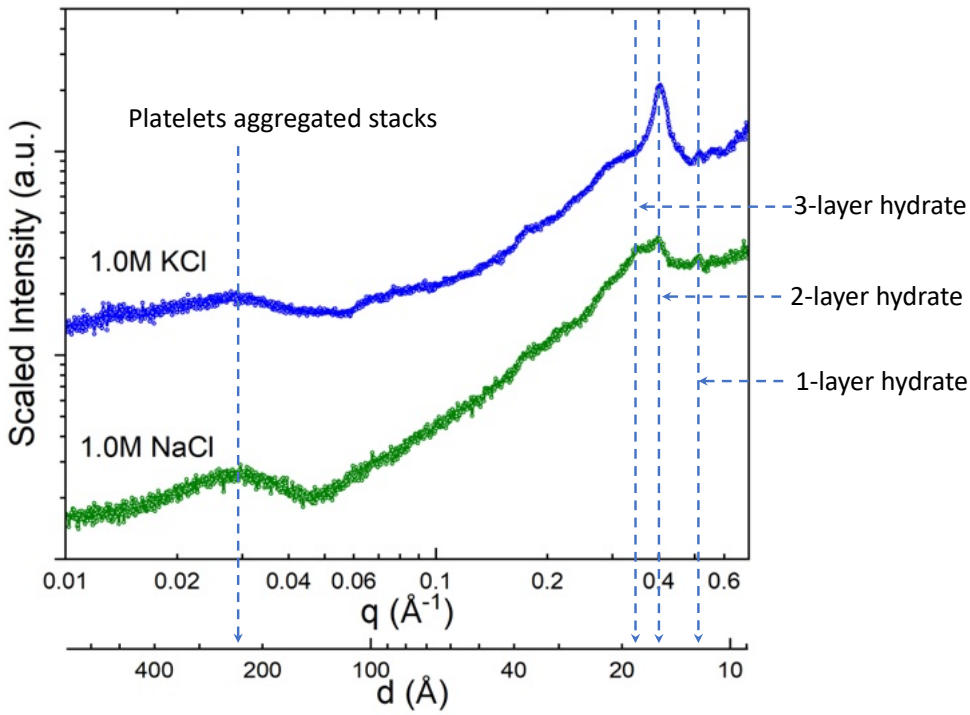

Figure 2-9. SAXS spectra of compacted montmorillonite saturated with 1.0 M KCl vs. 1.0 M NaCl

2.4 Summary and Future Work

We have designed a series of laboratory tests to better delineate the effect of chemical conditions on swelling. In FY23, we conducted the clay swelling and microstructure measurements as functions of aqueous ionic strength and variable Na+/K+ ratios using the modified μ-oedometer system and SAXS technique. Over the course of the experiments, we changed the injection solutions to have different ionic strengths and/or cations and swelling pressure, and the SAXS data was collected at ALS Beamline 7.3.3. We concluded that aqueous chemistry including ionic strength and cation type can strongly impact montmorillonite swelling pressure via changing the interlayer hydration states and osmotic swelling space.

The concluding remarks are summarized as below:

(1). The chemically and time-resolved clay swelling pressure increases with decreasing chemical ionic strength and decreases with increasing K^+/Na^+ ratios.

(2). The sequence of how solutions was introduced affected the swelling pressure, which indicates the chemical effect of swelling cannot be completely reversed and it is a dynamic process.

(3). Our chemically resolved SAXS profile shows that both interlayer crystalline and osmotic swelling space increase with decreasing ionic strength, which is in good agreement with our chemically resolved swelling pressure measurement. The clay interlayer basal spacing increases from 15.7 Å to 18.8 Å with decreasing ionic strength in response to the interlayer hydration state changing from 2-layer hydrate dominated at 5.0 M NaCl, to a transient mixture of 2- and 3-layer hydrates at 1.0 M NaCl, and 3-layer hydrate dominated at 0.1 M, 0.01 M and 0.001 M NaCl, while a small peak occurs at ~ 12.3 Å at all ionic strength which attributed primarily to 1-layer hydrate.

(4). The osmotic swelling peaks with an intermediate d spacing of 35.7 Å at 0.01 M NaCl and 40.3 Å at 0.001 M NaCl were observed using the SAXS technique, which has not been reported before for compacted clay systems to the best our knowledge.

(5). A wide peak with a intermediate peak *d* spacing of 210 Å (21 nm) was observed, which could be attributed primarily to the clay platelets aggregated stacks in compacted montmorillonite, similar to the tactoid formation in aqueous dispersions.

(6). Our SAXS measurement indicates that the basal spacing is 15.6 Å (2-layer hydrate) at 1.0 M KCl, which differs from those at 1.0 M NaCl (i.e., 15.8 Å for 2-layer hydrate, and 18.1 Å for 3-layer hydrate), indicating K^+ leads to lower swelling pressure.

(7). We also observed that the 2- and 3-layer's basal spacing as well as the osmotic swelling space depend on aqueous ionic strength or aqueous chemistry.

These observations are highly relevant to understanding and modeling hydro-mechanical-chemical coupling processes in clayey materials found in natural and engineered barriers for surface and subsurface energy applications such as nuclear waste storage.

In the remaining months of FY23 and in FY24, we will continue the experiments with the following focus:

(1). Since some of the experiments seem to indicate the chemical effect of swelling pressure are not completely reversible, we plan to conduct a series of clay swelling measurement experiments of longer duration to test the reversibility of the swelling. Using our μ-oedometer system and *in-situ* SAXS measurements to simultaneously test the swelling pressure and microstructural changes at the ALS to further quantify this effect.

We have been using pure montmorillonite (Kunipia-F) in the tests. But bentonite is composed of both montmorillonite and other non-swelling minerals. The next step is therefore to use bentonite instead of pure montmorillonite. One possibility is the bentonite sample retrieved from the prototype test by SKB in FY24.

This page left blank

3. MOLECULAR MODELING OF RADIONUCLIDE RETENTION BY BENTONITES

3.1 Introduction

The capability of a bentonite barrier to impede the transport of long-lived radionuclides is an essential aspect of the performance evaluation of any storage strategy. To assess the safety of the spent nuclear waste disposal sites in case of leakage, one must quantify the strength and extent of radionuclides retention by mineral/soil matrix. A scenario for radionuclide release involves a process of the interaction between groundwater (GW) and a corroded canister and mobilizing radionuclides, such as ^{233}U and ^{239}P. Thus, knowledge of these radionuclides' aqueous speciation and chemistry under relevant conditions, their interactions with the surrounding mineral matrix (e.g., bentonites), and their mobility within this matrix is critically vital for evaluating repository performance. Here we focused on uranium because it is the most abundant radionuclide in non-reprocessed spent nuclear fuel, and highly mobile if present in the oxidized form. Most of the repositories are planned deep underground, where reducing conditions prevail. In these conditions, uranium is present in a reduced form U(IV) and strongly attracted to negatively charged organic and inorganic surfaces, thus, immobile. In case of catastrophic leakage, released U(IV) could be retained within the leakage zone via sorption to mineral surfaces. However, the particles with adsorbed U(IV) can be transported upward, reaching oxic conditions (Figure 3-1(a)). The oxidized uranium, U(VI), remains stable in the solution and is considered an environmental threat if released into GW. Figure 3-1(b) shows a schematic diagram of the 2-pK Triple Layer Model (TLM) of the oxide/U-containing solution interface. Figure 3-1(c) and (d) show the traditional, numerical approach to predict thermodynamic properties of the mineral/electrolyte interface and the extent of ion sorption and its machine learning (ML) surrogate described in this report. The input contains a description of system conditions such as pH, ions concentrations ([i], i= C^+, A^-, UO_2^{2+}, U^{4+}), surface area (A), site density (N_s), and ion/proton affinity constants (log K_i). The output contains charge densities and electrostatic potentials at the surface, β- and diffuse layers (σ_0, σ_β, σ_d, ψ_0, ψ_β, ψ_d), and concentration of various types of surface species ([$\equiv SO_i$]).

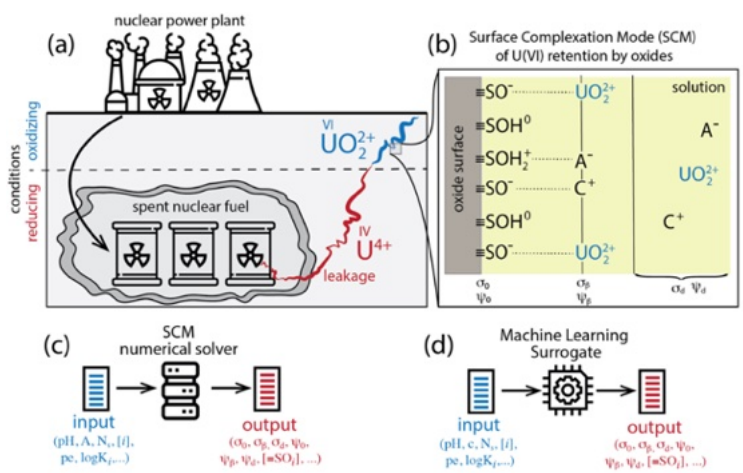

Figure 3-1. (a) Schematic diagram of hypothetical leakage of spent nuclear fuel from geological storage, showing migration upward, mobilization of uranium (U) oxidizing subsurface conditions, and retention by sorption to oxides minerals, (b) Schematic of the 2-pK TLM of the oxide/U-containing solution interface, (c) Traditional, numerical approach to predict thermodynamic properties of the mineral/electrolyte interface and the extent of ion sorption, and (d) a schematic pipeline of machine learning. Taken from Li et al. (2023).

Modeling of the radionuclide migration in soil or engineered mineral barriers remains a difficult problem. The radionuclide toxicity requires strict safety protocols and thus limits the number of laboratories in which measurements can be carried out and the analytical chemistry techniques that can be safely applied. This section describes our computational development to predict radionuclide retention in a mineral matrix. One direction of our research aims to use molecular modeling to parametrize meso- and macroscopic models, such as surface complexation and reactive transport, to develop a robust safety assessment model. Another direction of our research is to use artificial intelligence (AI)/machine learning (ML) methods to develop surrogates for the computationally expensive numerical models, explore the hidden relationships in the model parameters space/experimental databases, or accelerate numerical simulations by addressing limitations of existing methods (e.g., size- and time constraints on molecular simulation, convergence problems for Newton-Raphson solvers of nonlinear equations in complexation models).

The modeling presented here refers to a hypothetical leakage of spent nuclear fuel from multibarrier containers, followed by its upwards transport to the subsurface, where oxidation reactions mobilize uranium transport by transforming immobile uranium (IV) into mobile U(VI) (Figure 3-1). We consider a redox equilibrium between reduced and oxidized uranium but focus on the environment with a positive value of the redox potential (oxidizing conditions). Consequently, U(VI) is a dominant oxidation state, and U is present as a UO_2^{2+} ion.

3.2 Molecular and Thermodynamic Modeling of Radionuclides Sorption to Mineral Surfaces

One of the most successful macroscopic models of radionuclide retention is based on the thermodynamic ion sorption model that describes the ion sorption to the mineral surface as a complexation-type reaction and accounts for the electrostatic effects of charged mineral surfaces. These thermodynamics models, known as the surface complexation models (SCMs), have been successfully used to describe ion sorption isotherms, potentiometric and electrokinetic titration data, and some spectroscopic data. One of the limitations of these models is a lack of robust parametrization approaches and the abilities of the current solvers to find a unique algebraic solution. We developed the molecular modeling pipeline to estimate the values of SCM parameters and AI/ML-based surrogates that allow for ultrafast SCM parameter predictions (Li et al., 2023).

3.2.1 Surface Complexation Modeling

All oxide surfaces exposed to an aqueous solution become terminated by the amphoteric hydroxyl groups, which can donate or accept a proton (Dzombak & Morel, 1990; Brown et al., 1999). Several protonation schemes can describe this charging process (Yates et al., 1974; Davis et al., 1978; Westall & Hohl, 1980; Bolt & Van Riemsdijk, 1982; Hiemstra et al., 1989; Hiemstra & Vanriemsdijk, 1991; 1996; Hiemstra et al., 1996). Here, we used the 2-pK model assuming that two protonation reactions is one of the most generic and most frequently used models for interpreting experimental data for a wide range of mineral surfaces (Sverjensky, 2005).

To model the mineral surfaces, we used a generic oxide surface covered by reactive amphoteric surface sites (≡SOH). These sites can act as an acid or a base by either releasing a proton or binding an additional proton. The acid-base chemistry of the surface group is described using the 2-pK protonation/deprotonation:

$$\equiv \mathrm{SOH}_2^+ \rightleftharpoons \equiv \mathrm{SOH}^0 + \mathrm{H}^+ \qquad and \qquad K_1 = \frac{\{\equiv \mathrm{SOH}^0\}\{\mathrm{H}^+\}}{\{\equiv \mathrm{SOH}_2^+\}} \qquad \textbf{Eq. (3-1)}$$

$$\equiv \mathrm{SO}^- + \mathrm{H}^+ \rightleftharpoons \equiv \mathrm{SOH}^0 \qquad and \qquad K_2 = \frac{\{\equiv \mathrm{SOH}^0\}}{\{\equiv \mathrm{SO}^-\}\{\mathrm{H}^+\}} \qquad \textbf{Eq. (3-2)}$$

where $\equiv \mathrm{SOH}^0, \equiv \mathrm{SOH}_2^+, \equiv \mathrm{SO}^-$ represent charge-neutral, positively and negatively charged sites, respectively.

The electrolyte ions and uranium ions accumulate near the surface as outer-sphere complexes in the β-layer (Figure 3-1(b)). The ions accumulation is described as surface complexation. Here, we used the notation adopted by Sverjensky (2005) to describe ions accumulation via the following desorption reactions:

$$\equiv \mathrm{SO}^-\mathrm{C}^+ + \mathrm{H}^+ \rightleftharpoons \equiv \mathrm{SOH}^0 + \mathrm{C}^+ \quad and \quad K_C = \frac{\{\equiv \mathrm{SOH}^0\}\{\mathrm{C}^+\}}{\{\equiv \mathrm{SO}^-\mathrm{C}^+\}\{\mathrm{H}^+\}} \qquad \textbf{Eq. (3-3)}$$

$$\equiv \mathrm{SOH}_2^+\mathrm{A}^- \rightleftharpoons \equiv \mathrm{SOH}^0 + \mathrm{A}^- + \mathrm{H}^+ \quad and \quad K_\mathrm{A} = \frac{\{\equiv \mathrm{SOH}^0\}\{\mathrm{A}^-\}\{\mathrm{H}^+\}}{\{\equiv \mathrm{SOH}_2^+\mathrm{A}^-\}} \qquad \textbf{Eq. (3-4)}$$

$$\equiv \mathrm{SO}^-\mathrm{UO}_2^{2+} + \mathrm{H}^+ \rightleftharpoons \equiv \mathrm{SOH}^0 + \mathrm{UO}_2^{2+} \quad and \quad K_{\mathrm{UO}_2^{2+}} = \frac{\{\equiv \mathrm{SOH}^0\}\{\mathrm{UO}_2^{2+}\}}{\{\equiv \mathrm{SO}^-\mathrm{UO}_2^{2+}\}\{\mathrm{H}^+\}} \qquad \textbf{Eq. (3-5)}$$

$$\equiv \mathrm{SO}^-\mathrm{U}^{4+} + \mathrm{H}^+ \rightleftharpoons \equiv \mathrm{SOH}^0 + \mathrm{U}^{4+} \quad and \quad K_{\mathrm{U}^{4+}} = \frac{\{\equiv \mathrm{SOH}^0\}\{\mathrm{U}^{4+}\}}{\{\equiv \mathrm{SO}^-\mathrm{U}^{4+}\}\{\mathrm{H}^+\}} \qquad \textbf{Eq. (3-6)}$$

The electric field generated by charged mineral surface affects ion concentrations near the surface. SCMs account for this effect by weighting bulk concentrations with electric-field energy terms as follows:

$$\{\mathrm{X}^{z_x}\} = [\mathrm{X}^{z_x}] \exp\left(\frac{-z_x\, e\, \psi_j}{k_B T}\right) \qquad \textbf{Eq. (3-7)}$$

where $\{\mathrm{X}^{z_x}\}$, $[\mathrm{X}^{z_x}]$ represents the interfacial and bulk concentrations of ion X, the electrostatic potential ψ_j is equal to the surface potential for X=H^+ or β-layer potential for X=C^+, A^-, U^{4+}, UO_2^{2+} (see Figure 3-1(b)), z_x is the formal ion charge, k_B is the Boltzmann constant, and T is the temperature.

The SCM is a mathematical construct that combines the equilibrium interfacial chemistry with the geometric model of spatial charge distribution at the interface. Our preliminary study focused on one particular mathematical representation of the spatial charge distribution: the TLM combined with the 2-pK surface protonation/complexation model (Westall & Hohl, 1980).

In the 2-pK TLM framework, we distinguish two layers of localized charge: the surface layer with charge density (σ_0) due to proton uptake and release by surface hydroxyls, and β-layer with charge density (σ_β) due to co- and counter-ions accumulation, including uranium ions (Figure 3-1(b)). The sum of localized and diffuse charges is equal to zero to satisfy the charge neutrality condition:

$$\sigma_0 + \sigma_\beta + \sigma_d = 0 \qquad \textbf{Eq. (3-8)}$$

The diffuse charge (σ_d) space extends from the boundary defined by the position of the slip plane to infinity, and in our case of 2-pK TLM model with 1:1 electrolyte is given by the Grahame relationship:

$$\sigma_d = -\sqrt{8\epsilon_0\epsilon_r k_B T I}\ sinh\left[\frac{e\,\psi_d}{2k_B T}\right] \qquad \textbf{Eq. (3-9)}$$

where I is the ionic strength of the solution, ϵ_0 is the vacuum permittivity, ϵ_r is the relative dielectric constant of the solution, and ψ_d is the potential in the diffuse layer.

In the case of polyvalent ions sorption modeling, the Gouy-Champan equation that relates the diffuse layer potential with the diffuse layer charge (Eq. (3-9)) is no longer valid. Eq. (3-9) is only applicable if the electrolyte is symmetric, that is 1:1 or 2:2. In the case of non-symmetric electrolytes and polyvalent ions (e.g., U^{4+}, UO_2^{2+}) the relationship between diffuse layer potential and the charge is given by (Davis et al., 2004; Lutzenkirchen et al., 2015):

$$\sigma_d = \pm\sqrt{2\epsilon_0\epsilon_r k_B T \sum_i c_i(e^{-z_i e\psi_d/k_B T} - 1)} \qquad \textbf{Eq. (3-10)}$$

In the case of diluted electrolyte solution, the magnitudes of the diffuse potential and charge are small, and the relative error caused by using simplified Grahame Eq. (3-9) instead of Eq. (3-10) is negligible. However, in a case of the larger electrolyte concertation, the double layer thickness decreases, and both the diffuse potential and charge need to be linked through the full equation. The correct relationship between the diffuse charge and potential is also needed in the case of the overlapping or confined electrical double layers, due to increased ionic strength between the charged surfaces. We used Eq. (3-10) to generate synthetic dataset of radionuclides sorption to mineral surfaces. This dataset will be used to generate a new type of AI/ML surrogates that can handle multidentate/multinuclear radionuclide surface complexes.

The surface equilibrium reactions, charge neutrality, and surface site conservation conditions form a set of equations whose solution consists of the values for the surface concentration of all types of surface sites, charge densities, and potentials in each layer/region (0, β, d). To reduce the number of unknowns, the TLM model considers the compact part of the electric double layer as two capacitors connected in series. Consequently, the electrostatic potentials are coupled through capacitances c_1 and c_2, and thus only one potential value is needed:

$$\psi_0 = \psi_\beta + \frac{\sigma_0}{c_1} = \psi_d + \frac{\sigma_0}{c_1} - \frac{\sigma_d}{c_2} \qquad \textbf{Eq. (3-11)}$$

The final set of equations is numerically solved using an iterative procedure, here using a simplex minimization algorithm (Nelder & Mead, 1965). The lack of a standardized approach for SCM construction, evaluation, and fitting algorithm often results in the prediction of ion affinities (K_i) and capacitances (c_i) that vary between different research teams, even for the same experimental dataset. One of the goals of our project is to show that transferable deep neural network based surrogate models for various SCMs can be developed and used instead of the independently implemented analytical SCM solvers.

By solving the SCM described above, one can determine concentrations of all types of surface complexes, charge densities (σ_0, σ_β, σ_d), and potentials (ψ_0, ψ_β, ψ_d) at the surface, β– and diffuse layers (see Figure 3-1(b)). A detailed discussion of the SCM equations and numerical methodology can be found elsewhere (Li & Zarzycki, 2022).

The uptake of U(VI) by mineral surface depends on the surface charge of oxide at a given pH condition. The non-specific adsorption is electrostatically driven and increases with increasing pH above the point of zero charge (PZC). However, in the case of specific sorption, or sorption of UO_2^{2+} complexed with Cl^-, U(VI) accumulation can occur even at pH below PZC. To generate an extensive dataset that covers most situations as much as possible for the ML training, we developed a Python script that modifies the uranium thermodynamic database by varying the environmental conditions, such as pH and salt concentration. We also modified model parameters describing acid-base properties of the surface, surface

site density, surface area, capacitance, logK values, and electrolyte/uranium affinity to the mineral surface. Consequently, we generated over 1.5 million data by fully exploring the range of uranium sorption conditions. To prepare the generated dataset for the random forest algorithm, we extracted the modified inputs (12) in the SCM solver and the uranium thermodynamic database and their subsequent outputs (12) (Figure 3-2).

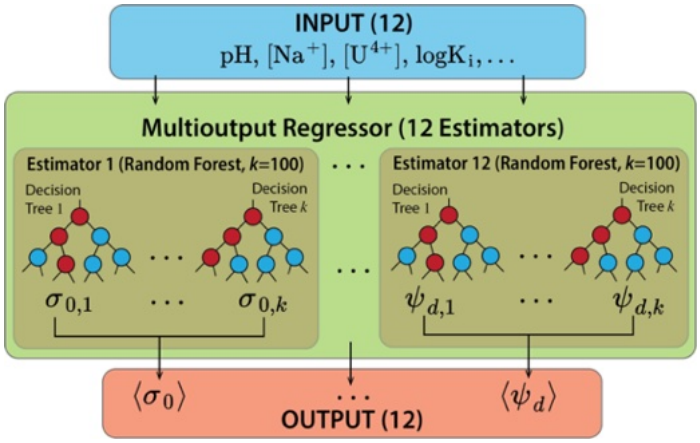

Figure 3-2. Multioutput regressor as an SCM surrogate. The architecture consists of 12 random forests (estimators), each trained to predict a single target value (output) based on a complete input vector. The input consists of a description of the oxide surface (surface area, site density), the SCM parameter values, such as affinity constants ($\log K_i$) capacitances, and a description of solution composition (12 values). The output consists of charge densities and electrostatic potential in each layer and concentrations of surface complexes (12 values) (Li et al., 2023).

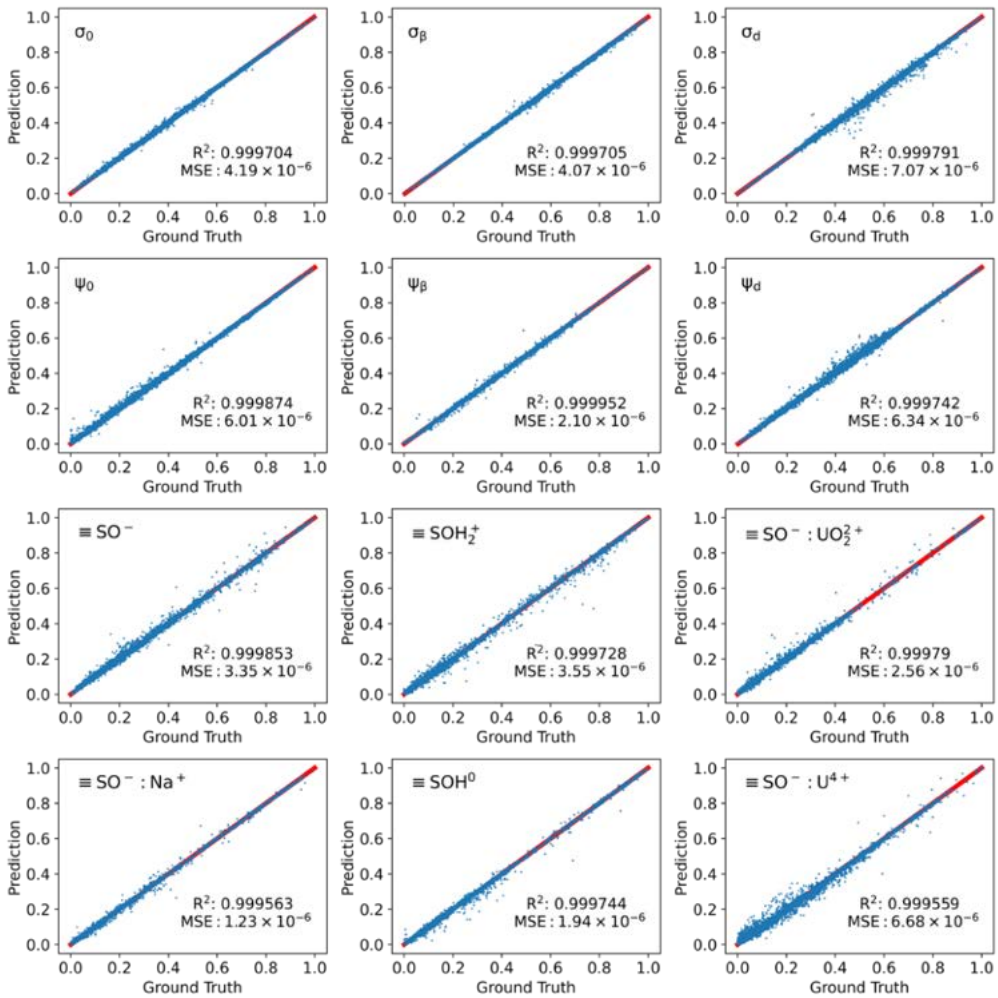

Figure 3-3. Surrogate model prediction vs. numerical SCM-based ground truth. The red solid line represents the ideal prediction, where prediction equals to ground truth value. R^2 score represents the goodness of fit of surrogate predictions to corresponding ground truth values. MSE stands for the mean squared error between prediction and target. See reference (Li et al., 2023) for details.

3.2.2 Machine Learning / Artificial Intelligence Model Construction

We used the open-source Python library Scikit-learn (Pedregosa, et al., 2011) for model development, training, and testing. As previously discussed (Li & Zarzycki, 2002), we used the MultiOutputRegressor module from Scikit-learn to estimate multiple output values. Here, we used Random Forest Regressor as the base estimator for predicting each target, and MultiOutputRegressor to support multi-target predictions. Our multioutput regressor used consists of 12 random forest regressors, and each random forest consisted of 100 decision trees (Figure 3-3).

We split the database of extracted input parameters and output values described above into training and test sets with a ratio of 80:20%. The min-max normalization strategy is applied to the data to improve training efficiency. We trained the model on the training dataset and evaluated the model performance on the test set. During the training procedure, mean square error (MSE) was used to minimize the loss between the ground truth and the surrogate prediction.

3.2.3 Results

We developed a multioutput regressor composed of an ensemble of random forests, each able to estimate values of one of the descriptors of the oxide/electrolyte interface. After training the model, we evaluated its performance on a subset of conditions outside of the training set. Here, we discuss the performance of a trained surrogate for 2-pK TLM of U sorption to oxides.

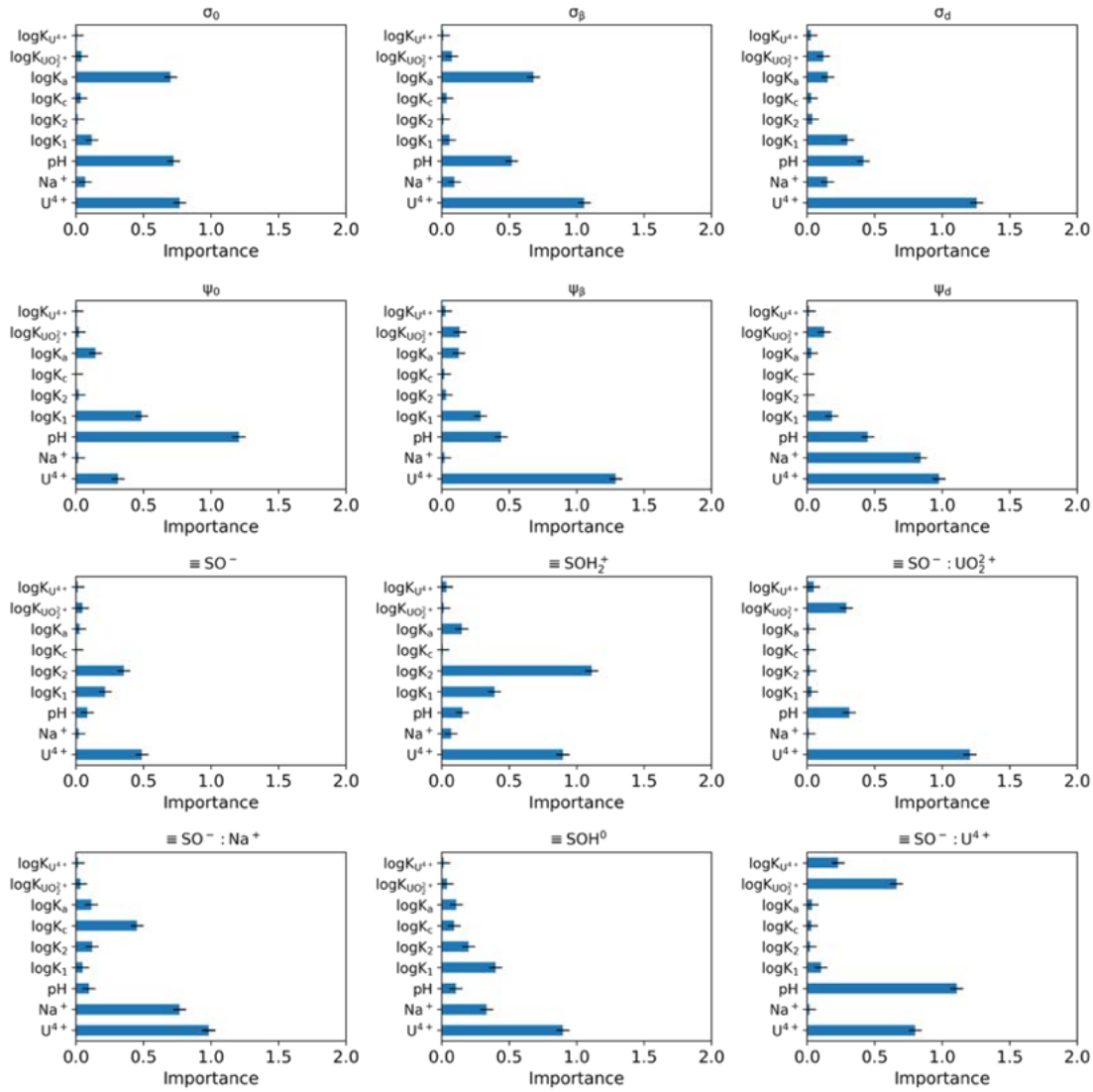

Figure 3-4 Importance of selected features (input values) in predicting target values (output values). See reference (Li et al., 2023) for details.

We evaluated our SCM surrogate on predicting U(VI) sorption to oxide surfaces by testing 317,883 conditions (input entries) simultaneously. All surrogate inferences were made within 34 seconds, compared with five hours needed for the numerical SCM solver using identical computational resources. The acceleration of the surrogate as compared with the numerical solver is not surprising. A trained SCM surrogate requires a simple vector-based pipeline computation, whereas the numerical SCM solver relies on iterative solving of a convoluted set of equations.

The parity plot (Figure 3-3) shows the correlation between our surrogate model predictions and corresponding ground-truth targets. The overall R^2 score is consistently higher than 0.999 for all targets, indicating that the multioutput random-forest-based regressor is able to accurately map system conditions (input) to the sorption behavior and interfacial properties (output). We also calculated the MSE for each target. MSE is in the order of 10^{-6} in all cases, clear evidence that the surrogate model can accurately reproduce the results obtained using the numerical SCM solver.

In order to better understand how our surrogate model learned to map an input to output, we measured how each input feature impacts output values by implementing the permutation feature importance algorithm, see Figure 3-4 (Breiman, 2001). The permutation feature importance is measured by a decrease in a model performance score when a single feature value is randomly shuffled. The underlying assumption is that when we are shuffling feature value, we break the relationship between the feature and the target, so that the model score should drop proportionally to how the model prediction depends on that feature.

It is important to note that permutation is used to assess how important a given feature is for a particular model: here, the mutlioutput regressor, but it does not necessarily reflect the physicochemical relationships between input and output in the SCM. The electrostatic potentials are coupled to the charge densities in the SCM, so we expect similar trends for both properties in terms of feature importance. The permutation importance analysis shows similar trends for both charge density and potential near the surface (0 and β layers), with pH, $[U^{4+}]$, and equilibrium constants being the most important features.

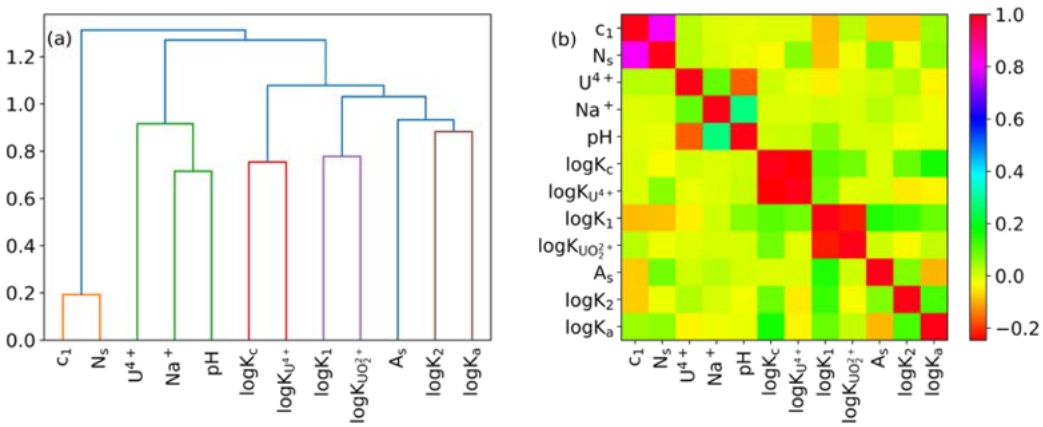

Figure 3-5 Correlation analysis on input features. (a) A dendrogram of input features. It divided features into different groups based on their relevance. The lower the height, the stronger the correlation. (b) Pair correlation between different input features.

However, not in all cases the charge density dependency on features is mirrored by potential. If two features are strongly correlated, shuffling one feature will change the apparent importance of the other, as shown in the correlation plot (Figure 3-4 and Figure 3-5).

Concluding, our surrogate model offers a significant acceleration with respect to the prediction of uranium sorption on oxides. This is a consequence of the fact that numerical evaluation of SCMs involves solving a set of non-linear equations, whereas our multioutput random-forest-based regressor is a simple one-directional evaluation of the vector function.

The permutation feature analysis reveals that our surrogate captures the intrinsic dependencies of sorption properties on the environmental conditions and mineral surface descriptors. However, we also discover that some descriptors are not independent.

3.2.4 Future Directions

We developed a computational pipeline to generate synthetic datasets, train AI/ML models, and use these trained models as the SCM surrogate in the case of uranium sorption to oxides at varying environmental conditions.

Our next step is to generate synthetic datasets for the radionuclide's sorption to mineral surfaces, considering the complexation of uranium ions by carbonates and the role of the pH and redox conditions on the uranium interfacial speciation.

Simultaneously, we are developing a set of molecular simulations to assist in the SCMs parametrization regarding the dielectric constant of the solution near the mineral surface, type and stoichiometry of the surface carbonate-uranyl complexes, and redox transitions between U(IV) and U(VI).

This page intentionally left blank.

4. EXPERIMENTAL INVESTIGATIONS ON BENTONITE AND OTHER CLAY-BASED MATERIALS

4.1 Introduction

Most high-level waste (HLW) and low-level waste geological disposal options, which are currently under investigation, use clay media (e.g., bentonite or shale) as engineered barriers or as the host rock for geologic storage (Altmann, 2008; Altmann et al., 2012; Delay et al., 2007; Guyonnet et al., 2009; SKB, 2011a; Tournassat et al., 2015). Clays are good barriers for HLW due to their low hydraulic conductivity, which restricts contaminant mobility to slow diffusion-based transport, and their high adsorption capacity for radionuclides, which slows transport even further. Montmorillonite ($M^{+}_{0.33}(Al_{1.67}Mg_{0.33})Si_4O_{10}(OH)_2$) is the dominant clay mineral found in bentonite. It has a 2:1 layer-type phyllosilicate structure, with a large specific surface area (~750 m^2/g) and CEC (~1 mol_c/kg), and strongly-sorbing surface complexation sites on clay edge surfaces.

In compacted clay, solute transport is controlled by diffusion, and adsorption of solutes to the clay can significantly retard transport. While uranium is the primary constituent of spent nuclear fuel, ^{79}Se is a minor component, but a major driver of the safety case for nuclear waste disposal due to its long half-life (3.3×10^5 yr) and presence as relatively mobile anionic species under a range of chemical conditions (*e.g.*, HSe^-, SeO_3^{2-}, SeO_4^{2-}). Se redox chemistry is complex, with oxidation states ranging from -II to +VI over environmentally relevant conditions. While Se(-II) and Se(0) are relatively immobile due to the formation of low solubility precipitates, Se(IV) and Se(VI) exist as the oxyanions selenite (SeO_3^{2-}) and selenate (SeO_4^{2-}) and are highly mobile in water due to their high solubility. Se adsorption to clay minerals is quite low compared to other important radionuclides such as U. K_d values for selenite adsorption to smectite are in the range of 1-50 L/kg (Missana et al., 2009; Montavon et al., 2009) compared to values up to 10^4 L/kg for U(VI) (Tournassat et al., 2018). Selenite and selenate adsorption to the clay minerals kaolinite and Ca-montmorillonite was studied by Bar-Yosef and Meek (1987) over the pH range 4-8. Both selenite and selenate adsorption decreased with increasing pH, with very low or negligible adsorption for pH>8 and selenate adsorption to kaolinite was lower than selenite adsorption (Bar-Yosef & Meek, 1987). Similar trends of lower selenate vs selenite adsorption and decreasing adsorption with increasing pH were observed on iron oxides and oxyhydroxides (Balistrieri & Chao, 1987, 1990). Montavon et al. (2009) observed higher Se(IV) adsorption to synthetic montmorillonite in the presence of Ca, and suggested that ternary surface complexes with Ca may explain this enhanced sorption effect.

Selenite diffusion through bentonite has been investigated in several studies (García-Gutiérrez et al., 2001; Idemitsu et al., 2016; Wang et al., 2016; Wu et al., 2017). Idemitsu et al. (2016) measured apparent diffusion coefficient (D_a) values of 2.5×10^{-11} to 1.9×10^{-13} m^2/s over a range of dry bulk densities (0.8-1.6 kg/L), ionic strengths (0.01-1.0 M NaCl), and temperatures (10-55°C) for purified bentonite consisting of 99% montmorillonite. Measured D_a values for bulk bentonite (*i.e.*, with lower smectite content) under similar conditions were 1-2 orders of magnitude higher (Sato et al., 1994; Wu et al., 2014). Under anaerobic conditions, it is possible for Se(IV) to become reduced to Se(0) or Se(-II) (Charlet et al., 2012; Charlet et al., 2007; Ma et al., 2019). Due to the lower adsorption of selenate compared to selenite, selenate diffusion may be even higher than observed for selenite, although we could find no studies on selenate diffusion through bentonite in the literature.

In the FY22 report, we presented the results from ^3H and Se(VI) through-diffusion experiments using a well-characterized, purified montmorillonite source clay (SWy-2) (Zheng et al., 2022). Experiments were conducted with the application of three different electrolyte compositions (under a single ionic strength of 0.1 M) representing pure Na, pure Ca, and a Na-Ca mixture in order to probe the effects of electrolyte composition on clay microstructure, Se(VI) aqueous speciation, and ultimately diffusion. Some preliminary modeling of these experiments was presented, however, the model results were limited by a

lack of information on the diffusion of ^3H and Se(VI) through the filters used in the experiment. In this report, we present results from diffusion experiments conducted on the filters, which will allow better modeling of the diffusion data. In addition, we present early results from a new set of ongoing diffusion experiments conducted with Se(IV) under the same conditions as the experiment with Se(VI) and Se batch adsorption experiments on montmorillonite. Lastly, we present in Section 4.4 a newly released graphical user interface, CrunchEase, which is based on the reactive transport code CrunchClay, and can be used to simulate diffusion processes in an explicit and user-friendly manner.

4.2 Experimental Materials and Methods

4.2.1 Filter Diffusion Measurements

Filter diffusion cells were custom built based on a modified design of Aldaba et al. (2014). The cells consisted of two polycarbonate reservoirs with a filter connecting the two reservoirs. The filter is held in place with o-rings on each side and the two reservoirs are held together in a base plate. A one-hole silicone stopper is fitted in the top of each reservoir with a conductivity probe inserted through the hole to monitor solute diffusion. In addition, a small needle (22 G) is inserted through each stopper to allow venting and pressure equalization with the atmosphere. Without this venting needle, a small pressure differential can develop between the two cells due to slight differences in stopper insertion, causing water to flow between the two cells. A picture of the experimental setup is shown in Figure 4-1. Filters were made of PEEK with a PCTFE ring (IDEX # OC-815). The filters had an overall diameter of 0.95 cm, filter diameter of 0.74 cm, thickness of 0.16 cm, 5 µm pore size, and porosity 0.26 according to the manufacturer.

The diffusion of sodium chloride was measured using this experimental setup in five replicate experiments. The filter was soaked in MilliQ water to remove air bubbles. 45 mL of MilliQ water was then added to each reservoir and allowed to equilibrate for at least 3 hours. The “low” and “high” reservoirs were then spiked with 5 mL MilliQ water or 1 M NaCl, respectively to start the experiment. This resulted in a concentration of 0.1 M NaCl in the high reservoir. Both reservoirs were stirred constantly throughout the experiment. The electrical conductivity of each reservoir was monitored with a conductivity probe and automatically logged every 30-minutes. The conductivity probes were calibrated with known concentrations of NaCl. During one experiment, 0.125 mL subsamples from each reservoir were collected and analyzed for Na by ICPMS in order to verify that the conductivity measurements were accurately representing Na concentration. The measured Na concentrations agreed within 3% for the two methods.

The cumulative mass (mol) of NaCl in the “low” reservoir was plotted over time (s). This results in a pseudo-linear breakthrough curve for the first ~100 hours during which the concentration of NaCl in the “high” reservoir did not change significantly. The curve was fit with a linear regression and the effective diffusion coefficient (D_e) was determined using the slope (a) from the equation given by

$$D_e = \frac{a\,L}{A\,C_0} \qquad \textbf{Eq. (4-1)}$$

where L is the thickness of the filter, A is the cross-sectional area of the filter, and C_0 is the initial concentration in the “high” concentration reservoir.

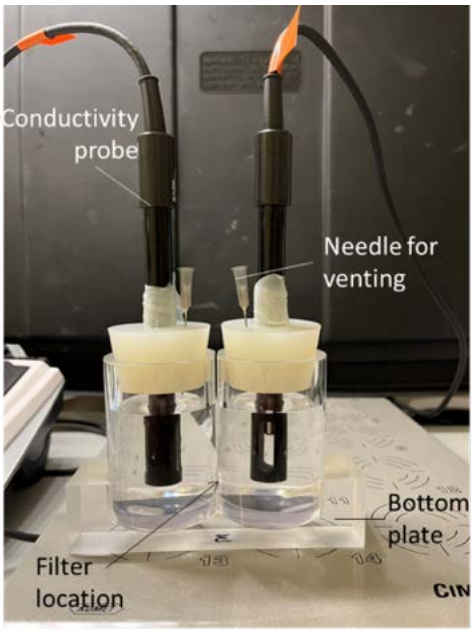

Figure 4-1. Custom-built diffusion cells for measuring diffusion properties of filters.

4.2.2 Clay Samples

Batch Se sorption and diffusion experiments were conducted with a well-characterized montmorillonite source clay (SWy-2) obtained from the Clay Minerals Society. The montmorillonite was purified in order to remove minor impurities (quartz, feldspars, and calcite). The purification procedure was adapted from (Tinnacher et al., 2016). The procedure included the following steps: (1) dialysis against sodium acetate at pH 5 for carbonate mineral removal, (2) dialysis against NaCl to remove acetate and complete Na-saturation, (3) dialysis against water to remove excess salts, and (4) centrifugation to remove particles greater than 2 μm as described previously (Zheng et al., 2022).

In order to ensure that aqueous porewater chemical concentrations were constant during the diffusion experiments, purified montmorillonite was pre-equilibrated with the appropriate background electrolyte prior to packing in diffusion cells. 2 g of purified clay was suspended in 100 mL of electrolyte solution and the clay suspension was transferred to pre-rinsed dialysis tubing (SpectrPor7, 8 kDa). Clay samples were dialyzed against 1 L of background electrolyte for 1.5 weeks, changing dialysis solution at least three times and manually adjusting pH daily. Once the pH was stable, the background electrolyte solution was replaced with MilliQ water, and dialysis was continued for five days, changing the MilliQ water daily. After dialysis was complete, the clay suspension was transferred to 40 mL polycarbonate centrifuge tubes and centrifuged at 39,000 x *g* for 20 minutes. The supernatant was removed, and the clay was dried at 60 °C and ground in ball mill with tungsten carbide balls and stored at room temperature prior to packing the cells. At the time of packing, a subsample of each clay was dried at 150 °C to determine the moisture content.

4.2.3 Se Sorption

Batch Se(IV) and Se(VI) sorption experiments were conducted with purified montmorillonite at 10 g/L. The clay was suspended in 0.1 M NaCl, the pH was adjusted to 6.0, and allowed to equilibrate for 24 hours. The clay suspension was then spiked with sodium selenate or sodium selenite to achieve a final concentration of 100 μM and the pH was adjusted again. After 96 hours, three 1-mL aliquots of the clay suspension were sampled into separate tubes for quantification of dissolved, adsorbed, and total Se. For

dissolved Se, the clay suspension was centrifuged then filtered through a 0.45 µm PVDF filter and analyzed for total Se by Inductively Coupled Plasma – Mass Spectrometer (ICP-MS) (Agilent 8900 ICP-MS Triple Quad) and Se(IV) and Se(VI) by HPLC-ICP-MS. Adsorbed Se was determined by adding 0.1 mL of 1 M KH_2PO_4 buffer at pH 8, mixing for two hours, then centrifuging, filtering, and analyzing the extract. The extract contains adsorbed and dissolved Se, with adsorbed Se determined by subtraction of the measured dissolved Se. Total Se was measured by adding 1 mL of 1 M HCl, mixing for 24 hours, then centrifuging, filtering, and analyzing the extract for total Se by ICP-MS. This separate total Se measurement allows us to ensure that no reduction to Se(0) or Se(-II) occurred during the experiment.

Aqueous Se speciation was measured using an HPLC-ICP-MS method based on that of Ge et al. (1996). Chromatographic separation was achieved with an Agilent 1260 Infinity II HPLC pump equipped with an autosampler. The analytical column was a Hamilton PRP-X100 anion exchange column (10 um, 250 mm long, 4.1 mm inner diameter). PEEK tubing was used to connect the outlet end of the analytical column directly to the nebulizer to allow for in-line quantification of Se. The mobile phase consisted of 5 mM ammonium citrate buffered at pH 5.2 with 2% methanol. The mobile phase was delivered isocratically at a flow rate of 1 mL/min. The sample injection volume was 100 µL. An Agilent 8900 ICP-MS Triple Quad was used to detect ^{78}Se. Hydrogen was used in the collision/reaction cell in order to remove interferences from the argon dimer $^{40}Ar^{38}Ar$ which interferes with the detection of ^{78}Se.

4.2.4 Se(IV) Diffusion Experiments

Diffusion experiments were conducted in the same manner as reported previously for Se(VI), however, Se(IV) was used instead (Zheng et al., 2022). Diffusion experiments were conducted with purified, pre-equilibrated montmorillonite at a dry bulk density (ρ_d) of approximately 1.3 kg/L using custom-built PEEK diffusion cells and PEEK filters with a PCTFE ring (described above). The clay plug had a length of 5 mm and a diameter of 9.5 mm.

Experiments were conducted under a single ionic strength (0.1 M) and three different electrolyte compositions: 0.1 M NaCl, 0.033 M $CaCl_2$, and 0.085 M NaCl + 0.005 M $CaCl_2$, representing pure Na, pure Ca, and a Na-Ca mixture, respectively. All experiments were performed at room temperature at pH 6.5 in equilibrium with atmospheric conditions (~20% O_2 and 400 ppm CO_2). The pre-equilibrated dry clay samples were carefully weighed into PEEK diffusion cells and compacted using a custom PEEK packing rod. Three phases of the diffusion experiment were conducted: (1) saturation, (2) tritiated water (^3H) diffusion, and (3) Se(IV) diffusion. The clay was saturated by circulating 200 mL of background electrolyte at both ends of the cell at approximately 1 mL/min using a peristaltic pump for 40-42 days. After the saturation period, the ^3H through-diffusion phase was started by replacing the background electrolyte solutions with a high ^3H reservoir containing background electrolyte spiked with 30 nCi/mL tritiated water (^3H) (100 mL) at one end and a low ^3H reservoir containing only background electrolyte (15 mL) at the other end. The high concentration reservoir was sampled at the beginning and the end of the ^3H diffusion experiment and did not change significantly over that time period. The low ^3H reservoir was changed at regular time intervals using an in-house built autosampler, and the ^3H concentration was measured in the low reservoir samples by liquid scintillation counting (Perkin-Elmer Liquid Scintillation Analyzer Tri-Carb 2900TR) by mixing 4 mL of sample with 18 mL of Ultima Gold XR liquid scintillation cocktail. The ^3H concentration in the low reservoir never exceeded 0.5% of the concentration in the high reservoir. The ^3H diffusion was continued for 16 days. After this period, the high concentration reservoir was replaced with a Se(IV)-spiked solution containing 1.0 mM sodium selenite in background electrolyte with a total volume of 200 mL, marking the start of the Se(IV) diffusion experiment. The low concentration reservoirs containing only background electrolyte (15 mL) were changed at regular time intervals and Se concentrations were measured by ICPMS (Agilent 8900 ICP-MS Triple Quad). This experiment is ongoing and the results to date are presented.

4.3 Experimental Results and Discussion

4.3.1 Filter Diffusion Properties

Diffusion of NaCl through PEEK filters was measured in five replicate experiments. An example plot of cumulative NaCl mass in the low reservoir over time is shown in Figure 4-2. There was an initial lag period, followed by a linear increase in NaCl in the low reservoir. This linear portion of the breakthrough curve was used to calculate the effective diffusion coefficient of Na through the filter according to Eq. (4-1), resulting in a measured D_e of 6.10 ± 0.29 x 10^{-11} m^2s^{-1} (Table 4-1). Effective diffusion coefficients measured for filters are dependent on characteristics of both the filter and the solute, according to the equation given by

$$D_e = \frac{\varepsilon}{G} D_w \qquad \textbf{Eq. 4-2}$$

where D_w is the bulk diffusion coefficient of a solute in water, which is largely dependent on the hydrated radius of the solute, while G is a geometric factor which accounts for the geometry of the filter pore network, including constrictivity and tortuosity. Given the known values for ε and D_w, we calculated G to be 7.13 ± 0.33 (Table 4-1). The measured D_e value is lower than for stainless steel filters with a similar pore size (1.6 x 10^{-10} m^2s^{-1}) (Aldaba et al., 2014). G and ε are slightly lower for the PEEK filters used in this experiment compared to those used by Aldaba et al. (2014), which had a smaller nominal pore size of 1 µm. However, the net result is a very similar D_e value for Na, which was calculated to be 6.74 x 10^{-11} m^2s^{-1} in Aldaba et al. (2014). Diffusion coefficients can be calculated for other solutes (*e.g.*, SeO_4^{2-}) using the filter parameters shown in Table 4-1 and the known D_w for a given solute.

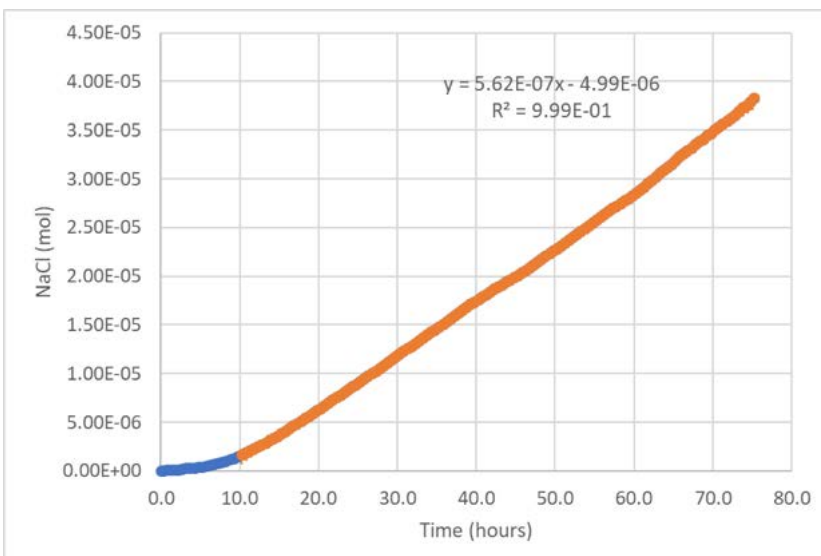

Figure 4-2. Example plot of NaCl mass (mol) in the "low" reservoir over time. The linear regression equation is also shown.

Table 4-1. Diffusion parameters for diffusion of NaCl though PEEK filters.

Parameter	Value	Source
D_e	$6.10 \pm 0.29 \times 10^{-11}$ m^2s^{-1}	this work
D_w[1]	1.68×10^{-9} m^2s^{-1}	Li and Gregory (1974)
ε	0.26	Manufacturer
G	7.13 ± 0.33	this work

[1] The D_w for NaCl was calculated as the average of D_w for Na^+ and Cl^-, given that they diffuse together in this experimental setup to maintain electroneutrality.

4.3.2 Se Sorption

Se(IV) adsorption to purified montmorillonite was observed at pH 6 in 0.1 M NaCl electrolyte solutions, with a K_d (adsorbed Se/dissolved Se) of 25.4 L/kg (Table 4-2). However, no Se(VI) adsorption was observed under the same conditions. It should be noted that K_ds less than ~5 L/kg can be very difficult to measure in clay suspensions. No evidence of Se oxidation or reduction was observed for either Se(IV) or Se(VI) batch experiments. Further batch experiments are underway to measure Se(IV) sorption under a wider range of chemical conditions.

Table 4-2. Results of Se(IV) and Se(VI) batch sorption experiments with 10 g/L montmorillonite in 0.1 M NaCl at pH 6. The starting Se concentration was 100 µM.

Se Species	Adsorbed Se (µmol/g)	Kd (L/kg)
Se(IV)	2.03	25.4
Se(VI)	0.00	0.0

4.3.3 Selenite and ^{3}H Diffusion through Compacted Montmorillonite

Normalized mass flux (J_N, in m/day) reaching the low concentration reservoir was calculated from the equation given by

$$J_N = \frac{C_{low} V_{low}}{C_{high} A \cdot \Delta t} \qquad \textbf{Eq. 4-3}$$

where C_{low} is the concentration in the low concentration reservoir, C_{high} is the concentration in the high concentration reservoir, V_{low} is the volume of the low concentration reservoir (approximately 15 mL), A is the cross-sectional area of the diffusion cell (0.709 cm^2), and Δt is the time interval since the previous sampling event. Two separate, ^{3}H pulses, were conducted for each cell. During the first pulse, the autosampler missed a number of samples for the Ca cell during the first 48 hours. This is a critical period when the tracer is breaking through. Therefore, after 300 hours, the tritium was flushed from the cells by replacing the high concentration reservoir with fresh background solution, and the tritium pulse was repeated. The normalized mass flux for both tritium pulses in the three cells is shown in Figure 4-3. The two pulses agree very well with each other. Tritium diffusion reached steady-state after approximately 70 hours, with higher flux in the Ca cell compared to the Na and Na-Ca cells. This observation is consistent with previous experiments (Zheng et al., 2022). Small differences in the measured ^{3}H normalized flux

may result from small differences in cell packing, which can in turn affect porosity or pore structure (*i.e.*, pore constrictivity or tortuosity). Total porosity (ε) depends on bulk density and can be calculated using the following equation.

$$\varepsilon = 1 - \frac{\rho_d}{\rho_g} \qquad \textbf{Eq. (4-4)}$$

where ρ_g is the crystal density of clay mineral layers (*i.e.*, grain density). For montmorillonite, ρ_g is approximately 2.84 kg/L (Bourg et al., 2006; Tournassat & Appelo, 2011). There were some small differences in the calculated bulk density and porosity for the three cells due to differences in the moisture content of the clays at the time of packing. A summary of the diffusion cell parameters, including an average normalized flux at steady state (>70 hr) is shown in Table 4-3.

After 15 days (360 hours) of Se(IV) diffusion, Se has not yet been detected in the low reservoir. This is in contrast to Se(VI) diffusion tested previously, in which Se(VI) reached steady state after approximately 300 hours. Given the higher sorption of Se(IV) to clay minerals compared to Se(VI), slower breakthrough of Se(IV) is expected. This experiment is ongoing.

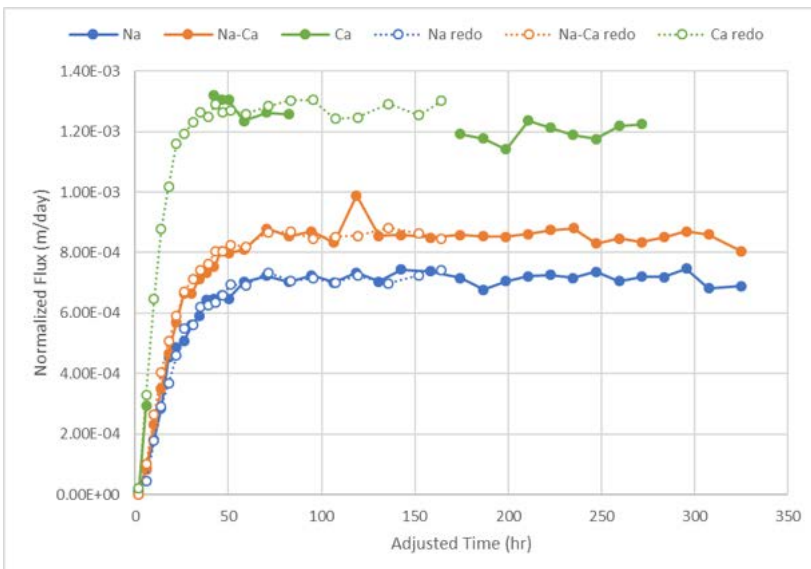

Figure 4-3 Normalized ^{3}H flux in three diffusion cells. Each cell received two pulses of ^{3}H, and data for both are shown. The autosampler missed several samples during the first pulse for the Ca cell.

Table 4-3 Summary of measured diffusion parameters, including dry bulk density, porosity, and normalized mass flux (J_N).

Soln	pH	dry density (kg/L)	porosity	^{3}H avg J_N (m/day)
0.1 M NaCl	6.5	1.34	0.53	7.18 ± 0.05 x10^{-4}
0.085 M NaCl, 0.005 M CaCl2	6.5	1.28	0.55	8.60 ± 0.04 x 10^{-4}
0.033 M CaCl2	6.5	1.24	0.57	± 0.01 x 10^{-3}

4.4 CrunchEase Graphical User Interface for Interpretation of Diffusion Results

A characterization of radionuclide diffusion parameters in clayey materials is essential for the performance assessment of engineered barrier systems (EBSs) in radioactive waste storage concepts (Altmann et al., 2012; Bourg & Tournassat, 2015). These parameters include the effective diffusion coefficient (D_e), effective porosity (ε), and adsorption distribution coefficient (K_D), which are characteristic of both clayey materials and the radionuclides under investigation. Values of D_e, ε, and K_D are empirically determined in the framework of the Fickian Diffusion theory. However, these parameters lump together a range of physical and chemical processes that can be unraveled only by applying multi-scale characterization and modeling techniques (Liu et al., 2022). The simplicity of the $D_e - \varepsilon - K_D$ modeling approach, as well as its robustness for cases specific to radioactive waste storage concepts (constant far-field conditions in space and time, trace concentration levels for radionuclides), is in stark contrast to the complexities of the underlying physical and chemical processes. However, the $D_e - \varepsilon - K_D$ modeling approach is the current norm in barrier performance evaluation methodology due to its simplicity.

Because the $D_e - \varepsilon - K_D$ modeling approach is empirical in nature, parameter estimation is most often carried out based on the fitting of experimental data. For this purpose, extensive diffusion datasets have been acquired over the past decades. The interpretation of such data relies on solving Fick's first and second laws of diffusion. Often, parameter estimation from diffusion experiments is carried out using analytical solutions rather than empirical models due, however these analytical solutions have certain limitations. For the experimental setups commonly reported in the literature, through-diffusion experiments with constant boundary conditions, *i.e.,* a constant concentration gradient across the diffusion cell over the course of the experiment (Figure 4-4(a)), are quite common. However, in practice (Figure 4-4(b)), the concentration in the high-concentration reservoir is kept as constant as possible by using a high volume, while the concentration in the low-concentration reservoir is kept as close to zero as analytically/practically possible by replacing the low-concentration reservoir periodically. The experimental tracer diffusive flux is then evaluated from the tracer accumulation in the low-concentration reservoir. Other practical necessities, including the use of tubing to connect the low and high reservoirs to the sample, and the use of filters at both ends of the sample to hold it in place complicate the interpretation of the results. Namely, the filters have diffusion properties that differ from the solid sample under investigation. An accurate evaluation of diffusion parameters requires that these experimental biases are specifically taken into account in the fitting procedure or are mitigated with special experimental procedures (Glauss et al., 2008). Experimental mitigation strategies include the development of (flushed) filters in which the reservoir solution is circulated inside of the filters (as opposed to filters at which the solution is circulated at the surface opposite to the sample), thus enabling a more homogeneous solute concentration in the filter and the connected tubing and reservoir (Glauss et al., 2015). However, all biases and their combinations cannot always be addressed using experimental mitigation strategies or analytical solution development. A literature survey reveals that many numerical tools have been developed to interpret diffusion experiments (Moridis, 1999; Savoye et al., 2012; Glaus et al., 2015; Chen & Wang, 2017). However, these tools lack either generality concerning the series of identified biases, easy accessibility by the scientific community, or both. Here we present a user-friendly, fast, generic, reliable, and free tool, namely the CrunchEase user interface to be used with the CrunchClay code for use interpreting diffusion data with $D_e - \varepsilon - K_D$ conceptual models.

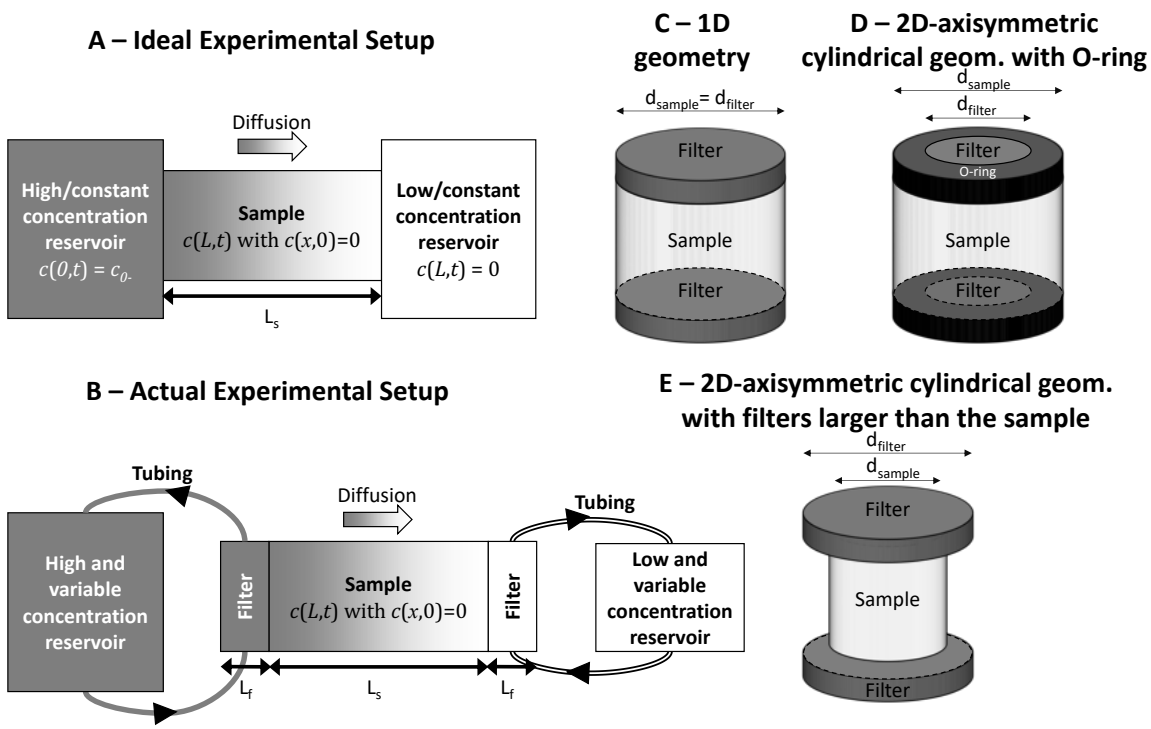

Figure 4-4. Schematic of an (a) ideal and (b) actual through-diffusion experimental setup with the goal of achieving constant boundary conditions (*i.e.*, with a constant concentration gradient across the diffusion cell at steady state). (c) 1D diffusion geometry, and (d) €: 2D- axisymmetric cylindrical geometries. Tracer cannot diffuse through the plain O-ring of the filter support (d), making the diffusional path 2D. The cross-sectional area available for diffusion in the filters is equal to $\left(\frac{d_{filter}}{2}\right)^2 / \left(\frac{d_{sample}}{2}\right)^2$ of the cross-sectional area of the sample.

4.4.1 Effect of Filters

The presence of filters has a marked influence on the outcomes for simulations. If the presence of filters is neglected in the fitting procedure, effective diffusion coefficients are underestimated, and rock capacity factors are overestimated. Furthermore, the influence of filter effects on the absolute D_e value increases with increasing K_D values and L_{filter}/L_{sample} ratios (Figure 4-5), as previously reported (Glaus et al., 2008). Since it is so easy to include filters in the proposed new modeling package, one should do so as a good standard practice, even when the filters are not expected to affect the results substantially compared to other sources of bias (Glaus et al., 2008).

The consideration of a 2D axisymmetric cylindrical geometry instead of a 1D geometry (Figure 4-4(d) and (e)) can also be explicitly modeled using CrunchEase, however, this increases the calculation time significantly. The result of a 1D simulation with a filter porosity scaled down to 49 % of its initial value (0.147 instead of 0.3) and a tortuosity value decreased from 0.3 to 0.11 after trial-and-error iterations proved to be in good agreement with the result of the 2D axisymmetric cylindrical geometry simulation in cases where the effective diffusion coefficient of the filter was higher than that of the sample.

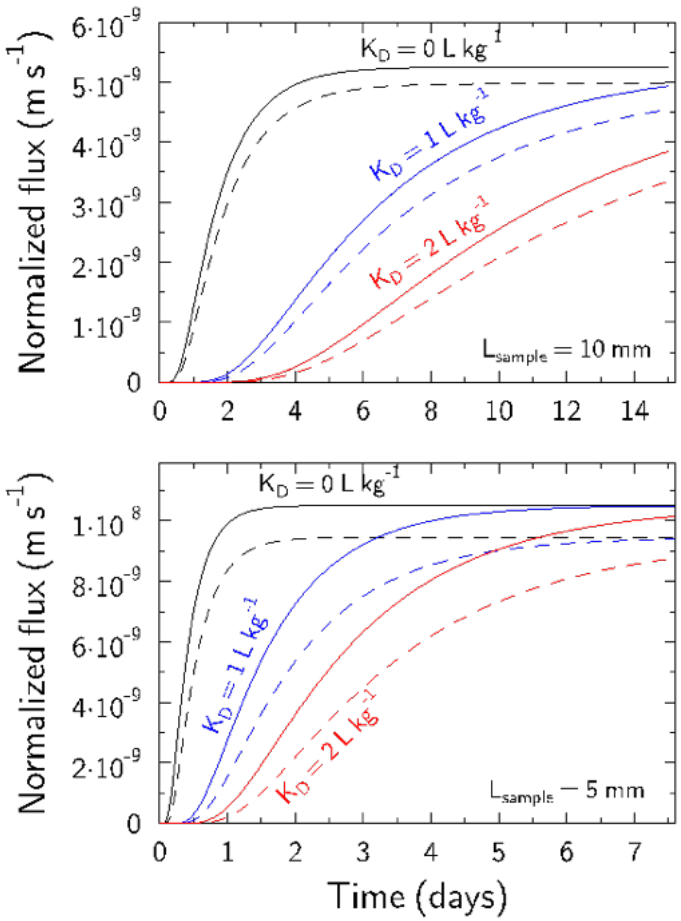

Figure 4-5. Comparison of diffusion breakthrough curves calculated in CrunchEase/CrunchClay in the absence (full lines) and presence (dashed lines) of filters, as a function of sample length (L_{sample} = 5 mm vs. 10 mm) and K_D value (from 0 to 2 L kg^{-1}).

4.4.2 CrunchEase Quick Tutorial

4.4.2.1 Installation (for Windows Users)

Download the file *CrunchEase_Setup.exe* from:
https://github.com/Tournassat/CrunchEaseForAll/releases/tag/v1.0.0.

Double-click on *CrunchEase_Setup.exe* to install CrunchEase in the directory *C:\Users* ***YourUserName*** *\Documents\CrunchEase* (follow the instructions and accept the installation). At the moment, you cannot change the install directory.

Go to *C:\Users****YourUserName****\Documents\CrunchEase*.

Double-click on *w_ifort_runtime_p_2022.2.0.3790.exe* to install the external Intel libraries that are necessary to run CrunchClay.

Reboot your computer.

Go to *C:\Users* ***YourUserName*** *\Documents\CrunchEase*.

Your directory should contain at least the items shown in Figure 4-6.

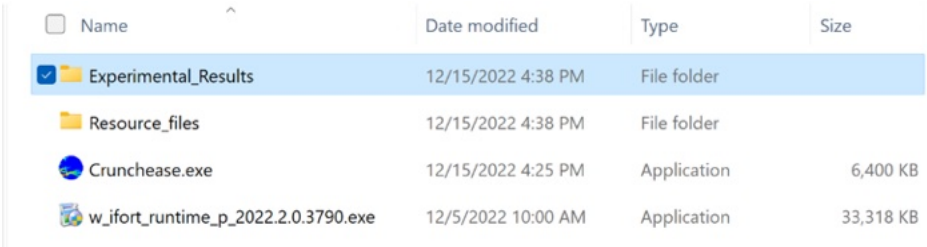

Name	Date modified	Type	Size
Experimental_Results	12/15/2022 4:38 PM	File folder	
Resource_files	12/15/2022 4:38 PM	File folder	
Crunchease.exe	12/15/2022 4:25 PM	Application	6,400 KB
w_ifort_runtime_p_2022.2.0.3790.exe	12/5/2022 10:00 AM	Application	33,318 KB

Figure 4-6 Screenshot of the CrunchEase install directory.

4.4.2.2 Example of a Simple Diffusion Calculation

Double-click on *CrunchEase.exe*.

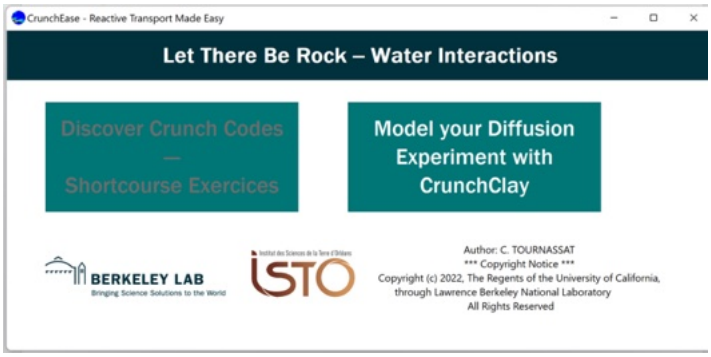

Figure 4-7. Screenshot of the main window of the CrunchEase interface.

Click on "**Model your Diffusion Experiment with CrunchClay**" (Figure 4-7).

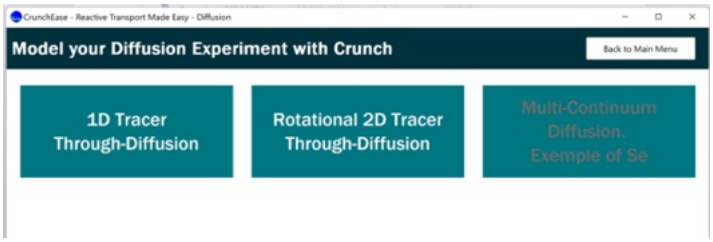

Figure 4-8. Screenshot of the Diffusion window of the CrunchEase interface.

Click on "**1D Tracer Through-Diffusion**" (Figure 4-8).

You are ready to run your first simulation with CrunchEase/CrunchClay (Figure 4-9).

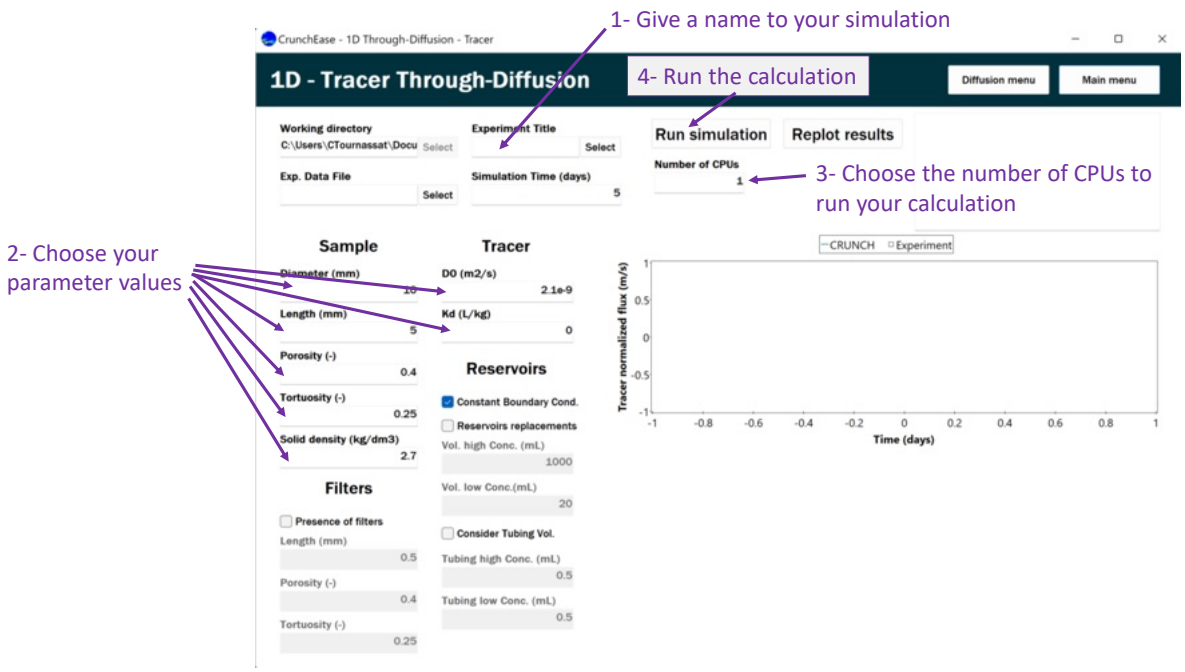

Figure 4-9. Screenshot of the 1D- Through-Diffusion window of the CrunchEase interface. Follow numbered instructions to run your first simulation.

After a short time, you obtain your results (Figure 4-10).

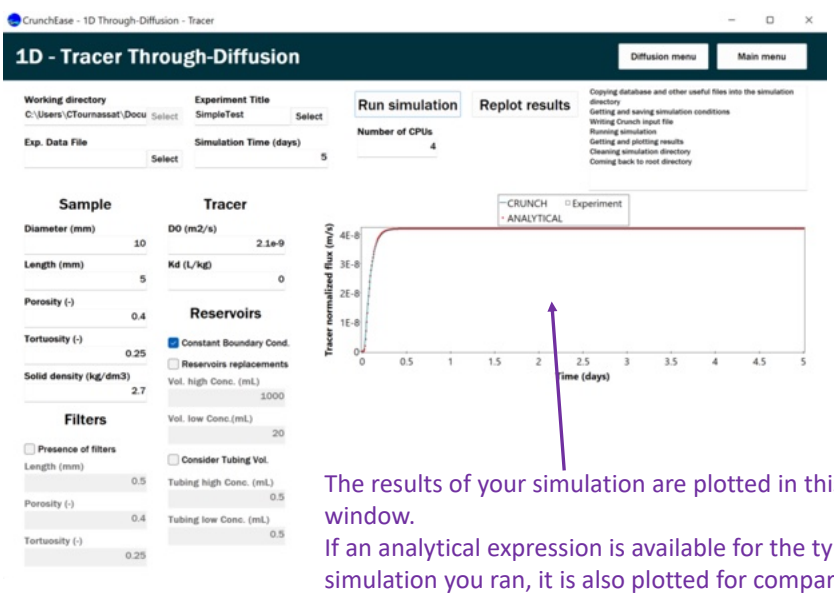

Figure 4-10. Screenshot of the 1D- Through-Diffusion window of the CrunchEase interface after calculation

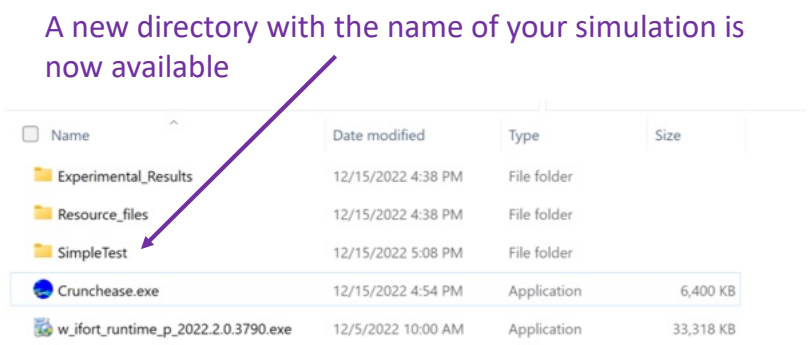

Figure 4-11. Screenshot of the Tutorial directory after calculation.

Open the newly created directory, which is named after your Experiment Title (Figure 4-11).

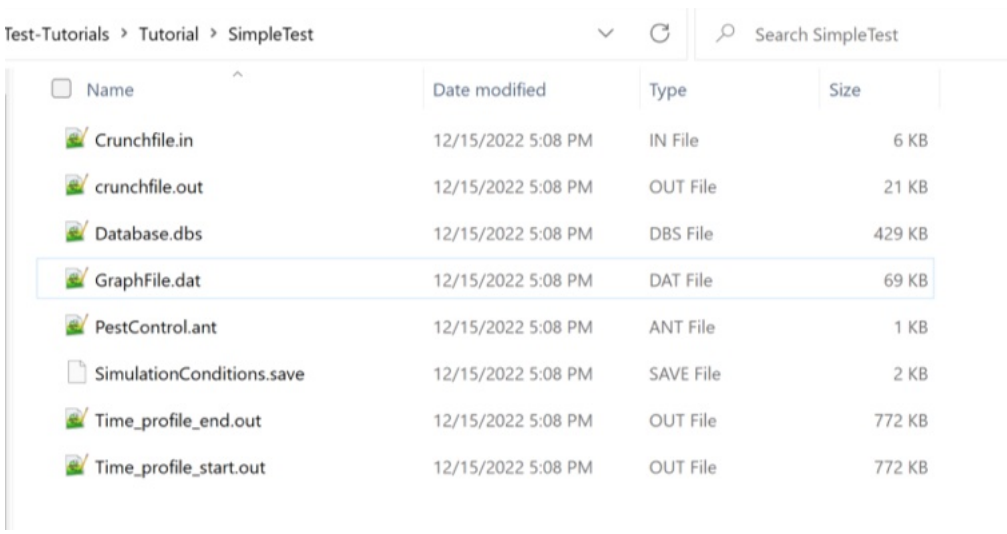

Figure 4-12. Screenshot of the simulation directory (named after your Experiment Title) after calculation.

You will find in the new directory a text file *GraphFile.dat* (Figure 4-12) that you can use to plot your simulation results with the plotting software of your choice.

Simulation conditions and parameters are saved in the file *SimulationConditions.save*, which is used by CrunchEase to reload saved parameters from an existing simulation name (in the box Experiment Title).

4.4.2.3 Compare Simulation Results with Experimental Measurements

It is always possible to compare the computed flux with your data using the output file *GraphFile.dat*. However, CrunchEase offers the possibility to directly compare tracer concentrations measured in the downstream reservoir with simulation results. This capability enables better characterization of diffusion parameters while considering experimental setup characteristics more accurately (see the text of the main paper for further explanations). The practical procedure is explained below.

Create a new simulation with a new name (*e.g.*, TestWithData).

In the field Exp. Data File, select a data file (take Ruth_Br.txt for example) in the directory.

If you want to create a new data file, it must be saved in the *Experimental_results* directory, so that CrunchEase can find it.

Experimental data files have a simple structure:

Elapsed Time (day)	Br rel. Conc	Vol low C res (mL).
0.25	2.22E-05	20.15
0.93	1.16E-03	19.7
1.23	8.37E-04	19.99
1.86	1.66E-03	20.03
2.23	1.01E-03	20.05

The first line is a header line that is not used by CrunchEase. Then, starting from the second line, the following data values must be entered on the same line for each sampling time:

- the elapsed time (in days),
- the tracer relative concentration in the downstream reservoir (dimensionless), and
- the volume of the downstream reservoir (in mL).

The three values may be separated with spaces, tabulations, commas, or semicolons.

Tracer relative concentration corresponds to the actual concentration divided by the initial concentration in the upstream (high concentration) reservoir.

Figure 4-13 shows the options and parameters selected to model Br diffusion data from Tinnacher et al. (2016).

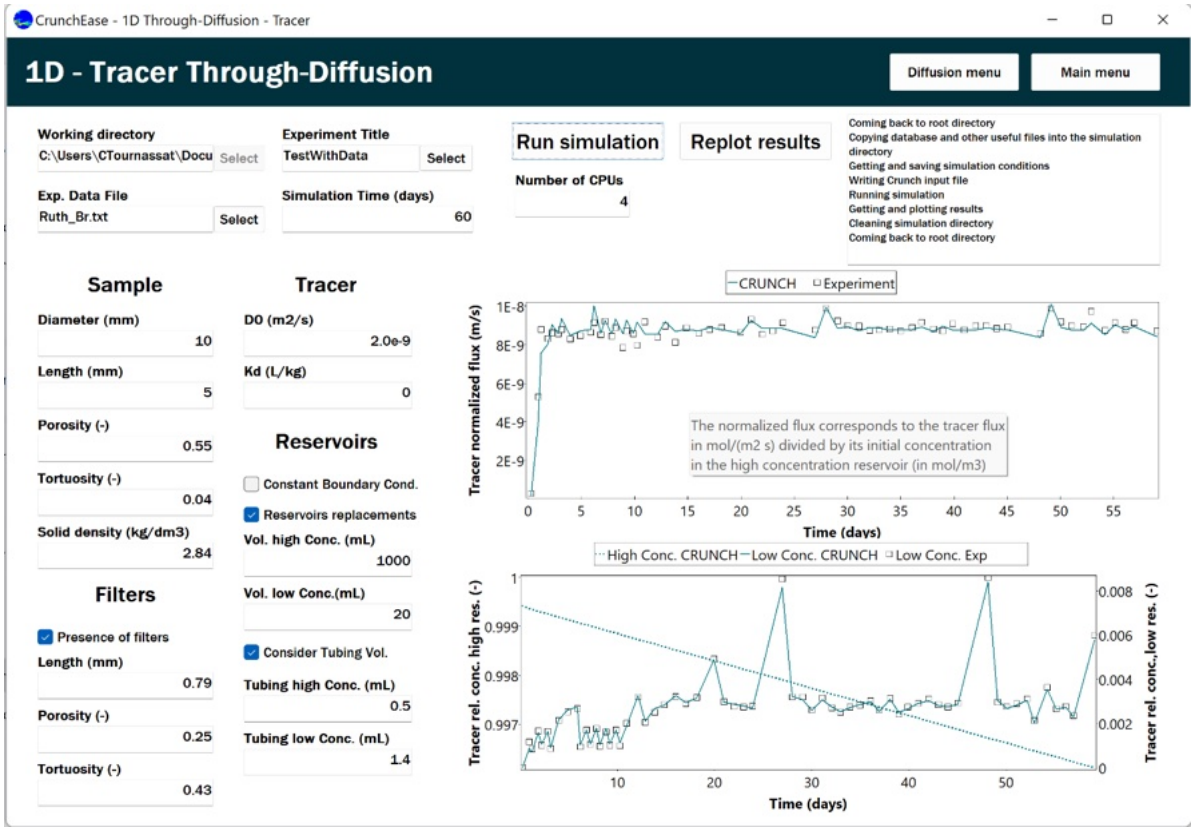

Figure 4-13. Screenshot of the 1D- Through-Diffusion window of the CrunchEase interface with options and parameters selected to model Br diffusion data from Tinnacher et al. (2016).

4.4.2.4 Adding Complexity to Your CrunchClay Simulation

The directory contains all files that are necessary to re-run the simulation with or without using CrunchEase (i.e., using directly CrunchClay). Running CrunchFile.in with CrunchClay will start the entire calculation. Files with the _resX.in termination (X is an integer) are restart files used by CrunchClay at each sampling event. These files must not be changed.

The chemical system considered in the simulation can be made more complex by changing chemical inputs in CrunchFile.in. These changes necessitate additional knowledge of CrunchClay, which is not covered in this tutorial. In the future, the interface will be enriched with additional capabilities that will help the users to learn and take full advantage of Crunch codes capabilities.

4.5 Summary and Future Work

Diffusion experiments were conducted to measure the diffusive properties of PEEK filters used in through-diffusion experiments. The effective diffusion coefficient of NaCl through the filters was 6.10 ± 0.29 x 10^{-11} m^2s^{-1}, and the geometric factor (G) representing the geometry of the pore network was 5.64 ± 0.26. These values are within the range of values in the literature (Aldaba et al., 2014). This data is necessary to accurately model solute diffusion through compacted clay, and will be used to refine the Se diffusion model for Se(VI) diffusion through montmorillonite. In addition, ^{3}H and Se(IV) through-diffusion experiments with compacted montmorillonite at a bulk density of approximately 1.3 kg/L are currently underway. These experiments investigate the diffusion of Se(IV) under three different

electrolyte compositions (0.1 M NaCl, 0.033 M $CaCl_2$, and 0.085 M NaCl + 0.005 M $CaCl_2$), allowing a direct comparison with Se(VI) diffusion experiments conducted previously (Zheng et al., 2022). We observed an increase in total porosity and diffusive flux for ^3H as you go from Na to Na-Ca to Ca-montmorillonite, consistent with previous results. This trend is interpreted as a consequence of differences in microstructure driven by pore water composition differences: Ca dominated surfaces have the tendency to stack clay layers, and so to open larger inter particles pores compared to Na dominated surfaces. Se(IV) diffusive breakthrough is delayed compared to Se(VI), with no Se(IV) detected after 15 days. This is likely due to the higher adsorption of Se(IV) compared to Se(VI). We have also developed a new graphical user interface, CrunchEase, based on the CrunchClay reactive transport modeling code. CrunchEase provides an easy-to-use interface, which allows experimentalists to simulate diffusion data, and to explicitly take into account experimental biases, including the presence of filters and tubing 'dead' volumes, and variable sampling events which are present in real experimental setups (Tournassat et al., 2023).

Future work for this task will focus on (1) completing Se(IV) diffusion experiments, (2) refining the Se diffusion model to include the filter properties, and (3) conducting batch experiments with Se(IV), Se(VI) and clay under a wider range of chemical conditions.

5. COUPLED MICROBIAL ABIOTIC PROCESSES IN EBS AND HOST ROCK MATERIALS

5.1 Introduction

Previous reports described experiments on residual microbial activity in FEBEX material samples that were collected from high heat, intermediate, and controlled temperature zones. Experiments were designed to determine if these materials possess residual microbial community capable of metabolic activity in the presence of H_2, O_2, and CO_2, and how the FEBEX treatment impacted those capabilities. In previous FYs, we conducted several sets of experiments on four different materials from a 'heater zone' (BD-48-6, high temperature), from a 'cold zone' (BD-59-10), and two mid temperature zones, BD-48-5 (mid high temperature) and BD-48-4 (mid low temperature). In FY22, focus shifted to data analysis and manuscript preparation with a particular focus on the microbial community analysis.

The objective was to test the hypothesis that even after long-term emplacement, viable organisms capable of various metabolic processes, including H2 utilization, persist in the system. Samples were incubated in non-enriched minimal conditions and experiments were designed to determine if these materials possess microbial communities with the ability to metabolize H_2 or other substrates, and how the FEBEX treatment impacted those capabilities. The findings indicate that there is still a considerable metabolic potential within the microbial communities, underscoring the significant role of microbial metabolism in long-term nuclear waste disposal repositories employing clay as a barrier material.

5.2 Methods

Four samples were collected in 2015 from several zones at the FEBEX site, as depicted in Figure 5-1. Sample BD-48-6 collected from the heater zone (T = 95 °C), sample BD-59-10 (a control) collected from the cold zone (i.e., under the ambient temperature), BD-48-5 collected from a zone with mid-high temperature (T = 50 °C), and sample BD-48-4 from the mid-low temperature zone (T = 35 °C). Prior to sampling, the clays were allowed to cool in the formation. Subsequently, in the laboratory, external surfaces, which had encountered extraction equipment, were removed, and subsampling was conducted. The final samples had an average volume of 18 cm^3, were wrapped in plastic, vacuum sealed in aluminized Mylar bags, and stored at room temperature.

To prepare the sample of each clay type, the Mylar bags containing the subsamples were opened and a piece was broken away from the large block. This subsample was placed on an autoclaved piece of aluminum foil in the biosafety cabinet and 0.5 cm was scraped with a sterilized razor blade to remove the outer surfaces. Scrapings and foil were removed, and the sample was placed on a new autoclaved piece of foil. A fresh sterile razor blade was then used to remove about 5 g of clay. This 'fresh' (newly exposed) layer of clay was mixed and distributed amongst 60 mL serum vials (six for each clay type) containing 10 mL of sterile minimal salts media (MSM) (Sigma M9 MSM), which contains 15 g/L KH_2PO4, 64 g/L $Na_2HPO_4 \cdot 7H_2O$, 2.5 g/L NaCl, 5.0 g/L NH_4Cl. MSM was purchased 5x concentrated (Sigma), so actual addition was 2 mL of MSM medium and 8 mL of deionized (DI) water (milliQ). The medium and water were added to 60 mL serum bottles through a 0.2 µm filter. 15 psi of gas mix was added to each serum bottle. This was done by starting with a full serum bottle of air, adding 7 mL of CO_2, and pressuring to 15 psi with a N_2/5% H2 mix. All gas was filtered through a 0.2 µm filter. This method provided a consistent gas mix for all bottles, with an average final composition of 5% CO_2, 2.8% H_2, 9% O_2, with a balance of N_2.

(a)

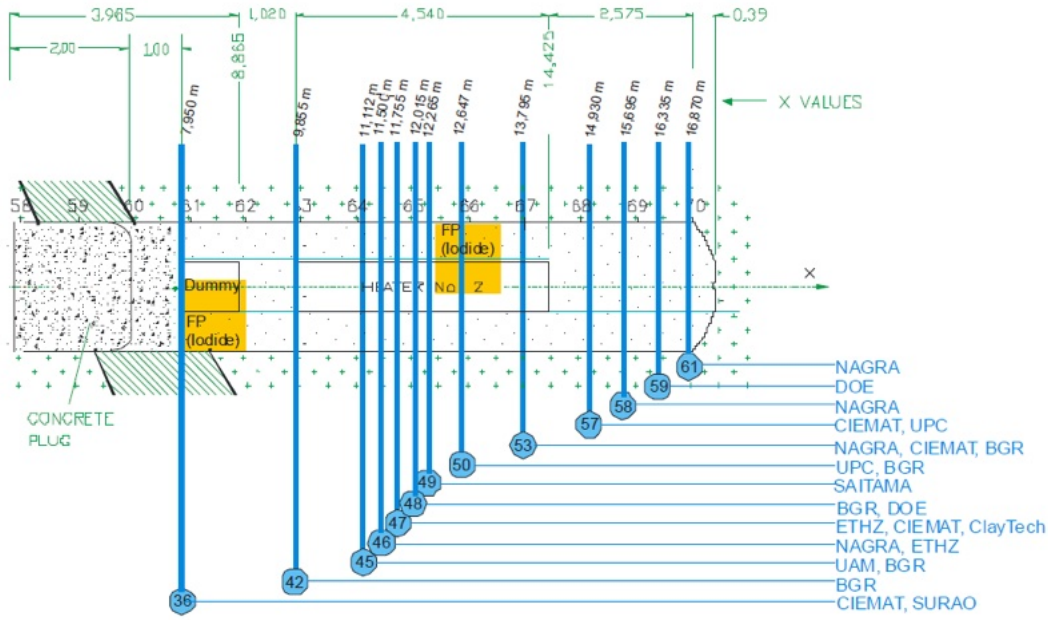

(b)

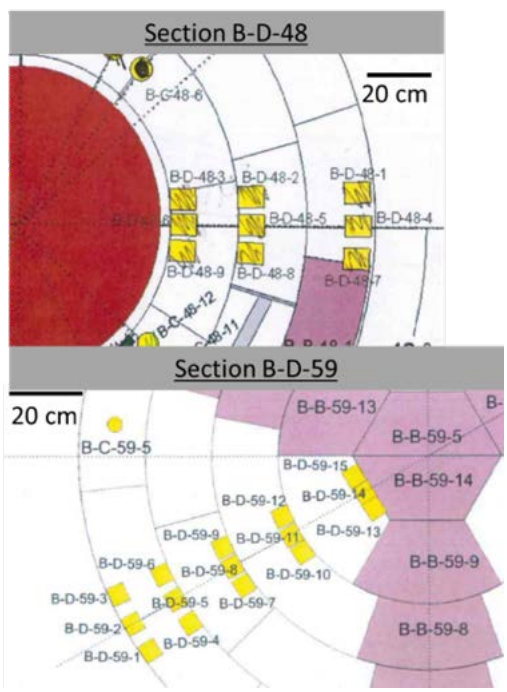

Figure 5-1. Locations of bentonite samples in original FEBEX experiment: (a) Longitudinal cross-section along FEBEX tunnel, and (b) cross-sections B-D-48 and B-D-69 (modified from Villar, 2017) Samples were taken from B-D-59-10 (T-ambient), B-D-48-4 (T-35), B-D-48-5 (T-50), and B-D-48-6 (T-90).

Sample designations were: 'T-ambient' (non-heated, from BD-59-10); T-35, (35 °C, from BD-48-4); T-50 (50 °C, from BD- 48-5); T-95 (95 °C, from BD-48-6) (Villar et al., 2018). For experiment 1 and 2, only T-ambient and T-95 were tested. In experiments 3 and 4, all four samples were included (Table 5-1). Sterile control samples (autoclaved clay) and blanks (no clay, only media) were run for assessment purposes. Four to six samples were prepared of each clay type, and an additional two to three samples of autoclaved controls for each clay, and three blank controls for each experiment.

Table 5-1. Experimental descriptions.

Experiment	FEBEX samples	Outcome	Initial O_2	Initial CO_2	Initial H_2	Solid/liquid ratio (mg/mL)	Test length (days)
1	B-D-48-6 (T-95) B-D-59-10 (T-ambient)	Stopped/no data	3-5.5%	1-3%	3-5%	25	60
2	B-D-48-6 (T-95) B-D-59-10 (T-ambient)	H_2 consumption in T-ambient samples	9.2%	6.0%	3.0%	25	379
3	B-D-48-6 (T-95) B-D-48-5 (T-50) B-D-48-4 (T-35) B-D-59-10 (T-ambient)	Low acivity observed possibly due to high solids content	10.6%	5.0%	2.2%	60	296
4a	B-D-48-6 (T-95) B-D-48-5 (T-50) B-D-48-4 (T-35) B-D-59-10 (T-ambient)	Low activity observed, O2 levels too hight	12.4%	5.4%	2.0%	46	120
4b	B-D-48-6 (T-95) B-D-48-5 (T-50) B-D-48-4 (T-35) B-D-59-10 (T-ambient)	O_2 consumption and CO_2 production in 59-10 and to a lesser extent 48-4	8.6%	6.5%	2.7%	46	287

Samples were placed horizontally on a rocking table and incubated at 35 °C. To monitor activity, gas composition of the serum bottle headspace was analyzed periodically. Gas analysis was performed on a Shimadzu GC-8AIT with Argon (Ar) carrier gas, which allowed for simultaneous quantitative determination of H_2, O_2, N_2, and CO_2. GC conditions were as follows: Ar flow 0.4 kg/cm^3, detector and injection temperature 150 °C, column temperature 35 °C, 80 mA current, CTRI packed column. Calibrations of H_2, O_2, N_2, and CO_2 were completed prior to sampling bottles with known concentrations of gases. Samples were analyzed immediately after removing from the incubator and replaced in the incubator after sampling. To sample, an alcohol saturated wipe was put on the serum stopper for five minutes to sterilize the surface of the stopper. A sterile 22-gauge needle connected to a gas tight syringe was then inserted into the stopper and 100 µL of headspace was removed and injected into the GC. A new needle was used for each bottle when sampled. With a headspace volume of 50 mL, and with each bottle sampled approximately 18 times over the incubation, this resulted in a 3.6% loss of gas pressure over the entire incubation period.

Incubated samples were depressurized and de-crimped, and the total sample (clay and media) were transferred to a sterile 15 mL tube and stored at -80 °C until extraction. Total genomic deoxyribonucleic acid (DNA) was collected in duplicates from each sample using the DNeasy PowerSoil kit (QIAGEN) following the manufacturer's instructions. The duplicate DNA extractions were combined prior to polymerase chain reaction (PCR) amplification. The 16S rRNA gene was amplified for the identification of bacteria and archaea using 515F (5′-ACT CCT ACG GGA GGC AGC A-3′) and 806R (5′-GGA CTA CHV GGG TWT CTA AT-3′) primers (Mori et al., 2013). The reverse PCR primer was modified to include Illumina Nextera adapters and 12-bp Golay barcodes. The PCR reactions were performed in triplicates in 25 µL reactions with the following reagents: Takara Ex Taq (0.025 units µL-1), 1X Takara Ex Taq PCR buffer, Takara dNTPs mix (200 µM), Roche bovine serum albumin (0.56 mg m

L-1), PCR primer (200 nM), and approximately 10 ng uL-1 DNA template. 16S gene amplification was performed with the following thermocycler settings, 95 °C for three minutes, 25 cycles of 95 °C for 45 seconds, 50 °C for 60 seconds, and 72 °C for 90 seconds with a final extension of 10 minutes at 72 °C. The PCR product triplicates were composited and purified using Sera-Mag (Thermo Scientific) Solid-Phase Reversible Immobilization (SPRI) paramagnetic beads. Quantification of the purified PCR products was done using the Qubit HS-DS-DNA kit (Invitrogen) and pooled in equimolar concentrations (10ng/µL for 16S) and sequenced on a single lane for 300 bp (basepair) paired-end Illumina v3 MiSeq sequencing completed at the Vincent J. Coates Genomics Sequencing Laboratory at UC Berkeley.

For Experiment 4 only, at the end of the incubation, the serum bottles were depressurized and opened, and the pH was measured immediately. The bottles were then mixed to suspend the solids and 0.5 mL of suspension was removed to quantify the solid/liquid ratio. Porewater was then separated for geochemical analysis by centrifugation (at 8000x g for 15 min) and porewater was filtered through a 0.45 µm PVDF syringe filter. Porewater samples were analyzed for anions by ion chromatography (Thermo Scientific Dionex ICS-2100) and metals by ICP-MS (Perkin-Elmer Elan DRC II).

Four experiments have been completed, as described in Table 5-1. Experiment 1 focused on working out experimental protocols. Experiment 2 consisted of the high heat samples (T-95) and the control, ambient heated sample (T-ambient). Gas composition data for H_2, CO_2 and O_2 from Experiment 2 is shown in Figure 5-2. These plots show the average of all replicates for each condition. On Day 150, the samples were re-gassed to the original gas composition due to consumption of H_2 in T-ambient samples, and again with the H_2 mix only for the T-ambient samples only on day 350, which lowered percent CO_2 content from 8% to 4%. Gas consumption was only observed in the T-ambient samples, and was not evident until Day 50, when loss of H_2 and O_2 was observed. Note that the rate of H_2 consumption in the replicates was not consistent, with a range of consumption rates observed (see Figure 5-2). No significant loss of gas was seen in the controls and T-95 sample.

At the conclusion of the experiment, three samples from the T-ambient incubation bottles, two with high, medium high, and one with low H_2 consumption rates, and one sample from the High T95 bottles (with no H_2 consumption) were sent for DNA microbial analysis.

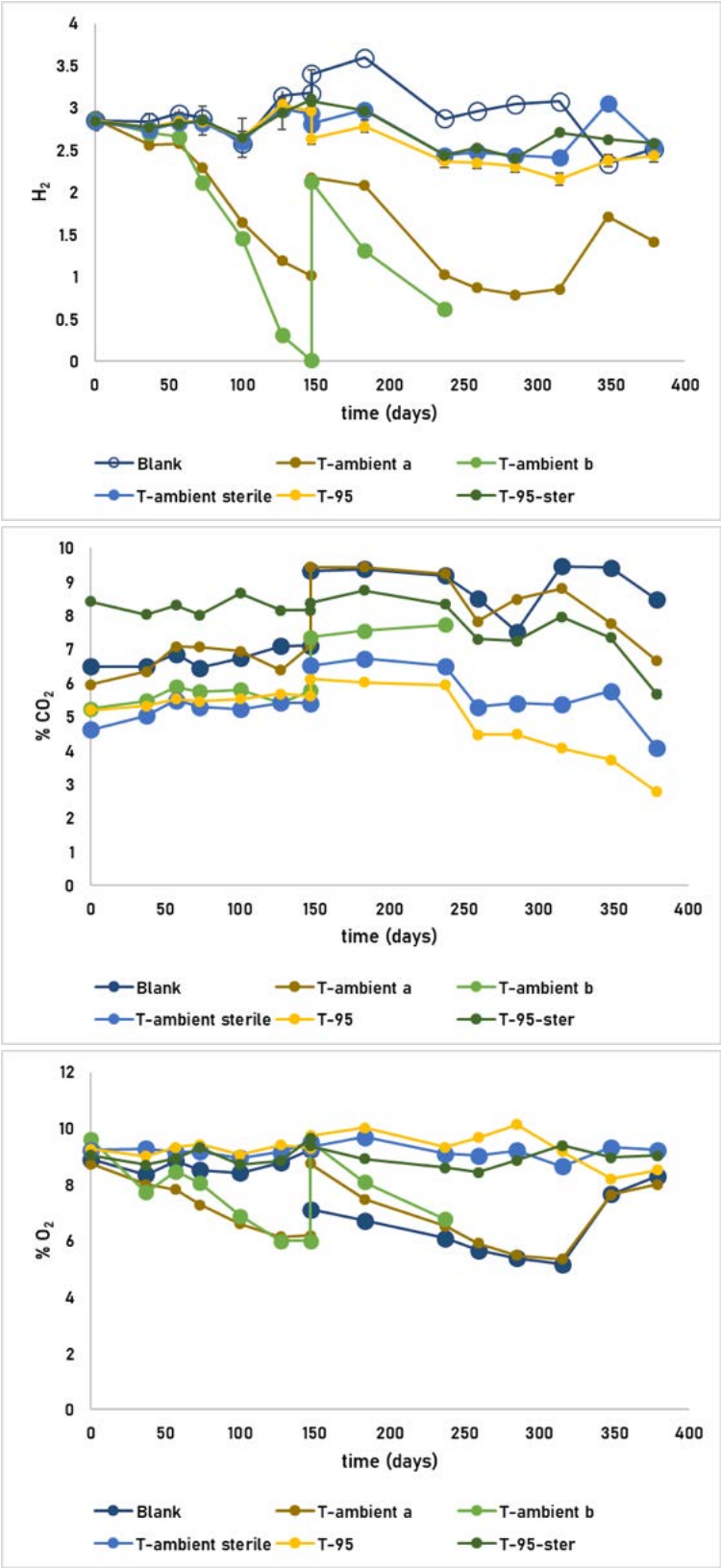

Figure 5-2. Percent H2, CO2, and O2 for Experiment 2. Experiments were re-gassed with hydrogen at 150 days.

5.3 Data Interpretation

The results from Experiment 2 are shown in Figure 5-3. The T-95 sample had very low DNA extraction amounts, but results show a variety of species present. In contrast, the T-ambient samples show enrichment of a specific organisms, which have the potential for hydrogen metabolism, including *Actinobacerium, Firmucutes,* and *Acidobacteria* (Giguere et al, 2020; Greening et al., 2014; Piche-Choquette, 2019; Kalam, 2020). Because DNA extraction efficiencies are related to several factors, including the difficulty in extracting from clay, we cannot infer absolute bacterial abundance or determine if there was selective harm to a specific group of microorganisms during heating. However, it does appear that certain organisms existing on the clay can become active in the non-heated clay and sequencing data suggest that there are bacterial community in the non-heated clay. The alpha diversity data (Figure 5-4) indicate that the microbial community exhibits greater diversity in samples without heat compared to those exposed to high heat. Furthermore, a positive correlation is observed between higher H_2 consumption rates and increased microbial diversity (Figure 5-5). This suggests that higher levels of H_2 reduction are associated with microbial activities, leading to enhanced microbial diversity.

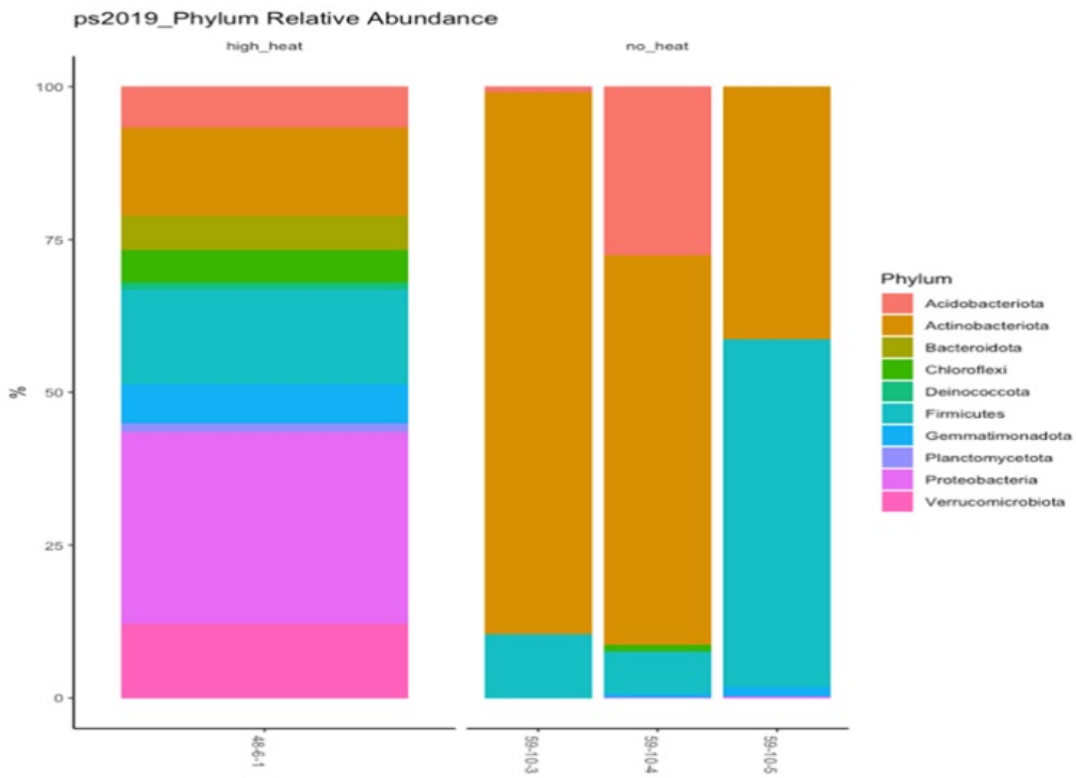

Figure 5-3. Relative abundance of phylum from DNA sequencing results for Experiment 2. Although in this figure the high heat samples shows higher diversity, due to low DNA recovery this data is probably due to noise.

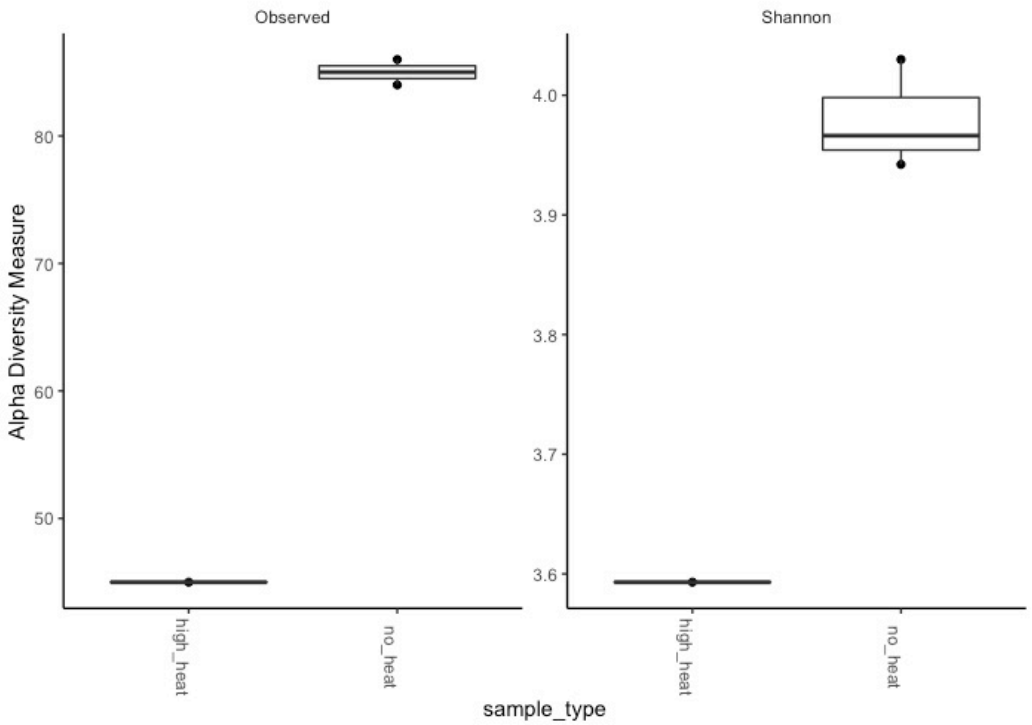

Figure 5-4. Alpha diversity from DNA sequencing shows the heated clays have reduced microbial diversity.

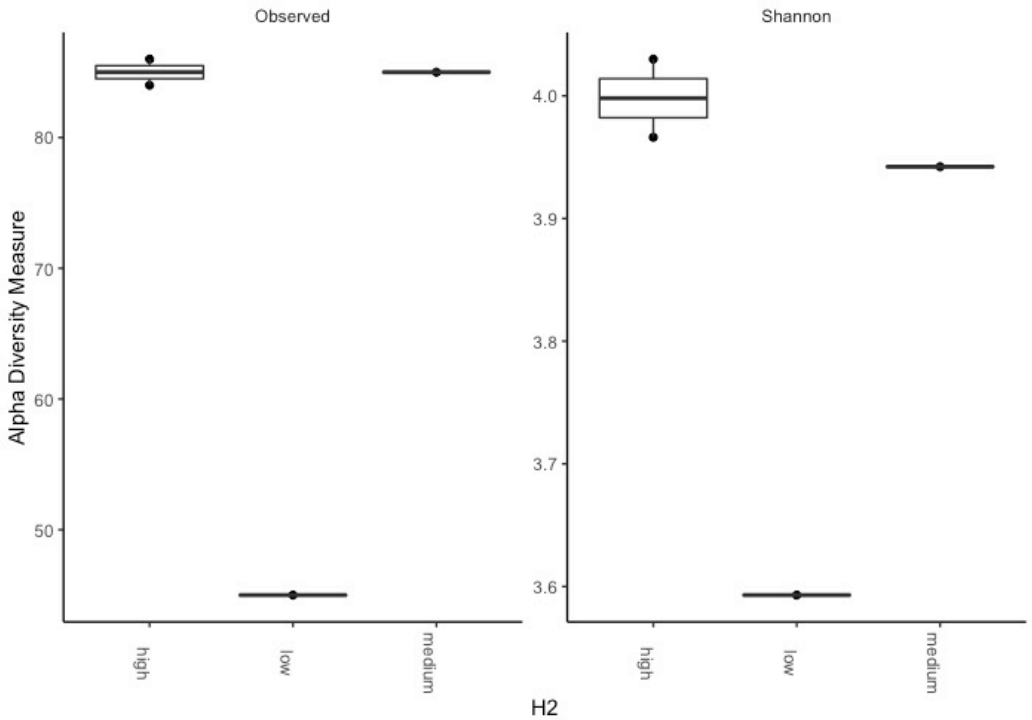

Figure 5-5. For the non-heated (T-ambient) samples different rates of H_2 consumption were observed. Analysis here shows alpha diversity is higher in samples with higher H_2 consumption.

Based on these results, Experiment 3 was initiated. Two intermediate heated samples, T-35 and T-50, were collected. After 157 days, little or no change in the gas composition was observed, whereas in the previous experiment consumption of H_2 was observed in the T-ambient sample after 50 days. These experiments contained a higher solid to liquid ratio than the previous experiment, which caused an increase in viscosity that limited the ability of the shaking tables to mix the slurry. It was suspected this was limiting activity, perhaps because of reduction in gas dissolution in the media due to poor mixing during incubation. An additional 5 mL of media was added at 157 days. This experiment ran for 296 days, and although some activity in the T-ambient and T-35 samples was observed, there were also some changes in the sterile controls (Figure 5-6). Some contamination from the media addition at day 157 was suspected so the experiment was restarted. Overall, the results of Experiment 3 emphasize the potential important role of solid to solution ratio in the rate of community development.

Experiment 4 utilized the same sample set as Experiment 3, but with the inclusion of additional samples containing higher salinity GW media instead of regular media. The T-ambient samples had an intermediate solid-to-solution ratio. Initially, no activity was observed in the early sampling points, but higher oxygen levels were noted compared to previous tests. At the 120-day mark, adjustments were made to lower the oxygen content by depressurizing and evacuating the bottles through a vacuum. The bottles were then allowed to equilibrate with air and supplemented with CO_2 and 5% H_2 in N_2. Following these adjustments, an increase in oxygen consumption and CO_2 production was measured in the T-ambient replicates (Figure 5-7).

Overall, activity was observed in all T-ambient replicates, while moderate activity was observed in the T-35 and T-ambient GW replicates. The T-50, T-95, and control samples did not show significant changes in gas composition. In comparison to Experiment 2 incubations, the consumption of gas exhibited a higher rate of oxygen consumption and CO_2 production. H_2 consumption was observed in two out of the four T-ambient replicates, with one demonstrating a higher consumption rate. This indicates that the potential for H_2 oxidation is present in many of the FEBEX samples, except for the hottest and driest samples, which may harbor different microbial communities or metabolic processes.

The increase in oxygen consumption and CO_2 production serves as strong evidence of an active microbial community. However, the specific nature of these other metabolic processes remains unclear, highlighting the importance of considering the metabolic potential of barrier materials. Obtaining community analysis from subsamples has been challenging due to the low biomass present in some of the replicates. Extraction of DNA from the clay samples proved to be challenging, and significant amounts of DNA were primarily obtained from the no-heat samples (T-ambient). In Experiment 2, DNA sequencing results indicated a higher utilization of H_2 compared to Experiment 4, where O_2 consumption and CO_2 production were demonstrated, but H_2 consumption was limited. Figure 5-8 presents the sequencing data obtained from Experiment 4. Although sequencing was attempted for all temperature pre-treatments, results were only obtained for the T-ambient, T35, and T50 samples.

At the phylum level, both experiments were primarily dominated by *Actinobacteria*, with some replicates from Experiment 4 also showing a significant abundance of *Firmicutes.* However, at the genus level, the abundance was mostly composed of rare taxa. Among the known taxa, the *Actinobacteria Saccharomonspora and Saccharopolyspora* were identified, which are similar to species observed in previous clay incubation experiments (Beaver et al., 2022; Engel et al., 2019; Gilmour et al., 2021; Leupin et al., 2017; Lopez-Fernandez et al., 2015; Meleshyn, 2014; Pederson, 1996, 2000, 1999; Sevcu et al., 2018; Taborowski et al., 2019; Villar et al., 2008). At the genus level, the relative abundance or rare taxa at genus level is significantly higher in the non-heated samples than the heated samples ($p < 0.5$). The relative abundance of *Saccharopolysporta* at genus level is significantly higher in heated groups than the non-heated group ($p < 0.005$). Figure 5-9 shows the Alpha Diversity calculated from the DNA sequencing results. Alpha diversity metrics assess the species diversity within the ecosystems. Non heated (T-ambient) had the highest alpha diversity.

The pH measurements of the samples showed only minor variations, ranging from pH 6.25 to pH 6.75. The average pH values ranged between 6.35 and 6.75, with the media sample having an average pH of 6.6 and the GW sample having an average pH of 6.45. Notably, there was no significant difference in pH between the samples (average pH 6.60) and the sterile controls (average pH 6.63).

Table 5-3 presents the cation measurements of the samples from Experiment 4. Several cations, including Li, Be, Al, Fe, Se (as SeO), Co, Mo, Ag, Cd, Sn, Sb, Ca, Eu, Pb, Th, and U, were below the detection limits of the analysis. Regarding anions, there are notable differences in the cation and anion content in the GW samples, particularly higher levels of sulfate, sodium (Na), and chloride (Cl) (Table 5-3). The solids content had an impact on certain cations, as evidenced by the differences between the blank samples and the clay samples, reflecting the influence of the clay. The blank samples exhibited higher levels of Na, phosphorus (P), potassium (K), and boron (B), while the clay samples showed higher levels of calcium (Ca). No nitrate was intentionally added with the media or GW, and significant amounts of nitrate were not observed in the porewater analysis.

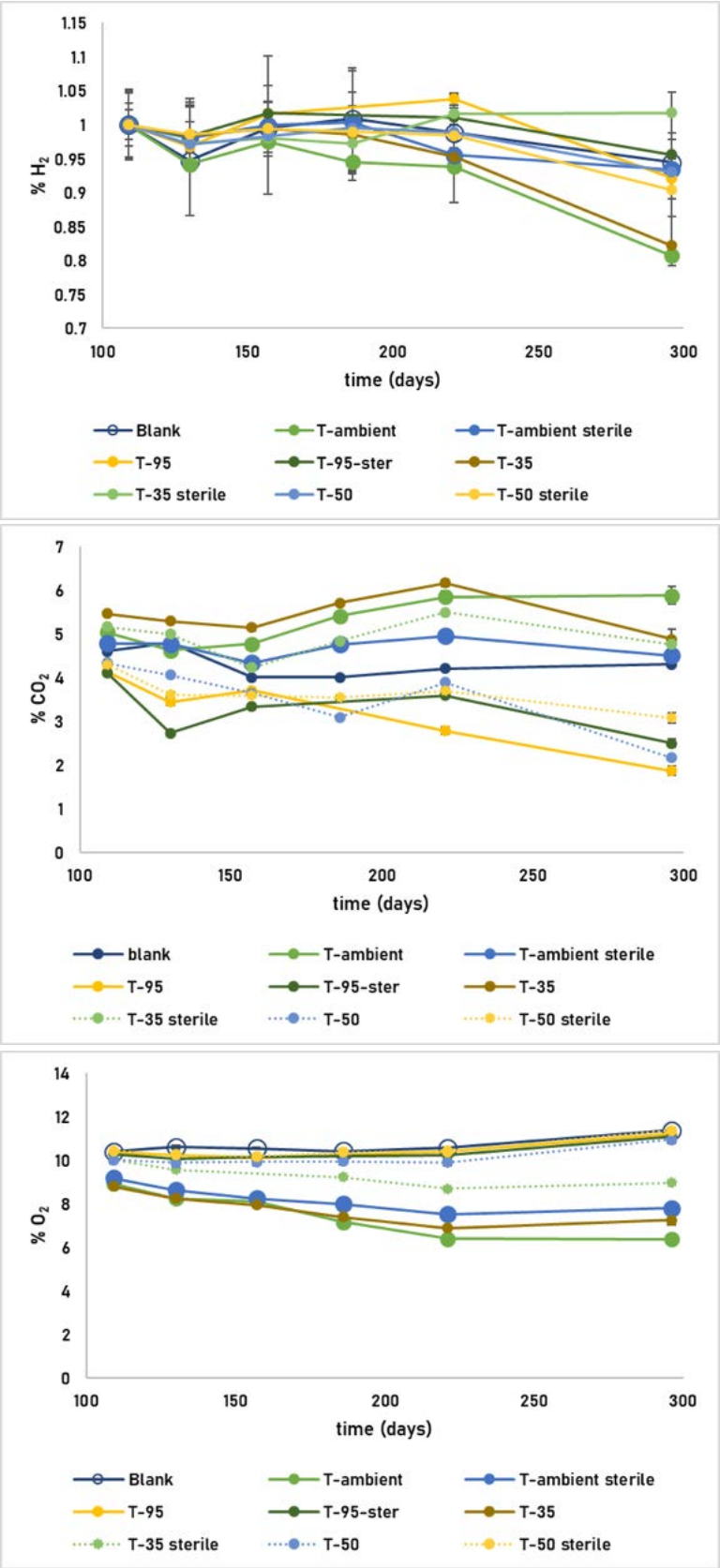

Figure 5-6. Percent H_2, CO_2, and O_2 for Experiment 3.

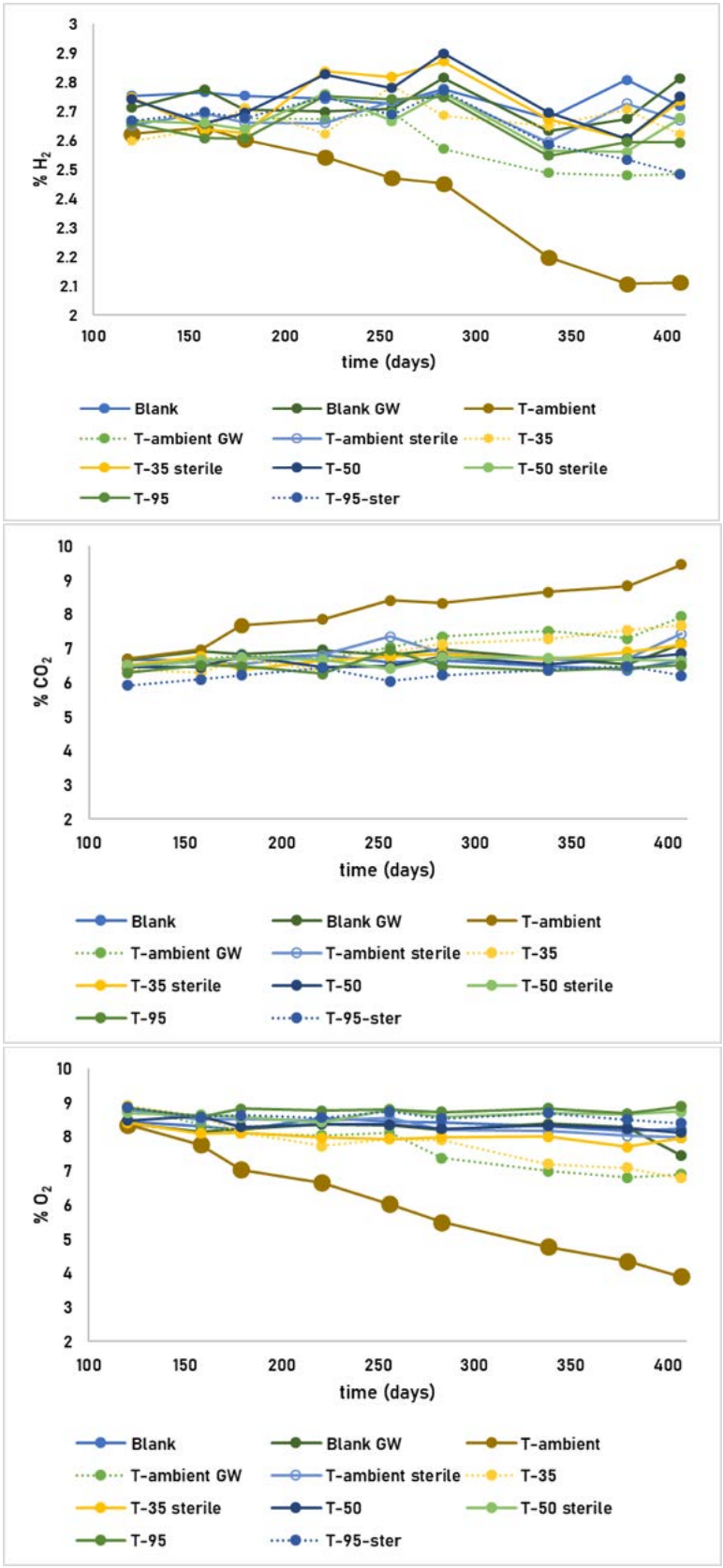

Figure 5-7. Percent H_2, CO_2, and O_2 for Experiment 4 after O_2 was reduced at 120 days.

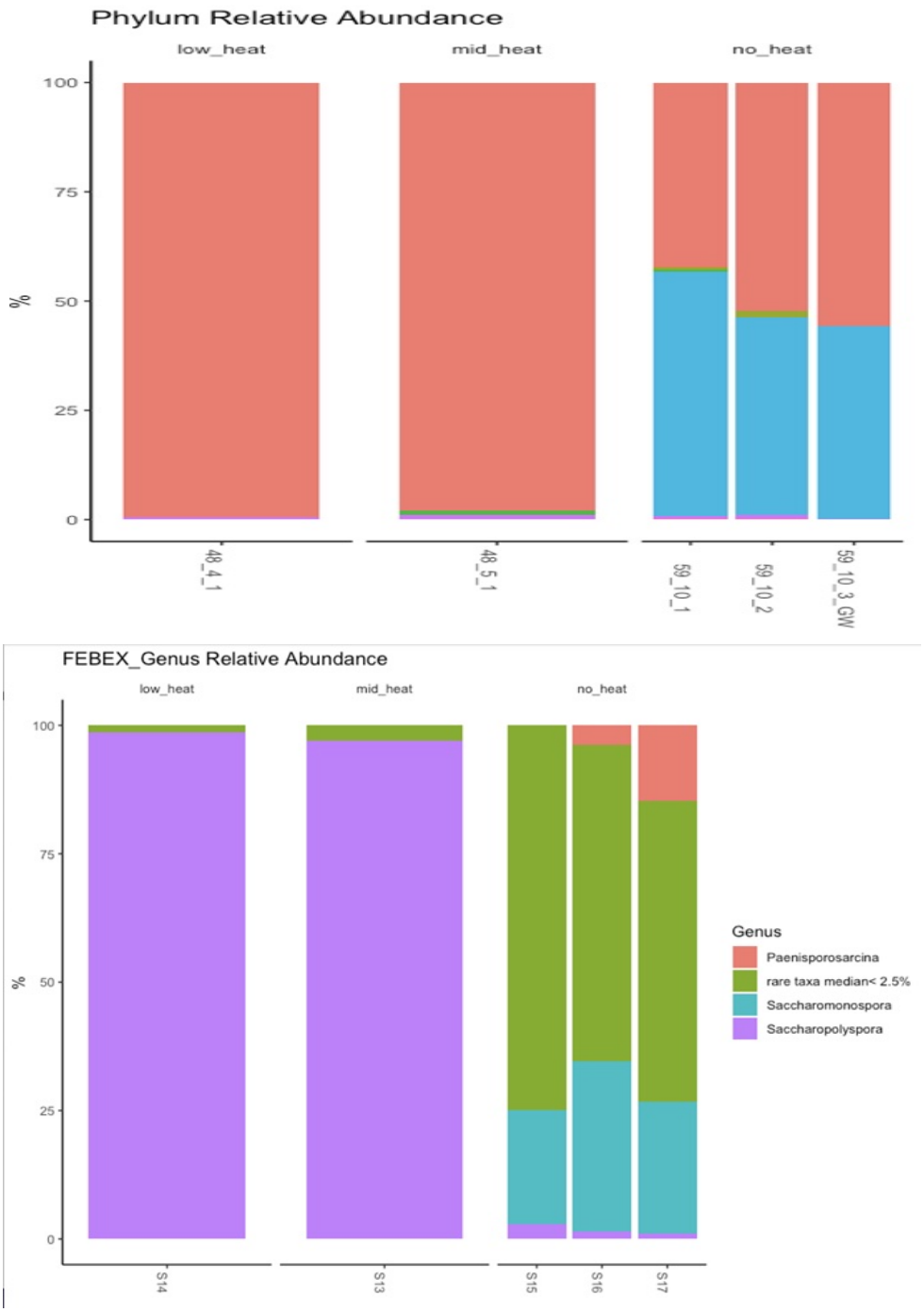

Figure 5-8. DNA sequencing results for Experiment 4.

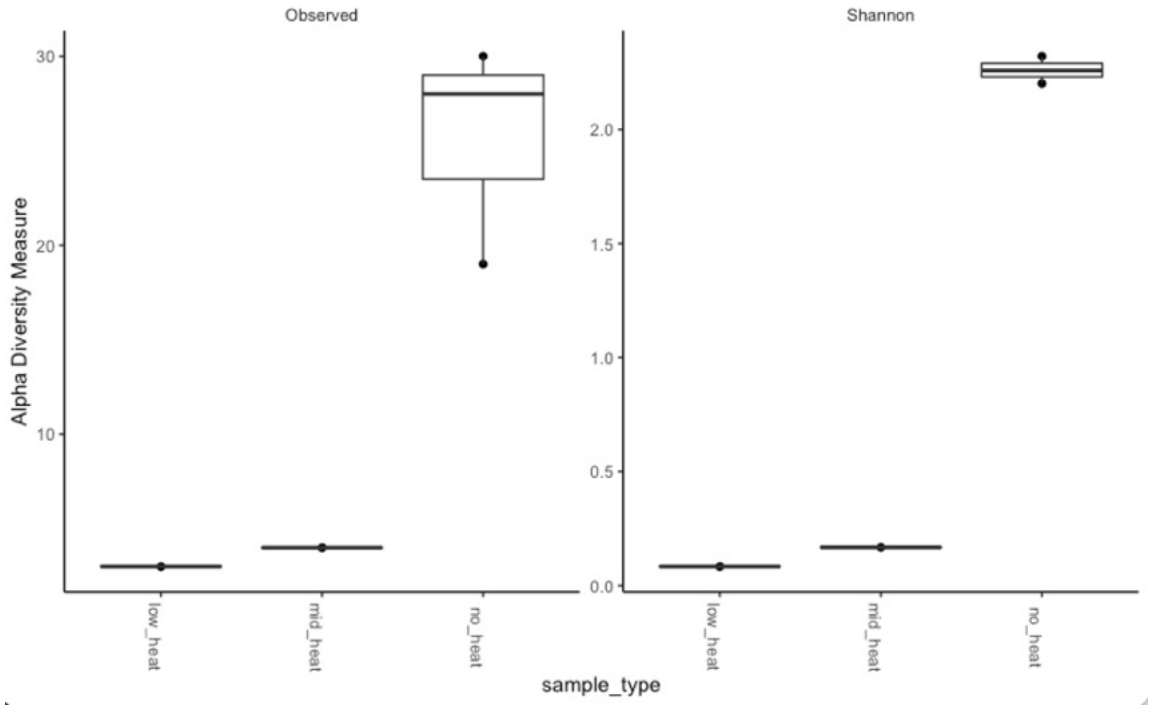

Figure 5-9. Alpha diversity index for Experiment 4, showing as before in Experiment 2 that heating reduces microbial diversity.

Table 5-2. Groundwater media used for Experiment 4

Compound	Molarity (mM)	Ion	Molarity (mM)
$NaHCO_3$	0.798	Na	243
Na_2SO_4	104	C	0.881
NaCl	34.2	SO_4	104
KCl	1.23	Cl	68.3
$CaCl_2*2H_2O$	9.35	K	1.23
$MgCl_2*6H_2O$	7.06	Ca	9.46
CaF_2	0.109	Mg	7.06
$SrCl_2$	0.0831	F	0.218
Si	0.183	Si	0.183
		Sr	0.0831

Table 5-3. Cation and anion data for Experiment 4. BDL = below detection limit. GW = artificial groundwater, st = sterilized sample

	Blank	Blank (GW)	T-ambient	T-ambient GW	T-ambient sterile	T-35	T-35 sterile	T-50	T-50 sterile	T-95	T-95 sterile
PO_4	264.6	148.9	148.3	69.3	158.3	150.0	140.5	139.1	139.7	140.1	190.3
Cl	40.2	88.1	45.2	98.4	38.5	37.2	36.6	37.6	35.1	43.4	37.4
SO_4	BDL	84.4	0.8	84.8	0.7	0.1	0.1	0.5	0.8	0.7	0.4
NO_3	BDL	BDL	BDL	BDL	BDL	0.154691	BDL	BDL	BDL	0.118752	BDL
Na	124.5	281.0	91.8	239.7	90.4	89.2	95.7	90.0	86.1	93.1	103.7
PO	62.9	43.6	34.3	25.4	36.0	35.2	39.9	36.6	33.6	34.9	45.3
K	25.0	18.8	6.3	8.8	8.4	5.6	7.6	5.7	5.7	5.7	11.6
Si	0.98	1.21	0.84	1.01	1.18	1.15	1.36	1.10	1.25	1.25	1.33
B	0.28	0.33	0.13	0.11	0.14	0.11	0.11	0.11	0.12	0.11	0.10
Ti	0.12	0.08	0.08	0.05	0.08	0.08	0.09	0.08	0.07	0.07	0.09
Ca	0.03	0.48	0.27	0.96	0.24	0.25	0.23	0.24	0.26	0.28	0.27
Mg	0.0	4.6	2.5	7.7	2.3	3.0	3.3	2.7	2.6	2.5	2.2
Cu	9.5E-04	2.2E-03	8.0E-04	1.9E-03	8.5E-04	2.0E-03	7.6E-04	8.8E-04	7.2E-04	6.7E-04	7.6E-04
Ba	8.6E-04	7.8E-04	2.6E-04	4.7E-04	2.3E-04	2.8E-04	2.0E-04	2.4E-04	2.2E-04	1.8E-04	1.5E-04
Co	6.2E-04	BDL	BDL	BDL	BDL	BDL	BDL	BDL	BDL	BDL	BDL
Mn	3.8E-04	2.3E-04	4.3E-03	9.2E-03	3.1E-03	8.8E-03	8.6E-03	4.7E-03	4.0E-03	3.4E-03	2.9E-03
Cr	1.9E-04	BDL	2.7E-04	BDL	1.5E-03	2.1E-04	2.4E-04	7.9E-04	3.0E-04	1.2E-04	1.9E-04
Sr	1.7E-04	1.9E-02	1.0E-02	5.1E-02	1.1E-02	1.1E-02	1.1E-02	1.0E-02	1.0E-02	9.1E-03	9.5E-03
Rb	1.2E-04	1.1E-04	3.6E-04	7.1E-04	4.0E-04	5.3E-04	4.2E-04	3.7E-04	3.6E-04	3.8E-04	4.9E-04
V	BDL	BDL	4.2E-04	2.7E-04	5.5E-04	5.1E-04	6.6E-04	5.3E-04	6.1E-04	4.6E-04	6.2E-04
Ni	BDL	BDL	BDL	3.1E-04	BDL	5.7E-04	BDL	BDL	BDL	BDL	BDL
Zn	BDL	1.1E-03	BDL	2.1E-03	1.4E-03	2.1E-03	BDL	2.8E-03	BDL	1.7E-03	BDL
AsO	BDL	BDL	3.0E-03	3.4E-03	2.0E-03	3.5E-03	2.1E-03	2.6E-03	2.8E-03	2.4E-03	1.2E-03

5.4 Summary and Future Work

The experimental results revealed that clay materials can sustain microbial communities with the potential for microbial growth. However, it is intriguing that the material from the hot zone did not exhibit the growth potential within the time frames of these experiments. It remains unclear whether this lack of potential is due to the heating process, the drying process, or a combination of both. Additionally, the specific communities that developed were found to be sensitive to the gas composition and solids content.

The absence of growth in the control sample indicates that the observed enrichment of communities originated from bacteria already present in the clay prior to the start of incubation. Although the duration of these experiments is relatively long by laboratory standards, they are considerably short in comparison to the time scales involved in repository dynamics. Over longer time scales, microbial activity within the barrier material is expected to be significant. Considering the limited moisture and presence of other chemical species, it is reasonable to assume that this microbial activity would primarily occur along fractures and at the boundaries of the formation.

This tendency is further supported by the influence of high solid-to-solution ratios observed in our second experiment, as well as the lack of significant microbial activity in the samples closest to the heaters. Moreover, the differential impact on GW media samples compared to MSM, along with the observation of non-H_2 metabolisms in several samples, underscores the importance of understanding the composition of fluids within the formation to predict the dominant metabolic processes.

To the best of our knowledge, this is the only experimental study demonstrating the activity of microbial communities from FEBEX materials under minimal media conditions, as opposed to growth media, and highlighting the presence of H_2 metabolism. Further research should explore the range of metabolisms possible within the barrier material's existing community and investigate how specific chemical and physical conditions regulate the rate of microbial growth.

Following work is to extend the DNA analysis to include detection of hydrogenase genes in the DNA through PCR amplification. This will help establish a direct association between H_2 reduction and microbial activities. When this work is complete, the experimental results will be included into the manuscript and submitted for publication in peer-reviewed journal.

This page intentionally left blank.

6. HEATING AND HYDRATION COLUMN TEST ON BENTONITE

6.1 Introduction

Research on EBS clay systems for nuclear waste storage at high temperatures has been ongoing for several years (Dohrmann et al., 2013). The thermal stability of clay minerals has been extensively studied in laboratory experiments and modeling (Zhang, 2018). Bentonite clay typically contains both smectite and illite minerals although the exact composition and proportion of smectite and illite in a bentonite deposit can vary depending on the geological origin of the clay and the depositional environment. However, most commercial-grade bentonites contain at least 50-80% smectite and 5-15% illite, along with other minerals such as quartz, feldspar, and calcite. MX-80 bentonite is a commercial-grade bentonite clay that is commonly used as a buffer material in nuclear waste repositories. It is a sodium-rich bentonite that is mined from a deposit in Wyoming, USA. The exact composition of MX-80 bentonite can vary depending on the specific deposit and processing methods used, but it typically contains around 60-80% smectite, specifically montmorillonite, minerals, along with other clay minerals and non-clay minerals (Karnland et al., 2006).

Overall, previous research suggests that EBS clay systems have the potential to provide a stable and effective barrier for nuclear waste storage at high temperatures. However, further studies are needed to fully understand the long-term behavior of these systems under realistic repository conditions. The HotBENT (Hot Biological Enhanced Natural Attenuation) field test is being conducted at the Mont Terri Underground Research Laboratory (URL) in Switzerland to investigate the long-term performance of bentonite-based buffer materials for nuclear waste repositories under high temperatures.

This chapter describes HotBENT-Lab experiments which are designed obtain well-characterized datasets to understand heating and hydration of bentonite clays and to provide modelling data to predict performance in the HotBENT field-scale test results. Furthermore, the aim is to develop standard systems for future studies of bentonite under conditions of high temperature.

As described in our FY22 report (Zheng et al., 2022), we conducted benchtop-scale column experiments with temperatures up to 200 ºC in the center of a packed bentonite cylinder. Two test columns were used—a control column undergoing only hydration, and an experiment column experiencing both heating and hydration. During the experiment, we took frequent X-ray computed tomography (CT) images to provide insight into the spatiotemporal evolution of (1) hydration/dehydration, (2) clay swelling/shrinkage, (3) displacement/deformation, and (4) mineral precipitation. A comprehensive post-dismantling characterization of bentonite samples was carried out after the column tests were run for 1.5 years.

In FY22, after we completed the first set of columns (Chang et al., 2023), a new heating test was started to investigate the impacts of (1) bentonite type, (2) initial bentonite density and water content, (3) water chemistry, and (4) hydration pressure. The parameters in the new column tests (named HotBENT Lab #2) as compared from HotBENT Lab #2 are shown in Table 6-1. Again, as in the first test, the experiment column was subjected to heating and hydration up to 200 ºC, while the control column underwent hydration only. The changes included (1) an increased bentonite dry density from 1.2 g/cm3 to 1.45 g/cm3-- a value that is similar to that used in the field, (2) reduced gravimetric water content to 5.3%, (3) used bentonite MX-80 clay sourced from HotBENT site, (4) utilization of lab-made hydration fluid based on analysis of Grimsel GW at a considerably lower salt content (See Table 6-2), and (5) increased of hydration pressure from 120 to 290 psi, and the flow rate constant at 0.11 ml/min. In addition, we implemented more sensing instruments for a better monitoring of the dynamic behavior of bentonite during heating and hydration. These included improved instrumentation for six electrical resistivity tomography (ERT) arrays, increased the number of thermocouples for temperature monitoring from 8 to 12, implemented strain gauges outside of the vessel to measure stress, emplaced 48 tracer

particles at different radial and axial locations to track clay swelling deformation, and emplaced 6 coupons close to the heater shaft to investigate potential corrosion.

After observing the newly packed HotBENT Lab #2 granulated bentonite samples for over one year, it was found that a steady state was reached where neither temperature nor hydration was not changing, and no water was able to flow in or out of the columns due to expansion of the clays into the hydration tubing. It was determined that the columns should be dismantled to understand chemical and physical changes with the clay, and plan for future experiments using information gathered from the first two column experiments.

Table 6-1 Differences in design between the two HotBENT experiments.

	HotBENT Lab #1	HotBENT Lab #2
Clay	MX-80 Bentonite	Granulated Wyoming bentonite (MX-80)
Water	Artificial ground water	Grimsel groundwater
Temperature	200°C	200°C
Initial Density	1.2 g/cm^3	1.5 g/cm^3
Initial Water content	0	0.05
Clay processing	Homogenized, large pellets removed	Heterogeneous bentonite powder w/pellets (as received)
Pressure	120 psi (0.8 Mpa)	290 psi (2 Mpa)
Experimental length	560 days	400 days
Metal coupons	none	5 coupons

Table 6-2. Differences in water chemistry in HotBENT Lab #1 and HotBENT Lab #2. For HotBent Lab #1 we used an artificial groundwater and HotBENT Lab #2 we used simulated Grimsel water.

	HotBENT Lab #1	HotBENT Lab #2
Compound	**mg/L**	**mg/L**
$NaHCO_3$	67.0	18.48
Na_2SO_4	14800	0.15
NaCl	2000	0
KCl	92	0.57
$CaCl_2*2H_2O$	1375	0.38
$MgCl_2*6H_2O$	1435	
$MgSO_4$	0	0.16
CaF_2	8.50	7.96
$SrCl_2$	13.18	0
Si	0	9.61
$CaSO_4*2H_2O$	0	12.81

6.2 Analysis of HotBENT Lab #1 and #2 Dismantled Samples

6.2.1 Characterization and Monitoring

X-Ray Computed Tomography (CT) Imaging

X-ray CT images were collected to provide a 3D visualization of the density distribution in the column, which can be used to visualize density changes due to water saturation, clay swelling or structural deformation during the experiments. A GE Lightspeed 16 medical CT scanner was used to scan the two columns periodically throughout the experiments. Based on the column dimensions, the spatial resolution of the CT images is 400 × 400 × 625 µm. Because of the large weight of the experimental columns (~55 lbs), a cart/lift was used to move the columns onto and off the CT scanner table. Alignment of the scans was achieved via markings on the CT table and on the outside of the column, as well as key features in the CT images (high and low-density anomalies) inside the column during post processing. The post processing and analysis of the obtained CT scan images were conducted using self-developed codes in ImageJ software (Rasband, 1997–2022).

The correlation between bentonite bulk density and CT number (i.e., the calibration curve and equation), was obtained by scanning separate columns compacted with bentonite of known bulk densities (see Figure 6-1). Note that CT numbers at 0 and 1 g/cm3 were obtained by scanning air and water, respectively. This close correlation between material bulk density and CT number has been suggested by Mull (1984). To further verify the calibration curve specifically for the experiment, seven bentonite

samples were collected in the heated column after dismantling using tube samplers at an internal diameter of 0.7 cm. The bulk wet mass was measured right after sampling. High-resolution X-ray CT scanning was then applied to obtain the sample volume, so that the bulk wet density can be calculated precisely and compared with CT density (density obtained from the CT images by applying the calibration equation). The CT density for each of the sample deviated <5% from the measured bulk density (ρ_wet), indicating the effectiveness and precision of CT images in predicating bentonite bulk density. Assuming ρ_CT = ρ_wet, the dry density (ρ_dry), degree of saturation (S_r) of the collected bentonite samples after the experiments can then be calculated as:

$$\rho_dry = m_dry/(m_wet/\rho_CT) \quad \textbf{Eq. (6-1)}$$

$$S_r = [m_wet - m]_dry/(\rho_water\ \phi\ m_wet/\rho_CT) \quad \textbf{Eq. (6-2)}$$

where m_dry refers to the stable sample mass measured after oven drying, and ρ_mineral is the mineral or grain density. ρ_water is water density at 1 g/cm3. The mineral density of 2.623 g/cm3 was used for MX-80 Wyoming bentonite, as measured by Karnland et al. (2006).

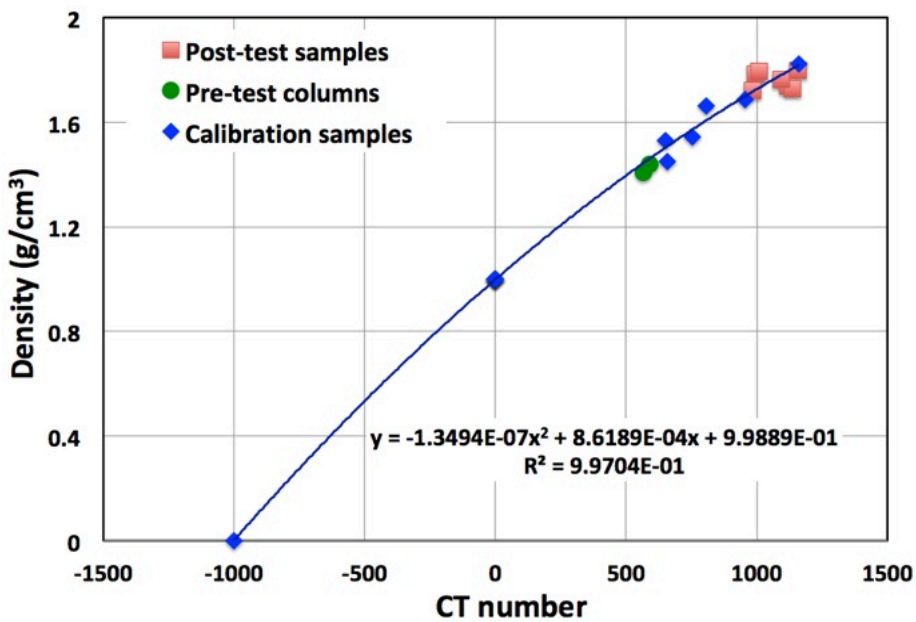

Figure 6-1. Relationship between measured gravimetric density of calibration samples and CT number from X-ray CT images. The equation derived from the data-fitting was then used to compute bentonite bulk wet density from X-ray CT scans during the experiment.

Continuous Temperature Monitoring

Temperature monitoring was conducted using thermocouples (type T) installed in the column. A total of 12 thermocouples were installed in each column between the heater shaft and the column. The distances of these thermocouples from the heater shaft were 0 (on the heater), 0.5, 1, 1.5 2, 2.5, 3, and 3.5 inches (the latter was on inside of the column wall). Two thermocouples were emplaced next to the two ends of the heater, while another two thermocouples were emplaced axially parallel and radially 1.5 inches away in the bentonite. These feedthrough-coupled thermocouples, with an accuracy of 0.1°C, were acquired from Conax Technologies. The temperature readings from the thermocouples were recorded at 20-second intervals with a data logger (Keithley 2017) throughout the experiment. In addition to the thermocouples inside the columns, additional temperature measurements were taken on the outside wall of the column.

Time Lapse Electrical Resistivity Tomography (ERT) Monitoring

ERT data were acquired using a DAS-1 ERT instrument (Multi-Phase Technologies, LLC, USA) and electrodes that were used to send electrical current or measure electrical potential. Measurements were conducted using a pre-defined monitoring schedule, where a total of ~2600 data points were collected for a single resistivity survey from each column, which took ~ 60 minutes. The data collection frequency was coordinated with CT scan frequency, with denser acquisition periods during the initial stage of the experiment and reduced for the long-term experiment as the rate of resistivity change decreased. Data collection was autonomously carried out via Multi-phase Technologies, LLC software. Analysis of the post-experiment collected datasets included data quality assessment, inversion and visualization. The open software BERT (boundless ERT, Günther & Rucker, 2012) and Paraview (Kitware, NY) were used for data inversion and visualization.

Metal Coupons

Figure 6-2 shows the metal coupons emplaced in the heated and non-heated column, including Stainless steel 316 (SS 316), Stainless steel 304 (SS 304), low carbon steel (LCS) and two coated coppers from the HotBENT field site. All metal coupons were imaged to have a detailed surface geometry before the experiments, so that a comparison after the experiments on potential corrosion is available. We induced dents to some of the coupon surfaces as marks for comparisons after the experiments. All of the coupons were recovered during the dismantling of the HotBENT Lab #2 experiments and analysis of any changes is underway.

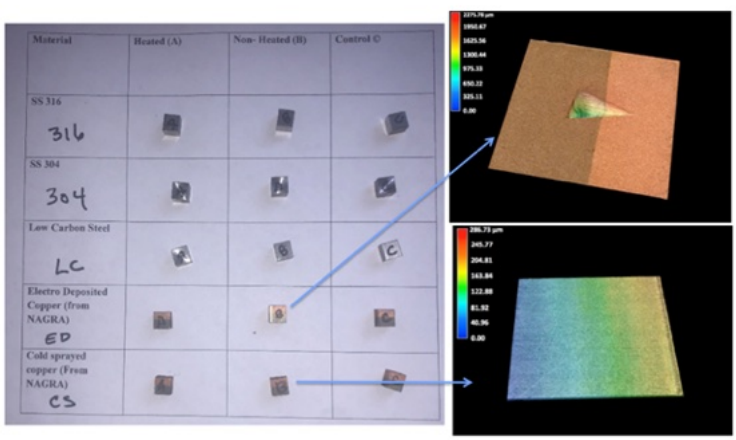

Figure 6-2. The metal coupons used in the heated and non-heated columns. The color bars in the figure bound the surface roughness, varying from 0 to 2276 um in the top right figure due to the induced dent, and 0-287 µm in the bottom right figure without dent.

Influent and Effluent Fluid Geochemical Analysis

The fluid used to hydrate the bentonite was sampled and analyzed to monitor geochemical changes in the bentonite system. Samples collected from the experiments were filtered, acidified, when necessary, prepared and analyzed using the standard ion chromatography and Inductively Coupled Plasmas – Mass Spectrometry (ICP-MS) protocols. Changes in water chemistry of the effluent fluid are being used to understand the geochemical processes in the column due to evaporation, dilution, diffusion, and other transformations.

6.3 Preliminary Results

6.3.1 X-ray CT

Baseline CT

Figure 6-3 depicts the cross-sectional CT images and density distributions of the non-heated and heated columns after compaction. The color bar bounds density changes from 1.2 to 2.4 g/cm3, with brighter yellow color indicating higher density. The blue curves show the dry density profile based on the bulk CT density and gravimetric water content (5.3%). The non-heated column presents the two segments with different packed wet and dry densities. The dry densities for the top and bottom segments are 1.52 and 1.62 g/cm3. By comparison, the heated column was compacted relatively uniform at a dry density similar to the field condition, at 1.45 g/cm3.

Figure 6-4 shows the 3-D view of the initial CT density distribution in both columns, including (1) the heater and heater shaft in the center, (2) bentonite compacted between the sand layer and the central shaft, (3) the sand layer surrounding the clay, (4) the ERT arrays emplaced at the sand-clay boundary, and (5) thermocouple sensor, tracer particles and metal coupons emplaced in bentonite. The density variations and bedding layers in bentonite were induced by uneven compaction were expected to result in preferential flow of brine in the following hydration process. Overall, for the heated column, the average CT density of bentonite is 1.54 g/cm3.

The dry density and porosity for the heated column were calculated as 1.46 g/cm3 and 0.44. For the non-heated column, the average CT densities for the two segments were 1.68 and 1.58 g/cm3, the corresponding dry densities and porosities thus were 1.59 and 1.50 g/cm3, 0.39 and 0.43. Figure 6-4(c) and (d) show the spatial distribution of the emplaced sensors, including ERT arrays, thermocouples, tracer particles and metal coupons.

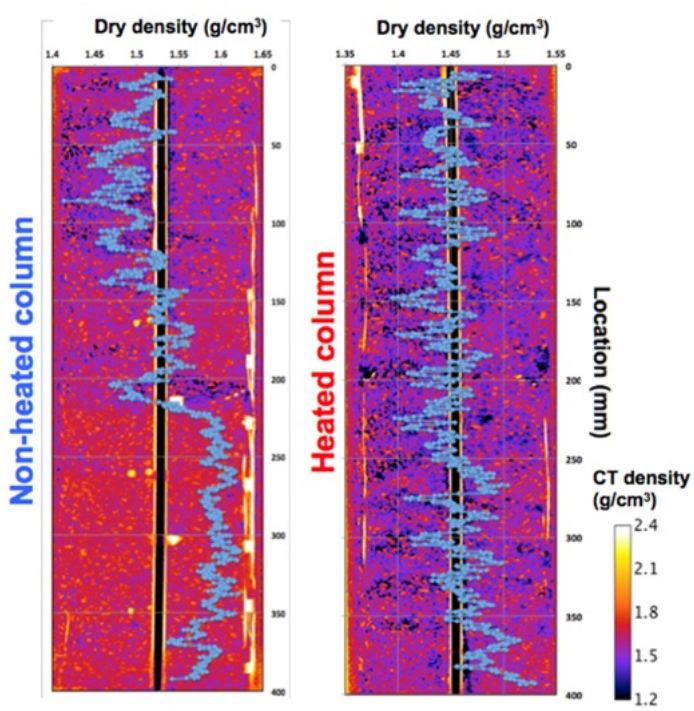

Figure 6-3. Cross-sectional CT images of the two compacted columns that are used for a heating and hydration experiments. The blue curve presents the dry density profile calculated from the bulk CT density and the water content.

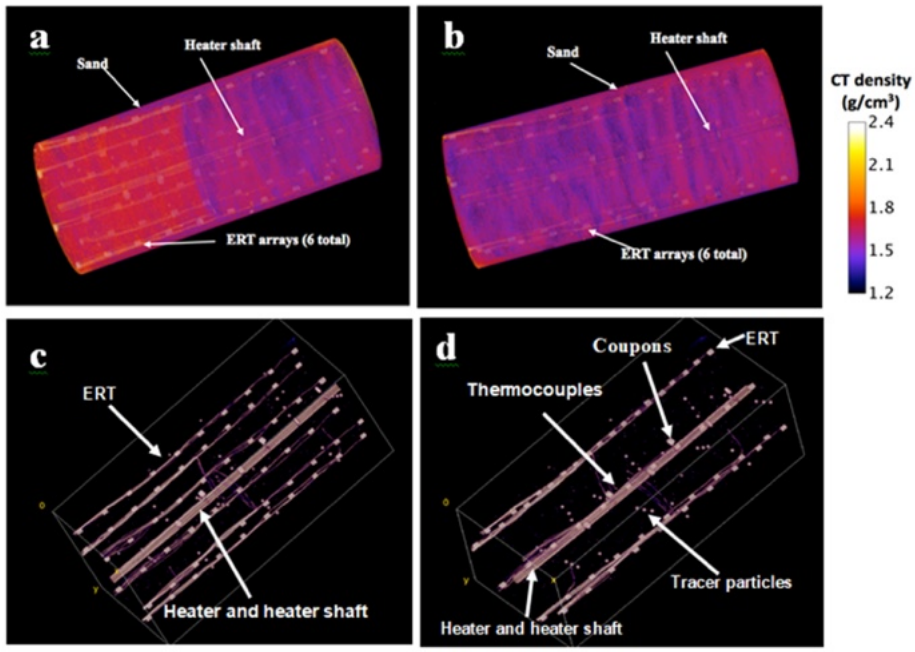

Figure 6-4. 3-D CT images showing the initial density distribution in the non-heated (a) and heated (b) columns. (c) and (d) present key instrumentations—heater and heater shaft, thermocouples, tracer particles, metal coupons, ERT and sensor wires

3-D Hydration

Figure 6-5 depicts the 3-D orthogonal view of CT density distribution and temporal changes in the non-heated column. The color bar bounds density changes from 1.2 to 2.4 g/cm3, and a brighter color indicates a higher density. The image at t=0 days shows the initial conditions and density distribution after packing, including the heater and heater shaft in the center (white color), the sand layer surrounding the clay (orange color), the metal coupons and tracer particles, and two clay segments packed between the sand layer and the central shaft (blue to orange color). The density variations, cavities and bedding layers are attributed to uneven packing.

At t=1 day, we saturated the sand layer with brine and kept fluid flowing at 0.11 mL/min under the pressure of 290 psi. Hydration was then initiated and controlled by the changes of clay density. At t=1 day, the increase in the CT density in the column indicates the considerable hydration. The density distribution, however, is not uniform. The high-density front represents the hydration front, which has advanced ~2 cm into bentonite from the sand boundary. The great density reduction at the sand-clay boundary relative to the hydration front indicates the dry density reduction by osmotic swelling after bentonite becomes fully water saturated. This bentonite swelling initiated at the sand-clay boundary may push and compact the interior clay and contribute to the high-density hydration front. We also show at t=1 day the seal of some low-density cavities by swelling along the boundary and compaction of interior clay. At t=10 days, the density distribution become more uniform. From 10 to 148 days, the overall CT density increases with hydration and becomes more uniform.

From 1 day to 10 days, we were able to maintain flow of brine through the sand layer at a desired pressure and a flow rate. At t=10 days, however, the water flow pathway was clogged, likely due to swelling of bentonite. As shown in Figure 6-5(b), the CT images clearly showed the invasion of the swelling bentonite into the sand layer at t=10 days. After that, we maintained a constant water pressure of 290 psi in the vessel and shut off the effluent valve. Figure 6-5 at 426 days depict the uniform CT density distribution at the end of the experiment.

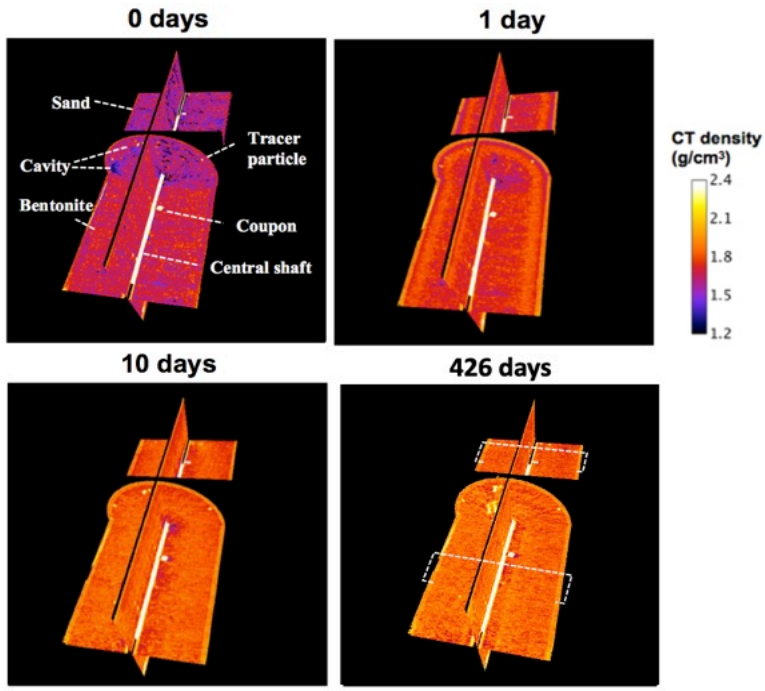

Figure 6-5. The 3-D clay density maps showing the spatial and temporal variations of clay density in the HotBENT Lab #2 non-heated column for 426 days. The sub-image at t=0 shows the initial condition after packing, with the low-density packing cavities. (b) Comparison of the 2-D images at 0 and 10 days when clogging of water flow path happened. The white arrows in (b) mark the invasion of swelling bentonite into the surrounding sand layer and water flow pathway. The yellow dotted box in (a) represents the axial location of the selected 2-D images in (b).

The 3-D images indicate overall radial symmetry of hydration distribution from the sand layer to the center shaft. We applied the radially averaged images to show the 3-D hydration process. For each CT scan, the obtained CT image stack was first orthogonally reconstructed by rotating a line at 360° around the center shaft. Then, an image was obtained by averaging over the 360° radially reconstructed images, and the CT number was converted into the density using the calibration curve shown by Figure 6-1. Figure 6-6 shows the radially averaged density map and changes with time for the non-heated column subject to hydration for 426 days. Figure 6-6(b) and Figure 6-6(c) present the radially CT density along the white dotted line #1 (b) and #2 (c) in each density segment, and their temporal changes subject to hydration from the sand layer. Note that each sub-image was radially averaged, thus the density profile along a single line represents the average density vs. radial distance from the heater shaft. Figure 6-6(b) and Figure 6-6(c) clearly show that the hydration is initiated from the peripheral sand layer. While the density increases of bentonite due to hydration from the sand boundary is the dominant process contributing to the spatiotemporal density distribution, both figures depict the bentonite density increase ahead of the density peak (the hydration front) at early time. For instance, at locations <40 mm away from the central shaft, bentonite density increases the same amount by 0.05 g/cm3 from 0 days to 1 day in the high-density segment (line #1), and 0.1 g/cm3 from 0 days to 1 day in the low-density segment (line #2). In addition, Figure 6-6(c) presents more density variations in the low-density segment, featured by the larger density drop along the sand-clay boundary and higher density increase of bentonite in the interior column. This indicates more considerable compression of interior bentonite after hydration compacted with a lower initial density. The propagation of hydration front, however, seems not affected by the initial compacted densities in the two segments. At t=148 days, the average CT densities are 1.86 and 1.82 g/cm3, respectively, in the high-density and low-density segments. Note the two segments were

compacted at initial densities of 1.68 and 1.58 g/cm3. The bentonite hydration results in a more homogeneous density distribution in the bentonite column than the initial packing condition. The CT density distribution then kept uniform until the end of the experiment. At t=426 days, the average CT density was measured as 1.83 g/cm3.

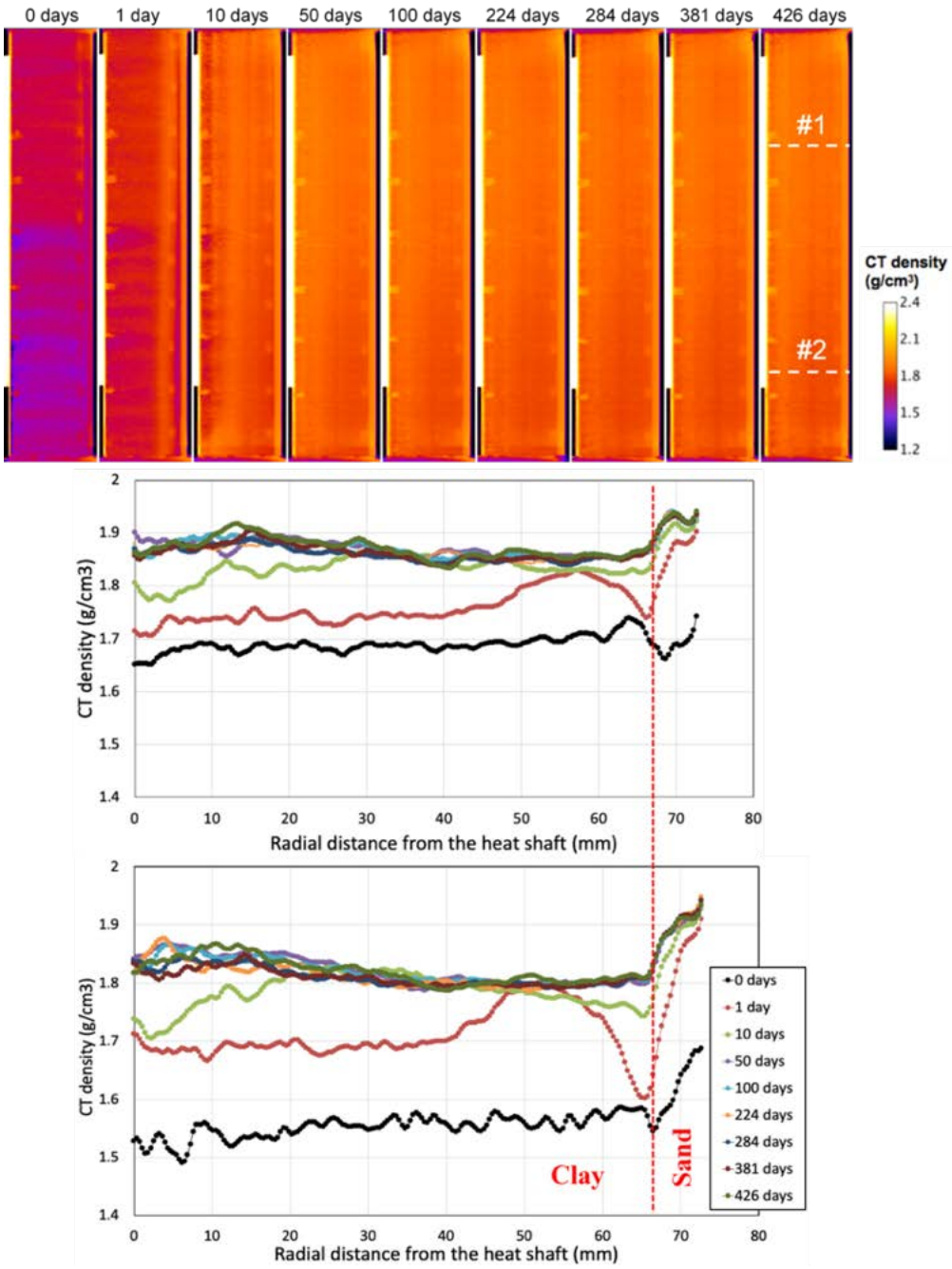

Figure 6-6. HotBENT Lab #2 non-heated column: (a) the radially averaged density map and changes with time for the non-heated column subject to hydration for 426 days, (b) the average density vs. radial distance from the center shaft along the white dotted line #1 in (a), and (c) the average density vs. radial distance from the center shaft along the white dotted line #2 in (a).

Temperature Profile from Heating and Hydration

In the heated column, we also saturated the surrounding sand layer with brine at t=1 day and kept water flow at 0.11 mL/min under the same 290 psi. At the same time, we turned on the heater and step-wisely increased the temperature on the heater shaft to 50, 100, 150 and maintained constant 200 °C after t=10 days. Figure 6-7 presents the temporal temperature variations at different radial distance from the heater shaft. After t=10 days, the temperature becomes stable, with a profile decreasing from 156 °C at 10 mm away from the heater shaft to 94 °C at 69 mm away from the heater shaft. Note the large temperature gradient (4.4°C/mm) within 10 mm away from the heater shaft, which is 1.8 times higher than that from 10 to 17 mm away from the heater shaft. This thermal gradient, however, is lower than the first set of HotBENT Lab test using MX-80 bentonite compacted at a higher initial water content. In HotBENT Lab Test #1, the temperature gradient within 10 mm away from the heater shaft is 5.6°C/mm. The reduced thermal gradient could be attributed to (1) the reduced initial water content, (2) higher compacted bentonite density. Xu et al. (2019) reported thermal conductivity of MX-80 bentonite moisturized at 0 to 22% water contents and constant dry density at 1.3 g/cm3. At 90 °C, the thermal conductivity of 17% water content sample could be four times higher than that of the dry sample. It was also recognized the increase trending of thermal conductivity with temperature increase for moisturized samples, while the dry sample presented constant thermal conductivity, independent of temperature changes. Although data above 100 °C is limited, we envision water evaporation and bentonite drying out near the heater shaft in the first set of column tests may result in the larger thermal gradient near the heater shaft. We do not observe any dry-out zone in the on-going column test. See more details in Figure 6-5 and Figure 6-6.

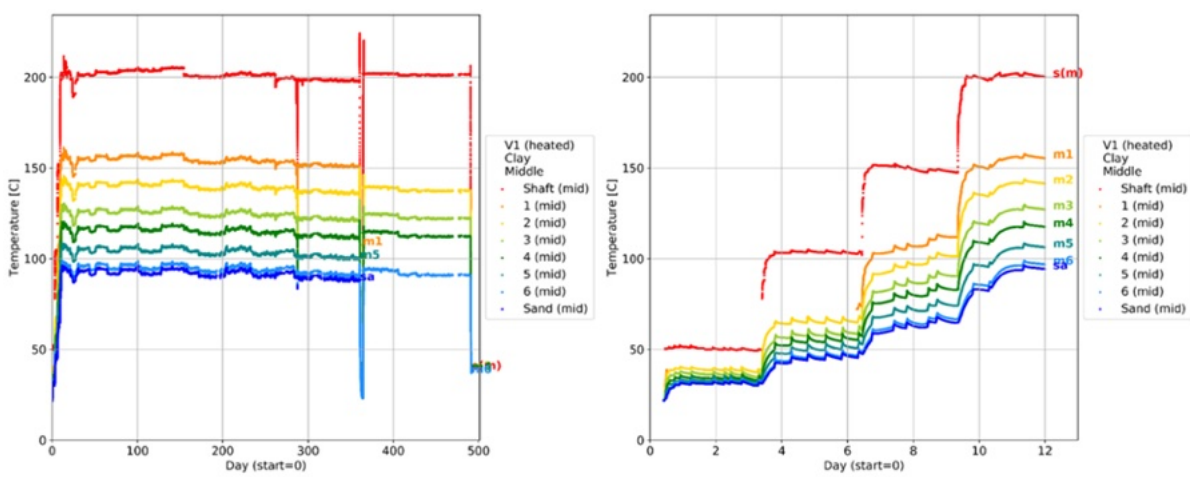

Figure 6-7. HotBENT Lab #2 temperature variations as a function of time and radial distance from the heater shaft in the heated column for 500 days (left) and for 13 days (right)

Density Distribution from Heating and Hydration

Figure 6-8 depicts the selected 3-D density distribution and changes with time in the heated column for 490 days, while Figure 6-9 shows the radially averaged density map (a) and the average density profile vs. radial distance from the heater shaft (b). Image at t=0 presents the initial condition before the heating and hydration experiment. The averaged CT density was 1.56 g/cm^3. The image also presents the patterned layers and low-density cavities. At t=1 day, we observe similar (1) swelling of clay and closing of the cavities after hydration, (2) density reduction at the sand-clay boundary due to clay swelling, and (3) bentonite density increased ahead of the hydration due to compaction. At t=10 days, we also observed the clogging of water flow in the vessel by the bentonite swelling and invasion into the sand layer. After 10 days, we switched to keep the column at constant 290 psi and stopped water flow by shutting off the effluent water port. At t=490 days, the average bentonite CT density was measured at 1.78 g/cm^3 in the heated column, lower than the value of 1.83 g/cm^3 in the non-heated column.

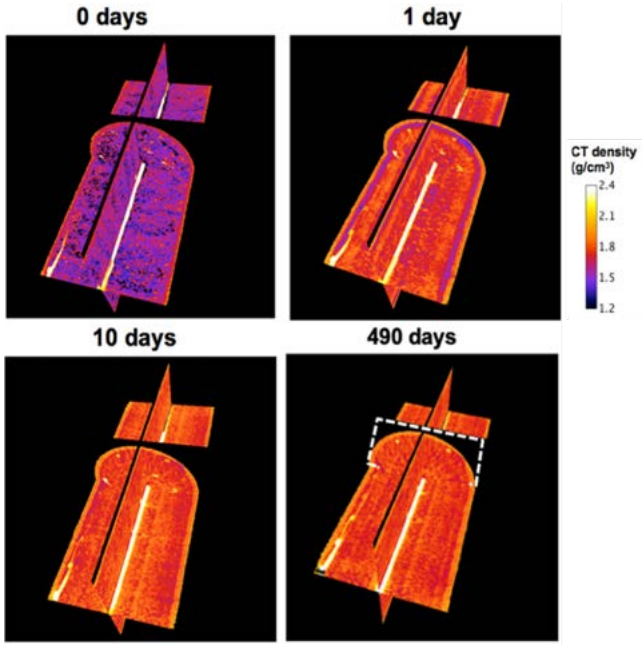

Figure 6-8. The 3-D clay density map and temporal variations in the heated column. The sub-image at T=0 day shows the initial condition after packing column packing and sensors installation.

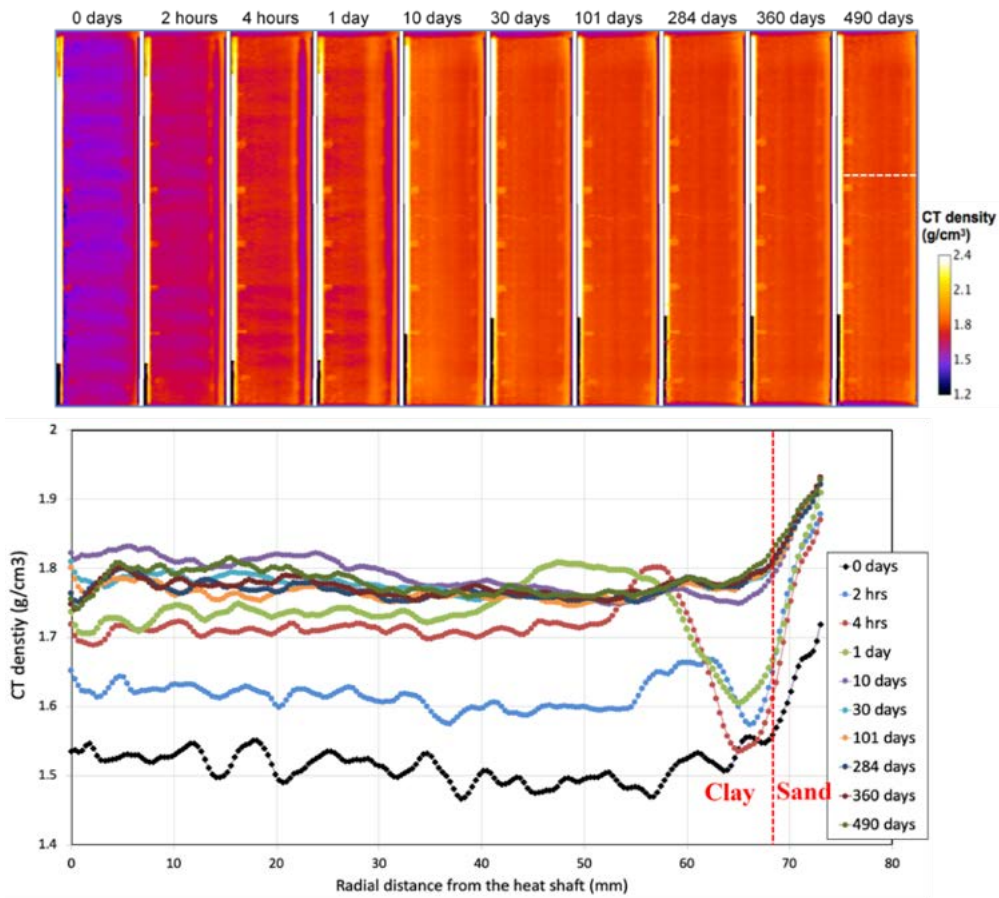

Figure 6-9. (a) The radially averaged density map and changes with time for the heated column subject to heating and hydration for 129 days. (b) The average density vs. radial distance from the center shaft along the white dotted line in (a).

In HotBENT Lab #1, we presented a low-density zone around the heater shaft after heating due to water evaporation. In this heating and hydration test, we no longer observed any water evaporation or dry-out zone from the CT images. This may be attributed to the increased water pressure in the sand layer from 120 to 290 psi. Note the boiling pressure of water at 200 °C is 225 psi, lower than the applied boundary pressure at 290 psi. Figure 6-10 compares the dynamic CT density change, relative to their initial conditions (ρ_CT-ρ_CT^i) before heating and hydration in the two sets of experiments. As we mentioned earlier, the initial conditions for this new heating and hydration experiments (HotBENT Lab #2) are different from the HotBENT Lab #1 tests, including

(1). Increased bentonite dry density from 1.2 g/cm^3 to 1.45g/cm^3,

(2). Reduced gravimetric water content at 5.3% water content, use the same clay from that is being used in the HotBENT field site,

(3). Used Grimsel GW at a considerably lower salt content, and

(4). Increased hydration pressure from 120 to 290 psi

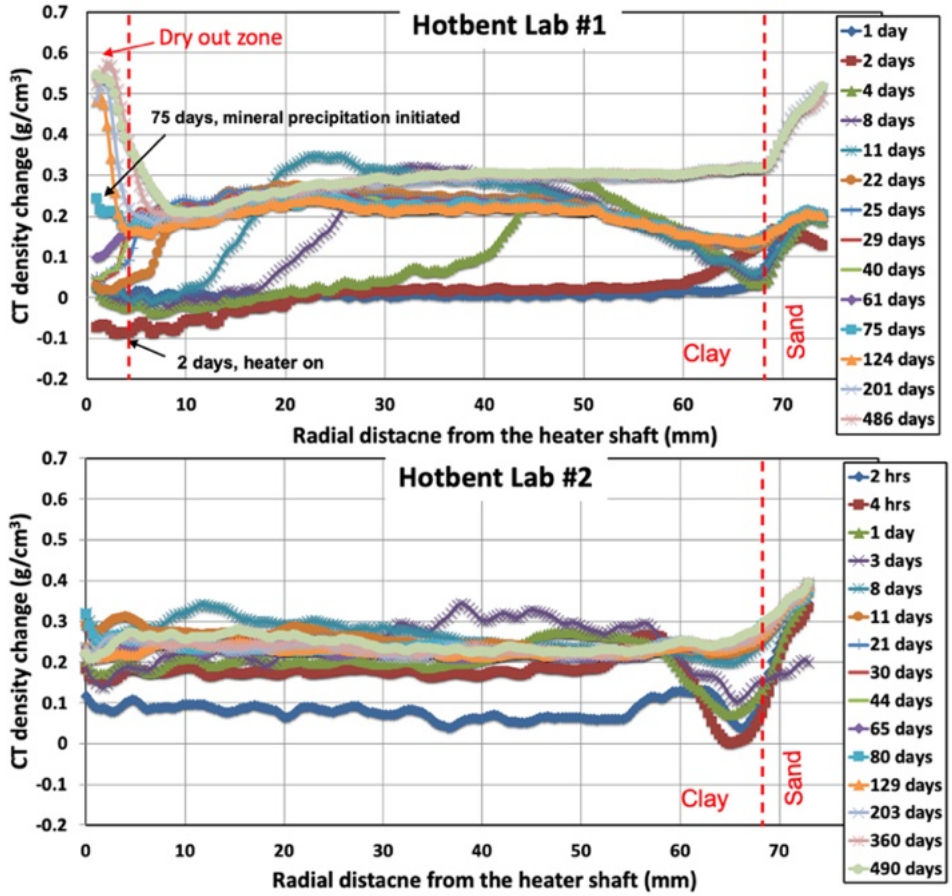

Figure 6-10. Comparison of the changes of radially averaged density vs. radial distance from the heater shaft in the two sets of heated columns in HotBENT Lab #1 and #2.

As shown in Figure 6-10, HotBENT Lab #1 test presents the larger density variations in bentonite, indicating a more complex and heterogeneous mechanical behavior of the bentonite buffer as it is subjected to heating and hydration with strong thermal and moisture gradients. In addition, a dry-out zone and mineral precipitation at the canister were observed, representing the strongly dynamic and coupled process in bentonite when exposed to heating, hydration and swelling. These considerable variations in density and porosity (thus permeability) challenge the feasibility and predication of high-temperature radioactive waste disposal. In HotBENT Lab #2 test, we applied a higher water injection pressure at 290 psi in the sand layer, which compressed the bentonite column more pronouncedly and led to the larger and wider density drop in Figure 6-10 ahead of the initial sand-clay boundary. By comparison in HotBENT Lab #1 test, in-situ bentonite swelling after hydration is the dominant mechanism accounting for CT density reduction at the clay-sand boundary as we applied a lower water injection pressure of 120 psi in the sand layer.

By comparison, The HotBENT Lab #2 test shows the improved performance in bentonite with much more homogeneous density distribution by the end of the experiment at 490 days. No dry-out zone or mineral precipitation was observed. The more pronounced density drop along the bentonite-sand boundary indicates a larger compaction of interior bentonite since the medium is more granular and is a mixture with pellets. It also indicates larger swelling of bentonite after water saturated along the boundary with a lower initial water content and higher compacted dry density. In this sense, the spatio-temporal density variations of bentonite after the experiments are affected by the initial bentonite density, water content, hydration pressure and temperature distributions. The lab experiment provide insight and

confident in the performance of field bentonite. The fast hydration in HotBENT #2 lab test may be attributed to the very heterogeneous bentonite structure mixed with fine powder with large mm cm-scale granulated grains (Figure 6-11).

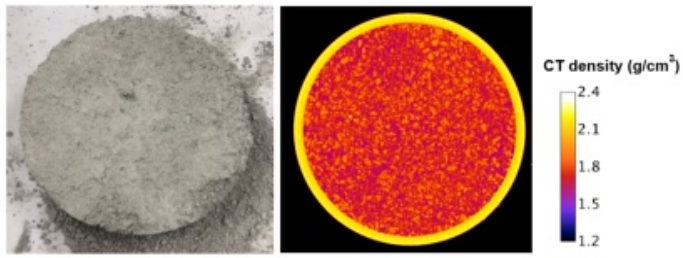

Figure 6-11. Photograph and CT image of the bentonite clay used for HotBENT Lab #2 test.

Displacement

We have shown the 3-D hydration and deformation of bentonite by heating and hydration through the dynamic CT density changes. We further quantify the mechanical behavior of bentonite subject to hydration and heating by tracking the displacements of tracer particles emplaced in both columns and imaged through frequent X-ray CT scans.

Figure 6-12(a) depicts the 2-D CT images selected from the high-density segment of the non-heated column at different times, while Figure 6-12(b) is the magnified image focusing on the displacement of the tracer particles. The crossings of the dotted lines in Figure 6-12(b) point to initial locations of the tracer particles before test (i.e., 40 and 59 mm away from the central shaft). We measured the distance between the particle and the central shaft during the experiments, and calculated displacements by subtracting the value before the experiment. Figure 6-12(c) presents the dynamic displacement vs. time in red curve, in which a negative displacement is defined when the particle moves towards the central shaft, whereas a positive displacement is defined when the particle moves outward from its initial position. Also shown in the Figure 6-12(c) is the dynamic displacement of two tracer particles selected in the low-density segment and at similar radial distance from the central shaft. As shown in the Figure 6-12, all tracer particles show comparable tendency in displacement dynamics. For instance, at t=1 day, all particles along with their surrounding clay are compacted inward towards the central shaft with minimum displacement (negative) values by swelling along the sand-clay boundary. After that, as hydration propagates to the center, all the tracer particles are pushed outward. Figure 6-12 also shows the decrease of displacements as bentonite compacted closer to the central shaft with a lower initial density. At t=148 days, the displacement ranges from -0.42 to 1.11 mm.

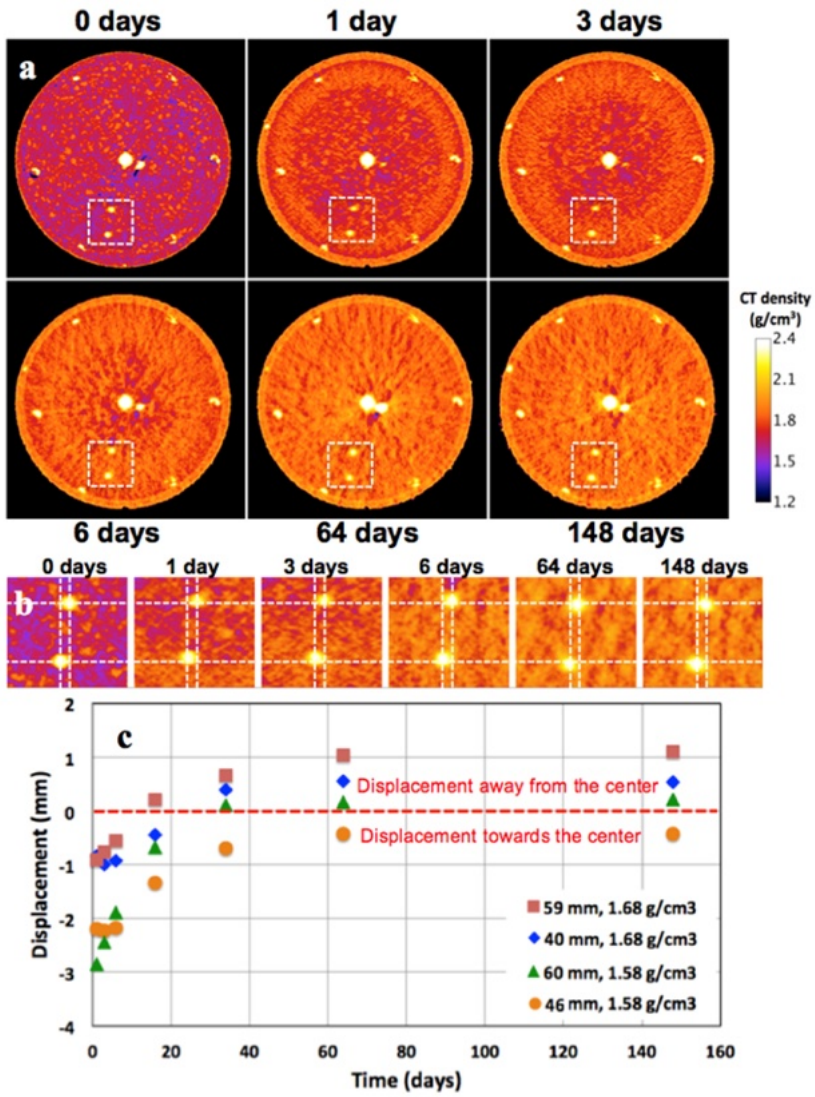

Figure 6-12. HotBENT Lab #2 non-heated column (a) Selected time-lapse 2-D CT images showing the displacement of the selected tracer particle and temporal density distributions in the non-heated column. (b) The magnified images showing the displacement of the tracer particle relative to its initial location marked by the crossing of the white dotted lines. (c) Variations of displacement as a function of time for the selected tracer particles in (a), and another two selected in the low-density segment. The white dotted boxes in (a) bound the magnified images in (b), and the particles selected in (c) at 59 and 40 mm away from the central shaft and at 1.68 g/cm^3 initial bentonite density.

Figure 6-13(a) and Figure 6-13(b) present the 2-D time-lapse CT images and displacement of the tracer particles selected at 48 and 61 mm away from the central shaft in the heated and hydrated column. Similar to the non-heated column shown in Figure 6-13, the dynamic displacement of the tracer particle (thus bentonite) is dominated by compaction as osmotic swelling after bentonite becomes fully water saturated. At t=129 days, the displacement ranges from -0.04 to 0.17 mm, similar to the displacement of low-density segment as both were compacted at similar initial densities (see Figure 6-4 through Figure 6-11).

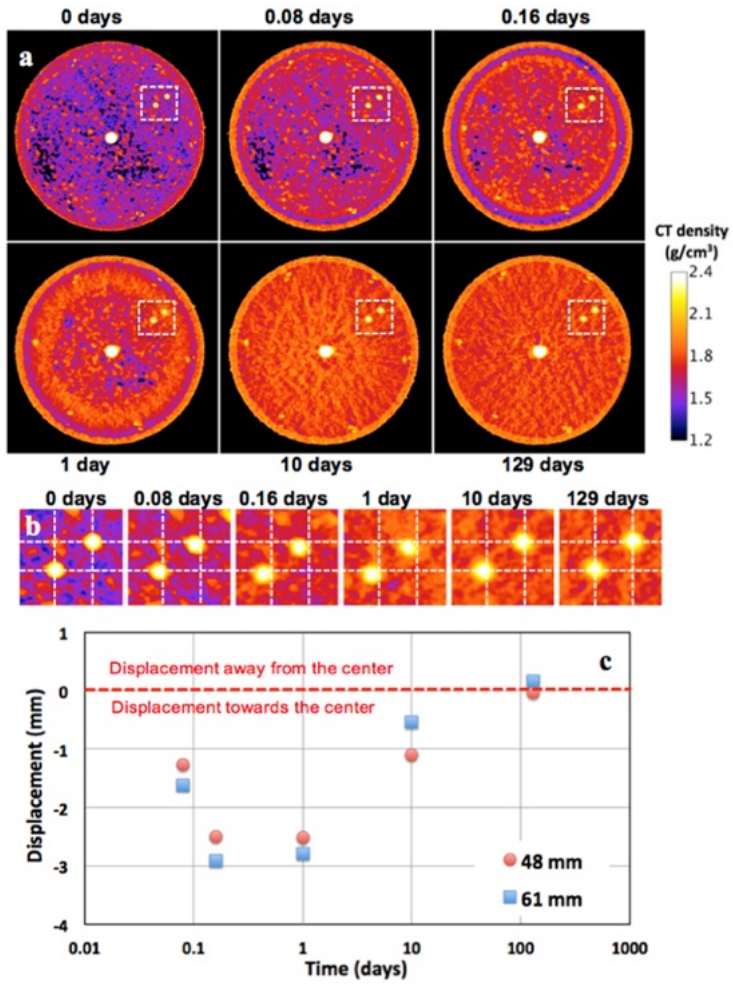

Figure 6-13. HotBENT Lab #2 heated column (a) Selected time-lapse 2-D CT images showing the displacement of the selected tracer particles and temporal density distributions in the heated column. (b) The magnified images showing the displacement of the tracer particle relative to its initial location marked by the crossing of the white dotted lines. (c) Variations of displacement as a function of time for the selected tracer particles. The white dotted boxes in (a) bound the magnified images in (b).

As mentioned in Section 6.3.1, we have emplaced tracker particles in each column. In each column, there are seven planes observable along the axial direction under X-ray CT imaging, and in each plane, six particles can be tracked at different radial distance from the central shaft. Figure 6-14 show the locations of each plane by CT images. These tracer particles will provide data on the radial displacement of bentonite, as well as potential axial displacement considering the density heterogeneity along axial direction. Assuming radially symmetrical deformation of bentonite induced by heating and hydration, the strain (ε) was calculated from displacement (ΔL) of the tracer particles and the column radius (R) (i.e., $\varepsilon = \Delta L / R$). A negative strain thus represents displacement towards the central shaft whereas positive strain indicates outward displacement towards the hydration boundary. Along the axial direction, a postive z value represent displacement occurred from left to right in Figure 6-14.

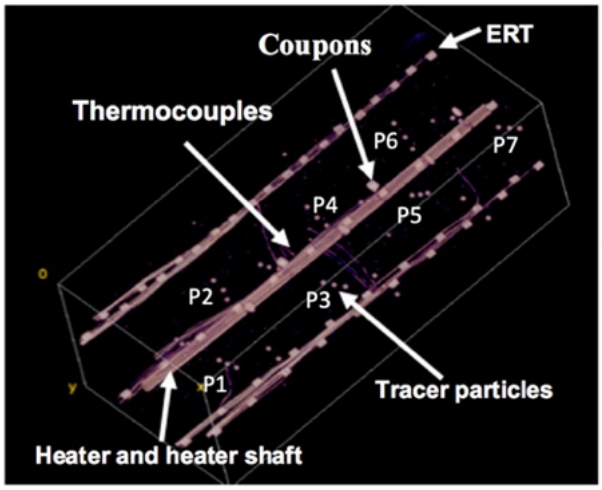

Figure 6-14. HotBENT Lab #2 plane locations of emplaced tracer particles along the axial direction of the column.

Figure 6-15 and Figure 6-16 show the radial strain and axial z-displacement and their variations in the non-heated column vs. time measured by tracer particles emplaced at different radial and axial locations. As shown in Figure 6-12, all particles overall moved with the surrounding clay and were displaced inward towards the central shaft. After that, as hydration propagated to the center, all the tracer particles were pushed outward towards their initial positions, similar to the observations in Figure 6-12. Along the axial direction and before 200 days, Figure 6-15 depicts positive and gradual increase of z-displacement, indicating the more pronounced swelling of the high-density segment after hydration. After 200 days, the value gradually reduced to zero until the end of the experiment. Figure 6-15 and Figure 6-16 collectively indicate the complex 3-D displacement of bentonite after hydration and the initial compacted density plays a critical role in affecting the spatio-temporal variations during hydration.

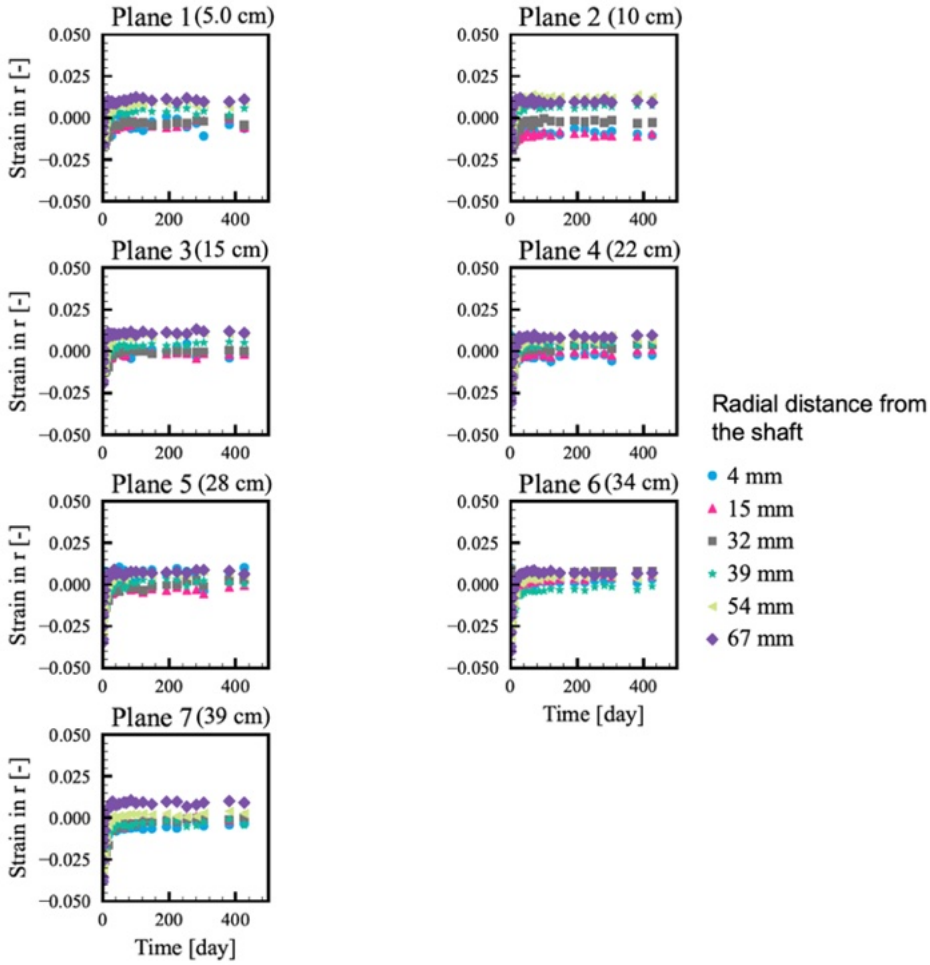

Figure 6-15. The radial strain vs. time in the HotBENT Lab #2 non-heated column measured by the tracer particles emplaced in different radial and axial locations.

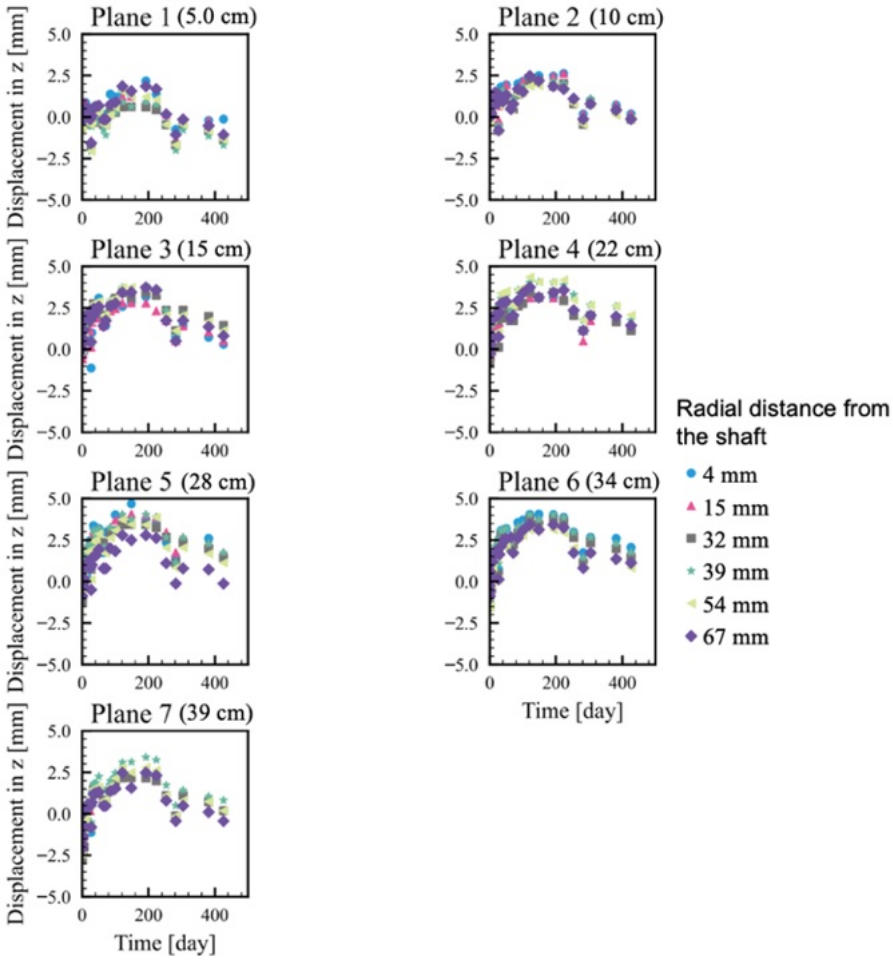

Figure 6-16. The axial z-displacement in the HotBENT Lab #2 non-heated column measured by the tracer particles emplaced in different radial and axial locations.

Figure 6-17 and Figure 6-18 show the radial strain and axial displacement in the heated column and their variations as a function of time. Similar to the non-heated column, the radial strain in Figure 6-13 indicates overall inward displacement of bentonite towards the central shaft at the early time, followed by gradually reverse displacement and towards their initial positions. Comparing to the non-heated column, the more negative r-strain represents more compression of bentonite after hydration along the clay-sand boundary. The z-displacement in Figure 6-17 represent a more dynamic variation, which will need to be interpreted with more comprehensive analysis including any image registration errors along the axial direction.

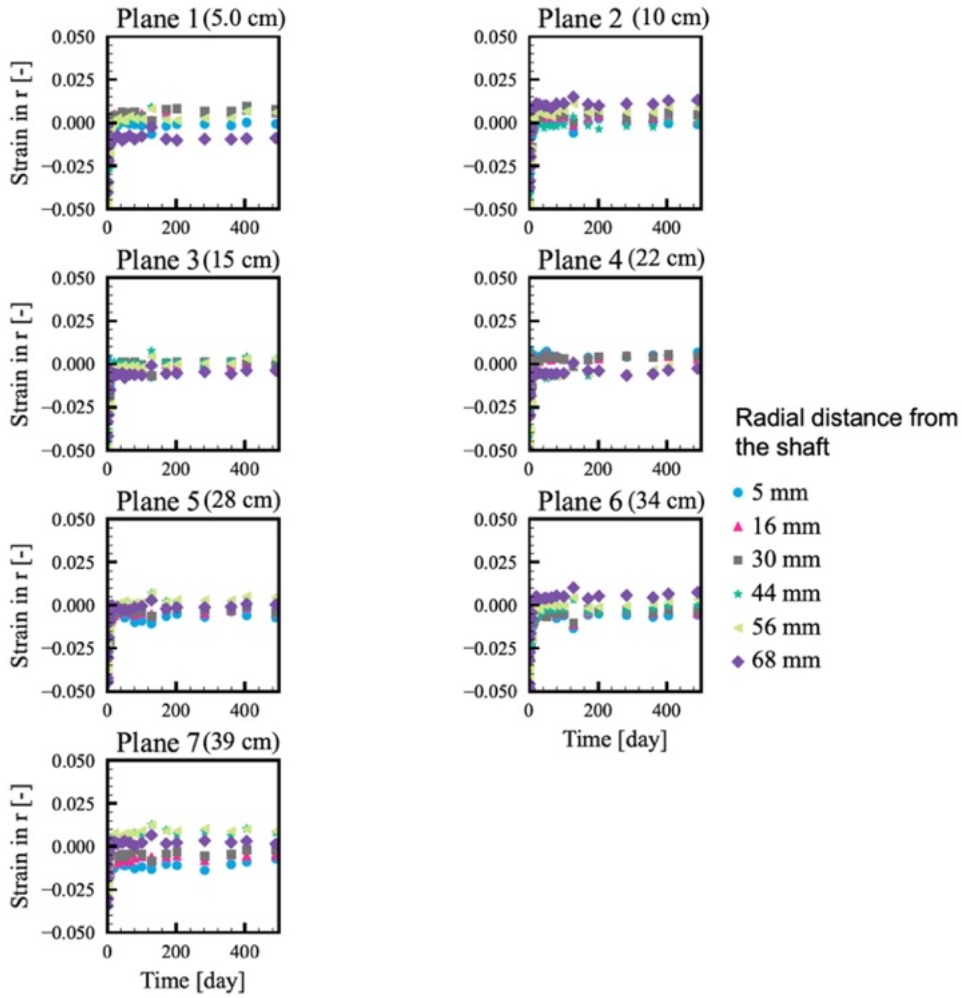

Figure 6-17. The radial strain vs. time in the HotBENT Lab #2 heated column measured by the tracer particles emplaced in different radial and axial locations.

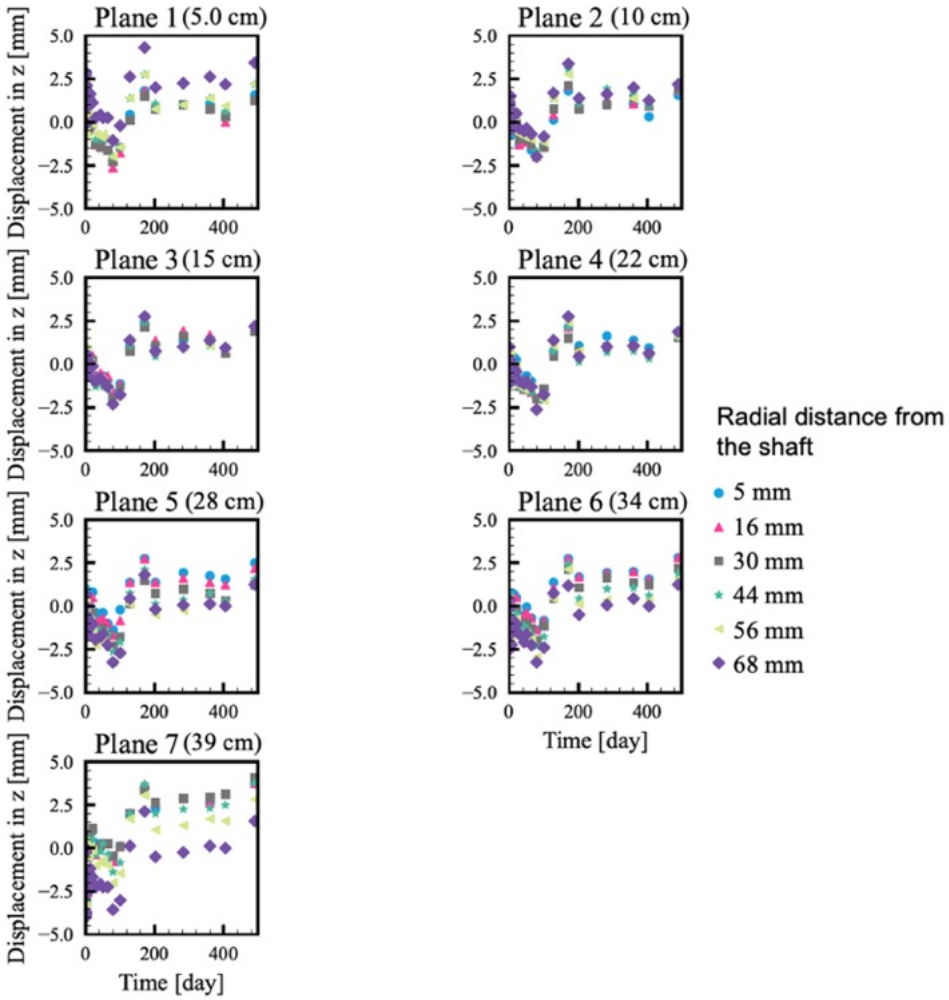

Figure 6-18. The axial z-displacement in the HotBENT Lab #2 heated column measured by the tracer particles emplaced in different radial and axial locations.

6.3.2 Electrical Resistivity Tomography (ERT)

As the core task of the geophysical monitoring effort, ERT data was periodically collected and analyzed throughout the experiment. In this section, we summarized the results from ERT data acquisition, processing and inversion (modeling), and post-inversion statistical and correlational analyses, which aim at investigating the THM processes of the bentonite clay undergoing heat and/or hydration and demonstrating the capability of ERT as a monitoring tool for such system.

ERT Data Acquisition and Processing

During this experiment, we noticed a gradual decrease in ERT data quality as the heating and/or hydration proceeded and were prompted to perform some quality checks on the electrodes – by measuring the contact resistance between all electrode pairs. From these tests, we identified a few shorted electrodes, which was likely caused by contact among exposed wires inside the column. When the clay became extremely conductive, the system ramped up its current injection to meet the targeted voltage, which could thereby melt the sheath. To prevent further deterioration of the connection between the wires and the electrodes, the injection current was reduced to the system minimum value (0.1 A). We also adjusted the data acquisition sequence (i.e., the electrode configuration) accordingly, so that the malfunctioning

electrodes were excluded from both current injection and potential measurements. A rigorous data filtering procedure – including setting stricter quality check thresholds on the reciprocal error, stacking error, contact resistance, apparent resistivity, and minimum percentage of valid measurements from each electrode – was applied to exclude data with ill-defined geometry due to these shorted circumstances (Figure 6-19).

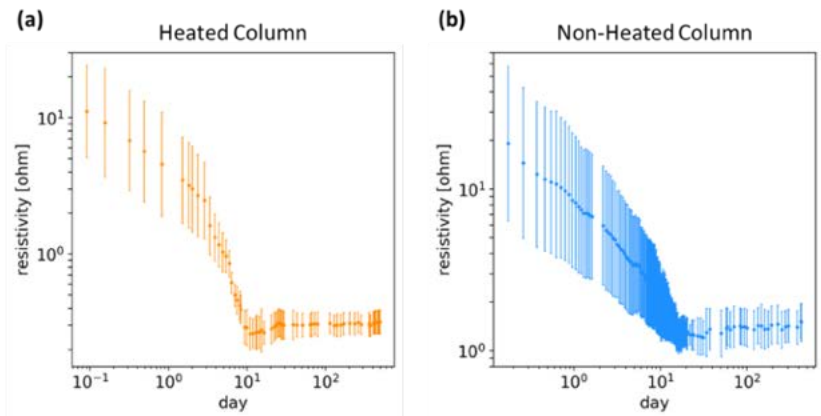

Figure 6-19. Apparent resistivity of the (a) heated and (b) non-heated column post data processing. The points mark the median apparent resistivity value from each data acquisition (i.e., time point), and the error bars show the log-scaled interquartile range of resistivity values.

ERT Data Inversion

Hydration (non-heated column)

Figure 6-20 shows the time-lapse ERT of the non-heated column on selected days (flow started on day 0, and the experiment was concluded on day 426). To investigate the radial hydration process, the cylindrical coordinate system is reduced and plotted onto the 2D radial-axial axes (r, z). The data visualization is based on a triangulated interpolation method, using the (r, z) coordinates of the mesh cell center and disregarding the angle. Therefore, the circumferential variation in the modeled (ERT) resistivity would also contribute to the apparent granularity. As expected, the clay near the flow boundary via the sand layer ($r > 0.07$ m) had the lowest resistivity as the hydration progressed, and the inward water infiltration can be visualized in terms of a gradual decrease in resistivity, which is analogous to the movement of a high CT density front. While CT does not show particularly low density near the end caps (note that CT data availability is also lower there due to thicker vessel wedges), ERT shows higher resistivity in those regions close to the model boundary.

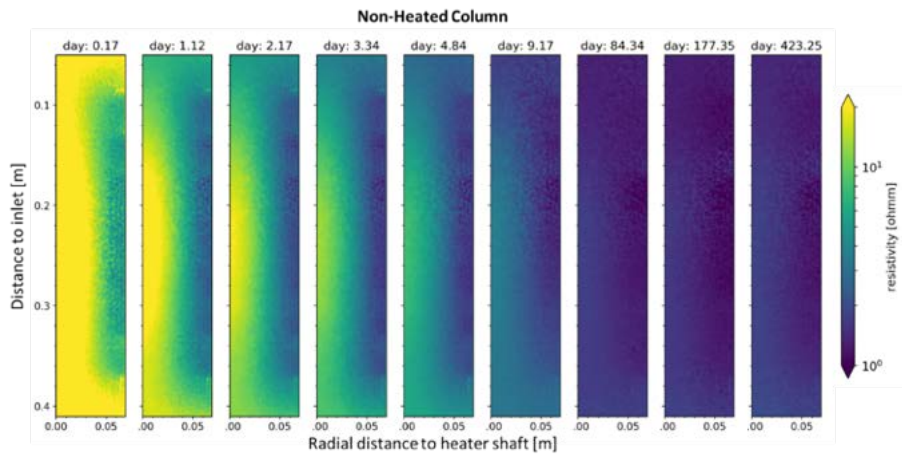

Figure 6-20. Time-lapse ERT of the non-heated column.

Next, we looked at ERT resistivity averaged over space and compared it between clay layers with contrasting dry bulk densities. Figure 6-21(a) shows the averaged resistivity of the entire column throughout the experiment. The decrease in resistivity predominantly took place in the first twenty days, beyond which the rate of change came very small. Because the resistivity is highly sensitive to the saturation degree of the clay, this observation indicates a significant hydration process during the beginning of the experiment. Figure 6-21(b) compares the averaged resistivity in the high (close to the inlet, $z < 0.23$) and the low (close to the outlet, $z > 0.23$) density layers of the non-heated column. The high-density layer was consistently, although not statistically significantly, more conductive, which was expected because of the larger clay surface area and thus higher surface conductivity in that layer, despite it having a smaller porosity. However, as observed in Figure 6-20, the resistive clay near the end caps also contributed to these average values. While the model boundary effect has not been ruled out, the outlet end, which is in the low-density layer and most loosely packed due to the technical nature of the packing procedure, is also shown to be more resistive compared to the inlet end.

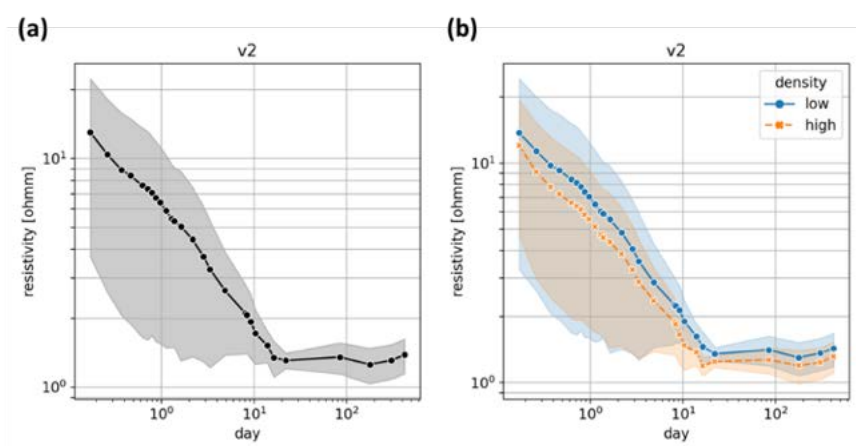

Figure 6-21. Time series of ERT resistivity of the non-heated column: averaged resistivity of (a) the entire column and (b) in the high and low dry bulk density layers. The shaded regions represent one standard deviation from the mean value.

Heating and Hydration (heated column)

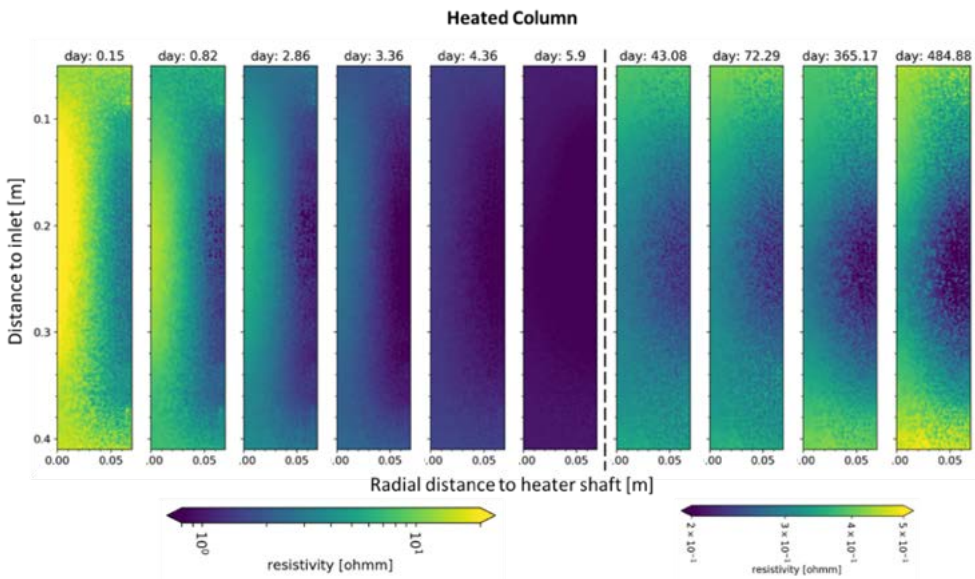

Figure 6-22. Time-lapse ERT of the heated column. The dashed line separated the reference color bars for visualization.

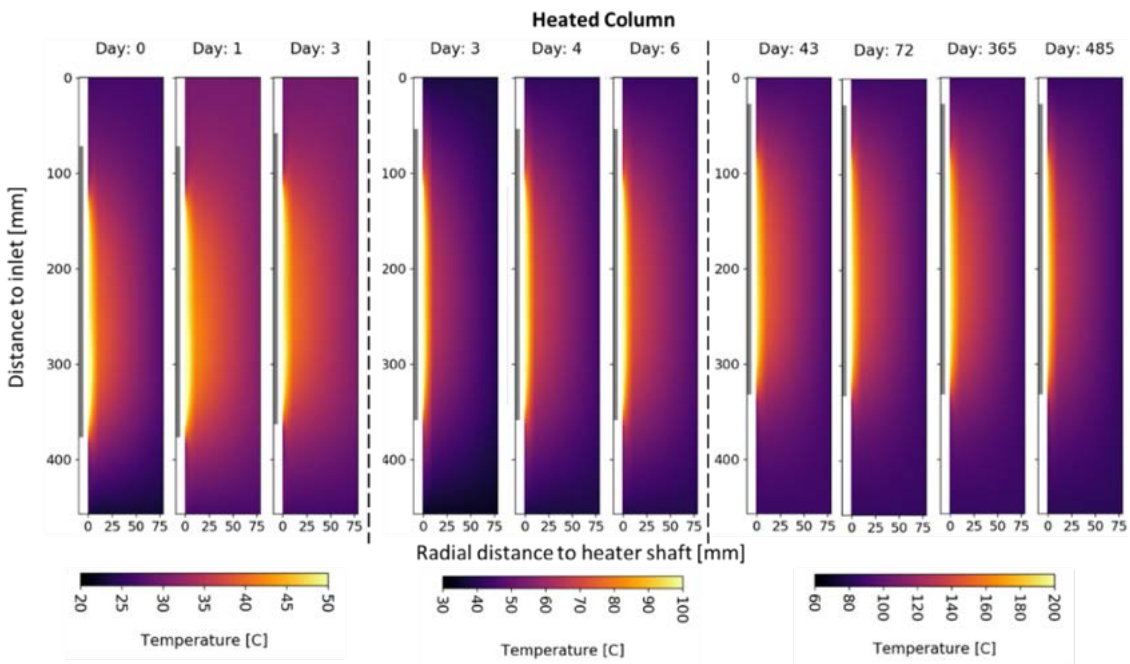

Figure 6-23. Time-lapse 2D temperature distribution of the heated column. The dashed line separated the reference color bars for visualization.

Figure 6-22 shows the time-lapse ERT of the heated column (heat and hydration started on day 0, and the experiment concluded on day 490), and Figure 6-23shows the temporally corresponding temperature models in the radial-axial coordinates. Because heating and hydration both makes the system more conductive, the change in resistivity is highly coupled, and the water infiltration was not as obvious. To decouple the temperature effect on the resistivity values, we performed a 2% temperature correction on the resistivity value:

$$\rho_{20} = \frac{\rho}{(1+0.02)^{T-20}} \qquad \textbf{Eq. (6-3)}$$

where ρ_{20} [Ωm] is the resistivity corrected to 20 C, ρ [Ωm] is the ERT resistivity, and T [C] is the temperature of the clay. The temperature data were generated by solving the two-dimensional Laplace equation: the boundary conditions were defined by the temperature measurements on the heater, heater shaft, end caps and vessel body. As observed in the previous experiment and modeling results, the cylindrical clay column seemed to have two radial zones with distinct thermal conductivities – one very slim zone adjacent to the heater with a larger temperature drop per radial distance, and the rest of the clay with a gentler change in temperature over space. The model was fitted by minimizing the misfit between the modeled values the temperature measured by the other ten thermocouples embedded in the clay, and the temperature-corrected resistivity is shown in Figure 6-24 as ERT time-lapse and in Figure 6-25 as averaged values over the entire column. Besides the gradual decrease in resistivity from the water infiltration, there also exists a more resistive zone adjacent to the heater, which was observed as a local low CT density (drier) zone from the CT.

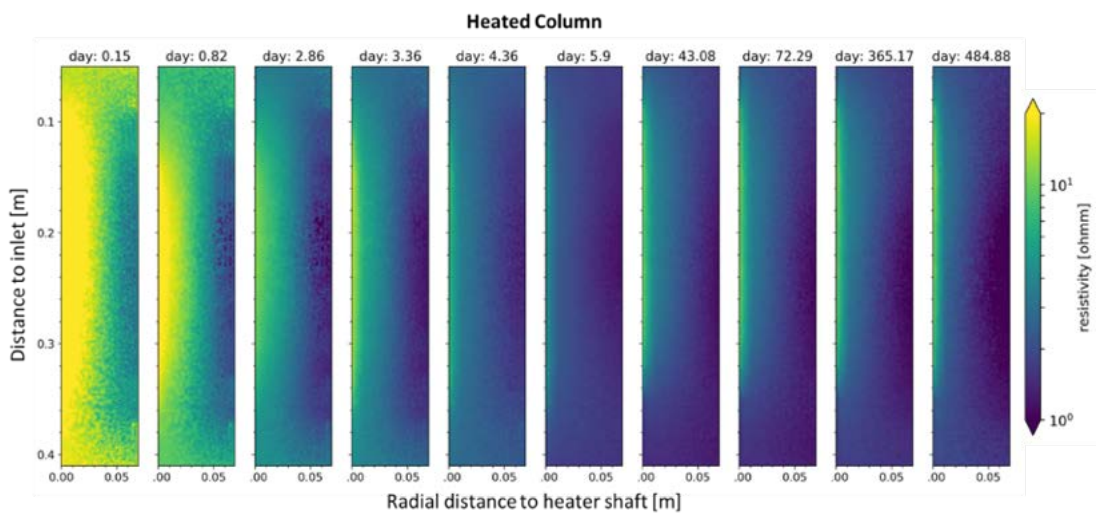

Figure 6-24. Time-lapse temperature corrected ERT of the heated column.

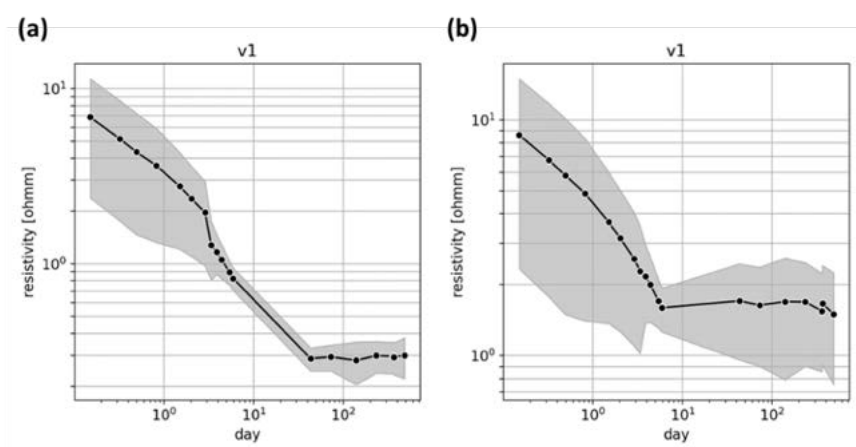

Figure 6-25. Time series of averaged ERT resistivity of the entire heated column (a) without and (b) with temperature correction.

Petrophysical Calibration

To demonstrate how ERT can be used to quantify the progression of water infiltration, we performed a petrophysical fitting between saturation degree and resistivity using a simplified Archie Law as the test model:

$$\rho = \rho_{sat}\, S^{-n} \qquad \textbf{Eq. (6-4)}$$

where ρ [Ωm] is the ERT resistivity, ρ_{sat} [Ωm] is the saturated resistivity, S [$m^3\ m^{-3}$] is the saturation degree, and n [-] is the saturation coefficient. The data inputs included (1) ρ: areal-weighted and temperature-corrected ERT resistivity averaged over the entire column and (2) S: the saturation degree of the entire column, calculated from the averaged CT density of the entire column and an estimated porosity (porosity = 1 – dry bulk density/mineral density, with mineral density taken as 2.6 g cm^{-3}). The fitting results are shown in Figure 6-26(a) (non-heated column) and Figure 6-27(a) (heated column). While the negative correlation between the two variables is evident, their (log-log) relationship is not linear as described in the simplified Archie Law, which lacks an additional surface conductivity term in the equation. Because surface conductivity of the clay plays a significant role in the electrical properties of the clay, this non-linear relationship is expected and calls for a more complex model to be adopted. On the other hand, the quite drastic difference in the saturation coefficients between the two columns suggests that it is also necessary to investigate on models that can better incorporate the different physical-chemical properties (i.e., porosity, pore fluid conductivity, temperature correction) to fit the data more consistently.

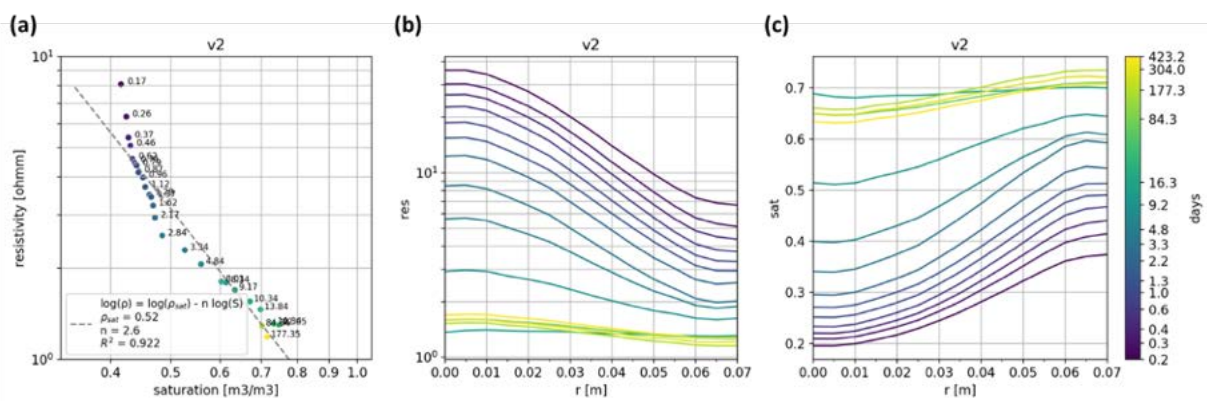

Figure 6-26. Non-heated column. (a) Petrophysical fitting result between column saturation degree and resistivity using a simplified Archie Law. Radial profiles of (b) depth-averaged ERT resistivity [Ωm] and (c) calibrated saturation degree [$m^3\ m^{-3}$]. Each curve represents one data acquisition with the corresponding day labeled on the color bar.

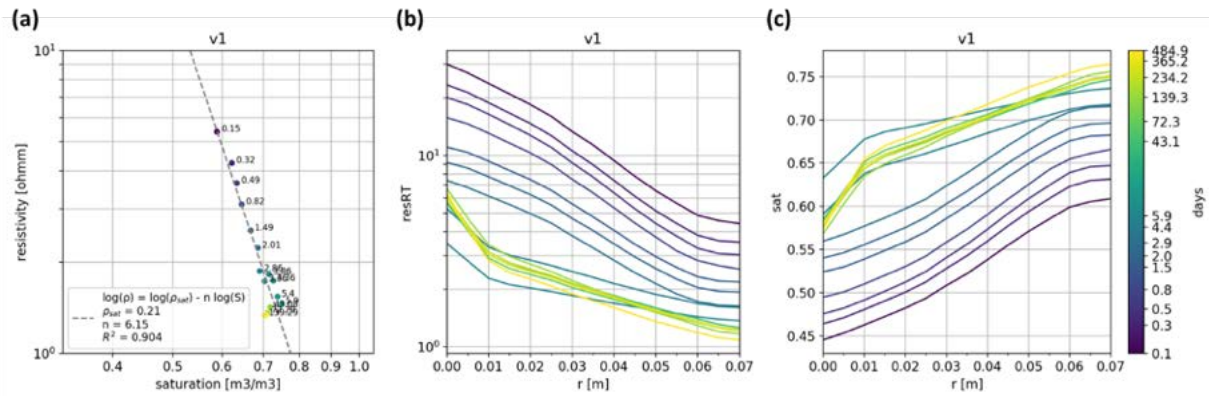

Figure 6-27. Heated column. (a) Petrophysical fitting result between column saturation degree and resistivity using a simplified Archie Law. Radial profiles of (b) depth-averaged, temperature-corrected ERT resistivity [Ωm] and (c) calibrated saturation degree [m^3 m^{-3}]. Each curve represents one data acquisition with the corresponding day labeled on the color bar.

We experimentally applied this petrophysical calibration to examine how the saturation degree of the clay evolved with time and space. Figure 6-26(b) and (c) (non-heated) and Figure 6-27(b) and (c) (heated) show the radial profile of the resistivity on the left and the converted saturation degree to the right. Besides the aforementioned limitation of this specific model on the lack of surface conductivity and other physiochemical terms, the different scales between the fitting data (column level) and the testing data (radial level) could also pose a challenge because of the spatial heterogeneity in the clay. Nevertheless, the methodology shows how ERT is used to visualize and quantify spatial and temporal changes in saturation, which could be a useful tool especially when other spatial measurements are difficult to implement. Currently, an effort is being invested in joint calibrating a petrophysical model with the high-resolution CT that could decode the centimeter-scaled hydrological process while taking the other TMC related processes (swelling/compaction, ion exchange at clay surfaces, etc.) into consideration.

6.3.3 Postmortem Sampling

Both HotBENT Lab #2 columns were dismantled, the hydration only after 13 months of hydration, and the heated and hydrated after 14 months of heating and hydration. Dismantling was accomplished by layers from the inlet and outlet ends. Sample tubes were emplaced in the clay and CT scans were done to identify the exact location and CT density of the extracted samples. Bulk clay outside the sample tubes was collected as well and were defined in three radial groups: (1) 0 to 2 cm, (2) 2-5 cm, and (3) 5-7.5 cm ring distances from the center of the column. The center most layer was kept intact and preserved for future analyses. Images from dismantling can be seen in Figure 6-28.

The samples that were removed from recorded locations within each layer were carefully weighed and dried to constant value and used to verify the water content in the bot the non-heated and heated column (See Figure 6-29 and Figure 6-30). These values will be used to verify CT and ERT measurements taken during the experiment and during the dismantling process.

Figure 6-29 and Figure 6-30 present characterizations on the bentonite samples after dismantling, including water content, dry density, and degree of saturation. Samples were collected axially from 7.5 to 38 cm in the non-heated column and 6.25 to 37 cm in the heated column. In the non-heated column, Figure 6-29 presents an overall decrease of bentonite water content and degree of saturation from the hydration boundary to the central shaft. Clay swelling along the hydration boundary induced slightly lower dry density at the hydration boundary than those closer to the central shaft. Comparing the low-

density segment vs. high-density segment indicates the impacts of initial conditions on hydration: the loose compacted bentonite with a lower initial dry density led to a higher water content and degree of saturation after hydration, and a lower dry clay density.

In the heated column, Figure 6-30 shows very similar variations to the non-heated column. Comparing to Figure 6-29 the higher water content, degree of saturation in (a) and (c) and lower dry density in (b) after heating and hydration could also be attributed to the lower initial compacted bentonite density. Meanwhile, comparing to our first set of HotBENT column test (Chang et al., 2023), the spatiotemporal density variations in HotBENT Lab #2 is less significant since there is no water phase changes or mineral precipitation near the heater. These characterizations from the postmortem samples are consistent with the CT density distributions shown in Figure 6-6 and Figure 6-9.

Figure 6-28. Images from dismantling of the HotBENT Lab #2 experiment. Clockwise from top left, (a) images of ring placement and map of sample removals, (b) sample removed for analysis, (c) residual central layer preserved for future analysis, and (d) bulk sample.

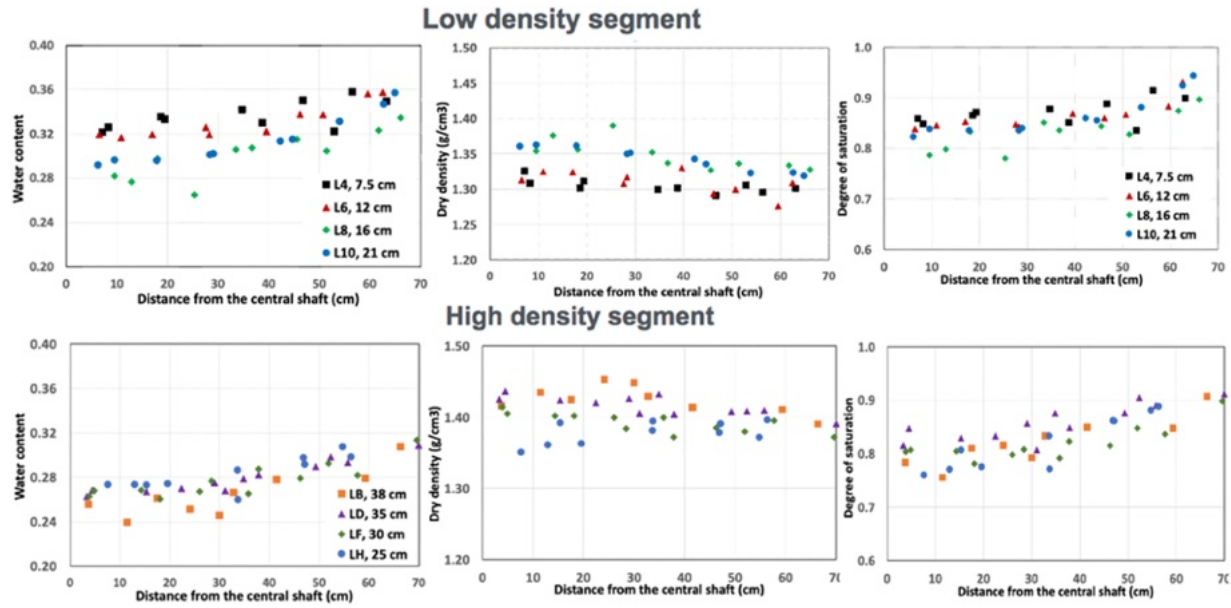

Figure 6-29. Water content, dry density, and degree of saturation measured from samples removed from the non-heated column.

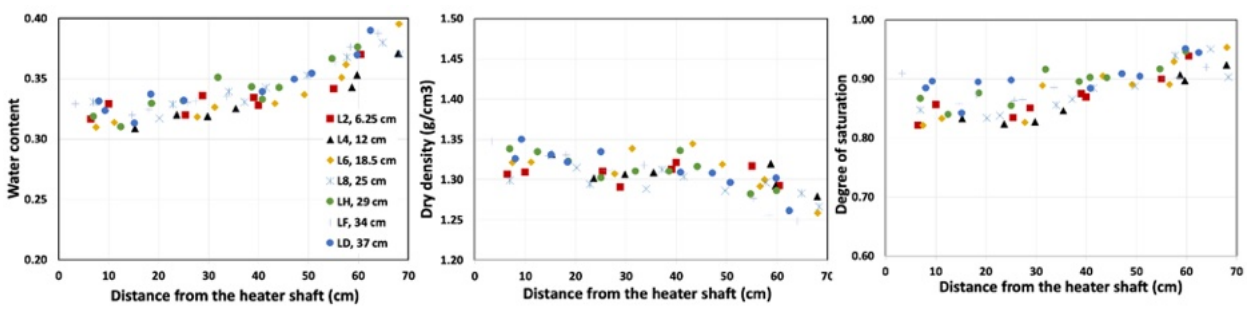

Figure 6-30. Water content, dry density, and degree of saturation measured from samples removed from the heated column.

6.4 Summary and Future Work

The current HotBENT Lab #2 test using granulated Wyoming bentonite has been conducted for 16 months and monitored for hydration, bentonite swelling, and temperature distribution. The improved packing procedure with more extensive ERT array, increased number of thermocouples, and embedded tracking particles have produced useful and interesting data. Results so far have shown more homogeneous distribution of bentonite density despite of the strong thermal gradients, compared to the HotBENT Lab #1, without a dry-out zone or mineral precipitation observed. The displacement data by tracking representative tracer particles in bentonite represents spatio-temporal evolution of bentonite deformations affected by hydration, heating and swelling. These spatio-temporal displacements have shown dependence on the initial dry density of compacted bentonite.

Issues with inlet and outlet clogging have caused difficulty in collecting effluent water samples for chemistry analysis, which reduced our ability to control and monitor the pressure of the system. The strain gauges are a helpful addition to monitoring the bentonite, but the electronic noise has limited their usefulness and would need to be improved upon for a new test. It would also be helpful to install

additional sensors for hydration monitoring (such as humidity sensors), as well as to monitor internal pressure independently of the inlet and outlet flow, and perhaps some fiber optic sensors.

Additional analyses are underway on the removed samples, including chemical analysis, CEC, XRD, which are listed in Table 6-3. The results of this analysis will help determine the analysis conditions of another set of columns. These analyses will be compared to analysis from the HotBENT Lab #1 experiment and summarized in a manuscript.

Table 6-3. List of analysis to be completed on the clay removed from the HotBENT experimental column.

Physical Parameters	Additional Analysis
Wet mass	Influent and effluent water chemistry
Dry mass	XRD on clay
Water content (g/g)	Metals analysis on clay
Dry density (kg/m^3)	SEM
Porosity	μCT
Degree of saturation (vol/vol)	Microbial community analysis
	Coupon evaluation

Future work in the remaining months of FY 23 and into FY24 will include the following:

- Analysis of clay removed from HotBENT Lab #1 and HotBENT Lab #2
- Repack columns with conditions to be determined, based on clay analysis and modelling results which may include:
  - Different types of bentonites (possibly Czech bentonite (BCV) that is used in H4 of the HotBENT field test)
  - Different configurations and updated instrumentation to further understand hydration rates.
  - Different hydration pressure to mimic current HotBENT field conditions. (0.7 MPa)
- Continued coordination with modelling efforts and preparation of manuscript on the clay analysis results.

7. MODELING THE CONCRETE/BENTONITE INTERFACE: TASK 12 IN SKB EBS TASK FORCE INTRODUCTION

7.1 Introduction

Compacted bentonite is the most commonly proposed buffer material for an EBS in a mined geological repository for HLW. After the emplacement of heat-generating waste, the bentonite buffer is expected to experience heating from the waste package and hydration from a host rock, which results in a series of thermal, hydrological, mechanical, and chemical (THMC) changes, which may affect the long-term performance of a bentonite buffer. These THMC processes are coupled and evolve temporally and spatially.

The geochemical changes of bentonite in the context of waste disposal have been studied extensively using laboratory experiments, numerical modeling, and field tests. Some of them focus on the alteration of bentonite as a result of heating (e.g. Caporuscio et al., 2021; Guillaume et al., 2004; Cheshire et al., 2014;2018); some are dedicated to the chemical changes in the interfacial areas such as bentonite/concrete (e.g., Fernández et al., 2009; Marty et al., 2015), bentonite/canister (Necib et al., 2017a; Bourdelle et al.,2014; 2017) and bentonite/host rocks (e.g., Sauer et al., 2020); or more comprehensive analysis of the geochemical changes at the near field (e.g., Bradbury et al.,2014). Because the life span of a repository is much longer than any test can run, numerical models, particularly reactive transport models have been used to predict the long-term alteration of bentonite (e.g., Mon et al., 2017; Chaparro et al., 2021). These models ideally should be built upon faithful representation of all relevant processes and formulated with parameters that are either calibrated at the scale close to the repository or measured reliably at conditions relevant to the repository, which however is proven to be very difficult because of (1) the failure of numerical models to capture all the relevant processes, (2) the inaccuracy of measuring the model parameters by current experimental techniques, and (3) the mismatch between what models need and what experiments can measure.

The geochemical change of bentonite is triggered by both the thermal perturbation and interaction between two different media, for example, canister and bentonite, bentonite and concrete liner, bentonite and host rock (if there is no concrete liner), or concrete liner and host rock. The alteration of the mineral phase around the interface area may significantly change the porosity and subsequently permeability, and, therefore, have a profound impact on the long-term migration of radionuclides through bentonite buffer. Concrete has been proposed to be used as backfill material, and cementitious materials are used as tunnel support (particularly for argillite host rock), mechanical plugs, backfill materials, buffer materials, and waste form (Abe & Iida, 2022). The geochemical alteration at the interfacial area between bentonite and concrete needs to be better understood (e.g., Fernández et al., 2009; Marty et al., 2015).

In Task 12 of the SKB EBS task force (Birkholzer et al., 2022), modeling teams collaboratively simulate long-term reactions occurring at cement-bentonite interfacial regions concerning mineralogical, chemical, or textural changes. Task 12 was established in FY21 and has currently been conducted by four modeling teams: SKB, Surao, LBNL, and SNL. Currently, Task 12 focuses on modeling of a benchmark problem, but experimental data might be brought in. In this section, we document LBNL's effort in FY23 to simulate the benchmark problem in Task 12 of the SKB EBS task force.

7.2 Description of Task 12

Task 12 was divided into three subtasks to simulate different initial saturation states of bentonite and types of concrete. Subtask A is conducted to study the interaction between MX-80 and Ordinary Portland Cement (OPC) (Figure 7-1). Given that developing reactive transport is a complex process, to make the models by different groups comparable, subtask A is a relatively simple case. The benchmark specifies the following conditions:

- A fully saturated isothermal system (25ºC) consisting of aged OPC concrete and MX-80 bentonite,
- A constant atmospheric pressure of 0.1 MPa,
- No-flux boundary conditions, assuming the transport is diffusive, and
- The bentonite-to-concrete volume ratio is assumed to be one (i.e., in a 1D model equally long domains (of 1 m each) are considered (Figure 7-4)).

The initial mineralogical and pore water conditions will be discussed later. The length of the simulation time interval is 100,000 years.

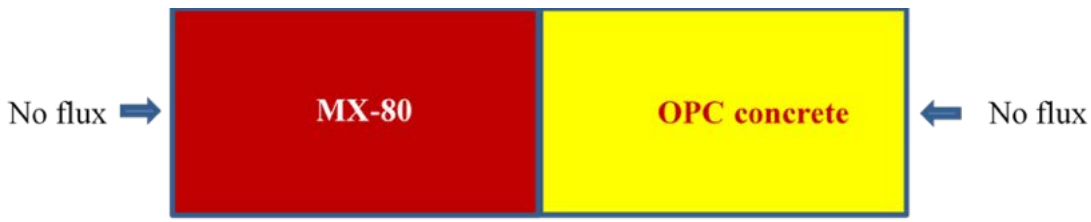

Figure 7-1. A benchmark model for Subtask A.

Subtask B focuses on the interaction between MX-80 and low pH OPC. Because high pH of OPC might lead to undesirable alteration of bentonite, usage of low pH OPC has been proposed. The specification of Subtask B will be the same as that of Subtask A. Conceptually, subtasks A and B correspond to a scenario that concrete is used as backfill material or plugs within the emplacement tunnel, as exemplified in Figure 7-2.

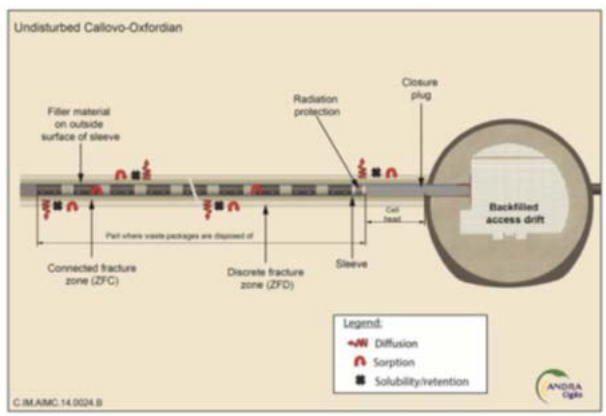

Figure 7-2. Schematic diagram of the HLW disposal cells for HLW waste packages (ANDRA, 2005)

Subtask C is designed to simulate a scenario that concrete is a liner in the emplacement tunnel (Figure 7-3), especially for argillite rock that is less indurated, in which case the GW from the host rock will infiltrate through the concrete liner and then into the bentonite buffer. The benchmark case Subtask C specifies the following conditions:

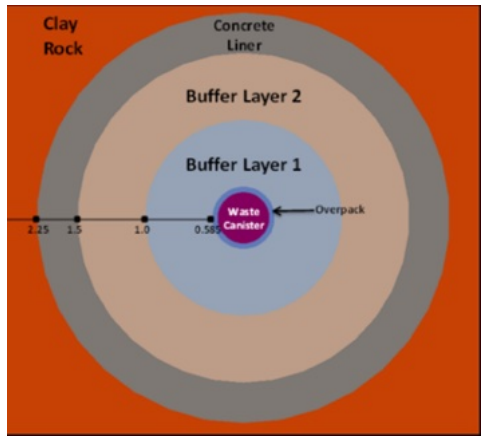

Figure 7-3. Schematic diagram of two-clay buffer layer EBS (Zheng et al., 2014)

(1). An isothermal system (25ºC) consisting of aged OPC concrete and MX-80 bentonite,

(2). Initially, bentonite is unsaturated, but OPC is fully saturated,

(3). Atmospheric pressure is 0.1 MPa.

(4). Water inflow from the concrete side will be prescribed with constant pressure, the pressure level hasn't been decided yet.

The bentonite-to-concrete volume ratio is assumed to be one, i.e., in a 1D model equally long domains (of 1 m each) are considered.

Figure 7-4. The schematic design of subtask C (Zheng et al., 2014).

7.3 Model Development

7.3.1 Initial Conditions

Mineralogical alteration of bentonite and concrete around the bentonite/concrete interface could be induced by (1) the initial disequilibrium between the porewater and minerals phase, and (2) the perturbation due to the interaction between bentonite and concrete. Because item #2 is what the current benchmark in task 12 is aiming for, it is critical to minimize initial disequilibrium between the porewater and minerals phases. Our first effort is to check the initial porewater in bentonite and concrete is close to equilibrium although a complete equilibrium between all the chemical species and minerals is not possible.

The initial mineral and exchanger composition of MX-80 is given in the Task 12 description provided by SKB (Rasmusson, 2022). Table 7-1 includes the initial mineral and exchanger composition of MX-80 according to Idiart et al. (2020). Note that the mineralogical composition of MX-80 has been reported by other studies and it is different from what is used in Task 12. For example, Bradbury and Baeyens (2003) measured the oven-dried MX-80 sample (Table 7-2), which is different from that in Table 7-1. The initial porewater composition of MX-80 is calculated by equilibrating the minerals and exchanger with GW at the Äspö hard rock laboratory (Svemar et al., 2016). The GW composition is listed in Table 7-3.

Table 7-1 Initial mineral and exchanger composition of MX-80 (Idiat et al., 2020)

Primary minerals	Weight (%)
Calcite (siderite included)	1
Gypsum	1
Montmorillonite	84
Illite	4
Quartz (cristobalite included)	4
Feldspar	4
Exchanger composition[a]	**Log K**
NaX	0
CaX_2	0.4
KX	0.6
MgX_2	0.34

Table 7-2 Mineral composition of oven-dried MX-80 (Bradbury & Baeyens, 2003)

Mineral	wt.%
Montmorillonite	75
Kaolinite	<1
Mica	<1
Quartz	15.2
Feldspar	5-8
Calcite	0.7
Siderite	0.7
Pyrite	0.3
Organic carbon	0.4

Table 7-3 Initial mineral and exchanger composition of MX-80 (Idiat et al., 2020)

	Groundwater
Temperature (°C)	25[a]
pH	7.05
pe	-2.83
Solutes	**Concentration (M)**
Alk. (HCO_3^-)	2.20×10^{-3}
Cl	1.39×10^{-1}
SO_4^{2-}	6.80×10^{-3}
Ca	2.33×10^{-2}
Na	8.88×10^{-2}
K	8.75×10^{-4}
Mg	9.30×10^{-3}
Fe	3.31×10^{-5}
Si	1.85×10^{-4}

[a]15°C in the original source.

Because of the slow reaction rate of Al-Si minerals, the porewater in bentonite is not expected to be in equilibrium with these minerals. The initial porewater is calculated by equilibrating with only calcite, gypsum, calcite, and phillipsite. SKB used Phreeqc to calculate the initial porewater composition, whereas LBNL has used TOUGHREACT. Table 7-4 shows the porewater calculated by both organizations. Also shown in Table 7-4 is a case without using phillipsite to equilibrate the GW because it is questionable whether phillipsite exists in the MX-80. There are noticeable differences in concentrations of all cations, which is caused by different methods of how Phreeqc and TOUGHREACT handle exchangers in the speciation calculation. In Phreeqc, exchangers are part of the mass balance and constrain the aqueous concentration of cations. In TOUGHREACT, exchangers won't constrain the aqueous concentration initially, instead, aqueous concentration is calculated from the mass balance with minerals, and exchangers will be "loaded" based on the CEC and their selectivities. After a discussion within the Task 12 modeling team, the porewater composition (column 1) calculated by SKB will be used for Subtasks A and B.

Table 7-4. Calculated initial porewater composition for MX-80 by SKB and LBNL

Species	SKB (table) [mol/L]	SKB (calculation w/a philipsite) [mol/L]	LBNL	GW SKB (table) [mol/L]
Na	2.30E-01	2.29E-01	1.01E-01	8.88E-02
Ca	1.40E-02	1.37E-02	3.16E-02	2.33E-02
Mg	6.90E-03	6.89E-03	1.35E-02	9.30E-03
K	1.50E-03	1.46E-03	1.02E-03	8.75E-04
S(6)	6.50E-02	6.50E-02	2.56E-02	6.80E-03
Cl	1.40E-04	1.39E-01	1.39E-01	1.39E-01
Si	1.80E-04	1.81E-04	1.82E-04	1.85E-04
C(4)	2.30E-03	2.30E-03	1.38E-03	2.20E-03
Al	6.90E-10	0	8.50E-09	0
Fe	0	0		3.31E-05
I_s	0.285	0.285		
pH	7.33	7.33	7.09	
pe	-	10.97		
Primary minerals	**Mineral** ***SI***	**Mineral** ***SI***	**Mineral** ***SI***	
	Calcite 0.0	Calcite 0.0	Calcite 0.0	
	Gypsum 0.0	Gypsum 0.0	Gypsum 0.0	
	Philipsite_Na 0.0	Quartz 0.0	Quartz 0.0	
	Quartz 0.0		Philipsite_Na 0.0	

The porewater in OPC is calculated by minerals of the hydrate assemblage (Table 7-5) with pure water. Because SKB used Phreeqc and LBNL used TOUGHREACT to do calculations, there are significant differences in the concentrations of K and Na, which can be attributed to how both codes handle exchangers in the speciation calculation. Because none of the minerals in the hydrate assemblage contain K and Na, mixing with pure water won't release any K and Na into the porewater, which is why the concentration of K and Na in the LBNL calculation is very low. On the contrary, the SKB calculation leads to high K and Na concentrations, because high K and Na concentrations are needed to balance with exchangers. However, it is practically unlikely that the porewater in OPC has high K and Na concentrations.

Table 7-5. Suggested mineralogical phase assemblage and exchanger composition of the OPC concrete (Rasmusson, 2022)

		OPC concrete		
Primary minerals		**Concentration (mol/L$_{medium}$)**	**Concentration (M)**	**Volume fraction (-)**
Portlandite		1.274	11.58	0.043
C3AH6		0.142	1.293	0.022
CSH 1.6		1.223	11.12	0.106
Hydrotalcite OH		0.015	0.138	0.003
Monocarboaluminate		0.031	0.286	0.009
Ettringite		0.032	0.291	0.023
Porosity				0.110
Inert mineral volume				0.683
Exchanger composition[a]	**Log K**			**Equiv. conc. (%)**
$CaXa_2$	0	0.0487	0.4424	78
K_2Xa_2	-2.6	0.0117	0.1060	19
Na_2Xa_2	-1.8	0.0020	0.0185	3

Table 7-6. Calculated initial porewater composition for OPC (Rasmusson, 2022)

Species	SKB (table) [mol/L]	SKB (calculation w/a Philipsite) [mol/L]	LBNL
Na	3.50E-02	3.49E-02	1.00E-10
Ca	1.60E-03	1.65E-03	2.06E-02
Mg	5.40E-10	5.41E-10	2.78E-09
K	2.10E-01	2.07E-01	1.05E-09
S(6)	4.20E-04	4.17E-04	6.87E-06
Cl	0	0	0
Si	4.20E-05	4.24E-05	6.05E-05
C(4)	2.00E-06	1.98E-06	2.28E-07
Al	2.80E-04	2.79E-04	2.67E-04
Fe	0	0	0
I_s	0.236	0.236	0.05392
pH	13.2	13.22	12.466
pe	-	5.39	
Primary minerals	**Mineral / *SI***	**Mineral / *SI***	**Mineral / *SI***
	C3AH6 0.0	C3AH6 0.0	C3AH6 0.0
	CSH1.6 0.0	CSH1.6 0.0	CSH1.6 0.0
	Ettringite 0.0	Ettringite 0.0	Ettringite 0.0
	Hydrotalcite 0.0	Hydrotalcite 0.0	Hydrotalcite 0.0
	Monocarboaluminate 0.0	Monocarboaluminate 0.0	Monocarboaluminate 0.0
	Portlandite 0.0	Portlandite 0.0	Portlandite 0.0

The initial pore water for low pH OPC is calculated with minerals in the hydrate assemblage listed in Table 7-7 and pure water. Like for the case of OPC, the SKB and LBNL calculated concentrations of K and Na in the porewater for low pH OPC differ significantly because of different ways of using exchangers by Phreeqc and TOUGHREACT in calculating the initial speciation.

Table 7-7. Suggested mineralogical phase assemblage and exchanger compositions of the low pH OPC concrete (Rasmusson, 2022).

Low-pH concrete				
Primary minerals		**Concentration (mol/L_{medium})**	**Concentration (M)**	**Volume fraction (-)**
SiO_2(am)		0.321	2.470	0.013
Katoite		0.061	0.465	0.013
CSH 0.8		1.385	10.65	0.124
Hydrotalcite OH		0.005	0.041	0.002
Thaumasite		0.006	0.042	0.005
Ettringite		0.011	0.086	0.012
Porosity				0.13
Inert mineral volume				0.7
Exchanger composition[a]	**Log K**			**Equiv. conc (%)**
$CaXa_2$	0	2.028×10^{-2}	1.560×10^{-1}	95
K_2Xa_2	-2.6	9.324×10^{-4}	7.172×10^{-3}	4
Na_2Xa_2	-1.8	1.620×10^{-4}	1.246×10^{-3}	1

Table 7-8. Calculated initial porewater composition for OPC (Rasmusson, 2022).

Species	SKB (table) [mol/L]		SKB (calculation w/a Philipsite) [mol/L]		LBNL	
Na	1.80E-02		1.83E-02		1.00E-10	
Ca	1.50E-03		1.45E-03		2.88E-02	
Mg	5.40E-10		6.59E-08		1.88E-06	
K	1.10E-01		1.07E-01		1.05E-09	
S(6)	2.90E-02		2.92E-02		8.06E-04	
Cl	0		0		1.00E-10	
Si	1.80E-02		1.80E-02		5.82E-03	
C(4)	3.00E-06		2.98E-06		3.91E-06	
Al	5.40E-02		5.36E-02		5.50E-02	
Fe	0		0		0	
I_s	0.143		0.143		0.08548	
pH	10.3		10.34		9.48	
pe	-		8.13			
Primary minerals	**Mineral**	***SI***	**Mineral**	***SI***	**Mineral**	***SI***
	CSH0.8	0.0	CSH0.8	0.0	CSH0.8	0.0
	Ettringite	0.0	Ettringite	0.0	Ettringite	0.0
	Hydrotalcite	0.0	Hydrotalcite	0.0	Hydrotalcite	0.0
	Katoite	0.0	Katoite	0.0	Katoite	0.0
	SiO2(am)	0.0	SiO2(am)	0.0	SiO2(am)	0.0
	Thaumasite	0.0	Thaumasite	0.0	Thaumasite	0.0

In summary, the porewater composition provided by SKB differs from that calculated by LBNL. However, to perform modeling be consistent with other teams, the LBNL model is based on the SKB calculated. Note that the initial composition of water for OPC and LPC is questionable, in particular the high concentrations of K and Na. Equilibrating minerals in OPC and LPC with pure water is also debatable, because, as shown in Figure 7-2, OPC/LPC will be hydrated by GW from the host rock instead of pure water. Subtasks A and B are therefore expanded to account for different ways of calculating initial water to evaluate the uncertainties caused by the initial water:

- Subtask A1: it is the original Subtask A, in which the initial porewater of OPC is equilibrated with pure water and exchangers;
- Subtask A2: it is similar to subtask A1, but the initial porewater of OPC is equilibrated with groundwater, and exchangers are considered;
- Subtask A3: it is similar to subtask A1, but the initial porewater of OPC is equilibrated with groundwater, and exchangers are not considered;
- Similarly, subtask B is divided into three subtasks:
- Subtask B1: it is the original subtask B, in which that the initial porewater of LPC is equilibrated with pure water and exchangers are considered;
- Subtask B2: it is similar to subtask B1, but the initial porewater of LPC is equilibrated with groundwater, and exchangers are considered;
- Subtask B3: it is similar to subtask B1, but the initial porewater of LPC is equilibrated with groundwater, and exchangers are not considered.

Up to now, LBNL scientists have worked on Subtasks A1 and A3.

7.3.2 Thermodynamic and Kinetic Data

Benchmarking a reactive transport model can be very challenging, because many aspects of developing the model can cause differences in model results. The first aspect is the thermodynamic data. Because Task 12 modeling groups are using different codes and the format of the database required for the code are different, it is difficult for all groups to use the same database. Eventually, LBNL has chosen to use a database that is largely based on data0.dat.YMPv4.0, database that was qualified by the U.S. DOE for the Yucca Mountain project. However, the thermodynamic data for minerals in OPC are taken from a database called "ThermoChimie_v11a" (https://www.thermochimie-tdb.com/), which is a thermodynamic database initially created and developed by Andra (French National Radioactive Waste Management Agency). The SKB and SURAU group are also using this database.

Another aspect that can lead to different modeling results is the kinetic rate for mineral dissolution/precipitation. In this report, we are using TOUGHREACT V3.32 to conduct all the simulations. In the code, mineral dissolution/precipitation can be specified as equilibrium-controlled or kinetically controlled. When the initial porewater is calculated (e.g., Table 7-4), the controlling minerals phase is calculated as equilibrium, but in the simulations presented in the next sections, kinetically controlled mineral dissolution/precipitation is used for all the minerals. The kinetic law for mineral dissolution/precipitation is given by Xu et al. (2011):

$$r=kA|1-〖(K/Q)〗^{\theta}|^{\eta} \qquad \textbf{Eq. (7-1)}$$

where r is the kinetic rate, k is the rate constant (mol/m2/s), which is temperature dependent, A is the reactive surface area per kg water, and K is the equilibrium constant for the mineral–water reaction written for the destruction of one mole of mineral, and Q is the reaction quotient. Here, for simplicity, the exponents θ and η are assumed equal to 1.

The kinetic rate constants can usually be summed for three mechanisms: neutral, acid, and base (Lasaga et al., 1994):

$$k = k_{25}^{nu} \exp\left[\frac{-E_a^{nu}}{R}\left(\frac{1}{T}-\frac{1}{198.15}\right)\right] + k_{25}^{H} \exp\left[\frac{-E_a^{H}}{R}\left(\frac{1}{T}-\frac{1}{198.15}\right)\right]\alpha_H^{n_H} + k_{25}^{OH} \exp\left[\frac{-E_a^{OH}}{R}\left(\frac{1}{T}-\frac{1}{198.15}\right)\right]\alpha_H^{n_{OH}} \quad \textbf{Eq. (7-2)}$$

where subscripts nu, H, and OH indicate neutral, acid, and base mechanisms, respectively, E is the activation energy, k25 is the rate constant at 25 °C, R is the gas constant, T is the absolute temperature, a is the activity of the species, and n is a power term (constant). It should be noted that reaction rates depend on the reactive surface area A in Eq. (7-1), which is a function of the product of the specific surface area and the volume fraction of each mineral. Therefore, the calibrated values of specific surface area and volume fraction of calcite should be viewed as arbitrary and non-unique (co-linearly varying) values, the product of which being of relevance but not each value separately.

The kinetic rates and surface areas for the minerals is the most uncertain aspect of reactive transport modeling, because the kinetic rate can vary up to five orders of magnitude depending on the scale of measurements or calibration (Zhu, 2005). Also, the reactive surface area, i.e., the area of a mineral phase in the assemblage that is exposed the pore water, is not accurately calculated. To focus on the effect of chemicals on the reaction paths of minerals in the OPC and MX-80, a kinetic constant of 7e-9 mol/m2/s, a surface area of 0.3 m2/g, and an activation energy of 105 KJ/mol were used for all the minerals (Table 7-9). These values are quite arbitrary, and somewhere between the kinetic rate for very soluble minerals like calcite and gypsum and very slow-reacting minerals like quartz.

Table 7-9. The kinetic rate for the primary and secondary minerals in OPC.

Mineral	A (cm^2/g)	Parameters for Kinetic Rate Law	
		Neutral Mechanism	
		k_{25} ($mol/m^2/s$)	E_a (KJ/mol)
Primary minerals			
Portlandite	0.3	7×10^{-9}	105
C3AH6	0.3	7×10^{-9}	105
Hydrotalcite	0.3	7×10^{-9}	105
CSH1.6	0.3	7×10^{-9}	105
Monocarboaluminate	0.3	7×10^{-9}	105
Ettringite	0.3	7×10^{-9}	105
Secondary minerals			
calcite	0.3	7×10^{-9}	105
quartz	0.3	7×10^{-9}	105
k-feldspar	0.3	7×10^{-9}	105
albite	0.3	7×10^{-9}	105
muscovite	0.3	7×10^{-9}	105
gypsum	0.3	7×10^{-9}	105
brucite	0.3	7×10^{-9}	105
CSH0.8	0.3	7×10^{-9}	105

The illitization is always a primary concern when bentonite undergoes mineral alteration. In this report, we used the illitization rate (the rate of illite precipitation and montmorillonite dissolution) that was calibrated in previous works (Liu et al., 2013). We also applied the rate for illite and montmorillonite for other Al-Si minerals. For the rest of the minerals the kinetic rate is taken from the previous model for bentonite (Zheng et al., 2017).

Table 7-10. The kinetic rate for the primary and secondary minerals in MX-80.

Mineral	A (cm^2/g)	Parameters for Kinetic Rate Law	
		Neutral Mechanism	
		k_{25} ($mol/m^2/s$)	E_a (KJ/mol)
Primary minerals			
gypsum	0.3	1.5×10^{-5}	105
calcite	0.3	1.5×10^{-5}	105
illite	151.6	1.3×10^{-13}	105
montmorillonite	151.6	1.3×10^{-13}	105
k-feldspar	9.8	1.3×10^{-13}	105
quartz	9.8	1.3×10^{-13}	105
Secondary minerals			
cristobalite	9.8	1.3×10^{-13}	105
kaolinite	151.6	1.3×10^{-13}	105
dolomite	9.8	2.9×10^{-8}	105
albite	9.8	1.3×10^{-13}	105
muscovite	9.8	1.3×10^{-13}	105

Table 7-11. The kinetic rate for the primary and secondary minerals in LPC

Mineral	A (cm^2/g)	Parameters for Kinetic Rate Law	
		Neutral Mechanism	
		k_{25} ($mol/m^2/s$)	E_a (KJ/mol)
Primary minerals			
Thaumasite	0.3	7×10^{-9}	105
Ettringite	0.3	7×10^{-9}	105
Hydrotalcite	0.3	7×10^{-9}	105
Katoite	0.3	7×10^{-9}	105
CSH0.8	0.3	7×10^{-9}	105
sio2(am)	0.3	7×10^{-9}	105
Secondary minerals			
calcite	0.3	7×10^{-9}	105
quartz	0.3	7×10^{-9}	105
k-feldspar	0.3	7×10^{-9}	105
albite	0.3	7×10^{-9}	105
muscovite	0.3	7×10^{-9}	105
gypsum	0.3	7×10^{-9}	105
brucite	0.3	7×10^{-9}	105
CSH1.6	0.3	7×10^{-9}	105

7.3.3 Model Setup

For the Task 12 simulations, we designed a 1-D reactive transport model to simulate the interaction between bentonite and concrete. The model extends 50 cm on each side and no-flux boundary conditions are imposed such that there is only diffusive flux across the interface. The model is intended to run for 100,000 years. The porosity is 0.111 for OPC, 0.13 for LPC, and 0.423 for MX-80, and it remains constant with time, because the change of porosity due to mineral precipitation/dissolution is neglected. The effective diffusion coefficient is assumed to be 2×10-10 m2/s, and the effects of porosity change, and tortuosity are disabled. The model considered aqueous complexation, mineral dissolution/precipitation, and cation exchange. Modeling was performed using the mineral composition and saturation index of the FEBEX bentonite.

7.4 Model Results

7.4.1 Subtask A1

As aforementioned, the mineralogical changes could be induced by both initial disequilibrium within OPC and MX-80 and the interaction between OPC and MX-80. It is therefore important to examine the initial minerals saturation index. The primary minerals for the OPC are portlandite (Ca(OH)2), C3AH6(Ca3Al2(OH)12), Hydrotalcite (Mg4Al2(OH)13·(H2O)3), CSH1.6((CaO)1.6 (SiO2) (H2O) 0.58), Monocarboaluminate (CaO)4Al3·(H2O)9.68, Ettringite ((CaO)6Al3(SO4)3·(H2O)9.68, and

their volume fractions are given in Table 7-5. The porewater provided by SKB is close to equilibrium with portlandite and is undersaturated with respect to all other minerals (Table 7-12), indicating the dissolution of these minerals will occur even if the system is not disturbed by the interaction with bentonite.

The primary minerals for the MX-80 are calcite (Ca(CO3)2), gypsum (CaSO4), montmorillonite (Ca0.17(Si4O10)(Al1.66Mg0.34)(OH)2), illite K0.75 (Al1.75Mg0.25)(OH)2(Si3.5Al0.5)O10, quartz (SiO2), and felspar (KAlSi3O8). The initial porewater is slightly undersaturated with respect to gypsum and quartz, slightly oversaturated with respect to calcite, but remarkably undersaturated with respect to illite and montmorillonite (Table 7-12). There might be a dissolution of both illite and montmorillonite without interacting with concrete.

Table 7-12. The saturation index (log (Q/K) for the initial pore water of OPC and MX-80.

Minerals	OPC	MX-80
monocarboaluminate	-1.46198	-31.67361
hydrotalcite	-1.2235	-16.07865
c3ah6	-1.53282	-33.35196
portlandite	0.01552	-10.48706
ettringite	-1.35563	-23.67271
csh1.6	-0.45281	-12.18416
csh0.8	-1.76324	-5.09177
gypsum	-3.25215	-0.06377
calcite	-1.47374	0.14853
illite	-17.14311	-5.42101
kaolinite	-13.56971	-3.73883
montmorillonite	-20.34901	-3.33258
quartz	-5.22875	-0.15919
k-feldspar	-9.3542	-2.23544
dolomite	-9.03674	1.07681
albite	-12.92118	-2.82488
anorthite	-11.37748	-12.03972
anhydrite	-3.42778	-0.23309
cristobalite	-5.51837	-0.44881
sepiolite	-22.04341	-6.1698
brucite	-1.54855	-5.18212
muscovite	-12.64152	-5.82785

The driving force for the interaction between OPC and MX-80 is the concentration gradients across the interface, which is assumed to be purely diffusive in Subtask A1, because there is no pressure gradient on both sides. Because of the large contrast of Mg concentration, the simulation was very slow and haven't run to the target simulation time of 100,000 years. Here we only report the results up to 1000 years. Because Cl is only affected by aqueous complexation, it is largely viewed as a conservative species here. Its concentration profile (Figure 7-5) is a marker of the diffusion process for both OPC and MX-80. This figure shows that the OPC undergoes an increase in Cl concentration and MX-80 experience a decrease in

concentration, after about 100 years, and a stable concentration profile is formed. All other species are affected by both diffusion and chemical reactions, their profile may look quite different from that of Cl, indicating chemical reactions dominate the tempo-spatial evolution (e.g., the C concentration profile shown in Figure 7-5; Al and Si in Figure 7-7) or somewhat similar to that Cl, meaning diffusion is still playing a major role in shaping the temporal-spatial evolution such as K profile in Figure 7-6. Some species have a profile that is controlled by chemical reactions in the early time, but dominated by diffusion later time such as S, suggesting chemical reactions occurred in the early time. pH in MX-80 increased significantly over time and after 10 years the profile maintains almost the same level at the entire length of bentonite.

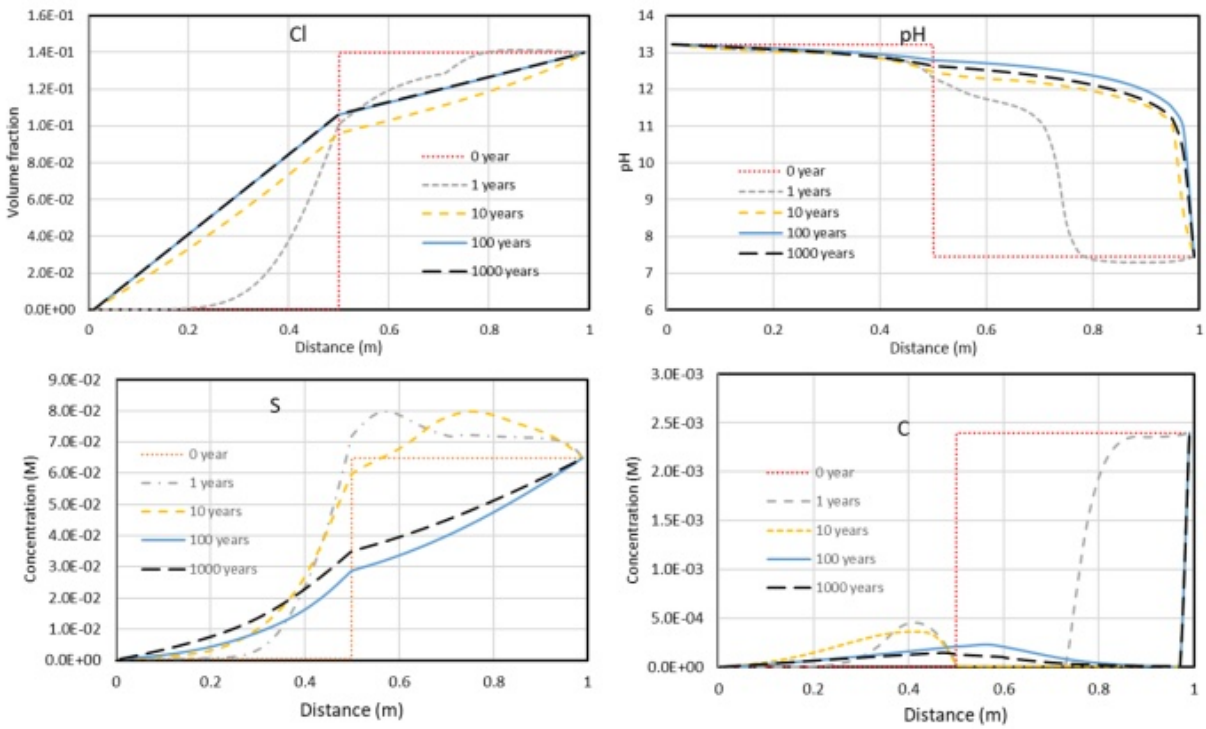

Figure 7-5. The concentration profiles of Cl, pH, C, and S at different times. The interface is located at a distance of 0.5m.

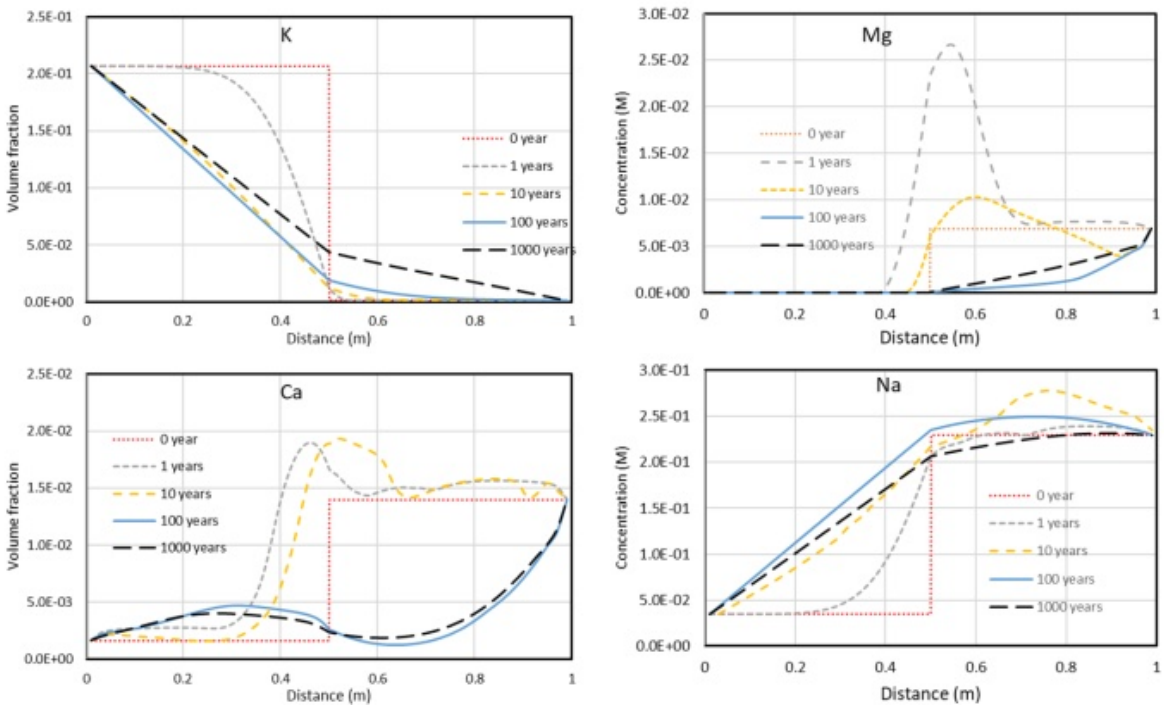

Figure 7-6 The concentration profiles of K, Na, Ca, and Mg at several times. The interface is located at a distance of 0.5m.

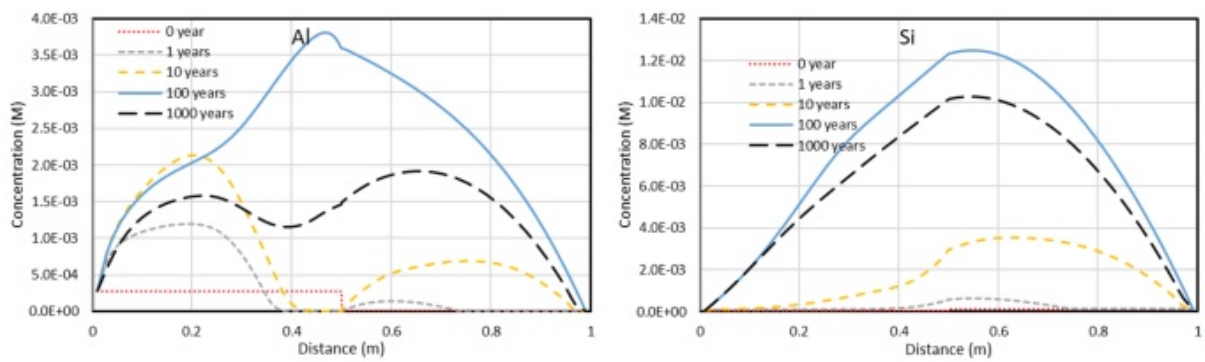

Figure 7-7 The concentration profiles of Si and Al at different times. The interface is located at a distance of 0.5m.

In OPC, as the pH decreases (Figure 7-5), portlandite, C3AH6, and monocarboaluminate dissolve (Figure 7-8), which leads to the increase in Ca concentration in the early times (Figure 7-6), CSH that is hardly affected by pH, has remained unchanged with time.

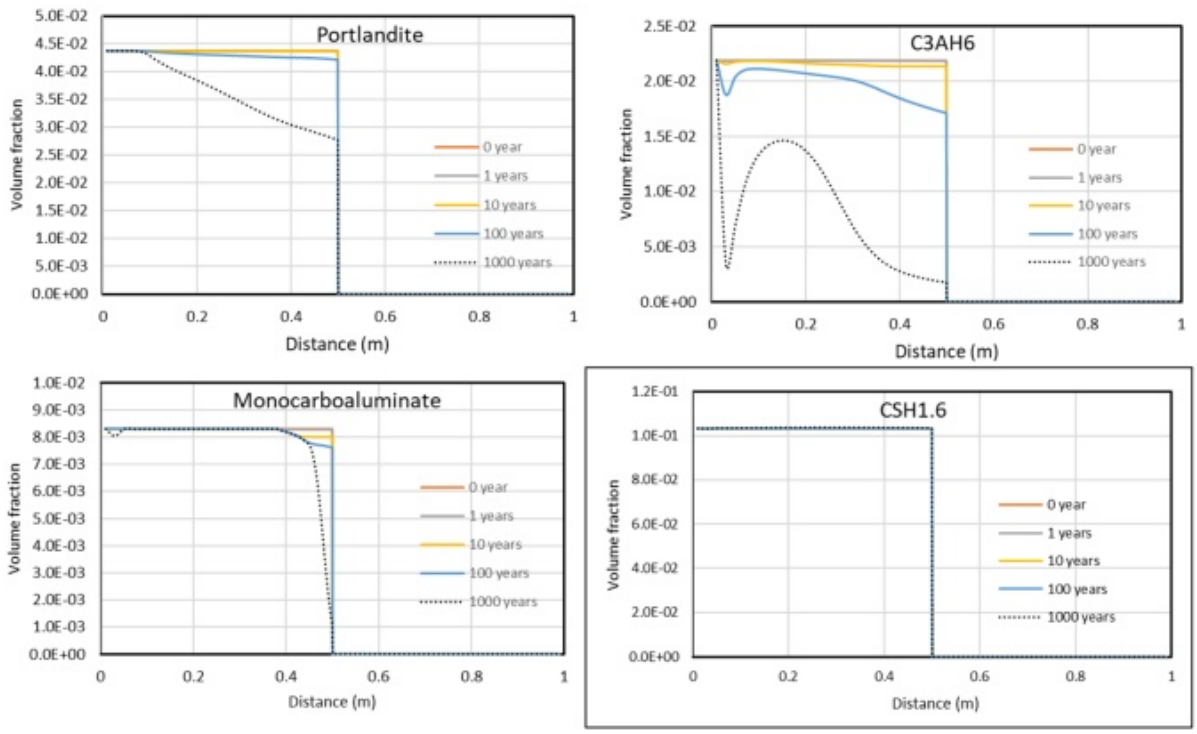

Figure 7-8. The volume fraction of portlandite, C2AH6, monocarboaluminate and CSH at several times.

Because of the dissolution of gypsum in MX-80 and a high initial concentration of S, the S concentration in OPC significantly increased (Figure 7-5), causing the precipitation of Ettringite (Figure 7-9). High Mg concentration in OPC at the vicinity of the interface causes significant precipitation of hydrotalcite (Figure 7-9)

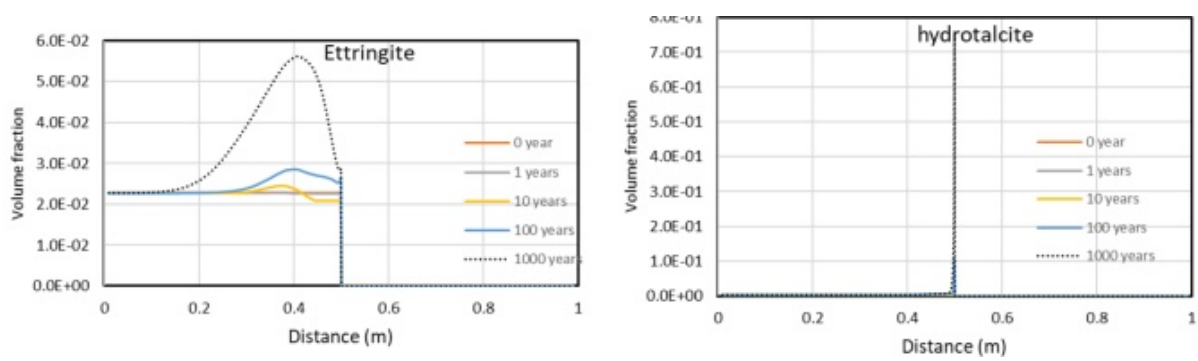

Figure 7-9. The volume fraction of ettringite and hydrotalcite at several times.

On the MX-80 side, gypsum quickly dissolves and is depleted after 10 years (Figure 7-10). Calcite starts dissolving in the early time, but the influx of Ca from the OPC leads to the precipitation of calcite near the interface area at 1,000 years (Figure 7-10).

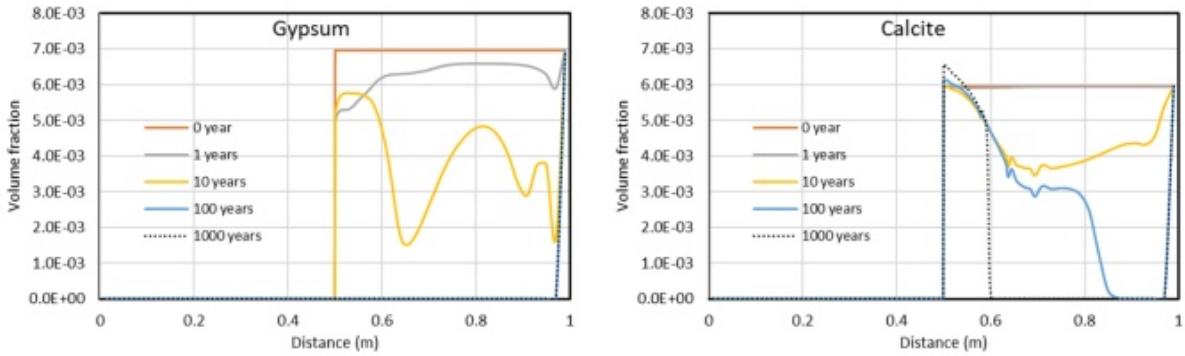

Figure 7-10. The volume fraction of gypsum and calcite at several times.

The model results show that the interaction between OPC and MX-80 does not affect the montmorillonite and illite. By 1000 years, both montmorillonite and illite dissolve slightly along the entire length of MX-80 (Figure 7-11), which is caused by the undersaturation of both minerals (Table 7-12) in the initial condition.

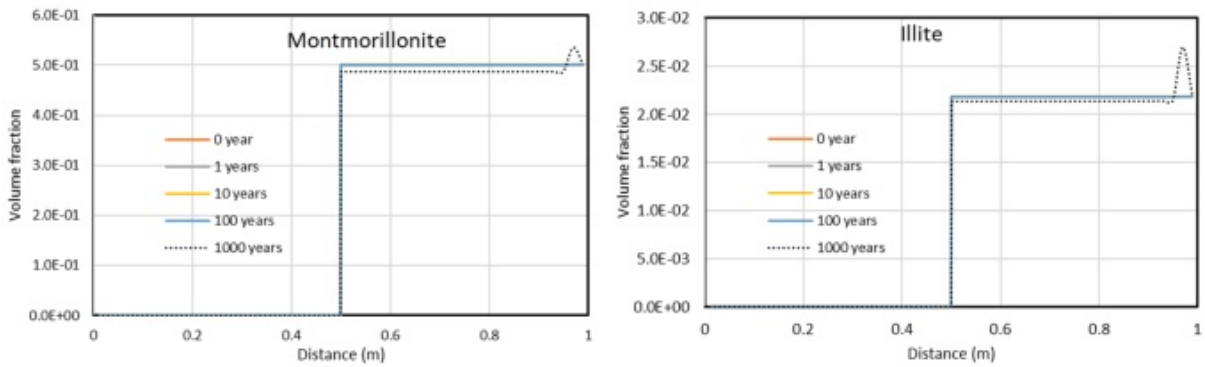

Figure 7-11. The volume fraction of montmorillonite and illite at several times.

7.4.2 Subtask A3

Contrary to Subtask A1, which showed an unusually high concentrations of K and Na (which are uncommon for OPC), in Subtask A3, we used a chemical composition of porewater, which was calculated by equilibrating with granite GW without considering the exchangers. Because granite GW has high Na and Cl concentrations, the porewater for OPC in Subtask A3 has higher Na and Cl concentrations than those in Subtask A1; because exchangers are not involved in the calculation, K concentration in Subtask A3 is lower than that in A1 (Table 7-13). Note that the pH in Subtask A3 is slightly lower than that in Subtask A1.

Table 7-13. The initial pore water composition for OPC in Subtasks A1 and A3.

Species	Subtask A1 [mol/L]	Subtask A3 [mol/L]
Na	3.50E-02	8.89E-02
Ca	1.60E-03	4.43E-03
Mg	5.40E-10	5.41E-09
K	2.10E-01	8.76E-04
S(6)	4.20E-04	9.61E-04
Cl	0	1.39E-1
Si	4.20E-05	3.22E-06
C(4)	2.00E-06	2.04E-07
Al	2.80E-04	3.87E-05
Fe	0	0
I_s	0.236	0.236
pH	13.2	12.24
pe	-	5.39

Unlike Subtask A1, where there is a significant increase in Cl in OPC, there is no concentration change of Cl in MX-80 and OPC after early time fluctuations (Figure 7-12), because MX-80 and OPC have the same initial concentration. The pH in Subtask A3 behaves similarly to that in Subtask A1: a gradual increase in MX-80 that is driven by the high pH in OPC and governed by chemical reactions (Figure 7-12). Sulfate concentration in MX-80 increased in early time (Figure 7-12) because of the dissolution of gypsum (see Figure 7-17). Carbonate concentration (Figure 7-12) is highly affected by chemical reactions on both the OPC and MX-80 sides.

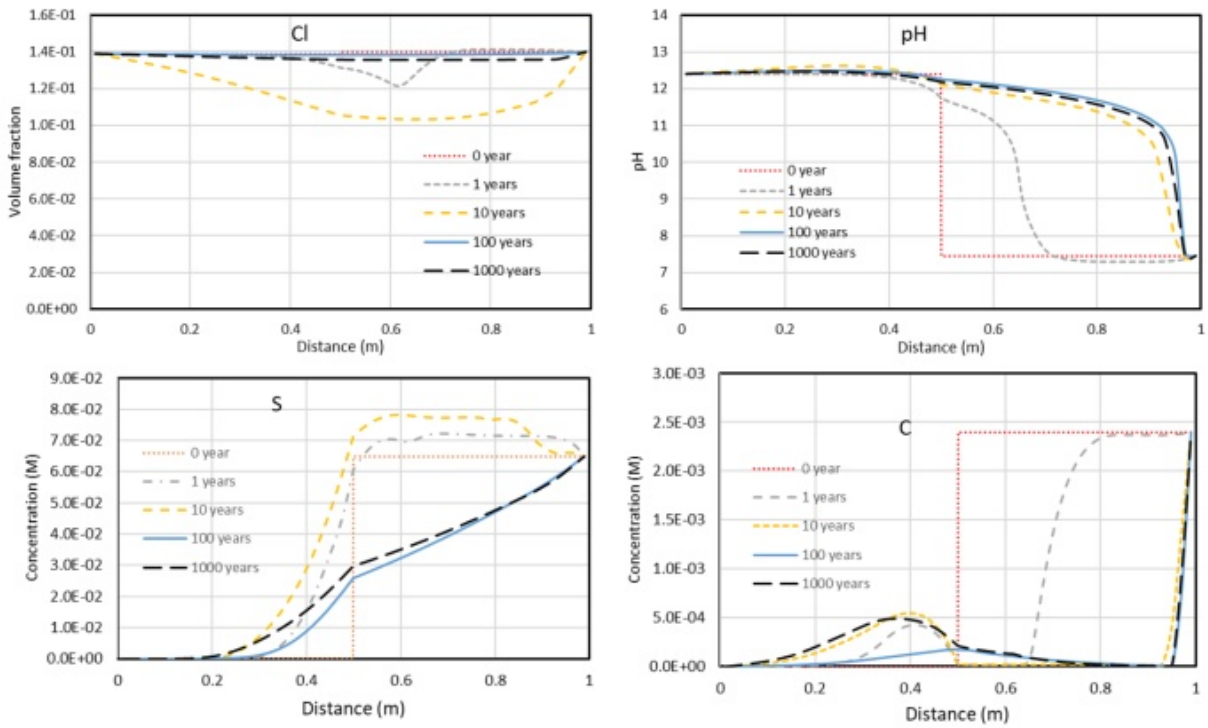

Figure 7-12 The concentration profiles at several times for Cl, pH, C, and S. The interface is located at a distance of 0.5m.

K concentration is affected by the dissolution of K-feldspar in the MX-80 in the early time, but eventually falls back close to the initial level (Figure 7-13) as neither reaction occurs in a large quantity. K in OPC is largely controlled by diffusion from MX-80. Na concentration in both OPC and MX-80 is also largely controlled by diffusion as no reactions affect its concentration. The decrease of Mg and Ca concentration in MX-80 is due to precipitation of dolomite; Ca concentration in OPC is affected by precipitation of ettringite (Figure 7-16).

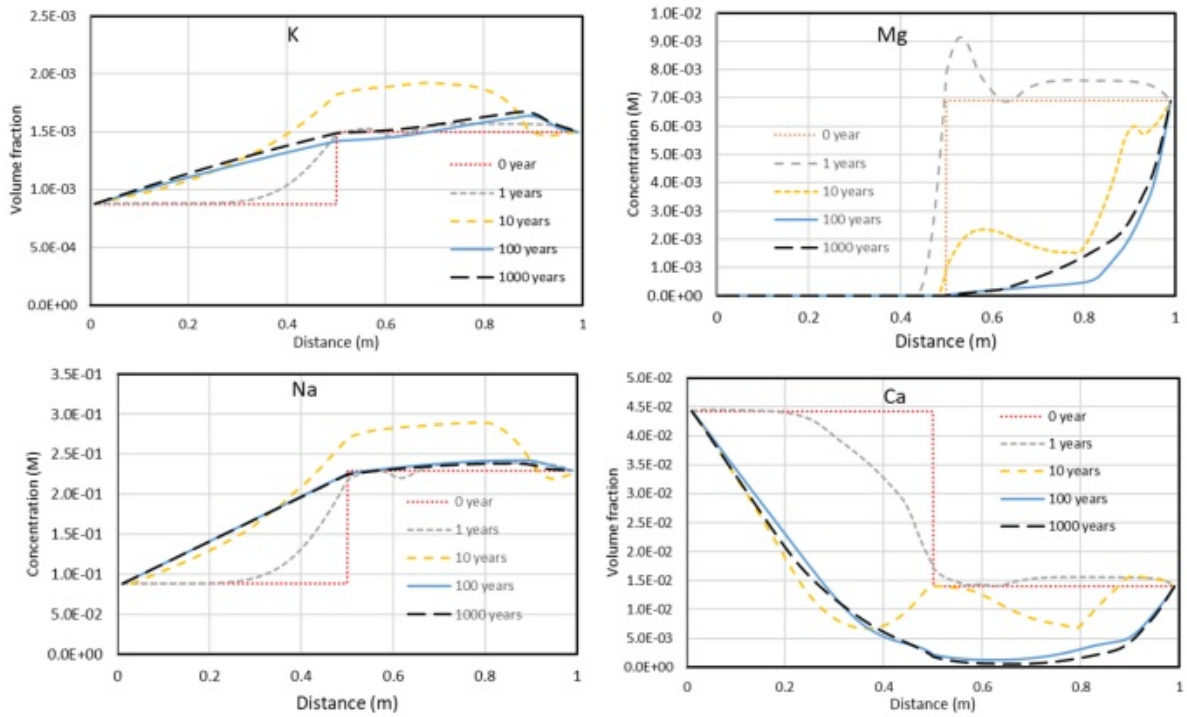

Figure 7-13 The concentration profiles at several times for K, Na, Ca, and Mg. The interface is located at a distance of 0.5m.

Si and Al concentrations significantly increased on both MX-80 and OPC (Figure 7-14) because of the dissolution of the Al-Si bearing minerals (Figure 7-15).

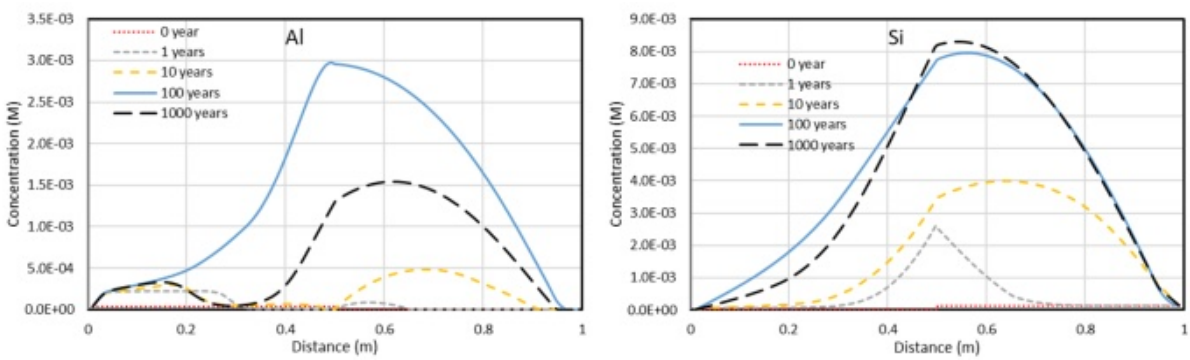

Figure 7-14 The concentration profiles at several times for Si and Al. The interface is located at a distance of 0.5m.

The mineral phase changes in OPC in Subtask A3 are similar to that in Subtask A1: as the pH decreased (Figure 7-12), portlandite, C3AH6, and monocarboaluminate dissolve, CSH that is hardly affected by pH, remained unchanged with time. Although the dissolved amount of these minerals differs, the general trend is similar. All this indicates that pH is an important factor that controls the mineral phase changes, but the difference in other species is less important.

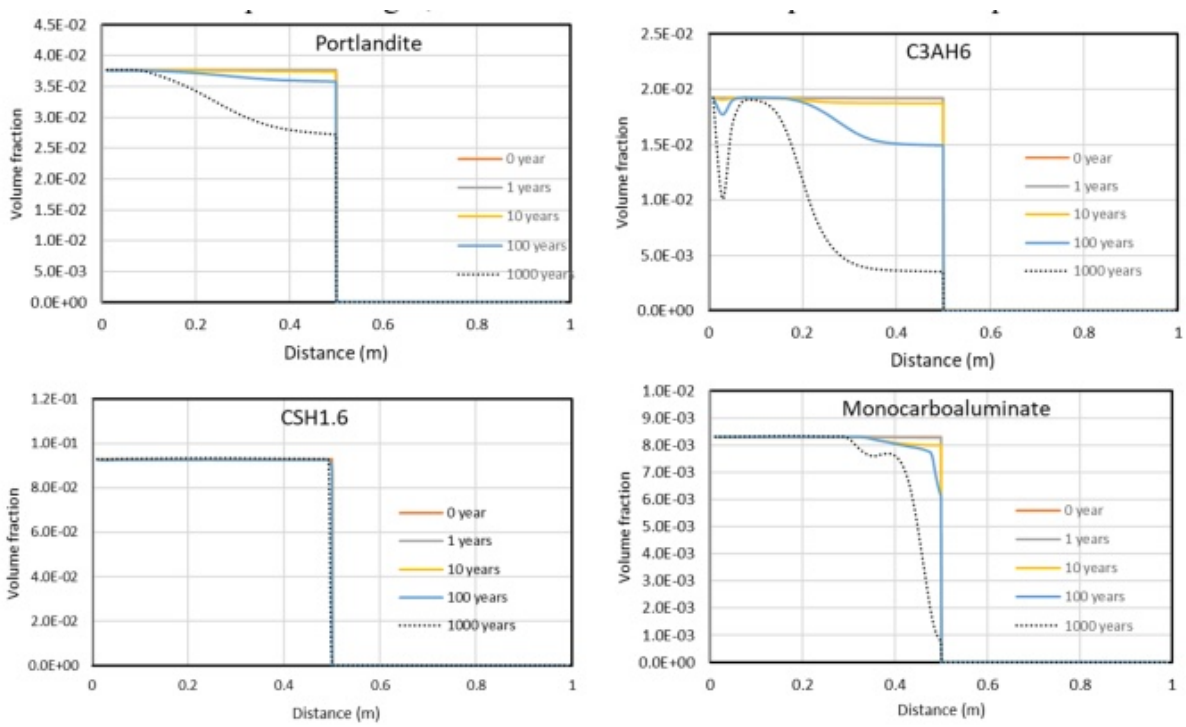

Figure 7-15 The volume fraction of portlandite, C2AH6, monocarboaluminate and CSH at several times.

Subtask A3 has similar results to Subtask A1 in terms of the behavior of Ettringite and hydrotalcite, drive the high level of S concentration in OPC (Figure 7-12) due to the dissolution of gypsum and high initial concentration of, S, in MX-80 leads to the precipitation of Ettringite (Figure 7-16). High Mg concentration in OPC at the vicinity of the interface cause significant precipitation of hydrotalcite (Figure 7-16).

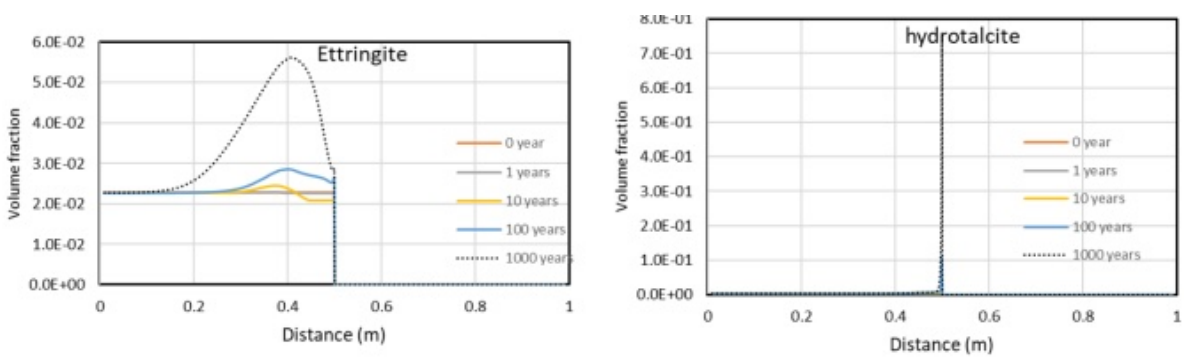

Figure 7-16. The volume fraction of ettringite and hydrotalcite at several times.

In Subtask A3, on the MX-80 side, gypsum quickly dissolved and was depleted after 10 years (Figure 7-17). Calcite started dissolving in the early time (Figure 7-17), but the influx of Ca from the OPC leads to the precipitation of calcite near the interface area at 1000 years.

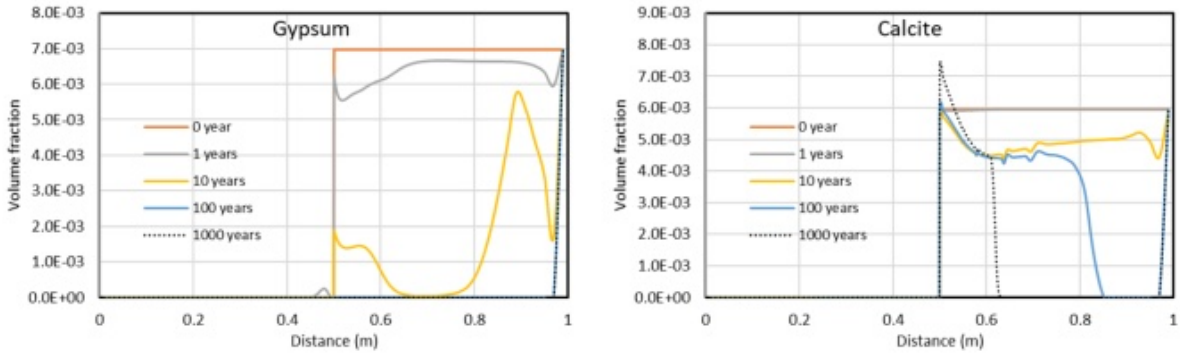

Figure 7-17. The volume fraction of gypsum and calcite at several times.

The model results show that the interaction between OPC and MX-80 does not affect the montmorillonite and illite. By 1000 years, both montmorillonite and illite are expected to dissolve slightly in the entire length of MX-80, which is caused by the undersaturation of both minerals (Figure 7-18).

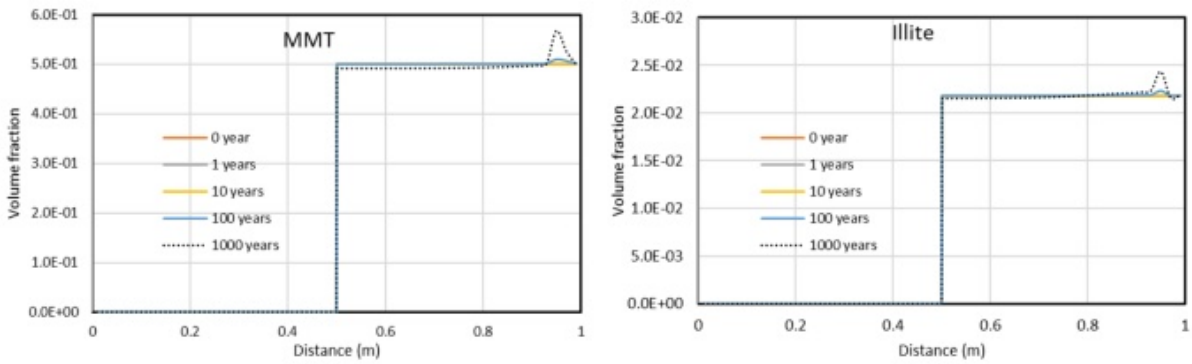

Figure 7-18. The volume fraction of montmorillonite and illite at several times.

7.5 Summary and Future Work

The geochemical change of bentonite is triggered by both the thermal perturbation and interaction between two different media, for example, canister and bentonite, bentonite and concrete liner, bentonite, and host rock (if there is no concrete liner), concrete liner and host rock. The alteration of the mineral phase around the interface area may significantly change the porosity and subsequently permeability, impacting profoundly the long-term migration of radionuclides through a bentonite buffer. Concrete has been proposed to be used as backfill material, cementitious materials are used as tunnel support (particularly for argillite host rock), mechanical plugs, backfill materials, buffer materials, and waste forms. The geochemical alteration at the interfacial area between bentonite and concrete needs to be better characterized. In Task 12 of the SKB EBS task force (Birkholzer et al., 2022), modeling teams collaboratively simulate long-term reactions occurring at cement-bentonite interfacial regions with regard to mineralogical, chemical, or textural changes. Task 12 was established in FY21 and currently has four modeling teams: SKB, Surao, LBNL, and SNL. Task 12 was divided into three subtasks: Subtask A simulates the interaction between the OPC under fully saturated conditions; Subtask B simulates the interaction between low pH OPC and MX-80 under different initial saturation conditions. This report documents LBNL's progress in Task 12. The major accomplishments and concluding remarks include:

- Benchmarking a reactive transport modeling for the concrete/bentonite interaction is very challenging, because many aspects of the model development, including database, kinetic

reaction rate, selection of aqueous complexes, and choice of secondary minerals. While the task force tried to harmonize these aspects, each team is allowed to make their choice.

- Recognizing that the mineralogical alteration could be caused by both the initial disequilibrium between porewater and mineral phase and the interaction between OPC and MX-80, checking the initial porewater is the first step for benchmarking. However, because different codes have different handling cation exchanges in the speciation calculation, the initial porewater composition for OPC, MX-80 and low pH OPC, calculated by LNBL, is different from those established by SKB. Eventually, the group decided to move on with the initial porewater composition calculated by SKB, but simulations with different initial porewater will be conducted to evaluate the effect of initial porewater on the interaction between OPC.

- In FY23, we conducted a simulation for Subtasks A1 and A3. Preliminary results in both simulations feature the following geochemical characteristics in MX-80: (1) pH increase dominates the subsequent minerals alteration; (2) significant dissolution of fast-reacting minerals like gypsum and calcite but clay minerals remain intact. In OPC, models show precipitation of ettringite and hydrotalcite and dissolution of portlandite, C3AH6, and monocarboaluminate.

In FY23, Task 12 gained significant momentum after participating organizations resumed in-person meetings and became very active. In the remaining months of FY23 and in FY24, we will continue the modeling work on Task 12. Specifically, we will:

- Finish the simulation for Subtasks A1, A2, and A3 with special attention to the change of porosity/permeability as a result of mineral dissolution/precipitation,

- Organize a group meeting to compare results of Task 12 participating teams and pinpoint the reason for the difference, as well as will establish ‘standard” practice for reactive transport modeling for bentonite.

- Finish Subtask B before the next large group for the SKB EBS task will arrive, which is scheduled in April 2024.

This page left intentionally left blank.

8. UNDERSTANDING THE THMC EVOLUTION OF BENTIONITE USING LARGE SCALE FIELD EXPERIMENTS: HOTBENT

8.1 Introduction

Compacted bentonite is the most commonly proposed buffer material for an EBS in mined geological repository for HLW. After emplacement of heat-generating waste, the bentonite buffer is expected to experience heating from the waste package and hydration from a host rock, which results in a series of thermal, hydrological, mechanical, and chemical (THMC) changes that might affect the long-term performance of bentonite buffer. These THMC processes are coupled and evolve temporally and spatially. As the temperature in the buffer increases and then decreases with time, the buffer, which is initially partially saturated, will experience desaturation followed by re-saturation and go through changes in stress due to swelling and thermal expansion. The thermal and hydrological perturbations in bentonite, and the interaction between bentonite and host rocks may lead to geochemical changes such as changes in pore water chemistry and minerals phase, which, in turn, affect the long-term stability of a bentonite buffer.

The life span of a repository is much longer than any test can run. Therefore, numerical models should be built ideally upon faithful representation of all relevant processes and formulated with parameters that are either calibrated at the scale close to the repository or measured reliably at conditions relevant to the repository. However, this is proven to be very difficult because of (1) the incapability of numerical models to capture all the relevant processes, (2) the inaccuracy of measuring those parameters by current experimental techniques, and (3) the mismatch between what models need and what experiments can measure. Over time, researchers keep expanding the modeling capability, for instance, expanding THC (Samper et al., 2008) to THMC (Zheng et al., 2010; Zheng et al., 2015), and including electrostatic potential in reactive transport model (Tournassat & Steefel, 2021) and improving experimental capability such as studying ion exchange selectivity at nano-scale using the high-resolution transmission electron microscopy at cryogenic conditions (cryo-TEM) (Whittaker et al., 2019). Before we can synergize all the latest modeling capability with thorough understanding of the key processes and parameters that can be reliably measured, model predictions based on the large-scale field test is probably still the best practice we have so far to predict the long-term evolution of a bentonite buffer. The FEBEX (Full-scale Engineered Barrier Experiment in crystalline host rock) in situ tests and the HotBENT field test and the corresponding THMC models are great examples of such practice.

LBNL/DOE joined the FEBEX-DP project in FY15. The goal is to use THMC data from FEBEX-DP to validate THMC models and, therefore, enhance our understanding of coupled THMC process. From 2015 to 2019, extensive THMC characterization of bentonite samples collected during the dismantling of Heater 2 was carried by partners of FEBEX-DP. Ion concentrations in the pore-water of bentonite were obtained via an indirect method, aqueous extract. These concentrations were used to initially constrain the chemical model. After the THMC model provided a coherent explanation of THMC data collected at the FEBEX in-situ test, we utilized the well-calibrated THMC model to conduct more exploratory simulations. The simulations conducted in the FY21 addressed the question about the long-term alteration of bentonite, up to 10,000 years under conditions similar to the FEBEX in-situ test. Because the concrete liner is part of the EBS in some design concepts, understanding the evolution of bentonite/concrete interface is critical for the long-term performance of EBS. In FY21 and FY22, we conducted a modeling effort to explain the data collected at the bentonite/concrete interface.

While bentonite behavior for temperatures at 100 °C has been well-documented based on laboratory and field experiments, data is very limited for high temperature (>100°C) conditions (Zheng et al., 2017). It is important to understand the behavior of bentonite at high temperature for the disposal of HLW to expand the knowledge base regarding the perturbation of bentonite buffer and open the possibility of designing a repository with higher thermal limits. The performance assessment of a repository requires prediction of

the long-term THMC evolution of bentonite. The reliability of model predictions is hinged on reliable constitutive laws and parameterization to describe the THMC process at scale appropriate for model parameterization for large scale model. Models for the FEBEX in situ test, (e.g., Zheng et al., 2020b), showed that parameters calibrated from modeling column tests can be used for large scale modeling. Currently, a high temperature experiment in a crystalline rock environment, called HotBENT, is being conducted under the leadership of NAGRA with several international partners (García-Siñeriz & Tuñón, 2020). This full-scale, high-temperature experiment will be conducted at the Grimsel Test Site. Such large-scale tests are extremely important for better understanding of the bentonite EBS system behavior under high temperature and conditions with strong thermal, hydraulic and density gradients. In this chapter, we give an update on the progress of field test and preliminary models for the field test.

8.2 HotBENT Project

A series of modeling studies, on the evolution of a bentonite buffer under high temperatures (up to 200 °C), showed that a bentonite buffer could sustain high heating temperatures in light of the concern of illitization and the resulting swelling stress change (e.g., Zheng et al., 2015; 2017). These studies suggested that the thermal limit for a repository of higher than 100 °C (that is commonly used in the design of repository in most countries) can significantly reduce the cost of repository. These modeling studies, along with large-scale tests, for example, HE-E heating test (Gaus et al., 2014), inspired the idea of conducting a large scale 1:1 field test on a bentonite buffer under high temperature (Vomvoris et al., 2015). This idea led the initiation of the so-called 'HotBENT' project in 2016.

After a design phase from 2017 to 2018, the construction preparatory work began at the gallery from 2018 to early 2020 (Figure 8-1). After roughly one year and half of effort, the construction of the field test was finished in August 2021, and heating started on September 9, 2021. A model platform was also established. LBNL actively participated in the project from the very beginning, including conducting scoping calculations to support the design (Zheng et al., 2017; 2018). In this section, an update is given on the development of the HotBENT project. DOE's participation in this collaborative effort is extremely beneficial; substantial cost savings would be achieved in the design of a repository, if HotBENT demonstrates that the maximum temperature of bentonite backfill can be raised without drastic performance implications.

8.2.1 Field Test Updates

The official HotBENT Project started in 2018 once all agreements with the partner institutions had been in place. In addition to DOE and NAGRA, the joint project has three full partner institutions (Surao from the Czech Republic, RWM from the United Kingdom, and NUMO from Japan) and four associated institutions (NWMO from Canada, BGR from Germany, ENRESA from Spain, and Obayashi from Japan). After the 9th partner meeting held on November 2nd, 2022, KORAD (Korea Radioactive waste agency) also joined the HotBENT Consortia. The updates in the following sections are also up to the 9th partner meeting. In the 9th partner meeting, a decision was made to extend Phase 1 to 2027, and H3 and H4 will be dismantled then.

The field test was constructed in the FEBEX gallery (drift) that starts at the northern entrance of the Grimsel Test Site (Figure 8-2). The experiment is constructed in a modular fashion, whereby a module represents a heater rested on a bentonite block pedestal and encapsulated by a granular bentonite backfill (Figure 8-3). Modules differ in their design temperature, bentonite type, experimental duration, and whether a liner is used or not. The two modules deepest in the drift are separated from the others by an insulation plug to enable excavation of part of the experiment with minimal perturbations to the remaining modules. The THM evolution of the HotBENT experiment will be monitored with ~1200 instruments, measuring parameters such as temperature, mechanical pressure, hydraulic pressure, water content, saturation, and humidity, displacements, gas concentration, and gas pressure.

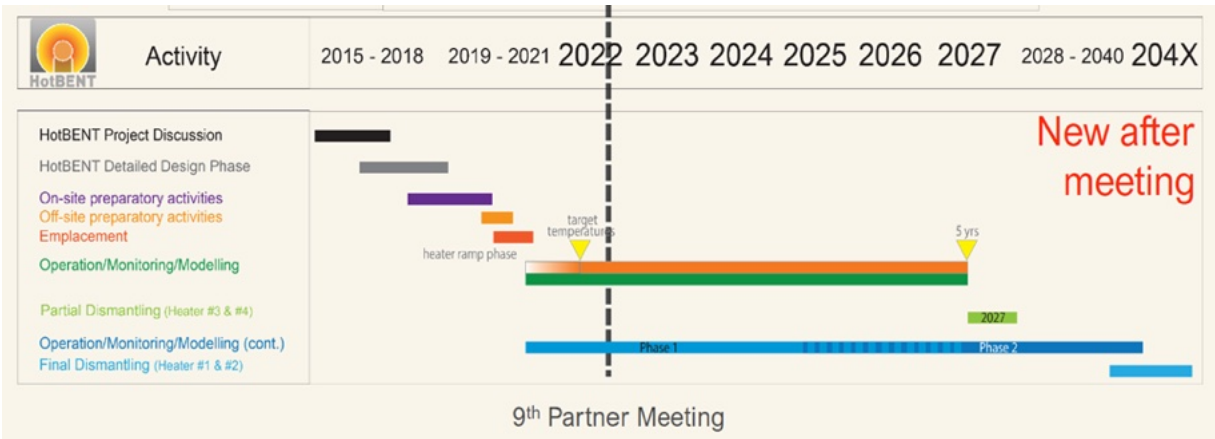

Figure 8-1. Planned timeline for HotBENT experiment (Kober & Schneeberger, 2022).

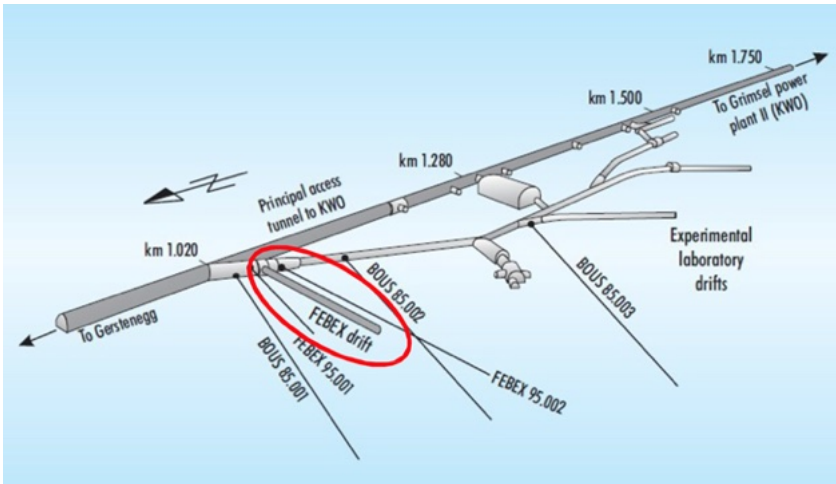

Figure 8-2. Location of the FEBEX Drift at the Grimsel Test Site (NAGRA, 2017).

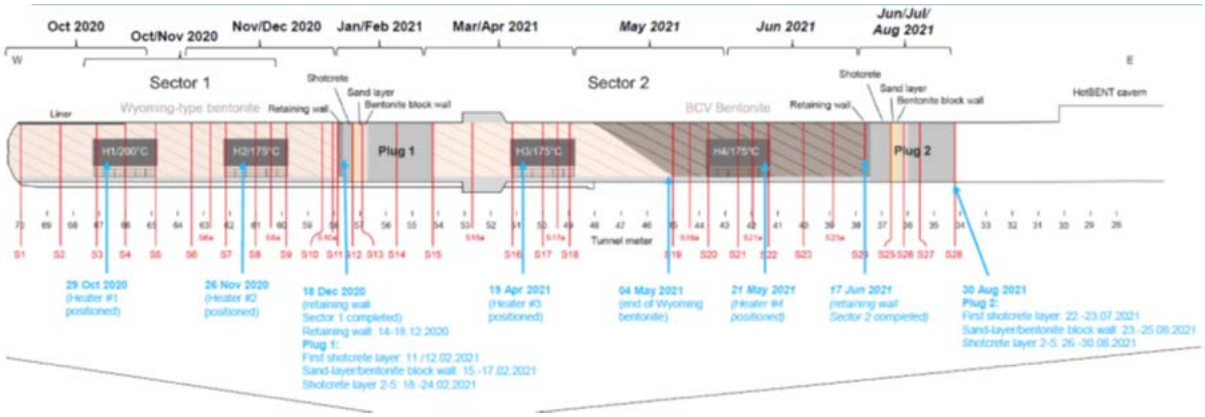

Figure 8-3. Final HotBENT design with individual modules and key construction milestones (Kober et al., 2022)

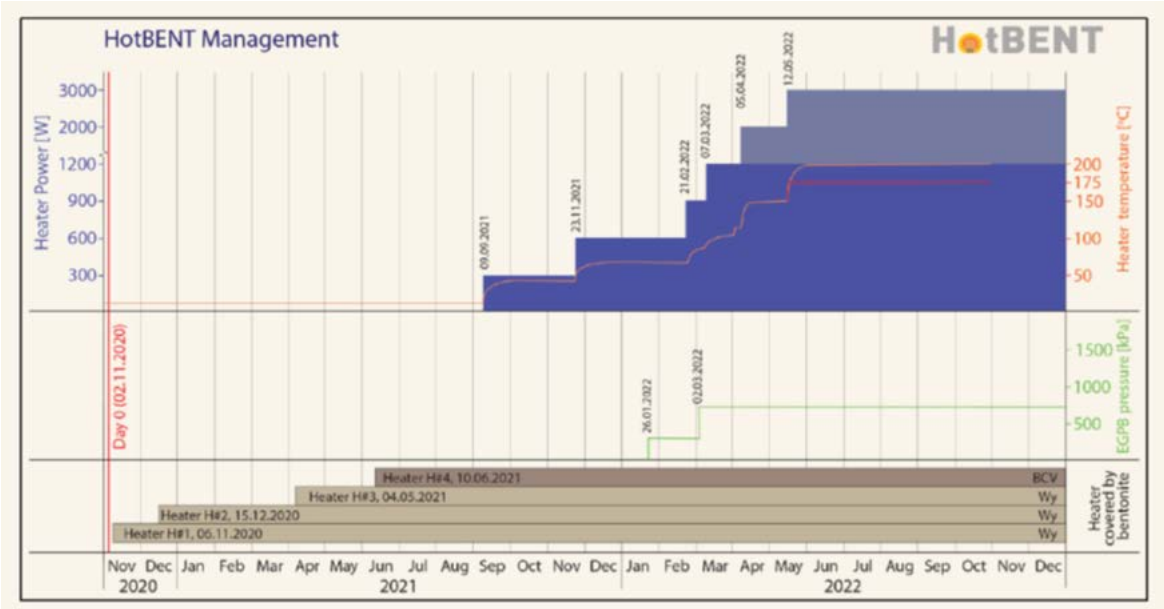

Figure 8-4. The heating procedure at HotBENT (Kober & Schneeberger, 2022).

The heating started on September 9, 2021, shortly after the construction of the second retaining wall. The plan was to increase the temperature stepwise to reach the target temperature in 4 1/2 months. However, due to the poor accessibility of the test site in winter, the heating was conducted at slower pace with close monitoring at the site. Eventually the heating was ramped up with a scheme as shown in Figure 8-4. At the time of the 9th partner meeting on November 2nd, 2022, all heaters had reached their respective target temperature.

While the heating was ramping up to the targeted temperature, sensors continued producing data. The variables that are monitored at the sites included temperature, pore pressure, relative humidity, water content, total pressure, thermal conductivity, heater displacement, plug displacement, and oxygen. A sensor layout around Heater 1 is shown in Figure 8-5. 447 temperature sensors were installed and 436 of them (98%) were still functioning at the time of the 9th partner meeting. An example of temperature measurement is given in Figure 8-6. 48 thermal conductivity sensors were installed and 42 (87.5%) were still functioning. Figure 8-7 shows thermal conductivity measurements for both Wyoming-type and BCV bentonite.

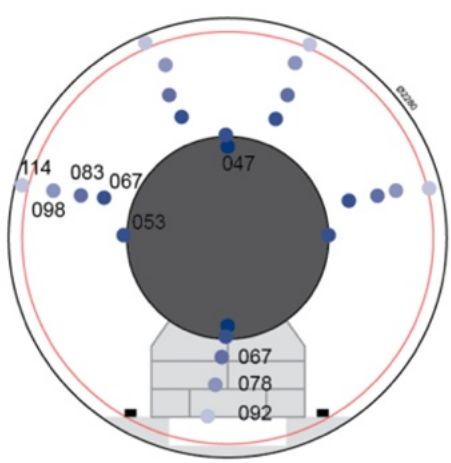

Figure 8-5. Sensor layout around Heater 1.

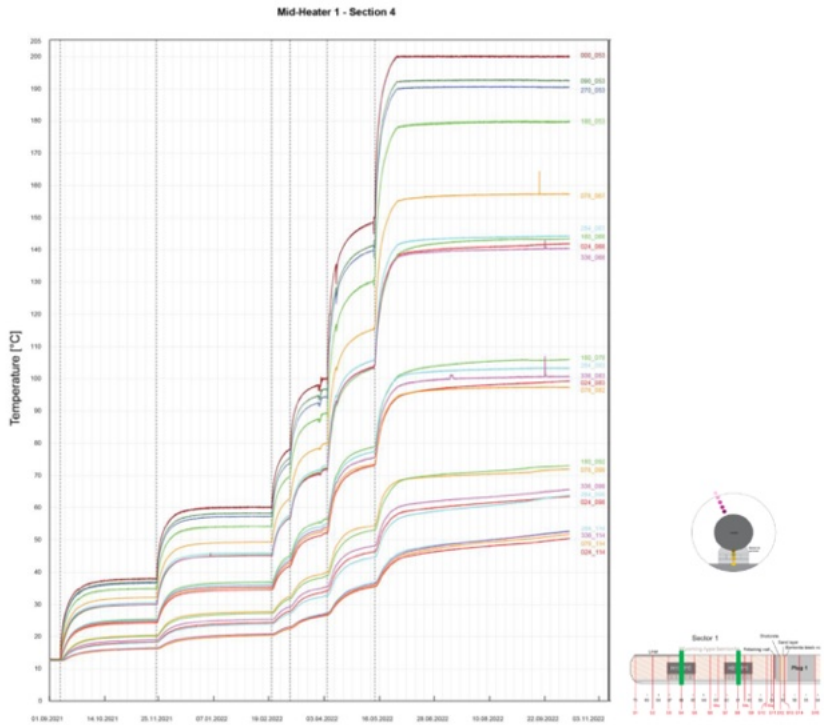

Figure 8-6. Graphs of temperature measured at S4 (the middle of H1) (Kober, 2022).

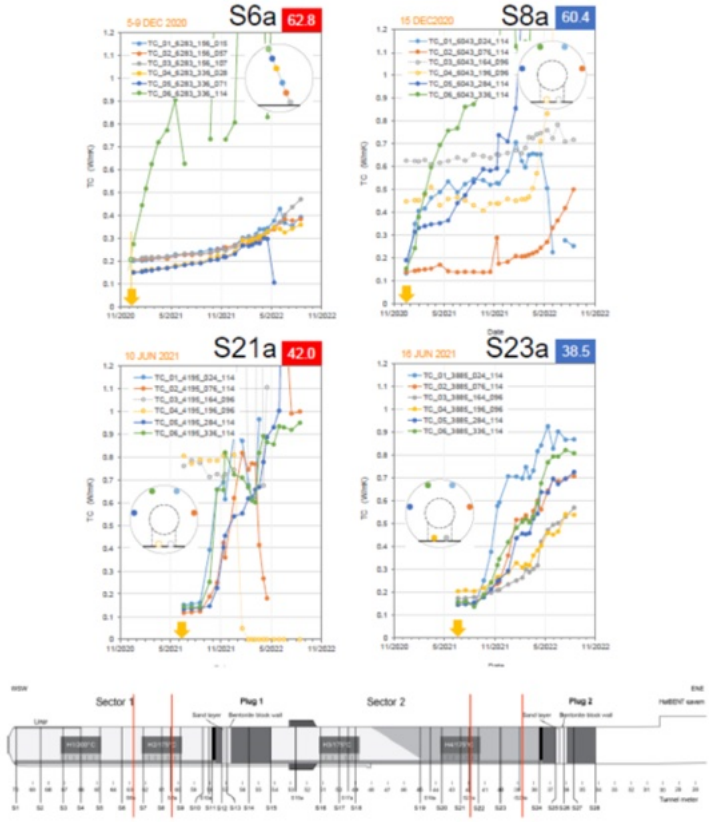

Figure 8-7. Graphs of thermal conductivity measured at S16, S8, S21, S23 (Kober, 2022).

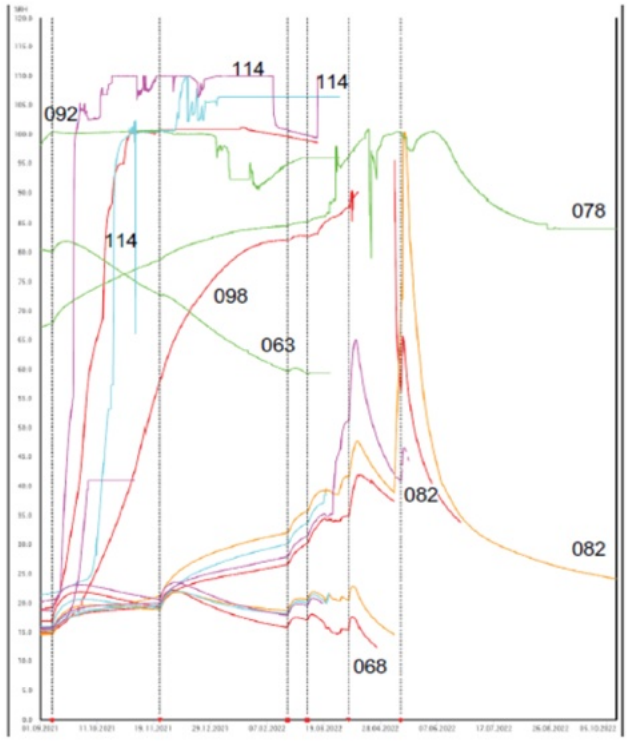

Figure 8-8. Graphs of relative humidity measured at S21, Heater 4 (Kober, 2022).

Pore pressure is an important variable to track the hydration of bentonite and constrain the model. 355 sensors were installed, all (100%) of them were functioning, and examples of measurements are given in Figure 8-9.

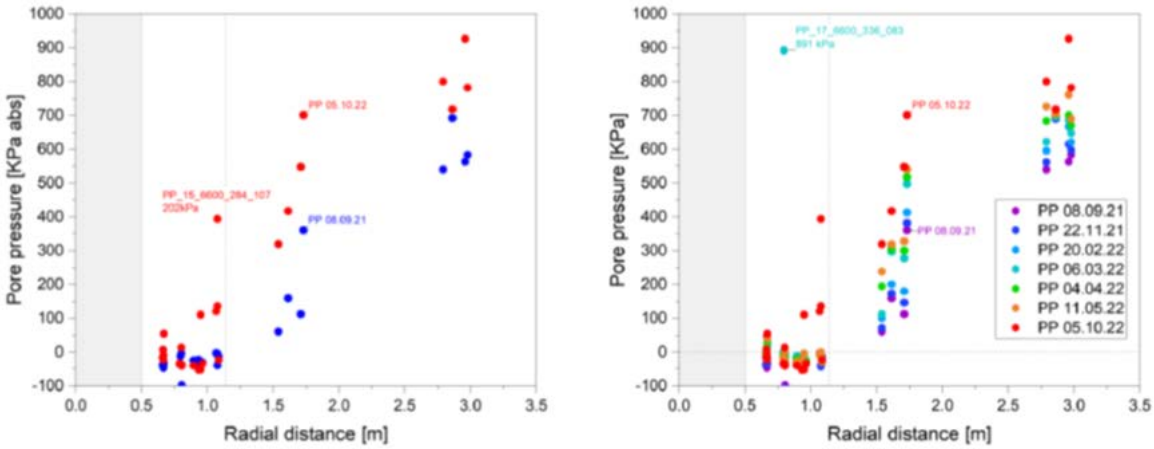

Figure 8-9. Graphs of pore pressure measured at S4 (Kober, 2022).

8.2.2 Modeling Platform

NAGRA and partners have initiated the HotBENT Modeling Platform, and the first kickoff meeting was held in 2020, folllowed by the second meeting in January 2022. Using this modeling platform, modeling groups associated with the individual partner organizations are working on predictive and interpretative

modeling of the test data. The participants and structure of the modeling platform are given in Figure 8-10.

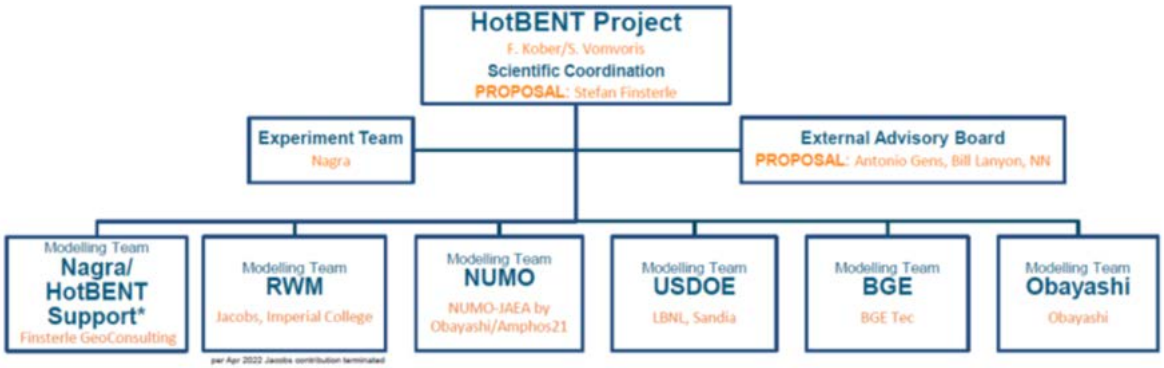

Figure 8-10. Structure of HotBENT modeling platform (Kober, 2022)

The preliminary tasks are listed in Table 8-1. The multi-institutional group was structured (Figure 8-14) so as to (a) increase the support provided to the HotBENT experiment and its interpretative evaluation, (b) broaden questions being addressed to advance fundamental understanding, and (c) address modeling issues, specifically the quantification of conceptual uncertainties. All partners encourage the Modeling Platform to pursue a broad spectrum of alternative conceptual models that address a common question or support a decision to be made jointly by the HotBENT participants. In addition, specific expertise and skills of the modeling groups can be used to examine particular aspects raised by the data collected as part of the HotBENT experiment or to make specific predictions. SFWD scientists from LBNL and SNL are participating in the Modeling Platform. LBNL's modeling plan is to start with a 2-D TH model and gradually increase the level of complexity until a 3-D coupled THMC model is developed and tested using experimental data. Preliminary modeling effort will be presented in the next section of the report.

In addition, specific expertise and skills of the modeling groups can be used to examine particular aspects raised by the data collected as part of the HotBENT experiment or to make specific predictions. SFWD scientists from LBNL and SNL are participating in the Modeling Platform. LBNL's modeling plan is to start with a 2-D TH model and gradually increase the level of complexity until a 3-D coupled THMC model is developed and tested using experimental data. Preliminary modeling effort will be presented in the next section of the report.

Table 8-1. Description of tasks of the model platform in the HotBENT project.

Tasks	Task Description (*proposal, to be discussed in first Modelling Meeting*)
1	Perform coupled TH (reference), TM/THM, THC, and THMC simulations of HotBENT
2	Repeated blind predictions of observable variables using models of different complexity
3	Model calibration or data assimilation using different conceptual models
4	Prediction of critical performance measures that affect decision points
5	Direct comparison of simulated output variables
6	Data-worth analysis
7	Conceptual models/uncertainty (summary task)

In addition to the field test and modeling platform, laboratory programs that mainly target the measurements of bentonite properties have also been established. One such effort is the high-temperature column tests (see Section 6 of this report), but certainly, other laboratory works are being encouraged.

8.3 Model for the Field Test

8.3.1 Model Set Up

As an initial step, a 2-D TH model was developed to simulate the coupled thermal and hydrological processes in the EBS of the HotBENT test. The numerical model was developed using TOUGH2 EOS 4 for non-isothermal two-phase flow with vapor pressure lowering effect. A cross-section surrounding Heater 1 (target temperature 200 °C) was modeled considering vertical symmetry about the axis of the gallery. Hydration and heat transfer processes in the EBS and the host rock are assumed to be predominantly radial. The model considered backfill of granular bentonite, bentonite block pedestal, concrete liner, and floor. The surrounding granitic host rock was also represented including an excavation damage zone (EDZ). The numerical grid used in the model is shown in Figure 8-11. The mesh extends 10 m in each direction from the center of the gallery with a total length of 20 m in the vertical direction and 10 m in the horizontal direction. The thickness of the bentonite buffer is 0.545 m. The simulation is run for five years, including the current heating phase that started in September 2021.

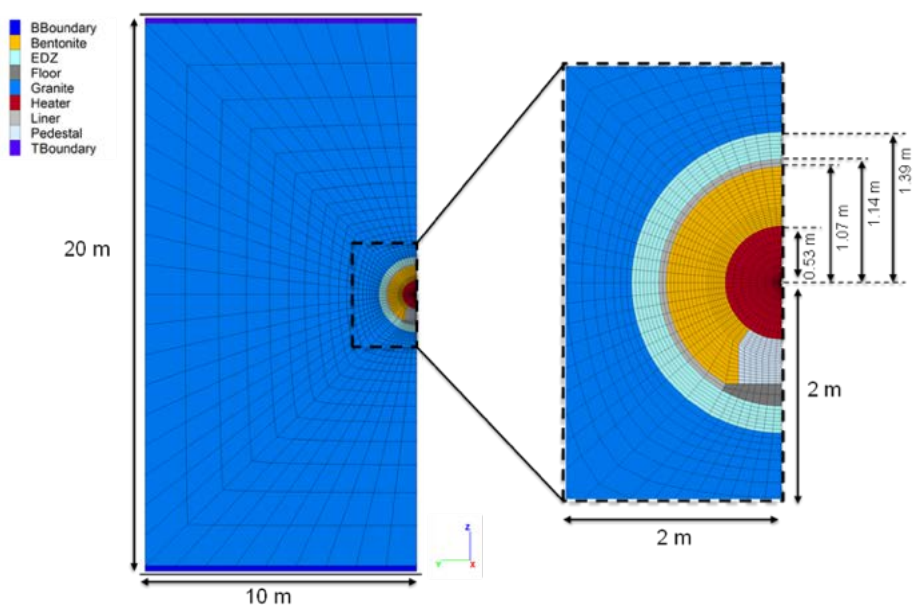

Figure 8-11 Numerical grid used in 2-D TH model (y-z cross section.

Thermal and hydrodynamic parameters for the TH analysis were obtained from the NAGRA database and studies on FEBEX in-situ test modeling (Seiphoori, 2015; Zheng et al., 2020b; 2022). Modeling included heat flow by both conduction and convection. The key parameter for heat distribution and evolution is thermal conductivity. Effective dry and wet thermal conductivities were specified, and the following relationship implemented in TOUGH2 (Pruess et al., 1999) was used to obtain the thermal conductivity (λ) as a function of liquid saturation (Sl):

$$\lambda = \lambda_dry + S_l\,(\lambda_wet - \lambda_dry) \qquad \textbf{Eq. (8-1)}$$

where λdry is the thermal conductivity under dry conditions, and λwet is the thermal conductivity at fully saturated conditions. Hydration of the bentonite buffer is impacted by permeability and the capillary

behavior of the engineered components. The following unsaturated hydraulic conductivity curves (Corey, 1954) were used to define relative permeability of the material zones in the EBS:

$$k_{rl} = \hat{S}^4$$

$$k_{rg} = \left[\left[(1-\hat{S})\right]^2 (1-\hat{S})\right]^2 \qquad \textbf{Eq. (8-2)}$$

$$\text{where } \hat{S} = (S_l - S_{lr})/(1 - S_{lr} - S_{gr})$$

krl is the relative permeability of liquid whereas krg is the relative permeability of gas, Slr and Sgr refers to residual liquid and gas saturations respectively, and Sl is the liquid saturation.

The capillary pressure (Pc) for the EBS components was obtained using the van Genuchten function (van Genuchten, 1980) as shown below.

$$P_c = -P_0 \left[\left([\left[S^*\right]\right]^{(-1/\lambda)} - 1\right)\right]^{(1-\lambda)}$$

$$\text{with } \left[-P\right]_{max} \leq P_0 \leq 0 \qquad \textbf{Eq. (8-3)}$$

$$\text{where } S^* = (S_l - S_{lr})/(1 - S_{lr})$$

P0 and λ are material parameters. The material properties used in the initial analysis are summarized in Table 8-2 and were considered to be independent of temperature.

A time dependent Dirichlet temperature boundary condition is prescribed to the heater where the temperature is increased from 13 °C to 200 °C in sequential steps. The temperature at far field boundaries was maintained at 13 °C. Hydrostatic pressure at the top and bottom boundaries was prescribed as 0.5 MPa and 0.69 MPa respectively. No-flow boundary conditions were maintained at the two vertical faces. The initial pressure distribution in the host rock was obtained by simulating the gallery excavation with Dirichlet atmospheric pressure boundary conditions within the gallery. The simulation was run for a period of 10 years to allow the pressures in the vicinity of the gallery to reach hydraulic equilibrium conditions. The initial domain temperature was prescribed as 13 °C and the initial pressure of engineered HotBent components was given as 0.101 MPa. The initial saturation of granulated bentonite and bentonite blocks was calculated based on the dry density and water content measurements. The granite host rock was assumed to be fully saturated. Initial saturation of each engineered material component is given in Table 8-3.

Table 8-2. Thermal and hydrodynamic material properties.

Parameter	Bentonite	Bentonite Blocks	Concrete	EDZ	Granite
Grain density (kg/m^3)	2700	2600	3200	2670	2700
Porosity	0.45	0.37	0.25	0.02	0.01
Permeability (m^2)	1.0×10^{-19}	3.47×10^{-20}	1.0×10^{-19}	1.0×10^{-17}	2.0×10^{-18}
Pore compressibility (1/Pa)	5.0×10^{-8}	3.0×10^{-9}	6.7×10^{-10}	1.0×10^{-9}	3.2×10^{-9}
Thermal expansion coefficient (1/°C)	3.0×10^{-4}	1.0×10^{-5}	1.0×10^{-5}	1.0×10^{-5}	1.0×10^{-5}
Thermal conductivity (W/m/°C) dry/wet	0.47/1.15	0.5/1.5	0.8/0.8	3.2/3.3	3.2/3.3
Specific heat capacity (J/kg/°C)	880	830	880	800	793
Van Genuchten m	0.45	0.296	0.5	0.7	0.7
Van Genuchten $1/P_0$ (1/Pa)	5.0×10^{-7}	2.19×10^{-8}	4.0×10^{-7}	1.10×10^{-3}	4.76×10^{-4}

Table 8-3. Initial liquid saturation of materials.

Material	Initial Liquid Saturation
Bentonite	0.19
Bentonite Blocks	0.85
Concrete	0.71
EDZ	0.91
Granite	1.0

8.3.2 Model Results

The coupled hydrodynamic effects in the EBS resulting from simultaneous heating and hydration are simulated in the numerical model. Field test data for temperature and relative humidity for the EBS sections in the vicinity of Heater 1 have been made available by NAGRA to its partners. The temperature sensors are placed at different radial distances and angles from the vertical axis. As only a half-space is simulated in the model, sensor data on either side of the vertical axis are compared with a representative element in the half-space. The time-series results for temperature during the 5-year simulated period at different radial distances are shown in Figure 8-12. The dotted lines represent field data whereas the solid lines represent simulated results. The notation of each data series includes a two-digit numeric figure followed by a three-digit value which refers to the sensor number and the placement angle respectively. For example, Exp03_024 will represent field data measured by sensor 3 which was placed at an angle of 24 degrees from the vertical axis.

Figure 8-12(a) shows the temperature evolution at the heater surface. The simulation period starts three months prior to the heating phase. The heating is conducted incrementally until the target temperature of 200 °C is reached. Some variation in heater temperature is observed in the field measurements. The temperature reported by sensor 12 is slightly lower as the sensor was located slightly below the heater within the pedestal. A step wise increase in temperature corresponding to the heating input at Heater 1 can be observed at different radial distances. At locations closer to the heater (up to a radial distance of ~0.85 m), the temperature reaches a steady state after approximately 500 days. However, at the outer boundary of the bentonite backfill, the temperatures are still increasing after a 5-year period. In general, the simulated results overpredict the temperatures compared to the measured data in the field. This may be due to several factors. The thermal conductivity value used in the model may be much higher than the actual thermal conductivity of the bentonite buffer. This is further confirmed by the slight increase in the rate of heating observed in the simulated results. Thermal conductivity can be affected by the input parameters for the dry and wet state values as well as the thermal conductivity function employed in the model. It should be noted that the current model only represents a 2-D cross section of Heater 1 and does not account for the heat transfer and losses along the length of the tunnel.

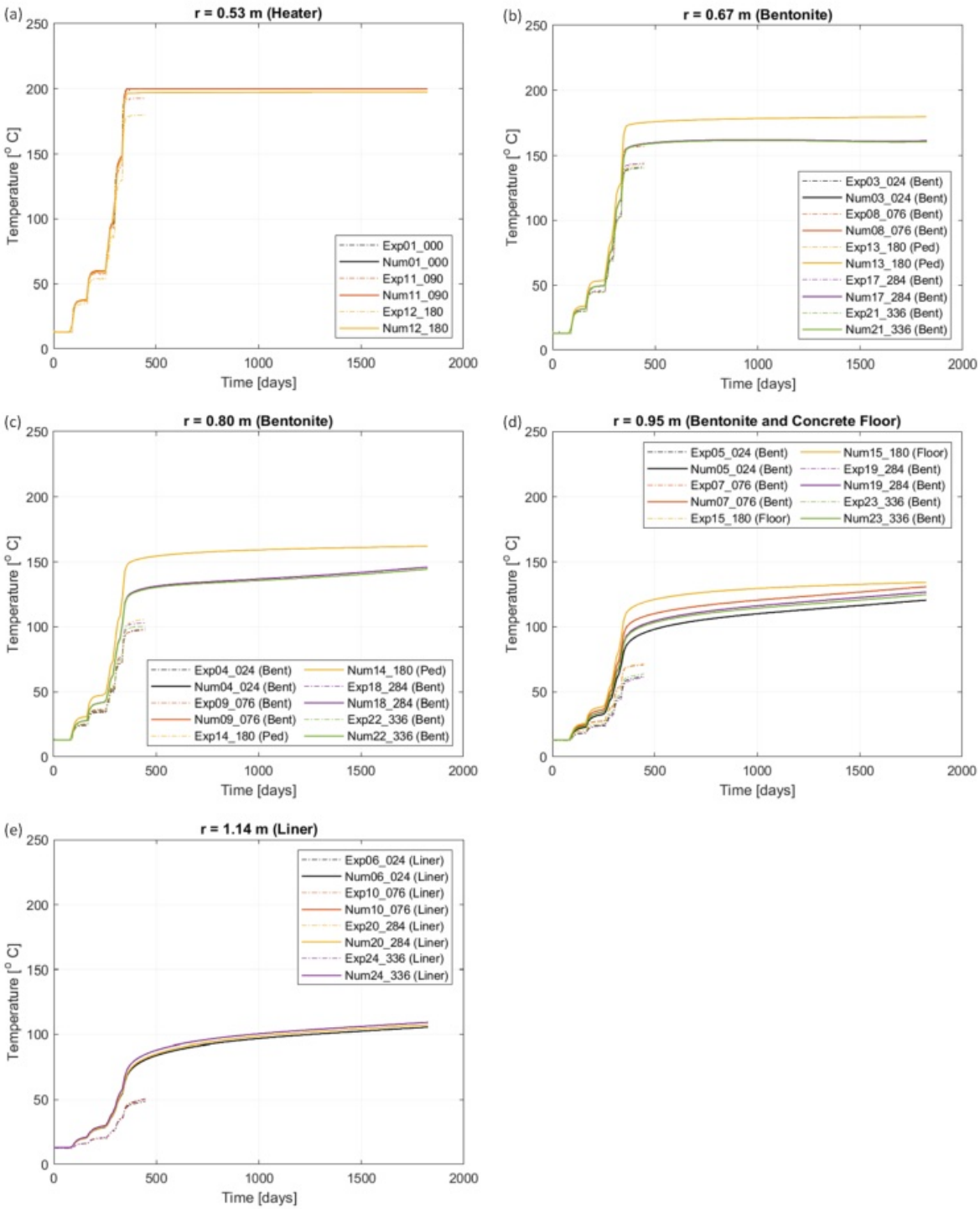

Figure 8-12. Time-series results of temperature in the buffer.

The temperature evolution in the EDZ and the granite is shown in Figure 8-13. The rock temperature at 5 m radial distance increased to 5 °C after heating for a period of 5 years. A further analysis included varying the thermal conductivity value to investigate its effect on the temperature evolution. The temperature evolution within the granular bentonite fill was dominated by the dry thermal conductivity. The best agreement with measured data was obtained with dry and wet thermal conductivity values of 0.1

and 0.9 W/m/°C, respectively. The results are shown in Figure 8-14. Within the pedestal, however, wet thermal conductivity was observed to have a significant impact on the temperature evolution and as the hydration continues with time the discrepancy between the simulated results and the measured data increased.

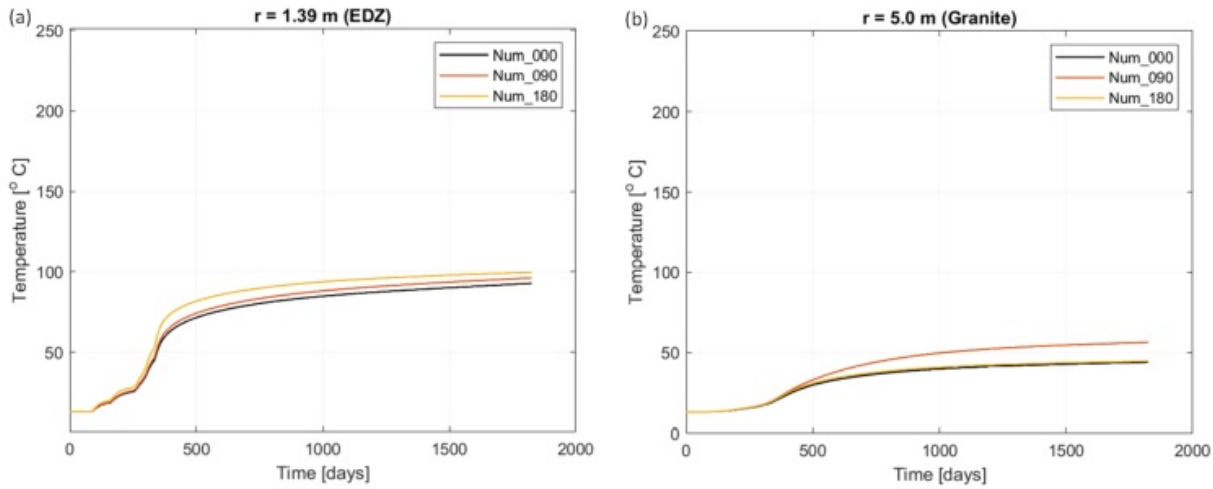

Figure 8-13. Time-series in the host rock.

The fully saturated surrounding rock is at a higher pressure in comparison to the bentonite barrier, which will lead to water flow inwards to the barrier. Due to the hydration of the barrier, an increase in the degree of saturation of its components can be expected. This will be more dominant at the boundary between the barrier and the host rock. On the other hand, in the inner boundary near the heater, due to the increase in temperature some degree of drying can be expected in the clay buffer. Simulated results for liquid saturation at different radial distances are shown in Figure 8-15. The initial saturation of the pedestal composed of bentonite blocks is much higher in comparison to the granular bentonite fill. In this simulation, the hydration process from the host rock starts prior to the heating phase. The relatively dry bentonite saturation remains unchanged prior to heating, whereas the saturation of the pedestal is increased. As heating progresses, a reduction in liquid saturation is observed near the heater. The bentonite saturation can be seen to increase as you move further away from the heater. Flow of water towards the buffer has resulted in an initial desaturation of the EDZ as seen in Figure 8-15(f).

Measurements of relative humidity (RH) available from the NAGRA database were also compared with the simulated results as shown in Figure 8-16. Unlike the temperature data, data collected for relative humidity show a significant variability. In some instances, the sensors in this sector have interrupted data records or have discontinued operation. Although the simulated results observe similar trends to the measured data, there exist some disparities between the predictions and the measured data. It is expected that improved data from other sectors of the test site will assist with better calibration of the numerical model.

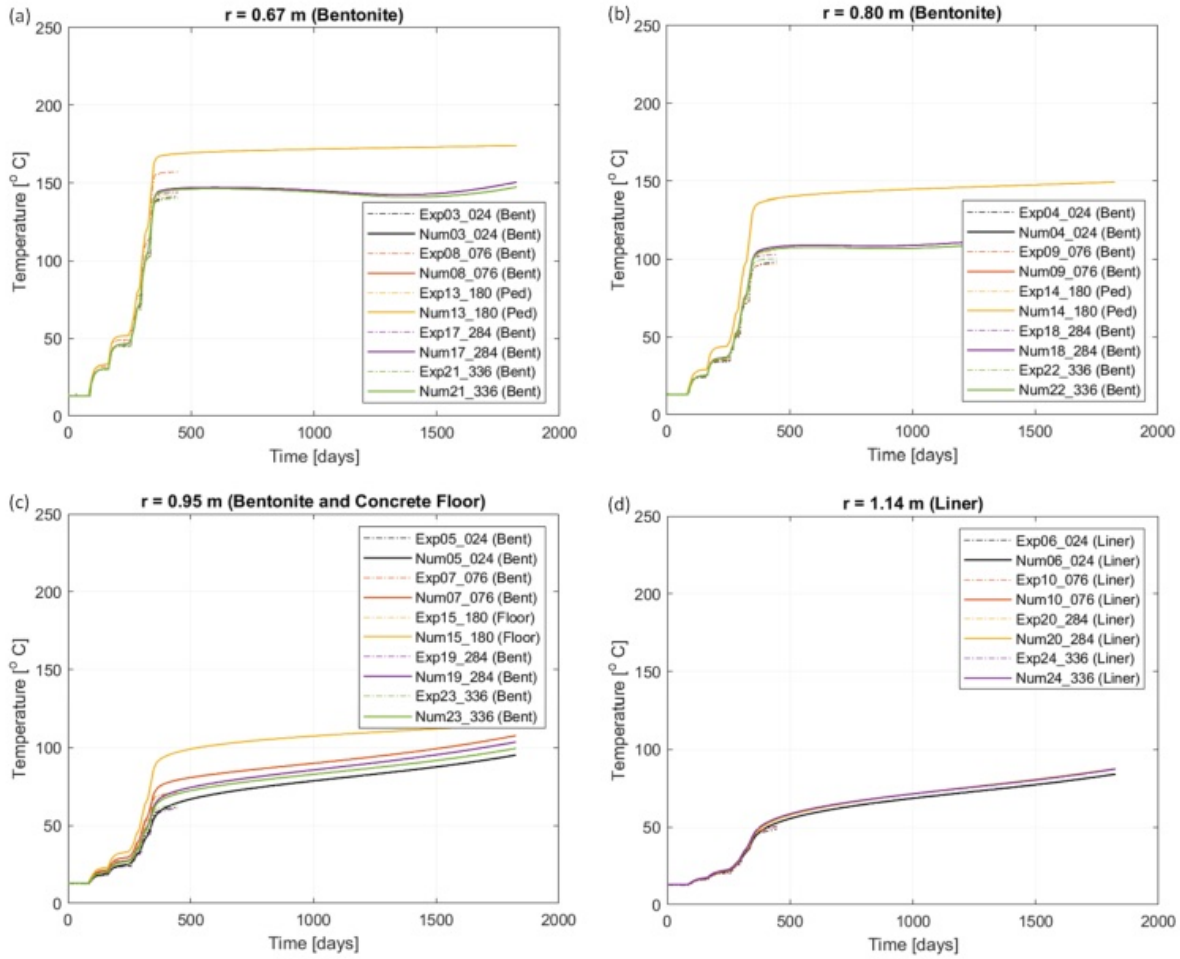

Figure 8-14 Time-series results for temperature (thermal conductivity of Bentonite (dry/wet) – 0.1/0.9 W/m /°C).

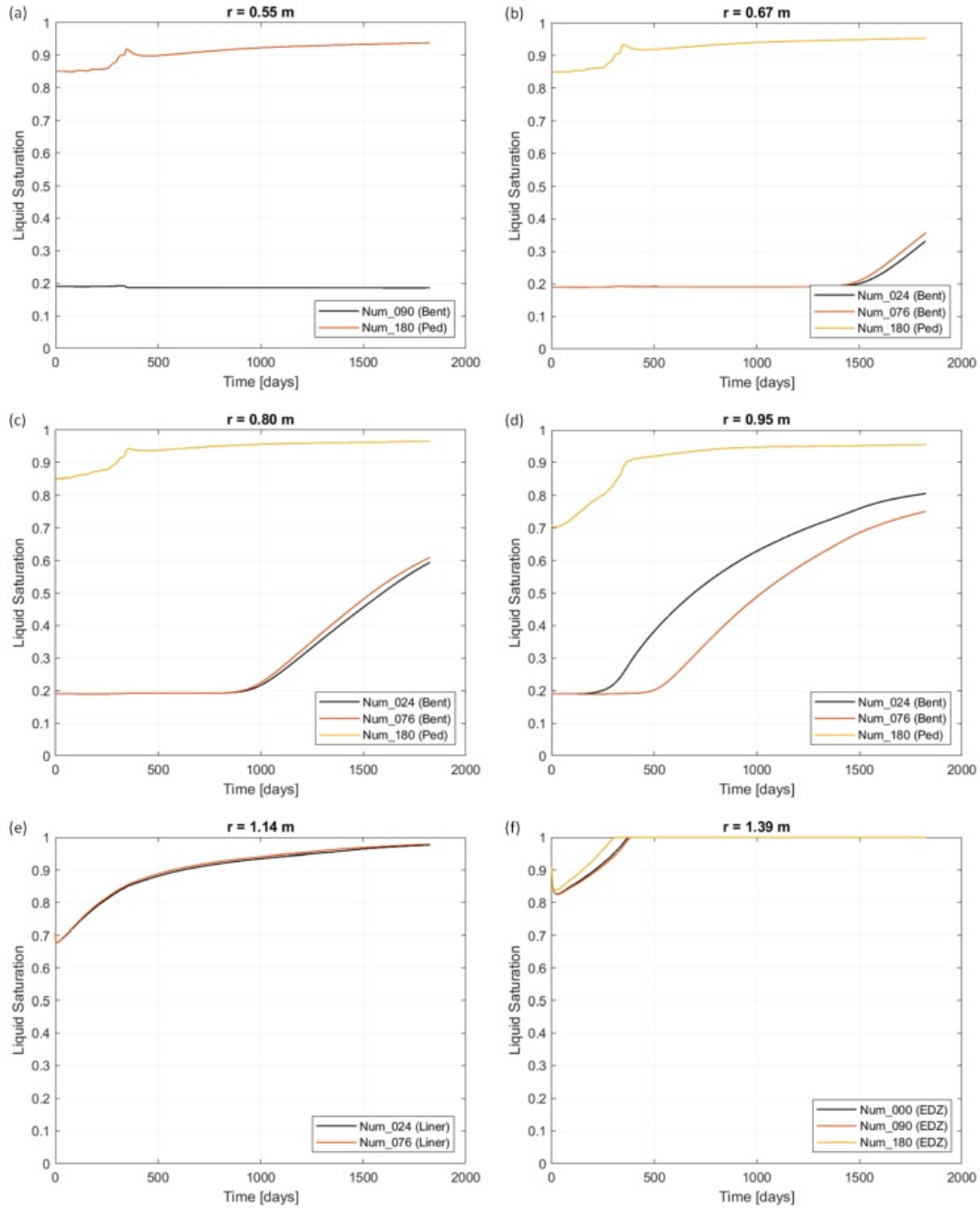

Figure 8-15. Time series results of liquid saturation.

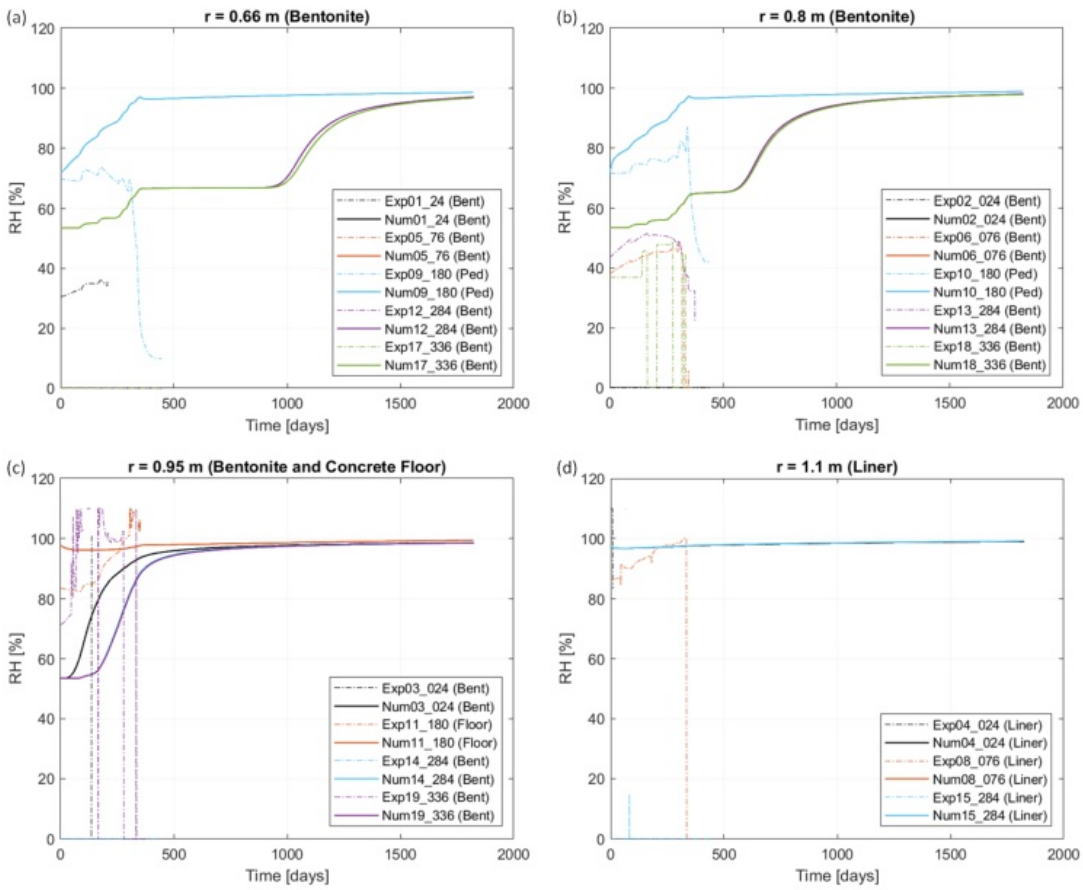

Figure 8-16. Time series results of relative humidity.

8.4 Summary and Future Work

Understanding the behavior of bentonite at high temperature for the disposal of HLW is important for expanding the knowledge base regarding the perturbation of bentonite buffer and opening the possibility of designing a repository with higher thermal limits. Currently, a high temperature experiment in a crystalline rock environment, called HotBENT, is being conducted under the leadership of NAGRA with several international partners including DOE. The HotBENT Project continued to make progress in FY22 and FY23: all the heaters have reached their respective target temperatures and the heating phase continues. Data is collected through the extensive sensor network and an initial set of data has been shared with partners. LBNL continues to actively participate in the HotBENT Modeling Platform and as a preliminary step, a 2-D TH model has been developed to simulate the field test. Initial 2-D TH model predictions match the trends in observed thermal and hydrodynamic behavior in the EBS. However, the temperature results are overestimated by the current model and significant variability is observed in the relative humidity data.

In the remaining months of FY23 and FY24, LBNL will gradually extend the 2-D TH model to a 3-D TH model and will include mechanical and chemical effects. In addition, to address the discrepancies with temperature and saturation predictions, efforts will be taken to investigate the effects of different thermal conductivity functions (i.e., Lu & Dong, 2015) and soil water retention curve on the thermos-hydrodynamic behavior of the EBS. The modeling efforts are expected to enhance our understanding and provide valuable information regarding the coupled THMC behavior of an EBS.

This page intentionally left blank.

9. HYDROTHERMAL ALTERATION OF EBS INTERFACES

9.1 Background

9.1.1 EBS Concepts in Crystalline Rock

The benefits of siting an underground spent fuel repository in a crystalline host rock include stability of excavated tunnels, reducing chemical conditions that are favorable to radionuclide immobilization, and low porosity/groundwater fluxes (Andersson et al., 2013). As with any potential host rock, however, specific local concerns must also be addressed. Crystalline rock may allow for the sustained presence of natural and manmade fractures (Figure 9-1), which can create pathways for radionuclide transport away from the repository near-field (Figueiredo et al., 2016; Missana & Geckeis, 2006). The long-term efficacy of EBS materials and design are then prerequisite for ensuring radionuclide retention for repository function (Mariner et al., 2011).

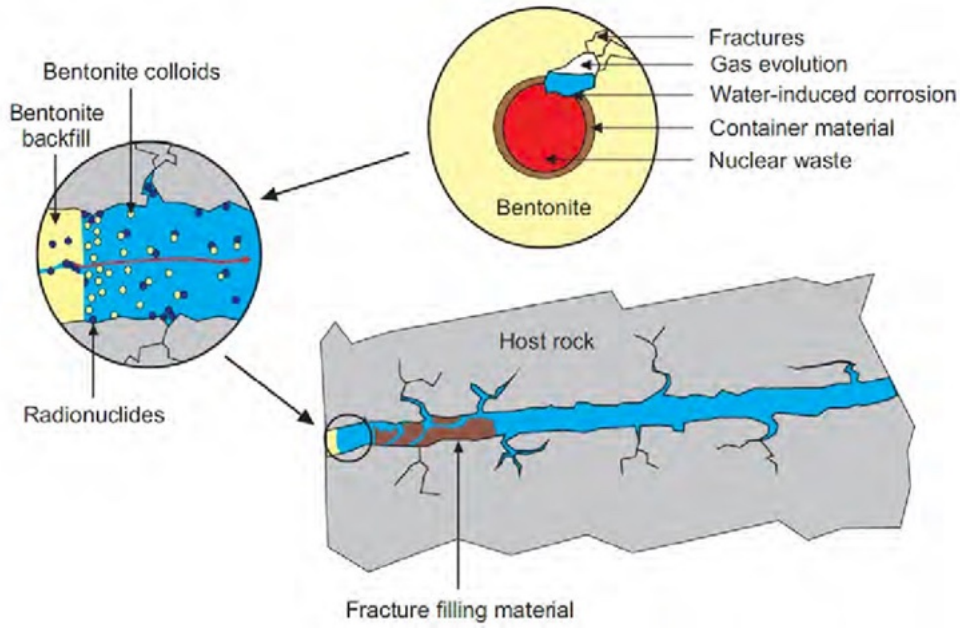

Figure 9-1 Possible scenario for bentonite-colloid facilitated transport of radionuclides away from a corroded waste package. Waste package breach coincides with fracture formation in the bentonite buffer and the formation of bentonite colloids at the buffer-host rock interface. Radionuclides sorbed to colloids are transported away from the EBS via fractures in the host rock. Figure from Missana & Geckeis (2006)

Several international approaches to protecting repository materials specify an 100 °C upper limit, to be achieved by placing design constraints on spacing and packing of spent fuel tailored to the properties of the local host rocks (SKB, 2011b; Sellin & Leupin, 2013; Kukkonen et al., 2011; Oy, 2012), since alteration of EBS materials is expected to be either minimal or inhibited by slow reaction rates below 100 °C (Zhou et al., 2021a; Zhou et al., 2021b). Potential alteration in crystalline rock repository concepts up to 100 °C have hence been widely evaluated in laboratory and full-scale experiments. The Grimsel Test Site in Switzerland specifically provides a platform for multinational exploration of repository concepts in a generic crystalline host rock underground research laboratory (URL). Additionally, Sweden and Finland have each submitted license applications for repository operations in crystalline (granitic) rock including temperature limits for buffer materials of 100 °C (Sellin & Leupin, 2013; Hedin & Olsson,

2016) and have completed extensive experimental programs to characterize barrier material stability in the proposed repository locations.

In experiments performed that heated bentonite blocks to temperatures between 60 and 85 °C at the Äspö Hard Rock Laboratory in Sweden, cation exchange was observed in reacted smectites after eight years of reaction time but no changes to the clay mineral structures were observed (Dohrmann & Kaufhold, 2014). In-situ heater tests also conducted at the Äspö Hard Rock Laboratory in Sweden characterized bentonite alteration in contact with heat sources in a crystalline rock environment. Initial tests heated different types of water-saturated bentonite blocks in contact with a heater maintained at 130 °C for 18 months. A final heater test conducted for 4.4 years experienced a maximum temperature (at the heater surface) of 250 °C. The results showed a loss of Si and increase in Mg with increasing temperature in the bentonite, as well as a potential slight increase in CEC in the regions that experienced the highest temperatures (Olsson & Karnland, 2011). In Switzerland, the FEBEX heater test that was recently completed at the Grimsel Test Site was an 18-year long full-scale EBS demonstration comprising a heater that maintained a temperature of 100 °C at a dummy canister surface. The results of the FEBEX experiment showed smectite recrystallization to saponite and chlorite, an accumulation of Mg near the heater, and decrease in clay mineral CEC and surface area. Clay alteration was restricted to areas directly adjacent to the heater surface (within ~10 cm, (Fernández et al., 2018).

9.1.1.1 Cement Components in EBS

Cementitious materials are a critical structural component of repository designs and the cement composition for use in any given repository setting is an area of active investigation. Ordinary Portland cement (OPC) and other traditional cements with a high portlandite content, however, can significantly increase the pH of infiltrating fluids due to the equilibration of pore water with portlandite through the following generalized reaction:

$$Ca(OH)_{2\ (Por)} \rightarrow Ca^{2+} + 2OH^{-} \qquad \textbf{Eq. (9-1)}$$

A pH of 12.6 is a critical value for detrimental changes of smectite. At this value, migration of calcium from the cement to the clay via ion exchange may lead to changes in the microstructure of the clay (Pusch et al., 2003). Cement-bentonite interaction is observed to be a non-linear system that involves multiple coupled processes that occur simultaneously and affect each other (Savage et al., 2010). These processes include transport of hydroxide and cations into bentonite, montmorillonite ion exchange and dissolution, precipitation of secondary phases, dissolution of accessory minerals, and changes in porosity and swelling properties (Takase, 2004; Savage et al., 2010).

Cement-bentonite interaction studies for repository research have been performed as part of the URL at the Grimsel Test Site (Martin et al., 2006). Results of 13 years of cement-bentonite interaction at the FEBEX demonstration are reported in Alonso et al. (2017) and Fernández et al. (2017). Spacing from the heater (maximum temperature 100 ºC) in the FEBEX demonstration resulted in an observed maximum temperature of 28 ºC in the concrete liner (Martínez et al., 2016). Both, the shotcrete plug and bentonite, experienced alteration due to GW interaction (Alonso et al., 2017). Portlandite dissolution occurred at the host rock-concrete interface. CSH phases in the concrete were altered due to the incorporation of Al, S, and Mg. At the bentonite-concrete interface, the main alteration mineral observed was ettringite ($Ca_6Al_2(SO_4)_3(OH)\cdot 26\ H_2O$), indicating that the breakdown of S-rich phases in the bentonite, concrete, and/or S sourced from the GW resulted in mineral precipitation (Alonso et al., 2017). In the bentonite, alteration was mostly limited to the immediate interface zone, mostly in the form of precipitated Mg-rich phases and the change in exchangeable cations in the bentonite (Fernández et al., 2017). These results highlight the potential for alteration at the cement-bentonite interface at ambient temperatures in a realistic repository scenario.

The potential for significant and wide-ranging geochemical and mineralogical effects of bentonite-cement interaction has led repository programs to implement a pH limit for cement porewater (e.g., B, pH < 11). The pH limit is achievable using low-pH cements that replace traditional cement components (e.g., limestone aggregate) with siliceous materials (e.g., fly ash, non-pozzolanic silica flour, blast furnace slag, and/or silica fume) resulting the reduced abundance of portlandite in the cured product and a lower Ca/Si ratio in the CSH minerals (Calvo et al., 2010; Savage & Benbow, 2007; Lothenbach et al., 2011). The effect of hydrothermal conditions on cured low-pH cement is an area of active study. Recent experimental studies evaluating a concrete composition expected to have lower porewater pH and including talc as a superplasticizer to negate the need for organic components showed that hydrothermal conditions actually improved the sealing properties of the concrete, specifically by increasing strength (Mohammed et al., 2015; 2016) and decreasing hydraulic conductivity (Mohammed et al., 2016).

Co-alteration studies of low-pH cement with bentonite have largely been conducted at or near ambient conditions. Pusch et al. (2003) performed an experiment involving low-pH cement (slag cement Merit 5000) with Friedland Ton (70% montmorillonite, 30% muscovite). From XRD data, they observed only slight dissolution of the clay minerals; paired with minor small changes of K concentration in the experimental fluid, they concluded that illitization of the bentonite was insignificant. González-Santamaría et al. (2018) conducted a small-scale laboratory experiment using distilled water, low-pH cement (60 wt.% OPC + 40 wt.% silica fume), and FEBEX bentonite (25 °C). At the cement-bentonite and cement-water interfaces, the cement experienced decalcification. Mg enrichment in the bentonite at the cement-bentonite interface was also reported. A subsequent laboratory-scale study from González-Santamaría et al. (2020) studied the interface of low-pH cement and FEBEX bentonite in a system with Grimsel Test Site groundwater. They reported that alteration in the dilute crystalline GW solution resulted in the precipitation of Mg-hydroxides and silicates forming within 100 µm of the cement.

One type of low-pH cement, ESDRED (Engineering Studies and Demonstrations of Repository Designs) shotcrete cement, was especially designed for repository applications. The cement was designed to be compatible with engineered barriers, such as bentonite, by substituting 40% of the cement with silica fume. As a result, fluid in equilibrium with the cement has a pH equal to or below 11 in accordance with repository program limits. Jenni et al. (2014) and Mäder et al. (2017) examined the in-situ interaction between ESDRED cement and Opalinus Clay at the Monti Terri URL. A field experiment consisted of two boreholes in the Opalinus Clay filled with three types of cements alongside two monitoring boreholes that recorded pore water pressure in the formation. After two and five years, respectively, both boreholes featured a de-calcification zone at the ESDRED cement interface which was overprinted by a carbonate alteration zone (i.e., calcite precipitation). The interface contained a wide Mg-enriched zone with claystone pore-water as the Mg source. When Mg migrated into the cement from the host rock, the Mg reacted with alite to form Mg-hydrate. There was a limited extent of reaction within Opalinus Clay itself.

9.1.1.2 Steel Alteration in Geologic Repositories

Repository designs in crystalline rock rely more specifically on the waste package as a primary mechanism to prevent radionuclide release rather than in ductile host rock lithologies, such as clay and salt, that provide a measure of self-sealing capacity. The stability of the metal canisters designed to contain waste packages is then of substantial importance in a crystalline repository. Under dry conditions, bentonite mineralogy will likely be stable (Wersin et al., 2007) and steel corrosion will be minimal. Infiltration of GW over time, however, is expected to result in in-situ reactions including canister corrosion, potential alteration of the bentonite, and reactions between corrosion products and the bentonite (Gaudin et al., 2013; Wilson et al., 2006a; Wilson et al., 2006b). This report focuses on a brief review of interactions of metal corrosion products with bentonite barrier materials that may impact barrier performance in a crystalline rock environment.

Formation of an Fe-oxide layer on steel

Design concepts for a crystalline rock repository in the United States are still being explored, but the current base case in crystalline rock includes stainless and carbon steel (Matteo et al., 2016). Steel will corrode at the bentonite-buffer interface in the presence of oxygen according to one of the following reactions (aerobic corrosion) (Kursten et al., 2004):

$$4FeO + 3O_2 \rightarrow 2Fe_2O_3 \quad \textbf{Eq. 9-2}$$

$$2Fe + 2H_2O + O_2 \rightarrow 2Fe(OH)_2 \quad \textbf{Eq. 9-3}$$

The resulting oxide film has been shown to act as a protective coating against further corrosion in an effect called passivation. The formation of even porous $Fe(OH)_2$ layers as are expected to form in cement-influenced alkali solutions in geologic repositories may still decrease corrosion rates (Kursten et al., 2004). In contrast, at lower pH values and/or as a result of reactions with aggressive aqueous species such as chlorides, oxide passive films can break down. Previous laboratory studies (25–100 °C) have shown the formations of the Fe-oxide layer at the steel-bentonite interface, with a range of different Fe-oxide/hydroxides observed to precipitate on the steel surface dependent on experimental conditions. (Alvarez et al., 2008; Bourdelle et al., 2014; Pignatelli et al., 2014; Smailos et al., 2002; Kursten et al., 1997). The main corrosion products observed are magnetite (Fe_3O_4) and goethite (FeO(OH)) in experiments below 100 °C, with hematite (Fe_2O_3) occurring in the experiments at 100 °C.

9.1.1.3 Mineral Reactions at Steel-Bentonite Interfaces

In the event of a canister failure, significant alteration of the bentonite immediately adjacent to the breached area (i.e., the steel-bentonite interface) could negatively impact the efficacy of the bentonite to arrest the movement of radionuclides. Higher temperatures at the clay/canister interface may cause a local increase in Fe-activity and dissolved SiO2, where the resulting chemical gradient causes migration of dissolved species radially away from the canister towards the colder rock, potentially leading to the silicification throughout the buffer during the cooling phase (Pusch & Madsen, 1995; Svemar, 2005).

Full-scale demonstrations at URL sites are used to simulate the long timeframes, realistic scales, and water/rock and clay/steel ratios applicable to proposed repository designs. Interaction of carbon steel and bentonite was examined in a full-scale experiment as part of the 18-year FEBEX full-scale EBS heater test at the Grimsel Test Site (Martin et al., 2006). Bentonite in contact with steel examined likely reached temperatures of 30 to 60 °C as part of this experiment. After 18 years of reaction in a saturated system, carbon steel corrosion resulted in a less than 140 mm layered zone of Fe enrichment extending radially into the interfacing bentonite. In the ~30 mm closest to the canister, Fe is hosted in newly formed goethite (Fe3+O(OH)) within the bentonite. The remainder of the Fe-enriched zone is interpreted to be a result of the diffusion and sorption to the clay mineral edge site of Fe2+ (Hadi et al., 2019). Substantial alteration of the interfacing bentonite was not observed at the relatively low temperatures achieved (Wersin & Kober, 2017; Hadi et al. 2019). The HotBENT (High Temperature Effects on Bentonite) experiment is currently being conducted by Nagra in the same manner as the FEBEX experiment to evaluate high-temperature processes in a full-scale demonstration. The peak temperatures of the HotBENT experiment are expected to reach between 175 to 200 °C and it will run for 15 to 20 years (AMBERG, 2019). The HotBENT experiment is discussed in further detail in Section 9.2 in relation to the EBS International work package.

Lab-scale experiments provide insight into transient reaction pathways, complementary to results from long-term full-scale experiments. Interaction between clay minerals/bentonite with steel/Fe-oxide/native Fe has been a subject of extensive characterization at a wide temperature range (25 to 300 °C: (Cathelineau et al., 2005; Wersin et al., 2007; Mosser-Ruck et al., 2010; Pignatelli et al., 2014; Bourdelle et al., 2014; Kaufhold et al., 2015; Cheshire et al., 2018; Lanson et al., 2012; Lantenois et al., 2005; Bourdelle et al., 2017). These studies show that steel corrosion has the potential to have wide ranging

effects on the physical and chemical properties of the bentonite buffer that are sensitive to bulk system chemistry. In lower temperature repository settings (< 100 °C), cation exchange of Fe into clays during steel corrosion may reduce the self-sealing ability in the clay (i.e., swelling capacity) (Pusch et al., 2015). Fe3+, generated under initially oxidizing conditions in a repository, may replace Al3+ in the octahedral sheet of montmorillonite. This exchange can accelerate alteration to non-swelling phases due to high crystal stresses and mineral instability due to the large cation size (Nguyen-Thanh et al., 2014). In addition, the combination of heating and the ion exchange between the Na2+ in the clay with the Fe2+ produced from corrosion under reducing (anoxic) conditions promotes the development of channel-type transport pathways for solutions migrating through the bentonite buffer (Gueven & Huang, 1990; Nguyen-Thanh et al., 2014; Pusch et al., 2012).

In > 100 °C water-saturated experimental systems with circumneutral pH values (such as where porewaters are buffered by clay and silicate minerals), the presence of Fe2+/3+ may result in the formation of Fe-rich phyllosilicate minerals (chlorite, Fe-saponite, berthierine, serpentine phases) in bentonite buffers (Guillaume et al., 2003; Mosser-Ruck et al., 2010; Cheshire et al., 2018; Jové Colón et al., 2019). Previous work completed at LANL showed that in hydrothermal experiments at 300 °C, the surface of steels embedded in bentonite had a zone of corrosion and metal oxide phases formed on the steel surfaces, as well as minor pyrrhotite, which was coated with a layer of Fe-rich smectite (Fe-saponite) at the interface with bentonite (Figure 9-2; Cheshire et al., 2018; Jové Colón et al., 2019). The formation of Fe-rich silicate phases as mantle on the steel surface is thought to provide corrosion protection in addition to that provided by passivation layers (e.g, Kaufhold et al., 2015; Cheshire et al., 2018). Future results from full-scale/long term experiments may additionally be used to confirm and evaluate this potentially protective effect.

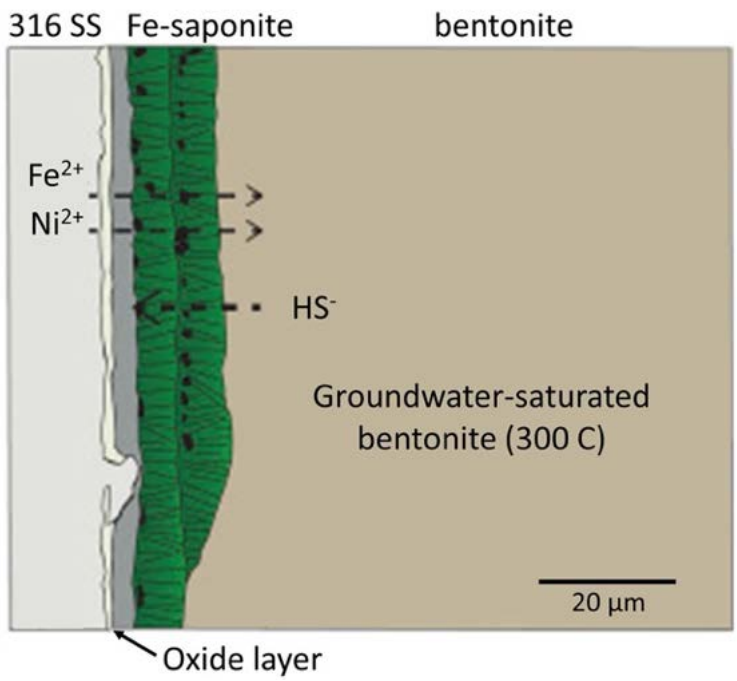

Figure 9-2. Conceptual diagram of high-temperature alteration products at a stainless steel-bentonite interface (modified from Cheshire et al., 2018).

9.2 Methods

9.2.1 Hydrothermal Experiments

The set of experiments completed in FY23 were designed to react a well-characterized low-pH cement material (ESD cement) with synthetic Grimsel GW at several temperatures. The experimental temperatures were selected to range from low-temperature hydrothermal to the maximum temperature expected at the heater surface (see Section 9.2). Experiments completed in FY21 and FY22 explored the reactions between Wyoming bentonite and different cement types including OPC and an experimental low-pH cement composition developed at Vanderbilt University in collaboration with Sandia National Laboratories (Vanderbilt University (VU) cement). An experiment completed in FY21 also characterized the alteration of Wyoming bentonite saturated with GW at similar conditions to the OPC experiment. This experiment acted as a baseline comparison for Wyoming bentonite hydrothermal alteration in the absence of cement. Parameters for all experiments are included in Table 9-1.

Reactants (listed in Table 9-1) were loaded into a flexible gold reaction cell and fixed into a 500 mL gasket confined closure reactor (Seyfried et al., 1987). Reducing conditions were maintained by including a redox buffer mixture of 1:1 (by mass) Fe_3O_4 and Fe^0 added at 0.07 wt.% of the total mass of solid + liquid reactants. Experiments in FY21 and FY22 reported here (Table 9-1) mixed the redox buffer directly with the solid reactants. In the CEM-series experiments completed in FY23, the redox buffer mixture was placed in a gold tube lightly crimped to create an enclosure where the redox buffer was in communication with the reactant solution but did not allow Fe-cement interface. All experiments were pressurized to 150 to 160 bar and isothermally heated at 100 to 200 °C for four to nine weeks. Temperature and experiment durations for each experiment are listed in Table 9-1. Reaction liquids were extracted periodically during all the experiments and analyzed to investigate the aqueous geochemical evolution in relationship to mineralogical alterations. The sampled reaction liquids were filtered by 0.22 µm syringe filter and analyzed by ion chromatography to quantify anions. An aliquot acidified to pH < 1 immediately after sampling was used for ICP-OES cation analyses and ICP-MS trace metals analysis. All aliquots were stored at 1 °C until analysis.

After experiment termination ("quench"), additional solution samples were collected directly from the reaction cell. Solid reactants were filtered from the solution, rinsed with ethanol to remove excess water and dissolved solutes, and stored in a desiccator until the weight stabilized. Reaction products and starting materials were characterized using XRD, electron microprobe (EMP(A)), and scanning electron microscopy (SEM). Detailed analytical methods are listed in Caporuscio, et al. 2023, Appendix A.

Table 9-1 Parameters for experiments completed in FY23 and experiments from previous years that had new analytical results collected in FY23. Detailed information on reactants is included in Section 9.2.2 below. All values are mass (g) except where otherwise noted.

Expt. ID	FY completed	Reactants	Temp (ºC)	Run time	GW	GG	WB	Cement (type)	316SS	Fe	Fe_3O_4	WRR
IEBS-0	FY21	WB	250	8 weeks	160	--	18.79	--	--	0.50	0.50	9:1
IEBS-06	FY21	WB+GG+OPC	250	8 weeks	125	2.11	6.60	2.07 (OPC)	–	0.50	0.50	11:1
IEBS-08	FY21	WB+GG+OPC+316SS	250	8 weeks	171	6.64	10.92	3.62 (OPC)	3.62	0.50	0.50	9:1
IEBS-09	FY22	WB+VU	200	9 weeks	147	--	12.34	3.09 (LpHC)	--	0.58	0.58	9:1
IEBS-10	FY22	WB+GG+VU	200	9 weeks	110	2.26	6.68	2.25 (LpHC)	--	0.42	0.42	9:1
CEM-1	FY23	ESD	100	4 weeks	112	--	--	11.71 (ESD)	--	0.45	0.45	9:1
CEM-2	FY23	ESD	150	4 weeks	120	--	--	12.50 (ESD)	--	0.34	0.34	9:1
CEM-3	FY23	ESD	200	4 weeks	115	--	--	13.19 (ESD)	--	0.45	0.45	9:1

Abbreviations: GW=Grimsel groundwater; GG=Grimsel granodiorite; WB=Wyoming bentonite: OPC=ordinary Portland cement; VU=experimental low-pH cement; ESD=ESDRED-like low-pH cement; WRR=water-rock ratio (by mass).

9.2.2 Materials

9.2.2.1 Materials Used in Experiments Completed in FY23

ESD cement. An ESDRED-like, low-alkali shotcrete product used a formulation developed as part of the Engineering Studies and Demonstrations of Repository Designs (ESDRED) project (Mäder et al., 2018). The general formula includes ~60% CEM I (cement product having at least 95% OPC) with ~40% microsilica, with variable amounts of a set accelerator (Lothenbach et al., 2014). The cement product was characterized by macro-scale heterogeneity between major phases (Figure 9-3), consistent with previous characterizations of ESDRED-like low-pH cements used in full-scale demonstrations (i.e., Jenni et al, 2014).

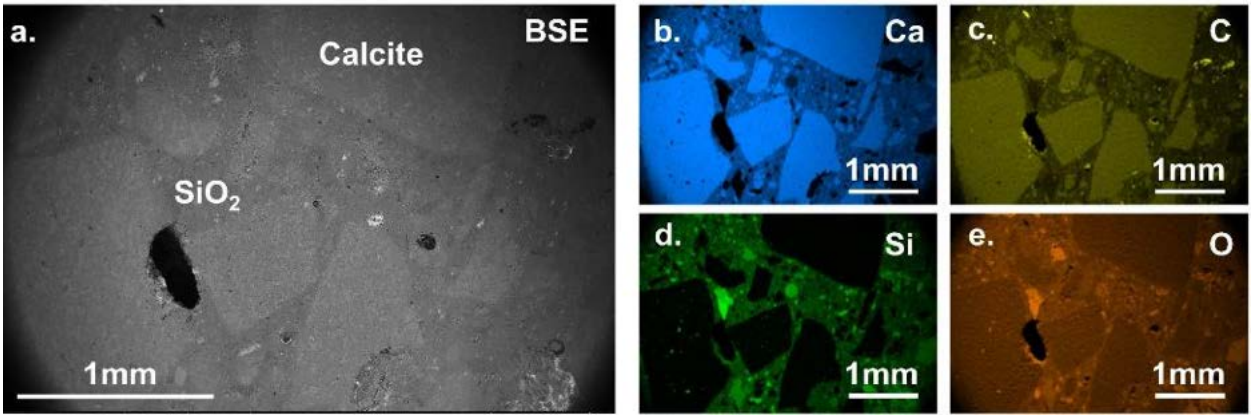

Figure 9-3. SEM-EDS characterization of unreacted ESD cement: (a) Backscatter (BSE) image of ESD cement, showing relative areas of high-calcium ("calcite") and high-silica (SiO2) regions at a mm scale; (b) EDS map of calcium abundance; (c) EDS map of carbon abundance; (d) EDS map of Si abundance; and (e) EDS map of O abundance. Note co-occurrence of relative abundances of calcium with carbon, and of silica with oxygen

Synthetic Grimsel groundwater. All experiments used a synthetic Grimsel GW solution based on chemistry reported by Kersting et al. (2012) that describes an average GW composition at the Grimsel Test Site as a Na-CO3 type water with pH ~ 8.5. The solution was synthesized using Milli-Q ultrapure water (18.2 MΩ·cm) and research-grade salts. Target chemistry of the synthetic fluid is presented in Table 9-2. All solutions were sparged with He for 30 minutes to remove dissolved gasses and pH-adjusted to pH 8.5 with analytical-grade HCl and/or NaOH before each experiment. Analyzed solution chemistries for each initial solution are listed with supplementary aqueous chemistry for each experiment in Caporuscio, et al. 2023, Tables B1-B26.

Table 9-2. Major element chemistry of the experimental and make-up fluids.

	Target solution (Kersting et al., 2012)	Synthetic Grimsel GW (this study)	Los Alamos Municipal Tap Water
	(mg L^{-1})	(mg L^{-1})	(mg L^{-1})
Na^+	127	116	2.50
K^+	3	3	12.8
Ca^{2+}	5	7	2.04
Mg^{2+}	13	12	9.62
Cl^-	11	14	3.24
CO_3^{2-}	219	203	24.7
SiO_2	21	34	n.m.
SO_4^{2-}	97	87	75.7
pH	8.6–8.8	8.5	6.93

9.2.2.2 Additional Materials Used in Experiments Completed in FY21, FY22

Wyoming bentonite. Previous experiments used an unprocessed Wyoming-type bentonite provided by Bentonite Performance Minerals LLC from Colony, Wyoming, U.S.A. It was composed dominantly of Na-montmorillonite (general composition: $Na_{0.33}(Al,Mg)_2(Si_4O_{10})(OH)_2 \cdot nH_2O$), lesser clinoptilolite and feldspar, and minor biotite, pyrite, quartz, opal, and sulfide minerals. The quantitative X-ray diffraction (QXRD) results from unheated bentonite are presented in Caporuscio, et al. 2023, Appendix C.

Grimsel granodiorite. The granodiorite used in the experiments was sourced from a drill core from the Grimsel Test Site. Major mineral phases include K-feldspar, plagioclase, and quartz. Minor phases are muscovite and biotite. Trace phases are allanite, zircon, titanite, and apatite. QXRD results from unreacted granodiorite are presented in Caporuscio, et al. 2023, Appendix C.

Ordinary Portland cement. Chips consisting of a mix of 100% OPC and Los Alamos municipal tap water (Table 9-2) were mixed according to API standards and cured for at least 28 days. Major mineral phases observed in the XRD pattern of the cured cement chip include portlandite ($Ca(OH)_2$), belite (calcio-olivine, Ca_2SiO_4), alite (Ca_3SiO_5), and brownmillerite ($Ca_2(Al,Fe)_2O_5$).

Vanderbilt University cement. An experimental low pH cement product was included as a reactant in EBS-33 and -34 (Caporuscio et al., 2022). The low-pH cement chips were developed and manufactured at Vanderbilt University using Type I/Type II cement powder (LafargeHolcim, USA), 50 wt.% silica fume replacement, and 2 wt.% Glenium (super plasticizer). A 0.6 water-to-binder ratio was used. The samples were cured for six months at 30 ºC and were at 100% relative humidity at the time of sample preparation.

316SS. 316-solid steel is an iron alloy primarily with 18.37 wt.% Cr, 12.35 wt.% Ni, 2.26 wt.% Mo, 1.619 wt.% Mn, 0.5093 wt.% Si, and 0.175 wt.% Cu.

9.3 Results

9.3.1 Aqueous Geochemistry

Evolution of pH and of cation and anion concentrations in the reaction fluids are interpreted to reflect mineral-solution reactions. Results are grouped by experimental set: experiments that were conducted at 250 °C that included Grimsel granodiorite and bentonite ± OPC ± 316SS; two experiments that were conducted at 200 °C that reacted VU cement with bentonite ± Grimsel granodiorite; and three experiments conducted with ESD cement in solution at three different temperatures (100, 150, and 200 °C). All experiments included in this report had initial water:rock ratios (WRR) of 9:1 (by mass). As experiments progressed, fluids were gradually extracted from the reaction vessel during sampling, which slightly lowered the WRR with every fluid extraction. Estimated WRRs were approximately 6:1 at experiment termination.

pH. The synthetic Grimsel granodiorite GW solution had a pH of ~8.5. In the baseline experiment IEBS-0, pH values initially decreased and after two weeks remained between 5.5 and 6 throughout the experiment duration. The pH values observed in IEBS-6 and -8, which contained OPC chips, evolved to slightly higher pH values (~7–7.5) (Figure 9-4). In contrast, in experiments IEBS-9 and -10 with VU cement, the pH decreased slightly over the experiment duration but remained > pH 8.5. In the CEM-series experiments that reacted ESD cement, pH increased to >9 within the first week of experiment time. pH of CEM-1 and -2 continued increasing throughout the experiment duration to pH ~9.6 just before experiment termination; the pH of samples collected from CEM-3 decreased after the initial increase to relative steady state at pH ~9.0. All pH values reported here were measured at 25 °C: calculated in-situ pH values are discussed in Section 10.4.2.1.

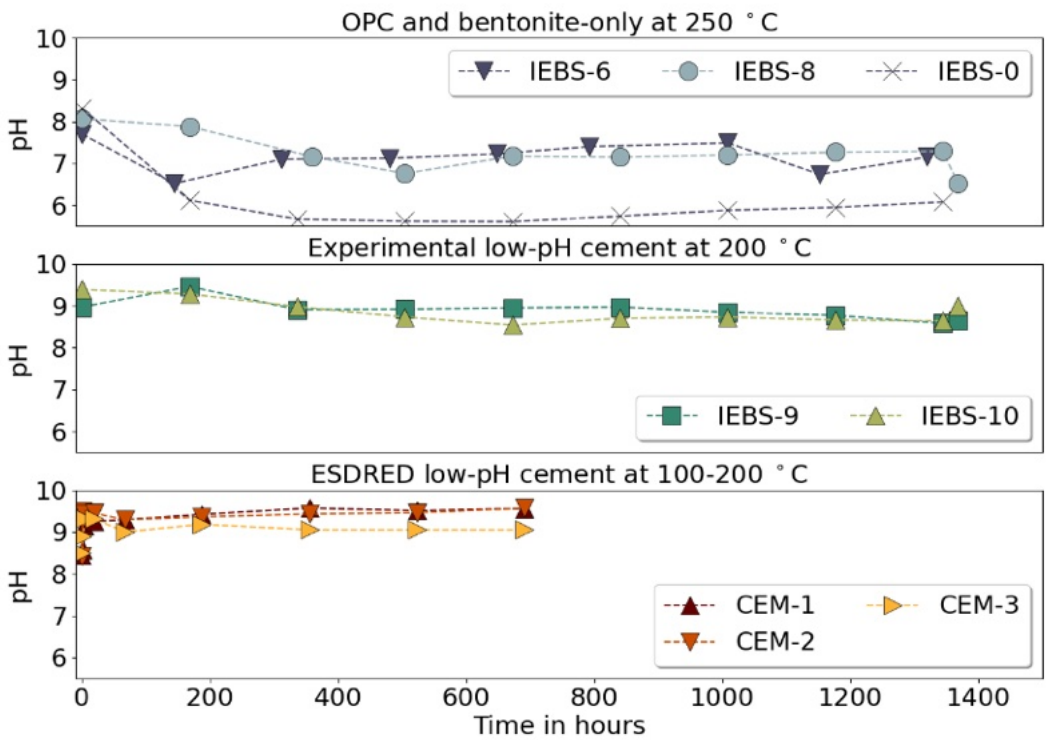

Figure 9-4. pH of the sampled fluids as measured at bench conditions.

Alkali/alkaline earth metals. Concentrations over time of selected alkali and alkaline earth metal cations (K^+, Na^+, Ca^{2+}, Mg^{2+}) follow different trends between the three groups of experiments (Figure 9-5). In the experiments completed at 250 °C, IEBS-0, -6, and-8, Ca concentrations initially decreased from the concentration of the starting Grimsel granodiorite synthetic GW (~7 mg L^{-1}) before arriving at apparent steady-state concentrations in each experiment after about two to four weeks. In two experiments reacting VU cement at a lower temperature (IEBS-9 and -10), Ca concentrations increased slightly throughout the experimental duration without achieving any apparent steady-state concentration, with final concentrations ~5–6 mg L^{-1}. In contrast, Ca concentrations increased in all of the three experiments reacting ESD cement. In CEM-1 and CEM-2, Ca concentrations increased to >50 mg L^{-1} by the end of the experiment without indication of reaching any steady-state. After week two, Ca increased at an increasing rate in CEM-1 and Ca concentrations in CEM-2 appear to have increased linearly with time. Ca concentrations in CEM-3 also increased, though less dramatically; concentrations appeared to level off between weeks two and four at ~15 mg L^{-1}.

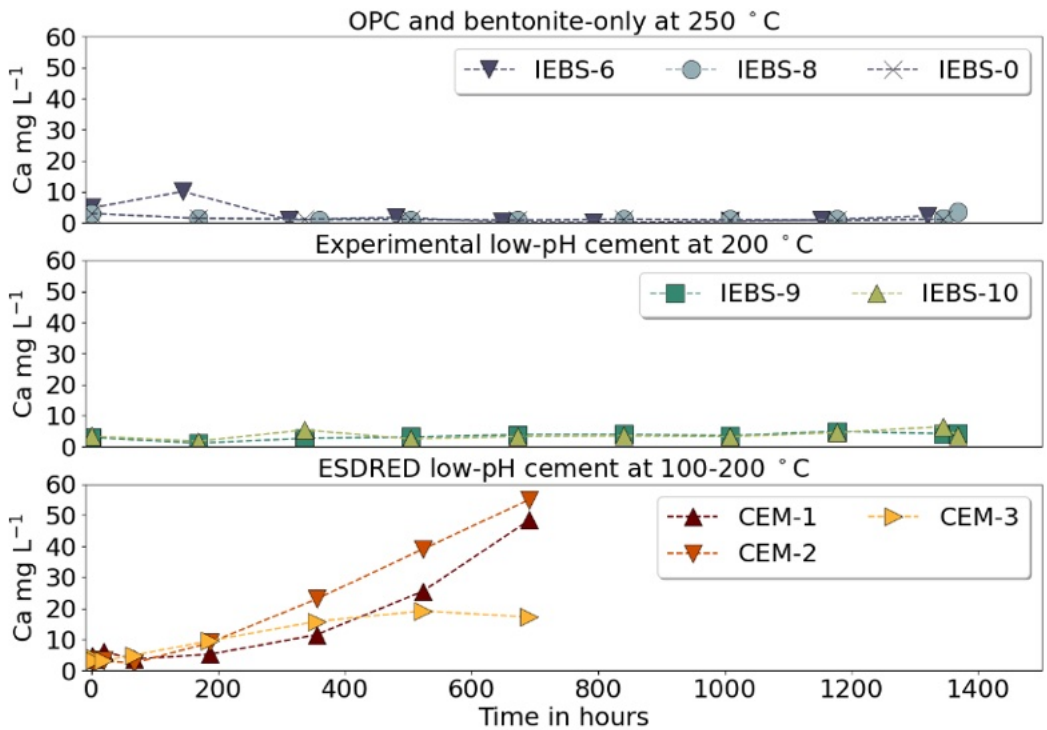

Figure 9-5. Concentration in mg L^{-1} of calcium in the sampled fluids.

In IEBS-0, -6, and -8, as well as in CEM-1, -2, and -3, Na behaved conservatively and remained similar in magnitude to the concentrations of the initial Grimsel GW solution (~116 mg L^{-1} for the IEBS series and ~130 for the CEM series) (Figure 9-6). In contrast, Na concentrations in IEBS-9 and -10 increased continually over the first two to four weeks before coming to a comparatively elevated quasi-steady-state concentration (~300–350 mg L^{-1}) after week four.

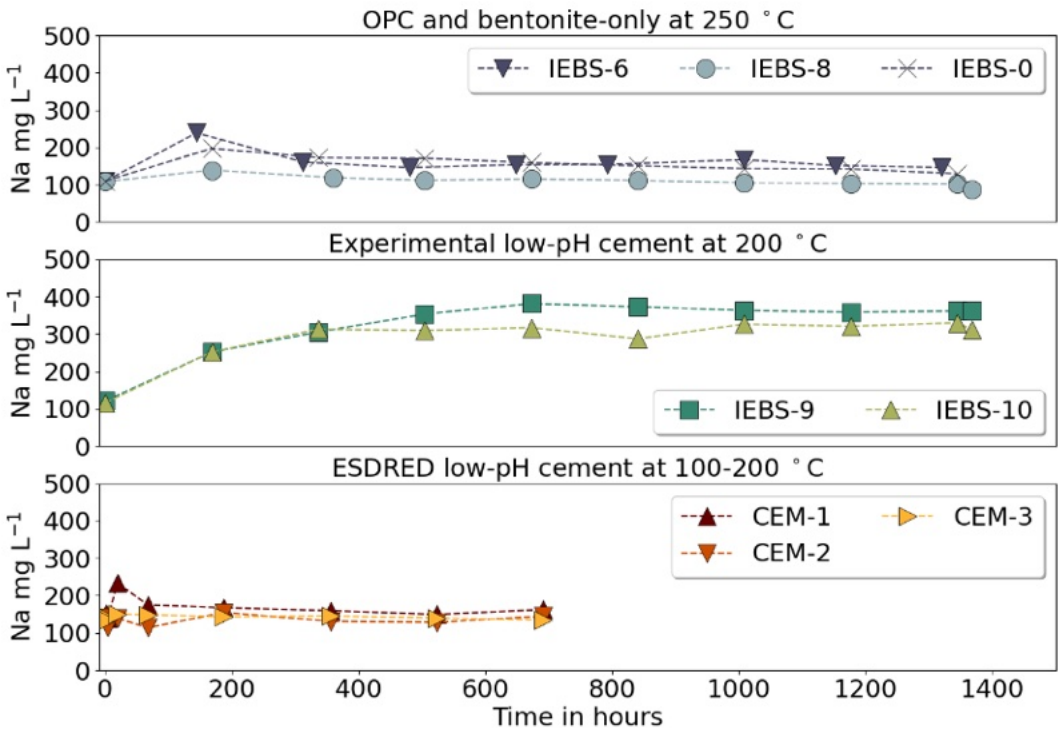

Figure 9-6. Concentration in mg L^{-1} of sodium in the sampled fluids.

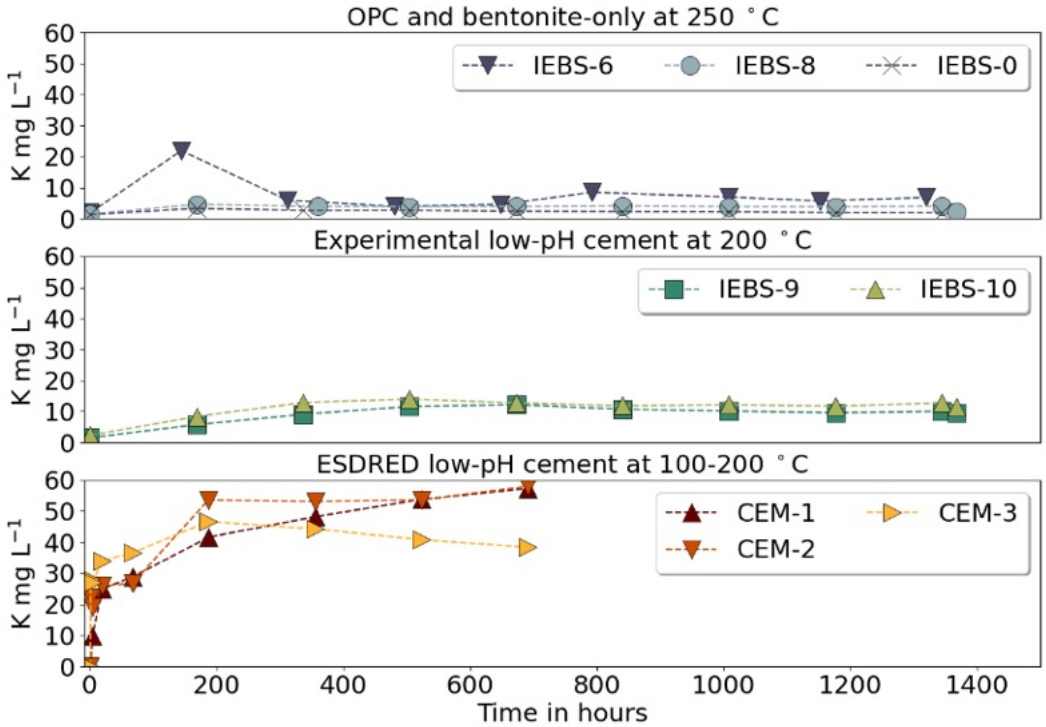

Figure 9-7. Concentration in mg L^{-1} of potassium in the sampled fluids.

Silica. Silica concentrations in all IEBS experiments increased rapidly during the first one to two weeks of experiment time (Figure 9-8), approaching apparent steady-state concentrations of 400 to 600 mg L^{-1} after the first one to two weeks of reaction time. SiO_2 concentrations were highest in the experiment that reacted only bentonite at 250 °C and generally remained slightly higher in the OPC experiments reacted at 250 °C than in the VU cement experiments reacted at 200 °C. In experiments reacting ESD cement and no bentonite, silica increased in all experiments to relative steady-state concentrations achieved within the first week of experiment time. The final/steady state SiO_2 concentrations of each CEM experiment increased with increasing experimental temperature, from 100 to 200 °C.

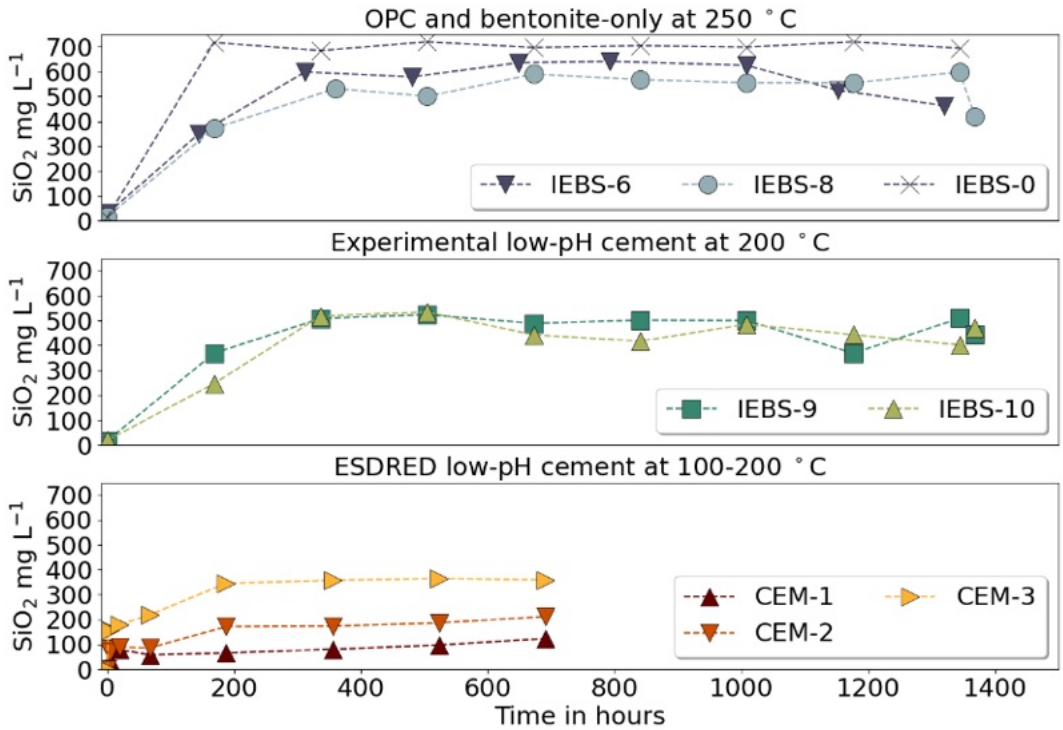

Figure 9-8. Concentration in mg L^{-1} of silica in the sampled fluids.

Aluminum. At 250 °C, Al concentrations were increased in the OPC experiments IEBS-6 and -8 compared to the bentonite-only experiment IEBS-0. Al concentrations in the two experiments reacting VU cement at 200 °C did not have elevated Al concentrations, having had an initial increase in Al to ~2 mg L^{-1} in the first week of reaction time before decreasing over the remaining experiment duration. Al concentrations in CEM-1 and CEM-2 were below detection limits (plotted at 0 mg L^{-1} on Figure 9-9) and increased slightly in CEM-3 in the first week of experiment time to just over 1 mg L^{-1} before decreasing throughout the experiment remainder (Figure 9-9).

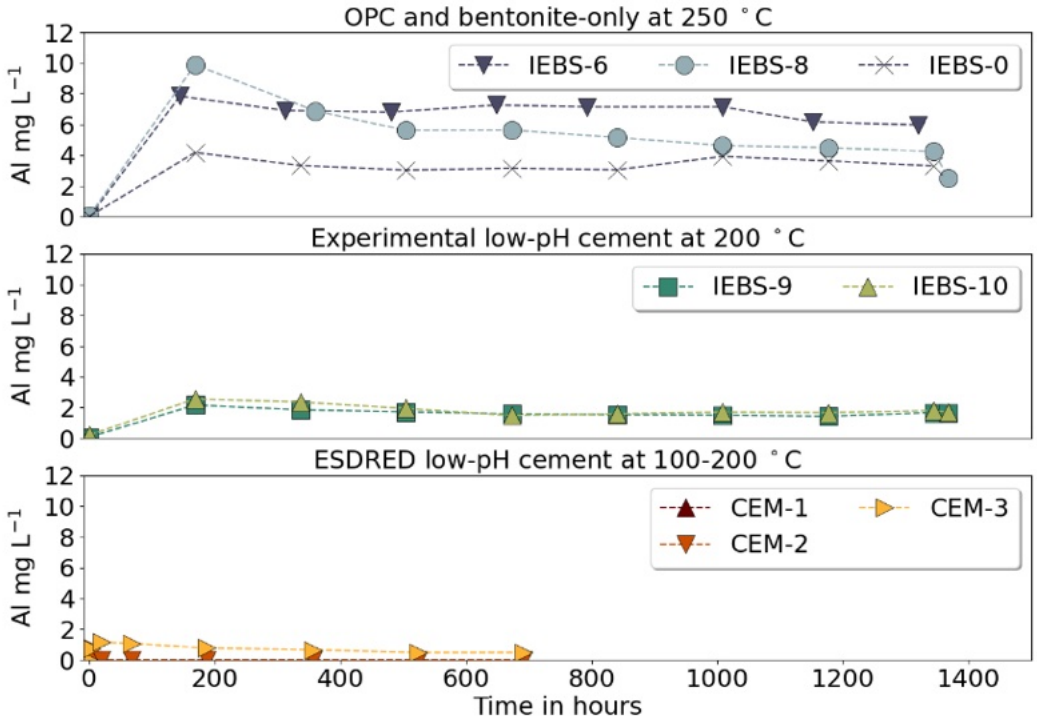

Figure 9-9. Concentration in mg L^{-1} of aluminum in the sampled fluids.

Iron and Magnesium. Iron concentrations in the IEBS experiments were generally below or near the minimum detection limits for the experiment duration and are not included in figures here. Magnesium concentrations in all experiments decreased from the initial concentration in the Grimsel GW solution (> 10 mg L^{-1}) within the first week of experiment time and remained below the minimum detection limits for the duration of all experiments.

Chloride. Chloride concentrations in the baseline experiment with Wyoming bentonite and Grimsel synthetic GW (IEBS-0) generally remained between 10 and 15 mg L^{-1}. In the experiments with the OPC, Cl concentrations were initially elevated in IEBS-6 starting around 33 mg L^{-1} and lower in IEBS-8 (~13 mg L^{-1}) before converging by the end of each experiment to values between 10 and 20 mg L^{-1}. Cl concentrations in IEBS-9 and -10 that reacted VU cement at 200 °C initially increased in the first week then remained at an apparent steady-state concentration of ~25 mg L^{-1}. In the CEM- series, Cl concentrations initially increased in the first week in all experiments, with greater increases at lower temperatures (Figure 9-10).

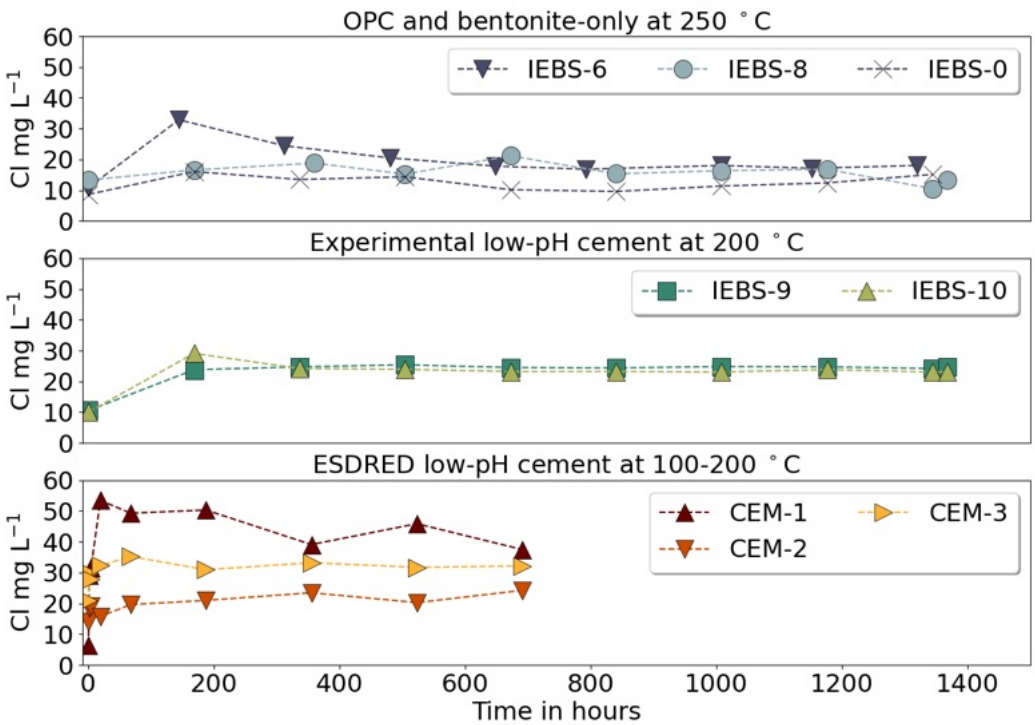

Figure 9-10. Concentration in mg L^{-1} of chloride in the filtered reaction fluids.

Sulfate. Sulfate concentrations in IEBS-0 initially increase sharply from the first to the second sampling, remain between 200 and 300 mg L^{-1} for the remainder of the experiment, and drop to 100 mg L^{-1} on experiment quench. SO_4^{2-} concentrations were less variable in the experiments with OPC (IEBS-6 and -8), mostly remaining between 150 and 250 mg L^{-1} and were higher in the two experiments reacting VU cement at 200 °C with final concentrations from ~550 to 650 mg L^{-1}. In the three experiments reacting ESD cement, SO_4^{2-} increased sharply in the first week of experiment time and continued increasing at a slower rate for the remainder of all experiments. Concentrations were relatively similar in CEM-1, -2, and 3, with final concentrations at ~400 mg L^{-1} (Figure 9-11).

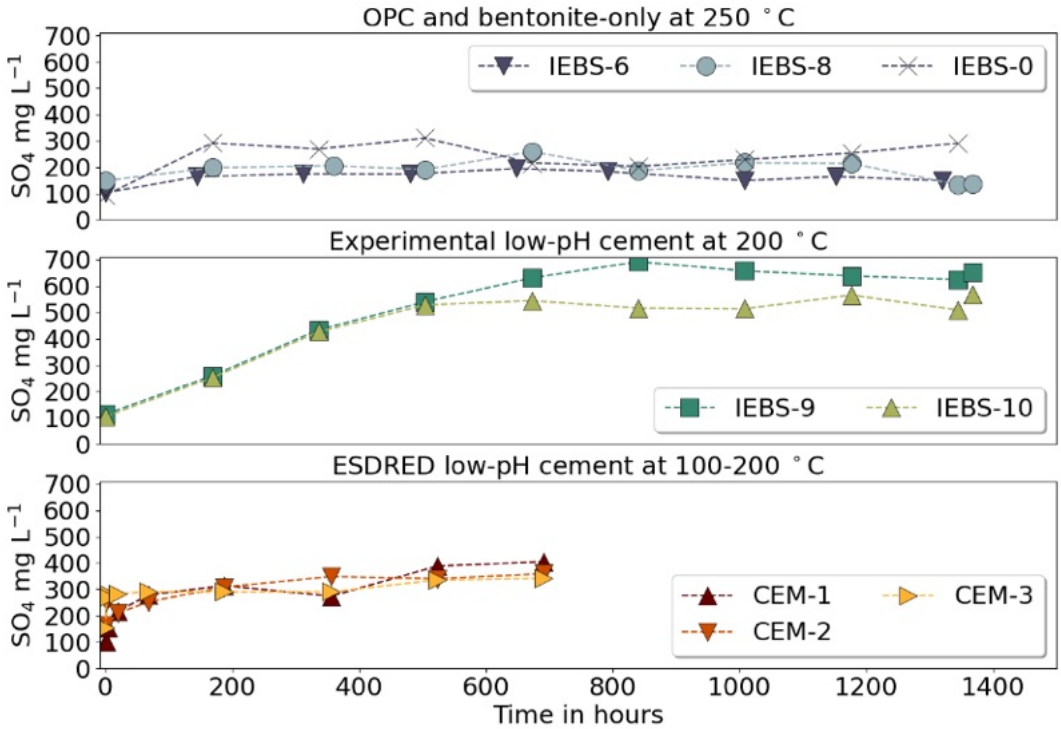

Figure 9-11. Concentration in mg L^{-1} of sulfate in the filtered reaction fluids.

9.3.2 Quantitative X-ray Diffraction (QXRD)

QXRD analyses of the starting material mixture and the bulk reaction products from IEBS-0, -6, and -8-10 are presented in Figure 9-12 and Caporuscio, et al. 2023, Appendix C. The results show changes in bulk mineralogy as the result of the hydrothermal reaction. The approximate starting reaction mixture for each experiment is listed in Table 9-1. The bulk mineralogy of a representative sample of Wyoming bentonite, Grimsel granodiorite, and the starting mixture is reported in Caporuscio, et al. 2023, Appendix C.

IEBS-0. Experiment IEBS-0 was a baseline experiment to explore Wyoming bentonite alteration in the synthetic Grimsel GW solution. Observed mineralogy changes include the reduction in feldspar and clinoptilolite and an increase in smectite/illite/illite-smectite.

IEBS-6 and IEBS-8. The inclusion of a cured OPC cement chip with Wyoming bentonite and Grimsel granodiorite reactants resulted in different mineralogical changes. The sample analyzed included bentonite and granodiorite components; the cement chip was intact and removed from the mixture for separate post experiment characterization. The main mineralogical changes in the bentonite groundmass included a reduction in clinoptilolite and the formation of analcime and amorphous material (Figure 9-12).

IEBS-9 and IEBS-10. IEBS-9 and -10 were conducted at a lower temperature than the other IEBS experiments (200 ° instead of 250 ºC) and included VU cement with Wyoming bentonite and Grimsel GW solution. IEBS-10 additionally included Grimsel granodiorite in the reactants. The major post-reaction change observed in the Wyoming bentonite in IEBS-9 was the reduction of the mass percent of clay phases coupled with an increase of heulandite-clinoptilolite. In EBS-10, the main mineralogical

changes include the reduction in mass percent clay and the increase of heulandite-clinoptilolite along with the formation of analcime and an amorphous material (Figure 9-12).

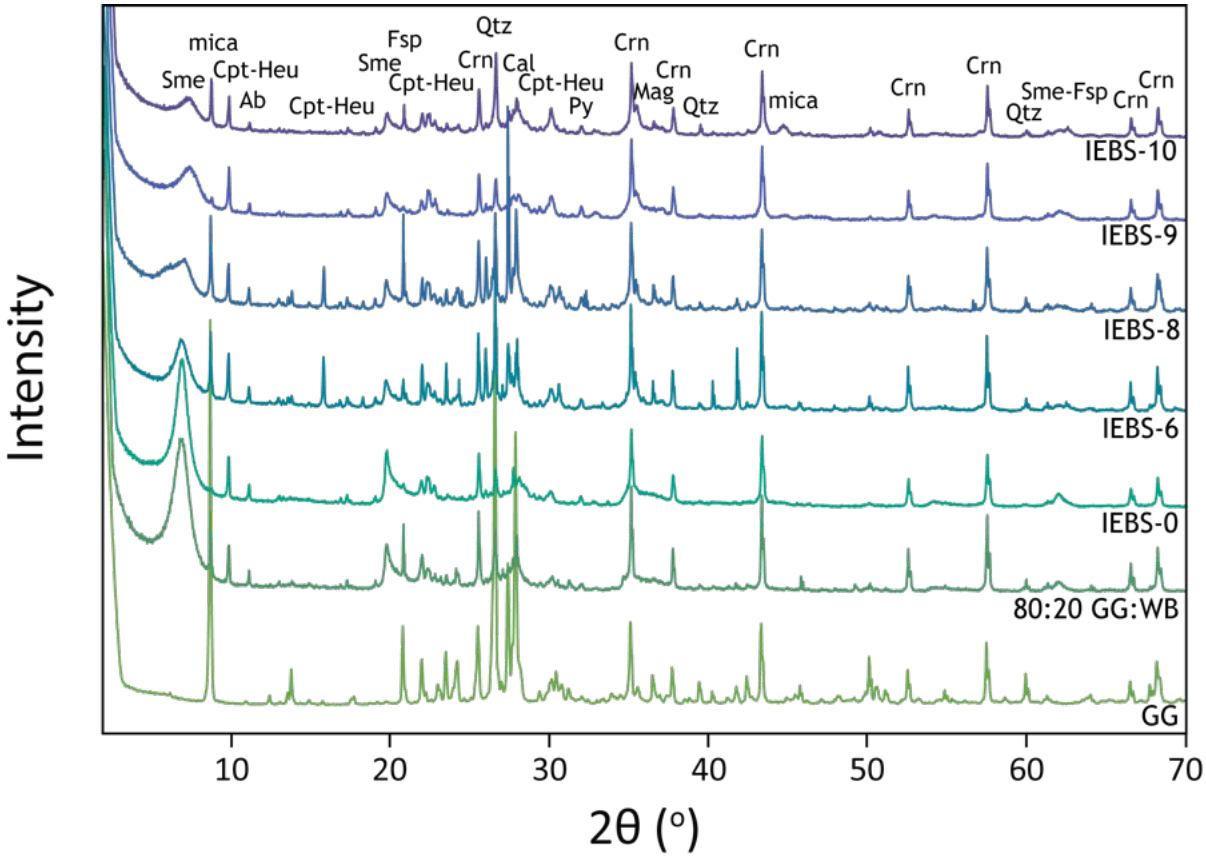

Figure 9-12. QXRD patterns of reacted bentonite and granodiorite from IEBS-0, -6, -8, -9, and -10 compared to unreacted bentonite and granodiorite. Peaks correspond to smectite (Sme), mica, clinoptilolite-heulandite (Cpt-Heu), albite (Ab), corundum (Crn), feldspar (Fsp), quartz (Qtz), pyrite (Py), magnetite (Mag), and smectite-feldspar (Sme-Fsp)

9.3.2.1 Cement Chip XRD

OPC. XRD of the OPC indicated the presence of portlandite, calcite, and minor amounts of brownmillerite, heulandite, and larnite in the starting mineralogy (Figure 9-13). Portlandite was completely absent in the reacted cements from IEBS-6 and -8. Interaction with EBS components (WB and GG) produced zeolites, clinoptilolite, and feldspars on the cement. Zeolites were particularly abundant after reaction with 316SS in IEBS-8.

VU Cement. The VU cement initially contained calcite and brownmillerite with minor amounts of a calcium aluminum silicate phase, potentially wollastonite (Figure 9-14). A broad hump between 20° and 40° 2θ represents the amorphous silica fume replacement. Reacted cement from IEBS-9 and -10 contained relatively less calcite and brownmillerite but included smectites, derived from the Wyoming bentonite included in both experiments. The amorphous signal is reduced or absent from the reacted cements.

ESD Cement. The unreacted ESD cement contained calcium carbonate and silicon oxide (Figure 9-15). In the three reacted CEM cement, calcium carbonate and silicon dioxide were still present, along with the addition of tobermorite.

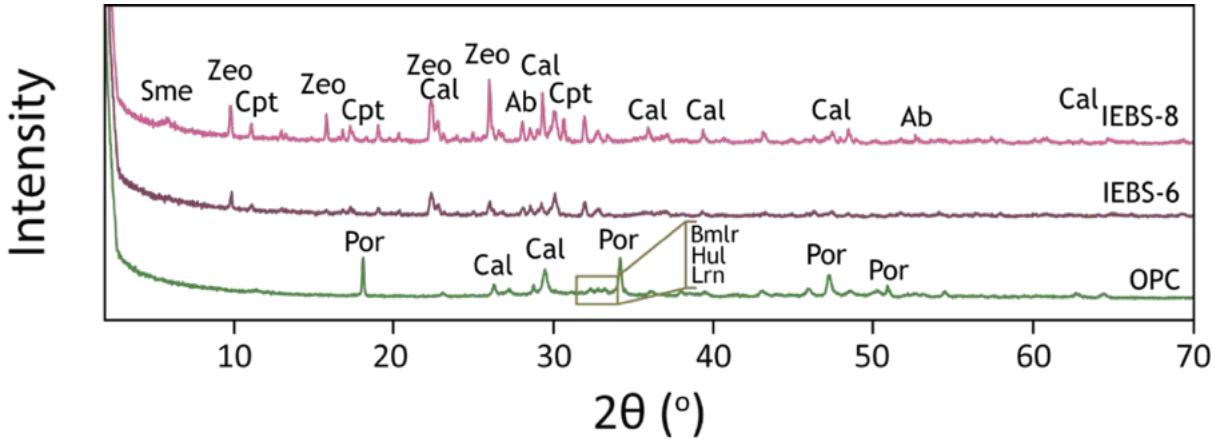

Figure 9-13. QXRD patterns of reacted cement from IEBS-6 and -8 compared to unreacted OPC. Peaks correspond to smectite (Sme), zeolite (Zeo), clinoptilolite (Cpt), portlandite (Por), albite (Ab), calcite (Cal), brownmillerite (Bmlr), heulandite (Hul), and larnite (Lrn).

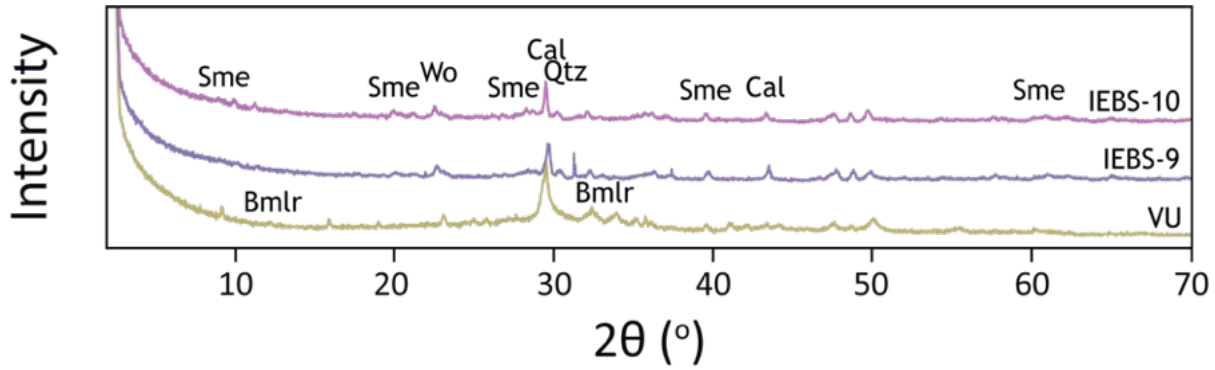

Figure 9-14. QXRD patterns of reacted cement from IEBS-9 and -10 compared to unreacted experimental low-pH cement. Peaks correspond to smectite (Sme), brownmillerite (Bmlr), wollastonite (Wo), calcite (Cal), and quartz (Qtz).

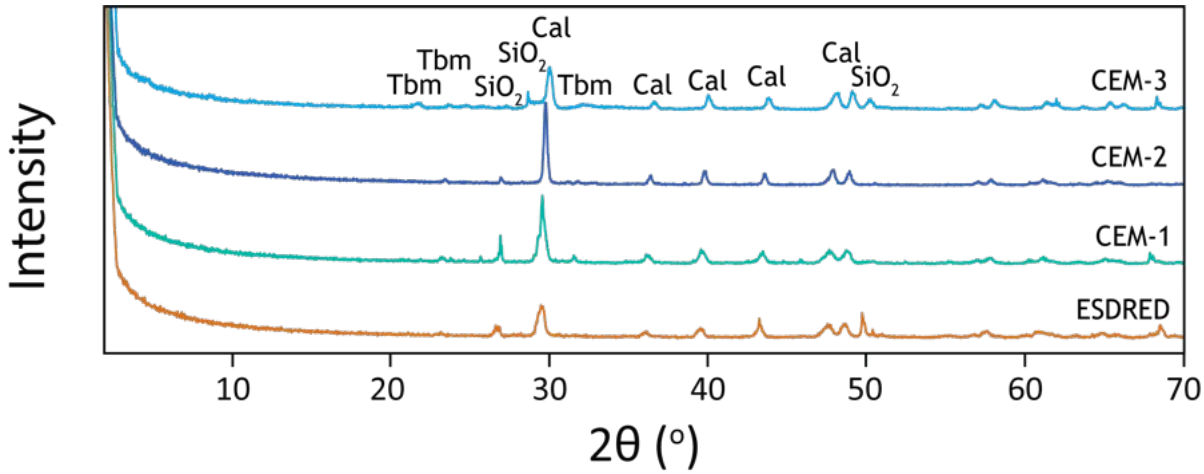

Figure 9-15. QXRD patterns of reacted cement from the CEM series experiments compared to unreacted ESD cement. Peaks correspond to tobermorite (Tbm), silica (SiO_2), and calcite (Cal).

9.3.3 Clay XRD

The clay-size fraction (< 2 µm) was separated via density separation in deionized water from a gently crushed portion of the reaction products from each experiment. While crushing, discrete particles of Grimsel granodiorite were removed. In the case of IEBS-6, -8, -9, and -10, the cement chips were separated before the clay sample was selected. The XRD patterns of the ethylene glycol-saturated, oriented clay fractions can be used to determine alterations to the clay mineral structure through shifts in the peak positions, which were used to calculate clay mineral expandability. The ethylene glycol-saturated peak positions are presented in Table 9-3 and the resulting XRD patterns are plotted in Figure 9-16.

Results from IEBS-0 show decreased clay expandability calculated from the difference between the d002 and d003 peaks from these samples show an increase in clay expansion. In comparison, results from IEBS-6 and IEBS-8 through -10, which included OPC and low pH cement chips, show slightly lower expandabilities than the clay fraction from experiments without cement, but still slightly increased in comparison to unreacted Wyoming bentonite. However, differences of less than several percent are not considered statistically significant given the natural variability of the Wyoming bentonite mineral assemblage.

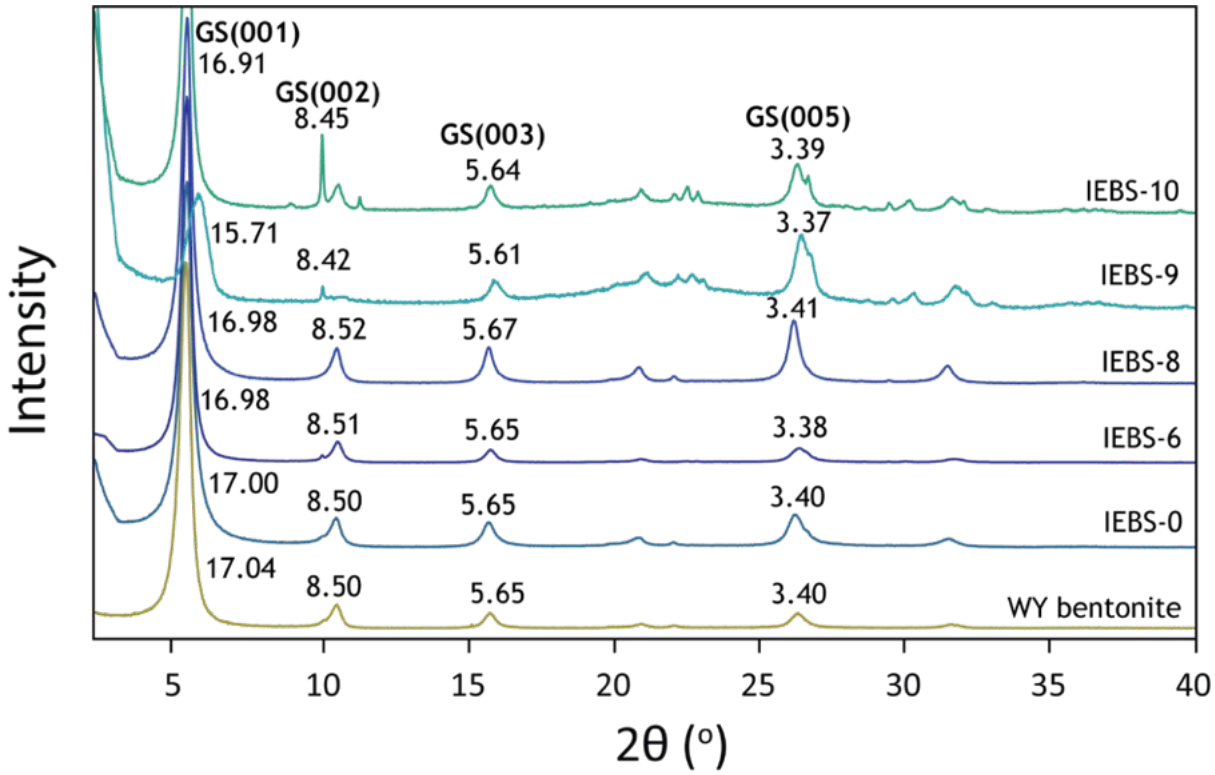

Figure 9-16. XRD patterns of the oriented, ethylene glycol-saturated, <2 µm fraction from IEBS-6, -8, -9, and -10 compared to that of unreacted WY bentonite. Presented values are d-spacings for major glycolated smectite (GS) peaks.

Table 9-3. Glycolated smectite (GS) peak positions for the < 2 µm clay fraction separated from the Wyoming bentonite. Expandability and percent illite (%I) were calculated based on the difference in position of the 002 and 003 glycolated smectite peaks.

Sample	1		2		3		5			1	2	3	
EG-smectite	**2Θ**	**d (Å)**	**2Θ**	**d (Å)**	**2Θ**	**d (Å)**	**2Θ**	**d (Å)**	**Δ2Θ**	**%Exp**	**%Exp**	**%Exp**	**%I***
WY bentonite	5.18	17.04	10.40	8.50	15.66	5.65	26.30	3.39	5.26	100	102	103	0
Wyoming bentonite control													
IEBS-0	5.20	17.00	10.40	8.5	15.60	5.70	26.20	3.40	5.20	103	106	106	0
OPC chip													
IEBS-6	5.20	16.98	10.38	8.51	15.68	5.65	26.34	3.38	5.30	98	99	100	1
IEBS-8	5.20	16.98	10.38	8.52	15.62	5.67	26.12	3.41	5.24	103	106	106	0
VU cement chip													
IEBS-9	5.62	15.71	10.50	8.42	15.79	5.61	26.44	3.37	5.28	99	100	101	0
IEBS-10	5.22	16.91	10.46	8.45	15.70	5.64	26.30	3.39	5.24	101	103	104	0

1: $\%Exp = 973.76 - 323.45\Delta + 38.43\Delta 2 - 1.62\Delta 3$ (Eberl et al., 1993)

2: $\%Exp = 1517.8 - 548.49\Delta + 68.35\Delta 2 - 2.90\Delta 3$ (Eberl et al., 1993)

3: $\%Exp = 766.01 - 194.10\Delta + 12.924\Delta 2$ (Moore & Reynolds, 1997)

*NEWMOD calibration from Leupin et al., 2014

9.3.4 X-Ray Fluorescence (XRF)

XRF analyses for bulk rock oxide chemistry were performed on the unreacted starting material and the bulk reaction products (Table 9-4). Fe-oxides increased in all samples relative to the initial Wyoming bentonite due to the addition of iron buffers (Table 9-1).

In the Wyoming bentonite control experiment (IEBS-0), the bulk chemistry of the reaction products was generally unchanged from the composition of the unreacted bentonite. The Wyoming bentonite + Grimsel granodiorite + cured OPC chip experiments (IEBS-6 and -8) were identical except for the stainless steel included in IEBS-8. The measured weight percent (wt.%) oxide values were fairly consistent between the two experiments. There were only slight variations in CaO, Fe_2O_3 and loss on ignition (LOI). In comparison to the starting mixture chemistry, wt.% SiO_2 and Al_2O_3 decreased and wt.% Fe_2O_3 increased.

The XRF results for the Wyoming bentonite ± Grimsel granodiorite + VU cement chip experiments (IEBS-9 and -10) varied in the measured weight percent oxide values due to the absence of Grimsel granodiorite in IEBS-9. Both IEBS-9 and -10 had increased CaO and decreased LOI, SiO_2, and Al_2O_3. Fe_2O_3 also increased in both experiments.

Bulk geochemistry (XRF) was not performed on the reacted cement cylinders or chips as of the end of FY23: due to the heterogeneity of the ESD cement (as described in Section 9.2.2.1), the mass of XRF sample needed to ensure reproducibility of measurement for the ESD cement is currently being evaluated.

Table 9-4. X-Ray fluorescence (XRF) analyses of the starting materials and solid reactants from IEBS-0, -6, -8, -9, & -10.

	No cement	OPC experiments		VU cement experiments		Unreacted Starting Material				
XRF Wt.%	**IEBS-0**	**IEBS-6**	**IEBS-8**	**IEBS-9**	**IEBS-10**	**OPC**	**VU cement**	**GG**	**WY Bent**	**WB:GG 80:20 (Calculated)**
Na_2O	2.94	2.71	3.43	2.41	2.57	0.09	0.08	2.97	2.85	2.87
MgO	1.60	1.16	1.20	1.39	1.14	2.60	1.21	0.62	1.64	1.44
Al_2O_3	18.70	14.34	16.71	16.76	15.20	3.21	2.07	11.34	19.50	17.87
SiO_2	60.73	57.11	60.02	58.03	55.31	17.43	51.52	76.18	61.90	64.76
P_2O_5	0.05	0.06	0.08	0.04	0.07	0.10	0.14	0.15	0.04	0.07
K_2O	0.67	1.57	2.34	0.69	1.41	0.43	0.56	3.57	0.57	1.17
CaO	0.81	2.34	2.12	2.56	2.12	55.00	29.93	1.52	0.86	0.99
TiO_2	0.23	0.52	0.43	0.32	0.48	0.17	0.13	0.4	0.14	0.19
MnO	0.03	0.07	0.07	0.04	0.09	0.09	0.04	0.06	0.01	0.02
Fe_2O_3	6.26	14.52	9.62	10.28	15.73	2.90	1.64	2.85	4.12	3.87
LOI	7.77	5.36	3.76	7.28	5.64	17.80	12.60	0.19	8.21	6.61
Total	99.79	99.75	99.76	99.81	99.75	99.81	99.93	99.85	99.85	99.85

9.3.5 Microprobe

Reaction products were analyzed via electron microprobe (EMP) to determine the major element composition of mineral phases. The EMP analyses primarily targeted the clay matrix, steel alteration products, altered glass shards, and other secondary minerals. Analysis of the reaction products from IEBS-6 were completed in FY22 and are reported in Caporuscio, et al. 2023, Appendix D. Analyses of reactants from IEBS-8, -9, -10, and -0 are complete or ongoing, and reactants from CEM-1, -2 and -3 will be analyzed in FY24. The data reduction and interpretation is ongoing and will be included and discussed in the FY24 report.

9.3.6 Scanning Electron Microscope (SEM)/EDS

9.3.6.1 Bentonite ± Grimsel Granodiorite Matrix

IEBS-0. Clay in the reaction products of IEBS-0 has a foily texture (E1). Analcime spheres are observed locally. Feldspar with dissolution texture was also observed (E1 [A, B]).

IEBS-6 and IEBS-8. The clay matrix of IEBS-6 and IEBS-8 is altered throughout to include analcime, garronite, feldspars, and erionite (Caporuscio, et al. 2023, Figures E2, E3, E4). The Grimsel granodiorite included in the experiments did not experience any significant mineral reactions.

IEBS-9 and IEBS-10. The montmorillonite from the experiments reacted with low pH cement was foil-like in texture with minor feldspars (Caporuscio, et al. 2023, Figures E6, E7). In IEBS-10 only, there was no alteration texture or new mineral growth on the Grimsel granodiorite fragments.

9.3.6.2 Steel-bentonite Interface

The surface of the 316SS reacted in IEBS-8 was also coated in Fe-saponite. Clusters of analcime, garronite, and clay were locally attached to the mineralized surface (Caporuscio, et al. 2023, Figure E5).

9.3.6.3 Cement

OPC. SEM and XRD analyses of the unreacted OPC material showed various cement phases. In IEBS-6 and IEBS-8, which contained OPC in the starting materials, Na-rich analcime was prevalent throughout the reaction product (Caporuscio, et al. 2023, Figures E3, E5) along with minor erionite-Ca and garronite (Caporuscio, et al. 2023, Figure E2 [C], E3 [B]). The fragments of the Grimsel granodiorite did not experience significant alterations and only occasional dissolution texture on the surface of feldspar grains was observed (Caporuscio, et al. 2023, Figure E2 [D]). The OPC chips extracted from IEBS-6 and IEBS-8 both have a layer of clay with zeolite embedded on the surface (Caporuscio, et al. 2023, Figures E3 [A, B], E5 [D]). A thin section showing a cross section of the cement chip was created and will be characterized in FY24.

VU cement. Backscatter (BSE) images of the unreacted low pH cement consisted of a calcium silicate with a minor amount of lime and ferrite embedded in the matrix. SEM of the low pH cement included in IEBS-9 has a calcium silicate matrix with the formation of platy calcium silicates on the surface and in dimples on the surface. Ferrite was exposed at the surface. The reacted low pH cement from IEBS-10 was partially covered in a layer of calcium silicate spheres with patches of smectite (Caporuscio, et al. 2023, Figures E7).

ESD cement. SEM-BSE imaging of ESD cement rounds embedded in epoxy and prepared cut in cross-section showed the formation of a reaction rim that formed at the cement-solution interface at all reaction temperatures (100, 150, and 200 °C). The reaction rim appeared to completely cover the surface of the cement, forming a 10 to 20 µm rim of secondary alteration products at the surface. The apparent thickness of this rim in cross-section was not substantially different or increased with increasing temperature. Positive identification of the chemistry of the reaction rims was complicated by the carbon-rich epoxy

intermingled with the phases at the cement surfaces in the epoxy-mounted samples. Complementary investigation of the surfaces of cement chips additionally reacted in all of the CEM experiments indicated that the secondary minerals formed at the surfaces of experiments CEM-1 and CEM-2 (reacted at 100 and 150 °C, respectively) was largely calcite, while the secondary reaction rim at the surfaces of ESD cement chips reacted in CEM-3 (200 °C) was dominated by CSH minerals (Figure 9-17).

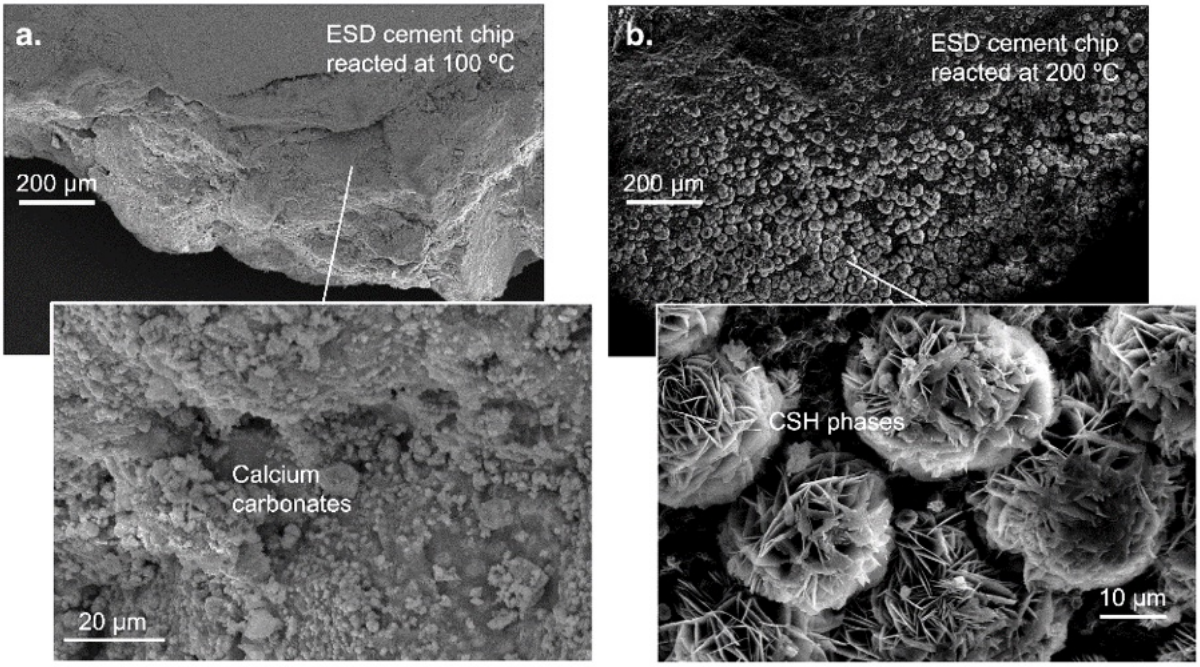

Figure 9-17. SEM micrographs of ESD cement chips reacted in CEM-1 and CEM-3. (a). BSE images of the surface of a ESD cement chip reacted at 100 °C, with inset showing the morphology of secondary phases at the cement surface. EDS analyses showed these phases are chemically consistent with calcium carbonate species (calcite, aragonite). (b). SE images of the surface of a cement chip reacted at 200 °C showing the morphology of secondary phases at the cement surfaces. The phases were identified as CSH by morphology and EDS analysis.

9.4 Discussion

9.4.1 Hydrothermal interaction of Wyoming Bentonite, Grimsel Granodiorite, and Groundwater Solution

Interaction of Wyoming bentonite and synthetic Grimsel GW was characterized in IEBS-0. QXRD results showed a decrease in clinoptilolite and plagioclase and an increase in smectite. XRD results showed that smectite structures were not altered during the 8-week experiment. Locally, analcime crystals were observed. Observed pH values were around 6. Overall, at 250 ºC, smectite appeared to remain stable, and form from the alteration of minerals such as plagioclase feldspar during the experiment.

Secondary electron SEM imaging of loose powder mounts of the reaction products from all experiments reacting Wyoming bentonite revealed the development of a foily texture in the fine-grained clay matrix. Recrystallization of montmorillonite to non-swelling phases, such as illite or muscovite, was not observed. XRD patterns from the oriented clay fraction indicated that there was no substantial alteration to the montmorillonite structure or expansion capacity (Figure 9-16, Table 9-3). EMP analyses from the clay matrix of all the IEBS experiments had very similar compositions (Caporuscio, et al. 2023, Appendix

D). In terms of alkali elements, the matrix was most enriched in Na (0.15–0.17 atoms per formula unit (apfu)) compared to K (0.02–0.03 apfu) and Ca (0.02–0.03 apfu). Previous hydrothermal studies have illustrated that Na-montmorillonite is not subject to substantial illitization or loss of swelling properties where the bulk system is limited in K availability (Cheshire et al., 2014; Mills et al., 2023). This has been observed in previous experimental work completed at LANL relevant to conditions in argillaceous systems with Wyoming bentonite ± Opalinus Clay (Cheshire et al., 2014; Sauer et al., 2020) and for crystalline systems with Wyoming bentonite ± Grimsel granodiorite (Zandanel et al., 2022; Caporuscio et al., 2020).

Elevated pH may also have a negative impact on the swelling properties of clays even in systems with limited K, particularly leading to the formation of non-swelling clays. Chermak (1992) showed that under pH conditions of 11 to 13, Na-rectorite was formed at 150 to 200 °C within 17 days and fully formed Na-mica (paragonite) developed after 32 days. At relatively high WRRs used in the present cement alteration experiments, such extreme bulk system pH was not achieved. The results from our experiments that did not identify significant alteration of montmorillonite in the bentonite groundmass to non-swelling clay species is then consistent with previous work and adds to a growing body of literature that confirms the possible long-term stability of bentonite in repositories that may experience heating events over their lifetimes.

9.4.1.1 H_2S Generation

Sulfide-induced corrosion of the waste canisters is the primary concern for the Swedish repository systems (Börjesson et al., 2010). Therefore, the Swedish Nuclear Fuel and Waste Management Company (SKB) have emplaced strict sulfur specifications (sulfide content < 0.5 wt. %; total sulfur < 1 wt. %) for the bentonite buffer used in their repositories (Börjesson et al., 2010). Fluid extraction from the IEBS experiments was accompanied by strong $H_2S_{(aq,g)}$ smells during the course of the 250 °C experiments. The reducing conditions in the experiments preserved the $H_2S_{(aq,g)}$ species. Pyrite content of the Colony Wyoming bentonite used in the experiments was ~0.4 wt. % (Table 9-3) and the synthetic Grimsel GW solution contained appreciable SO_4^{2-} (Table 9-2). The $H_2S_{(aq,g)}$ is then likely related to pyrite solubility from the starting Wyoming bentonite in a Cl-bearing solution and the SO_4 concentration of the initial solution (Crerar et al., 1978; Ohmoto et al., 1994). Pyrite dissolution is tentatively corroborated by QXRD results that showed a slight decrease in the abundance of pyrite in the reaction products; however, the low bulk abundance introduced some uncertainty in this result (additionally discussed in Section 9.3.2 on QXRD results).

9.4.1.2 Summary

The mineralogical and geochemical changes observed in the Wyoming bentonite-Grimsel granodiorite experiments can be applied to understanding potential material interactions in a high-temperature, crystalline repository. Montmorillonite remained stable in the 250 ºC hydrothermal experiments, indicating the relatively K-poor bulk composition of the system likely prevented smectite illitization. Preliminary findings suggest that the clay barrier material (Wyoming bentonite) may only experience slight alteration in the initial thermal pulse in a repository setting. These findings will be compared to results after the initial and final stages are completed of the long-term, full-scale demonstrations (HotBENT).

9.4.2 Steel-Bentonite Interface

The findings from our previous investigations on mineral precipitation at the steel-bentonite interface in hydrothermal experiments mimicking a crystalline rock environment have been described in Caporuscio et al. (2018; 2019). These previous reports describe the layered alteration sequence observed on the surface of steel coupons included in experiments with Wyoming bentonite, Grimsel granodiorite, and synthetic Grimsel GW. In general, an Fe-oxide layer is observed to form an alteration layer on the surface

of the steel coupons after six to eight weeks of hydrothermal conditions. The Fe-oxide layer is followed by a thin layer of chlorite and sulfides precipitated from H_2S-bearing fluids. This thin layer is followed by a ~0.30 to 150 µm thick layer of newly crystallized Fe-saponite. The observation of Fe-saponite and sulfide formation was consistent with anticipated results of the Fe-bearing/Si-rich fluids from the leaching of the steel and bentonite dissolution (Cheshire et al., 2018; Jové Colón et al., 2019) as described by the following equation:

$$\begin{aligned} &Fe^{2+} + Ni^{2+} + Cr^{3+} + H_2S_{(aq)} + (Na,K,Ca)_{0.33}\left(Al_{1.67},Fe^{3+}_{0.20},Mg_{0.13}\right)Si_4O_{10}(OH)_{2\ (Sme)} \\ &\quad \rightarrow (Fe,Ni,Cr)_9S_{8\ (Pn)} + (Na,K,Ca)_{0.33}Fe_3(Si_{3.67},Al_{0.33})O_{10}(OH)_{2\ (Fe\text{-}Sap)} \end{aligned} \qquad \textbf{Eq. (9-4)}$$

In previous experiments completed at LANL, the formation of chlorite and CSH minerals were also observed locally attached to steel surfaces. Fe-saponite alteration to chlorite has been achieved by Mosser-Ruck et al (2016) through long duration experiments (up to 9 years), demonstrated by the following equation showing that smectite consumed by dissolution may produce chlorite (chamosite):

$$3\ \text{smectite} + 3Fe + 4H_2O \rightarrow 1\ \text{chlorite} + 3\ \text{quartz} + 2\ \text{albite} + 1\ \text{zeolite} + 3H_2 \qquad \textbf{Eq. (9-5)}$$

In general, higher pH environments associated with cement are expected to inhibit steel corrosion (Kursten et al., 2004). IEBS-8 included 316SS reacted with GG+WB+OPC in a Grimsel GW solution. The results of this reaction showed a layer of Fe-smectite (likely saponite) formed on the steel surface (Figure 9-18, Caporuscio, et al. 2023, E5). Na-smectite, apparently unaltered from the Wyoming bentonite matrix, was found in several sections overlying the Fe-smectite at the steel surface. Calcium alumino silicate hydrate (C(A)SH) minerals (Figure 9-18(b)) and potential zeolites (Caporuscio, et al. 2023, E5 [A, D]) were also embedded in the Na-smectite found at steel surfaces, consistent with the widespread occurrence of zeolites identified in the clay matrix. Cross-sectional BSE analyses from a steel billet embedded in epoxy show a lack of leached layer at the steel surface underlying the secondary precipitates (Figure 9-18(c)).

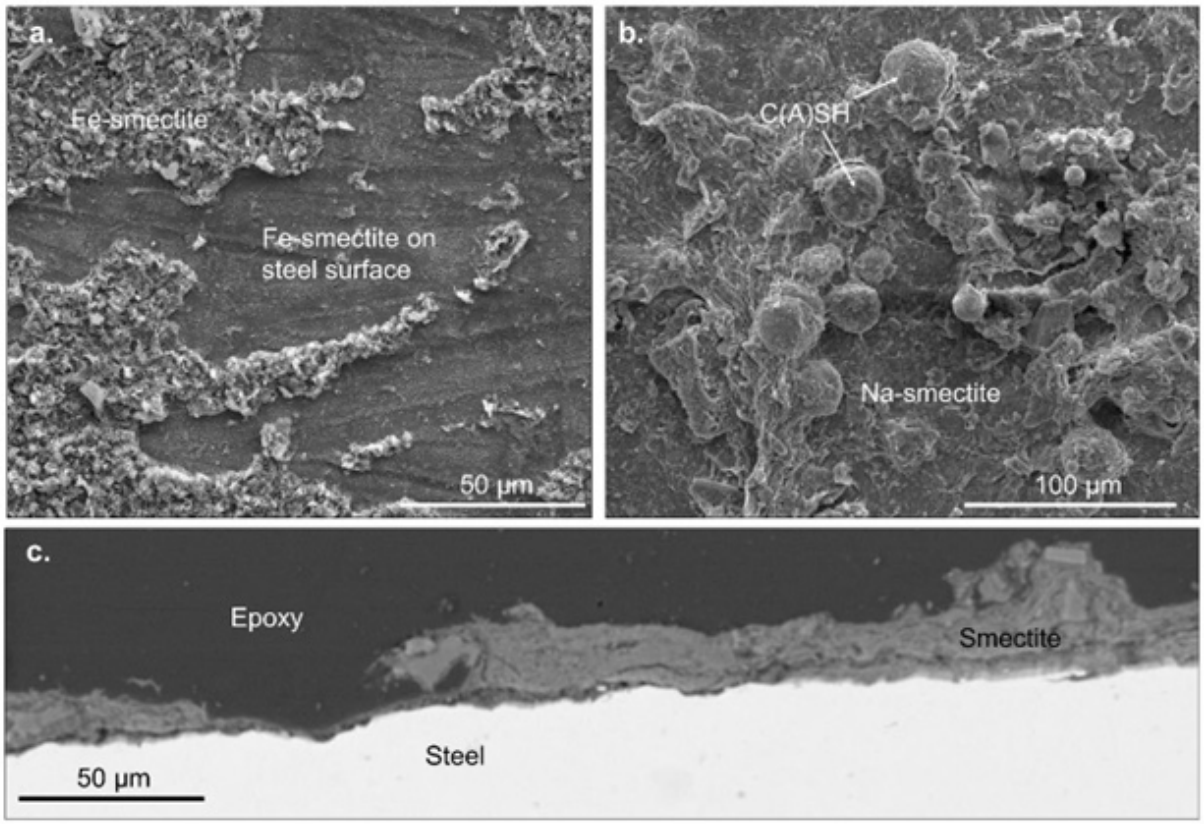

Figure 9-18. SEM micrographs of 316SS reacted in IEBS-8: (a). SE image of smectite or Fe-smectite directly at the steel surface with an overgrowth of Fe-smectite directly overlying the initial formation of smectite. Chemical identification of the smectite directly overlying the steel was complicated by BSE signal from the steel itself. (b). SE image of Na-smectite and C(A)SH phases locally identified overlying the Fe-smectite at the steel surface. (c). BSE image of reacted 316SS billet embedded in an epoxy mount post-reaction and cut in cross-section. Note the smectite overlying the steel directly with no apparent change in density of the steel approaching the reacted surface.

The results from the experiments discussed here indicate that the waste container may act as a substrate for mineral growth in response to steel corrosion. In IEBS-8, a lack of Fe-smectite identified in the bentonite matrix compared to the abundance of Fe-smectite formed directly at the reacted 316SS surface indicates that the Fe in the newly precipitated mineral layers at the steel interface was sourced from the corroding steel. Future work is needed to address the extent these mineral precipitates influence the EBS performance or the repository system, and to whether the minerals observed to form at the steel surface, such as Fe-saponite, will act as a passive protecting layer against further corrosion of the waste containers.

9.4.3 Effects of Cement on EBS Alteration (IEBS-6 and -8 through -10)

The four completed experiments containing cement chips (IEBS-6 and -8 containing OPC; and IEBS-9 and -10 containing low-pH cement) introduced multiple mineral phases and chemical species that were reactive at the high temperature and pressure conditions of the experiments. Both OPC and low-pH cement chips increased solution pH values and resulted in diverse mineral reaction products in

comparison to bentonite only (IEBS-0) or bentonite in contact with other EBS materials sans cement (Zandanel et al., 2022; Jové Colón et al., 2019; Caporuscio et al., 2020).

9.4.3.1 OPC

The inclusion of OPC in IEBS-6 and -8 resulted in elevated bulk solution pH compared to IEBS-0 (pH = ~7.5 versus pH = ~6, respectively: Figure 9-4). It appears that OH^- derived from the OPC chips was either quickly consumed by mineral-forming reactions and/or the system was buffered by zeolite/clay mineral-forming reactions. SEM characterization of the reaction products from IEBS-6 and -8 show zeolite formed throughout the reacted groundmass (Figure 9-19) as well as on the cement chip surface and on the surface of the steel coupon included in IEBS-8 (Figure 9-18, Caporuscio, et al. 2023, E5 [D]). Zeolite phases identified by SEM-EDS include garronite and analcime as well as Ca-bearing analcime (Figure 9-19). The identification of Na-Ca bearing zeolites is consistent with at least the partial solid solution understood to occur between analcime [$Na(AlSi_2O_6)\cdot H_2O$] and wairakite [$Ca(Al_2Si_4O_{12})\cdot 2H_2O$]. In addition, QXRD results from the clay groundmass show the proportion of clay and other precursor mineral phases that were consumed in zeolite and CSH mineral forming reactions (Caporuscio, et al. 2023, Appendix C and Results Section 9.3.2). The formation of 3 to 6 wt.% analcime in the clay groundmass of experiments IEBS-6 and -8 was observed, coupled with a decrease of similar magnitude in wt.% of smectite. Changes in the abundance of other mineral phases was similar to those observed in the experiments without cement. Thus, the formation of zeolite reaction products likely occurred from the interaction of experimental fluids with elevated pH and with the release of elements from minerals in the OPC in a silica-rich environment.

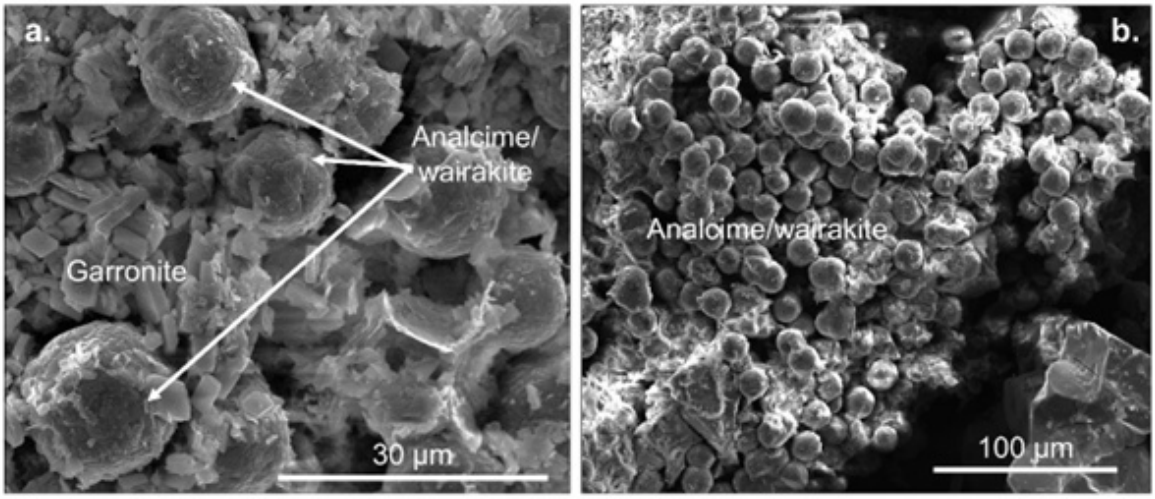

Figure 9-19. Zeolite formation in experiments that reacted OPC. (a). Zeolites (Na-Ca bearing analcime) formed in the clay groundmass reacted in IEBS-8, along with collocated garronite. (b). Na-Ca bearing zeolite noted as analcime/wairakite, identified in the bentonite groundmass reacted in IEBS-6.

9.4.3.2 VU Cement

The addition of VU cement in IEBS-9 and -10 resulted in increased pH of the bulk solution compared to both the experiments without cement and to the experiments reacting OPC chips (Figure 9-4). C(A)SH phases of spherical and plate-like morphologies were identified at the low-pH cement chip surfaces. In contrast to the IEBS experiments that reacted OPC, extensive formation of zeolites (analcime, analcime-wairakite, garronite, erionite) were not observed at the cement surface or in the clay groundmass. In addition, the apparent extent of alteration was substantially greater than that observed of the reacted OPC

in previous experiments (Figure 9-20). The formation of zeolites in the IEBS-6 and -8 and C(A)SH phases in IEBS-9 and 10 is consistent with previous work showing that zeolite formation within bentonite in contact with cement is favored at comparatively lower pH values, while C(A)SH mineral formation occurs at higher pH. However, the impact of system pH vs. temperature on the experimental results is still being evaluated as part of the ongoing experimental collaboration.

C(A)SH Formation

Previous experiments completed at LANL that reacted Grimsel granodiorite with Wyoming bentonite and without cements resulted in the abundant formation of CSH minerals, such as tobermorite ($Ca_5Si_6O_{16}(OH)_2 \bullet 4(H_2O)$) (Caporuscio et al., 2020). C(A)SH phases identified in IEBS-6 and -8 that included OPC as a reactant were comparatively scarce. C(A)SH phases of varying morphologies were identified at the surfaces of the VU cement chips reacted in IEBS-9 and -10 (Caporuscio, et al. 2023, Figures E6 and E7, additionally discussed in Section 9.4.3.4). The formation of tobermorite has previously been experimentally shown to form through bentonite-cement interactions in highly alkaline bulk solutions where pH > ~10 (Savage et al., 2007), and as part of low-temperature (< 120 °C) hydrothermal reactions (Fernandez et al., 2017). Our results where C(A)SH minerals were more abundantly observed in the experiments with VU cement (IEBS-9 and -10) may then reflect the influence of the elevated bulk system pH achieved in IEBS-9 and -10, as compared to IEBS-6 and -8.

The formation of C(A)SH minerals may also affect the pH of the system. Savage et al. (2002) described the formation of the CSH mineral tobermorite with the generalized reaction:

$$Ca^{2+} + SiO_{2\,(aq)} + H_2O \rightarrow \text{tobermorite} + H^+ \qquad \textbf{Eq. (9-6)}$$

in which H^+ is produced. Thus, the formation of C(A)SH minerals, such as tobermorite, may cause the solution to achieve lower pH values. Savage (1997) reported that C(A)SH mineral formation is favored at high pH (> 11.5). It is notable that IEBS-9 and -10 had bulk system pH at or below ~9 for their experimental durations (as measured at 25 °C, Figure 9-4). This suggests a potential pH gradient may have occurred at cement surfaces where the release of Ca^{2+} and OH^- from portlandite alteration creates a local environment that drives the formation of CSH or C(A)SH minerals, which in turn lowers the bulk pH by release of H^+ as in Eq. (9-6).

Additional characterization of the reacted cement was performed by researchers at Vanderbilt University and Sandia National Laboratories in preparation for future work.

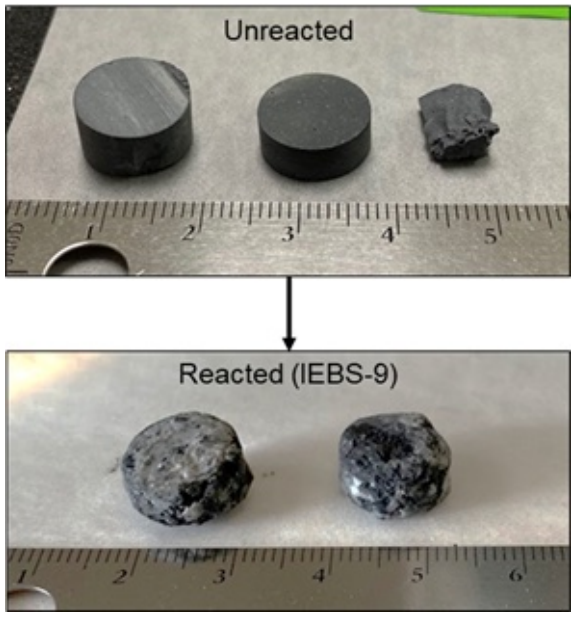

Figure 9-20. VU cement reacted in IEBS-9. Substantial deterioration of the cement product is visible at the macroscale.

9.4.3.3 Summary

The comparison of results between OPC and reacted VU cement may indicate alteration pathways of VU cement at elevated temperature (200 ºC) hydrothermal conditions, both distinct from the alteration pathways of OPC and potentially more rapid. Further study of low-pH materials at elevated temperatures may define temperature thresholds or solution chemistry parameters that are critical to the success of low-pH cement in a crystalline environment.

In full-scale EBS demonstrations, such as FEBEX, the alteration zones observed in bentonite at the cement-bentonite interfaces (at ambient temperatures) only extended several cm into the buffer (Fernández et al., 2017) even after years of interaction at saturated conditions. The experimental results described here provide insight into mineral alteration that may be expected at higher temperatures, such as the observed differences in zeolite types and abundances and sensitivity of solution pH to the reacted cement type, at the timescales of the experiments. The initial results comparing OPC to VU cement alteration processes suggest that, in repository conditions where elevated temperature conditions are possible, the choice of cement products is a factor that should be carefully vetted to optimize long-term performance of the EBS.

9.4.3.4 ESDRED-like low-pH Cement Alteration

Three experiments completed in FY23 reacted ESD cement with the synthesized GW at three different temperatures. Comparing results between experiments then may isolate effects of temperature on the extent of reaction expected from ESDRED-like low-pH cement types over the course of a heating event in a groundwater-saturated environment. The experiments may additionally be compared to previously completed experiments reacting OPC and VU cement at 250 and 200 ºC, respectively. The CEM-series experiments differ from the IEBS experiments reported on above in that they include cement and solution as the sole reactants, without including other materials (bentonite, steel, host rock). The results from these experiments are not then directly analogous to the results of the IEBS experiments reacting OPC and VU cement; however, comparisons can be made between the experiments to isolate trends correlated to

different reactants in the interest of informing future work on the stability of cements in the context of repository EBS materials.

Effect of Temperature on Formation of Reaction Rims

Cross-sectional analyses of the reacted cements from all three reaction temperatures showed the formation of a reacted rim at the cement-solution interface (Figure 9-21). The apparent extent or thickness of this reaction rim was heterogeneous, with the linear extent of reaction at the cement surfaces being similar (~10-30 µm) in each experiment, regardless of the reaction temperature. Cement chip XRD corroborated the heterogeneity of secondary phases, showing that the overall mineralogy of the ESD cement as analyzed by XRD was largely unchanged from the unreacted cement (described in Section 9.3.2.1).

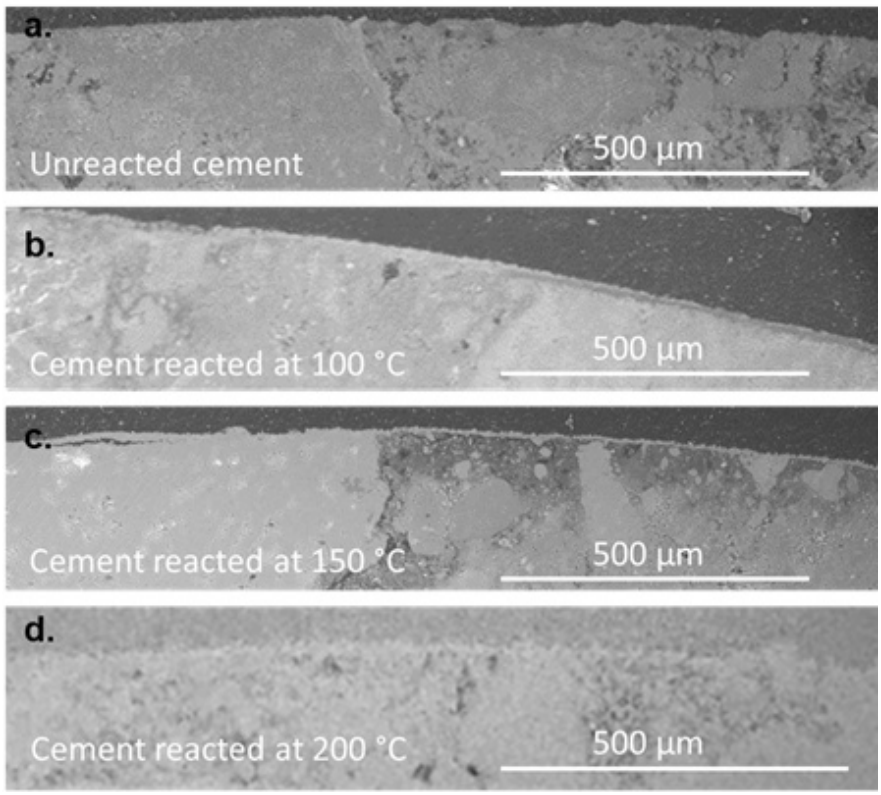

Figure 9-21. BSE images unreacted ESD cement and of the reaction rims at formed at three different temperatures, as viewed from cross-sections formed from the ESD cement cylinders. (a). BSE image of unreacted ESD cement; (b). ESD cement reacted at 100 ºC in CEM-1; BSE image of unreacted ESD cement; (c). ESD cement reacted at 150 ºC in CEM-2; BSE image of unreacted ESD cement; (d). ESD cement reacted at 200 ºC in CEM-3

Effect of Temperature on Secondary Mineral Formation

The types of secondary minerals (calcite, CSH) formed at the surfaces of the ESD cement in experiments completed in FY23 were correlated to the temperature of reaction. Carbonatation of cement is a known process where portlandite in contact with atmospheric CO_2 is altered through the following reaction:

$$\mathrm{Ca(OH)_{2\,(Por)} + CO_{2\,(aq,g)} \rightarrow CaCO_{3\,(Cal)} + H_2O_{(l)}} \qquad \textbf{Eq. (9-7)}$$

During the curing process, carbonatation through exposure to atmospheric or supercritical CO_2 has been extensively studied for industrial applications to tune cement parameters (Šavija & Luković, 2016; Zhang et al., 2017). In hydrothermal conditions, the carbonatation process is dependent on the local availability of CO_2 in solution which will be dynamically responsive to changes in pH and temperature (i.e., Marx et al., 2017). Additionally, carbonatation in hydrothermal conditions will be competing with other processes facilitated by the infiltrating solution chemistry. Figure 9-22 illustrates some of these competing pressures: in all experiments the solution chemistry just before experiment termination is undersaturated with respect to portlandite and oversaturated with respect to calcite. At higher temperatures with lower Ca concentrations, the degree of oversaturation with respect to calcite decreased; in other words, thermodynamic pressure toward precipitation was also decreased. In the CEM-series experiments completed in FY23 at LANL, $CaCO_3$ phases formed at the lower temperatures of reaction (100 and 150 ºC), while dominantly CSH species formed at 200 ºC. Generally, $CaCO_3$ (calcite, aragonite) and CSH minerals (here illustrated by tobermorite) both have decreasing solubility with increasing temperatures (Figure 9-22). At lower temperatures (100 and 150 ºC), fluid is oversaturated with respect to calcite and tobermorite, while at 200 ºC the Ca concentration measured from CEM-3 plots as undersaturated with respect to tobermorite and oversaturated with respect to calcite. In CEM-1 (100 ºC) and CEM-2 (150 ºC), the Ca concentrations increased up to the experiment termination and achieved no steady state, indicating that carbonatation as a process did not consume all of the Ca released from the ESD cement even at lower temperatures where calcium carbonate phases were formed.

The Ca concentrations of the previously completed IEBS experiments plotted against the selected mineral solubilities in Figure 9-22 illustrates the potential impact of $CaSO_4$ minerals (here plotted as anhydrite) on the Ca concentrations in solution. Though $CaSO_4$ minerals were identified in previous experiments, none were identified through XRD or SEM-EDS analyses of the reacted ESD cement from CEM-1 through-3. It is notable that Ca concentrations in CEM-1 and -2 had not achieved an apparent steady-state by the experiment termination. Small amounts of minerals especially formed proximal to the cement surface in the reaction rims may not have been identified by these methods. Future work that includes replicate experiments with longer reaction times may allow the formulation of kinetic rates of alteration of low-pH cements at elevated temperatures.

Zeolite minerals were identified in previously completed IEBS experiments that reacted OPC at 250 ºC (IEBS-6 and -8, discussed above). Analcime and analcime-wairakite were identified extensively at the cement surfaces and in the bentonite matrix reacted in those experiments, and were not identified in any of the experiments reacting VU cement or ESD cement. All of the experiments, however, had solution chemistry that was oversaturated with respect to analcime (Figure 9-22) and wairakite by the time of experiment termination. The lack of formation of zeolite minerals in the experiments is then attributed to lower temperatures, and our results do not preclude the possibility that the zeolite mineral formation is kinetically rather than thermodynamically inhibited at temperatures < 250 ºC.

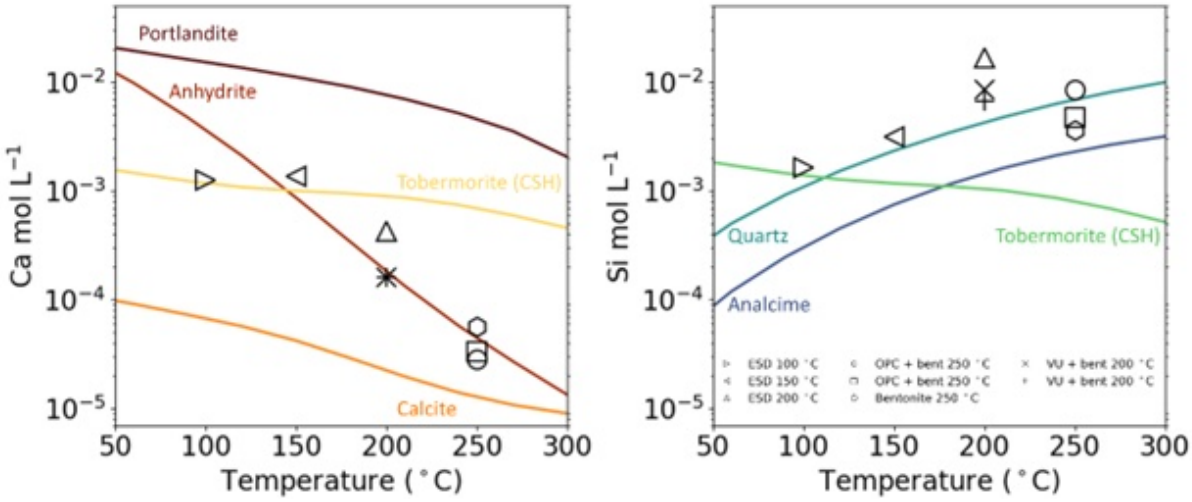

Figure 9-22. Ca and Si solubility with respect to select minerals of interest at the conditions of the initial GW solution. Each curve represents a concentration where the saturation index (SI)=0 in the GW solution over temperature. The area above a curve then indicates oversaturation and thermodynamic pressure toward precipitation, while the area below a curve indicates undersaturation and tendency toward dissolution. The symbols mark the concentration of Ca or Si in each experiment as analyzed in the penultimate sample collected before experiment termination. a. Geochemical stability with respect to Ca-bearing minerals portlandite, anhydrite, tobermorite, and calcite. b. Geochemical stability with respect to SiO_2-bearing minerals quartz, analcime, and tobermorite.

In contrast to Ca solubility results, Si concentrations in all experiments plot above solubility curve for the tobermorite. As tobermorite stability increases with increasing temperature, the increased Si concentrations in CEM-3 then resulted in a greater degree of fluid oversaturation with respect to that mineral, and greater thermodynamic pressure toward precipitation. We note that tobermorite is used in these calculations as a reference CSH mineral with a single idealized formula ($Ca_5Si_6H_{21}O_{27.5} + 10H^+ = 5Ca^{+2} + 6H_4SiO_4 + 3.5H_2O$). During cement alteration, CSH minerals are known to form with a wide range of Ca/Si ratios (0.7 to 2 (Mindess et al., 2003). That the analyzed Ca concentrations plot below the calculated solubility curve of tobermorite while Si concentrations plot above it in the experiments reacted >150 ºC suggests that the CSH minerals formed in CEM-3 had lower Ca/Si ratios than the reference formula for tobermorite used in Figure 9-22. This is consistent with the results calculated from energy dispersive spectroscopy (EDS) analyses that showed atomic Ca/Si ratios of ~0.75 in the CSH minerals formed at the cement chip surfaces reacted in CEM-3, compared to the Ca/Si of ~0.83 in tobermorite. At elevated temperatures the increased Si release from ESD cement in our experiments appears to result in the preferential formation of high-silica CSH minerals. In EBS systems where solution chemistry will be heavily influenced by contributes from silicate and/or carbonaceous host rocks as well as bentonite buffer materials, the Ca/Si ratio may be affected by these inputs. In addition, Al contributions from EBS materials and host rock may result in the formation of C(A)SH phases in addition to CSH phases, as observed in IEBS-9 and -10 and discussed in Section 9.4.3.2, above.

ESD Cement Impacts on Solution Chemistry

The aqueous chemistry additionally illustrates the impact of the ESD cement on bulk system chemistry in the absence of bentonite or host rock minerals. As discussed in Section **Error! Reference source not found.**, alteration of portlandite in water is known to result in elevated porewater pH (Eq. (9-1)). ESD cement and other low-alkali cement formulas are designed to have lower porewater pH by decreasing the

portlandite-to-silica ratio, as discussed in Section **Error! Reference source not found.**of this chapter as well as in Section 9.2. However, bulk solution pH values in the ESD cement experiments and previously completed VU cement experiments were elevated compared to the previously completed OPC experiments (Figure 9-4). The mechanism of increased bulk pH in the ESD and VU cement experiments is still being evaluated. If elevated pH in the ESD and VU experiments was driven by increased portlandite dissolution in cements with less portlandite, this in turn suggests water-portlandite interaction may be increased in low-alkali cements compared to OPC. In OPC, portlandite replacement by calcite during carbonatation (Eq. (9-7)) results in volumetric expansion of the minerals in the cement structure and a systematic loss of porosity in the carbonated zone (Zhang et al., 2017; Šavija & Luković, 2016; Rimmelé et al., 2008; Mindess et al., 2003). In CEM-1 and -2, the calcite-rich reaction rim on the ESD cement may indicate the incipient phase of a carbonatation front advanced into the cement structure that did not form in the cement reacted at 200 ºC. The formation of different types of reaction products at elevated temperatures may then indirectly result in increased porosity or permeability in low-alkali cements, facilitating faster overall dissolution rates for minerals in low-alkali cements than in OPC.

Porosity and/or permeability may also change dynamically during the experiments due to alteration of the non-portlandite fraction in the low-alkali cement. Silica concentrations increased over the course of all three CEM experiments, and the steady-state silica concentrations of the experiments were positively correlated with increasing temperature (Figure 9-8). This is consistent with the increased solubility of many silicate minerals with increasing temperature, including that of amorphous silica and quartz that comprise part of the ESD cement that was reacted in these experiments. XRD results also showed that the quartz fraction identified at the ESD cement surfaces decreased with increasing temperatures (Section 9.3.2). At elevated temperatures, then, low-alkali cement formulations that include increased silica proportions may experience a greater overall mass loss through increased silicate dissolution, and a resulting increase in porosity and permeability throughout the cement structure. This may then increase the susceptibility of portlandite and other highly reactive cement minerals to increased dissolution.

9.4.3.5 Implications for Cement-Bentonite Interactions

The K and Na concentrations are of interest in these experiments as Na/K ion exchange in the montmorillonite fraction of bentonite assemblages may result in loss of some swelling properties. Previous work has shown that K-limited environments result in little exchange and largely preserve the swelling properties of the bentonite matrix, even in hydrothermal conditions (Cheshire et al., 2014; Sauer et al., 2020; Mills et al., 2023; Zandanel et al., 2022). Sources for K in these experiments include the cement reactants, Grimsel granodiorite, and accessory minerals in the bentonite matrix (feldspars, clinoptilolite). The results from the CEM-series experiments indicate a contribution of K from low-alkali cement in the experiments that may impact swelling properties of montmorillonite in the bentonite barrier over time. Comparing results of the low-alkali cement (VU and ESD) experiments with the bentonite-only experiment illustrates that K increased to > 40 mg L^{-1} in CEM-3, while the K increased to ~10 mg L^{-1} in IEBS-9 and did not substantially increase above the initial concentration in IEBS-0 (Figure 9-23). In contrast, Na concentrations in CEM-3 behaved apparently conservatively after an initial increase to ~150 mg L^{-1}, while in IEBS-9 Na concentrations increased to >350 mg L^{-1}. Na concentrations in IEBS-0 increased initially to ~190 mg L^{-1} and decreased for the remainder of the experiment.

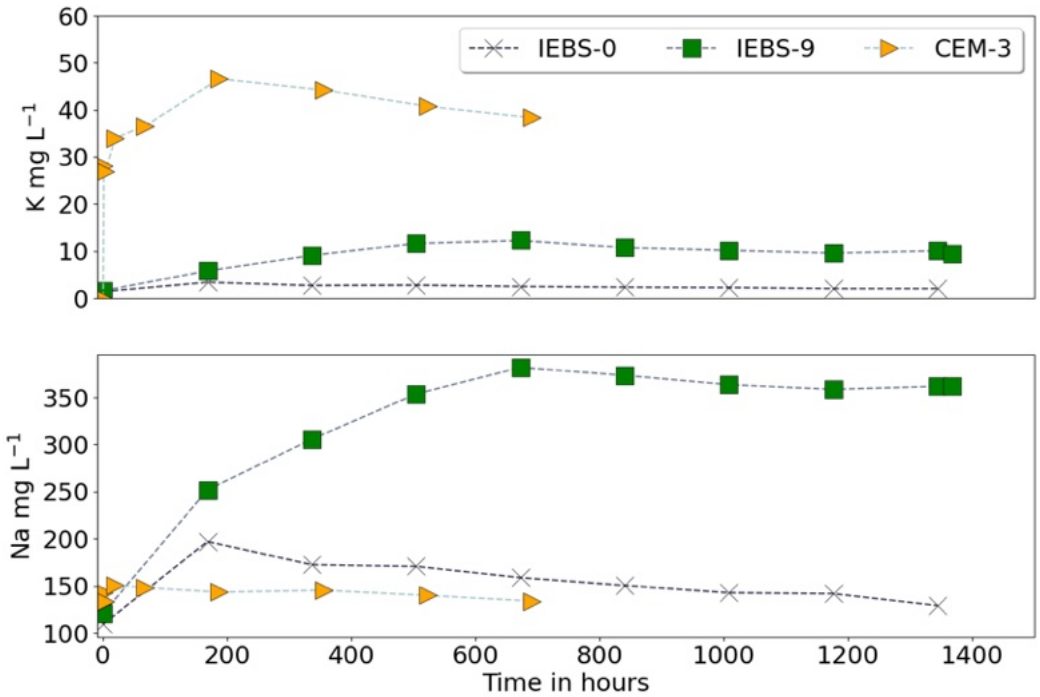

Figure 9-23. Comparison of K and Na concentrations from three selected experiments: IEBS-0 (bentonite and GW at 250 ºC), IEBS-9 (bentonite, GW, and VU cement at 200 ºC), and CEM-3 (ESD cement and GW at 200 ºC).

The paired Na increases with the comparatively minor increase in K in IEBS-9 (and -10) suggest that K that was released from the reacted cement was incorporated into the montmorillonite adjacent to the reacted cement, resulting in increased Na concentrations in the bulk solution. Clay swelling XRD of the bentonite matrix reacted in IEBS-9 and -10 did not show substantial changes to the swelling properties of the bentonite. However, such ion exchange processes may become of concern at industrial scales and on longer timescales than captured in these experiments. Future work may evaluate potential impacts of the observed lab-scale phenomena to the field scale, including by extraction of reaction kinetics and comparisons to mineralogical results from full-scale experiments conducted in repository URL sites.

9.5 Conclusions

This document summarizes three experiments completed in FY23 evaluating the effect of temperature on hydrothermal alteration of a low-pH cement. These experiments combined an ESDRED-like low-pH cement with a Grimsel granodiorite synthetic GW solution at three temperatures: 100 ºC (experiment CEM-1); 150 ºC (CEM-2); and 200 ºC (CEM-3). Results presented and discussed include XRD, SEM-EDS analyses and aqueous geochemistry data; additional results from XRD and EMP analyses are subject to ongoing data interpretation and will be included in the report for FY24. Results from experiments completed in previous years at LANL are also discussed where interpretation of results is ongoing, specifically for QXRD, clay mineral XRD, and EMP analysis. Experiments discussed include IEBS-0, that reacted Wyoming bentonite with Grimsel GW solution at 250 ºC and 150 bar; IEBS-6 and -8, that reacted Wyoming bentonite and Grimsel GW solution with OPC at 250 ºC and 150 bar; and IEBS-9, and -10, that reacted Wyoming bentonite and Grimsel GW solution with an experimental low-pH cement at 200 ºC and 150 bar.

9.5.1 Research Concepts Developed in FY23:

- The results of experiments discussed that reacted Wyoming bentonite showed that no substantial alteration of the montmorillonite in bentonite to secondary non-swelling clay phases occurred at experimental conditions. Experimental conditions included alteration of bentonite in the GW solution with no co-reactants, co-alteration of the bentonite + OPC + Grimsel granodiorite ± steel, and co-alteration of bentonite + low-pH cement ± Grimsel granodiorite. The alteration of the swelling clay montmorillonite to non-swelling illite (illitization) in Wyoming bentonite in a Grimsel granodiorite wall rock environment is interpreted to be restricted due to the bulk chemistry of the overall system (i.e., low K) and/or kinetics.

- Hydrothermal alteration of 316 stainless steel in IEBS-8 (bentonite + OPC + Grimsel granodiorite) resulted in newly crystallized Fe-saponite formed at the steel-bentonite interface. Saponite was observed as formed perpendicular to the steel surface, morphologically similar to secondary phases formed in experiments without cement reactants. Fe enrichment of the bentonite due to interaction with steel corrosion products was observed to extend < 50 µm from the steel surface.

- The addition of OPC as a reactant in bentonite + granodiorite + groundwater solution experiments had steady-state pH values slightly increased (by ~1.5 pH units) to those of analogous experiments that did not include cements. The inclusion of OPC did result in the abundant formation of zeolite minerals (dominantly analcime/wairakite) at the experimental conditions (250 ºC and 150 bar). Clay is interpreted to be consumed as part of the zeolite-forming reactions, facilitated by the conditions created by OPC (elevated pH and Ca concentration).

- The addition of VU cement (experimental low-pH cement) resulted elevated pH of the experimental solutions in IEBS-9 and -10, as compared to experiments with no cement reactants as well as analogous experiments with OPC. C(A)SH phases were also observed to have formed at the surface of the low-pH cement chips reacted in IEBS-9 and -10: abundant zeolite formation, such as had formed in experiments with OPC chips, was not observed. The comparatively elevated pH of these experiments is interpreted as a driver of the increased C(A)SH formation.

- ESD cement reacted at 3 experimental temperatures (experiment CEM-1 at 100, CEM-2 at 150, and CEM-3 200 ºC) in Grimsel GW solution with no other reactants resulted in elevated steady-state pH values similar to those observed in VU cement experiments IEBS-9 and -10. Ca concentrations decreased with increasing temperature while Si concentrations increased with increasing temperature. At all temperatures, a reaction rim of similar heterogenous thickness (10-30 µm) formed at the cement-solution interface. At 100 and 150 ºC, the reaction rim mineralogy was dominated by calcite; at 200 ºC, the reaction rim was observed to be composed largely of CSH phases.

- Comparison of the Na and K trends in all discussed experiments suggests that K contributed by the cement reactants was exchanged for Na in the Na-montmorillonite present in the reacted bentonite matrices of IEBS-9 and -10. The extent of reaction did not quantifiably reduce the swelling properties of the reacted bentonite as evaluated through clay XRD methods.

9.5.2 Research Avenues to be Emphasized in FY24:

- Continue incorporating results into a database of Grimsel granodiorite and EBS experiments for use in evaluation of EBS materials performance at elevated temperatures in crystalline environments.
- Complete data analysis focused on evaluating effects of temperature and time on the formation of CSH and zeolite minerals. Continue data analysis and design future experiments to isolate rates of formation of secondary minerals. Complete further work to understand formation of C(A)SH and zeolite minerals at unexpectedly low pH (< 9.0) in EBS systems.
- Extract reaction rates of low-pH cement alteration responsive to increased temperatures that can be incorporated into sensitivity analyses.
- Develop conceptual models of alteration pathways of low-pH cement through hydrothermal experiments at different temperatures and solution compositions.
- Complete EMP analysis of all reactants to date to identify reaction pathways from EBS material alteration to secondary mineral formation.
- Continue to build a database of Grimsel granodiorite and EBS experiments.
- Incorporate results into geochemical modeling codes.

The developing database of reacted EBS materials, along with summary conclusions of alteration of EBS materials in a crystalline rock environment, will be of use to other experimental teams in the DOE complex, system modeler, and the international repository science community in the development of concepts related to high-temperature crystalline repository environments.

10. HYDROTHERMAL TESTING TO SUPPORT THE HOTBENT FIELD TEST

10.1 Introduction

To address the temperatures involved with the disposal of DPCs as discussed previously, data from elevated-temperature, full-scale experiments are invaluable to characterizing alteration of barrier materials as may occur in future repository sites. One such long-term experiment is HotBENT (High Temperature Effects on Bentonite), performed by the Swiss National Cooperative for the Disposal of Radioactive Waste (NAGRA) at the Grimsel Test Site as a generic crystalline repository concept (Blechschmidt et al., 2020; Matteo et al., 2018). The HotBENT experiment is divided into two physical sectors to allow phased dismantling that are separated by plugs constructed of low-pH cement (shotcrete). To simulate a heat source, heaters are encased in bentonite in each sector. Sector 2 of HotBENT, located between the plugs 1 and 2 (Figure 10-1), hosts two heaters with estimated high temperatures of 175 ºC and is planned to be dismantled after five years. Sector 1, located behind plug 1, hosts two heaters with estimated temperatures at the heater surface of 200 °C and 175 °C, respectively and will be dismantled after 15 to 20 years. Construction for HotBENT started in 2019, and phases of the experiment are planned to run for 5 to 20 years before dismantling (Grimsel Test Site, 2023). Table 10-1 lists the expected temperature gradient for the 200 ºC heater scenario (AMBERG, 2019).

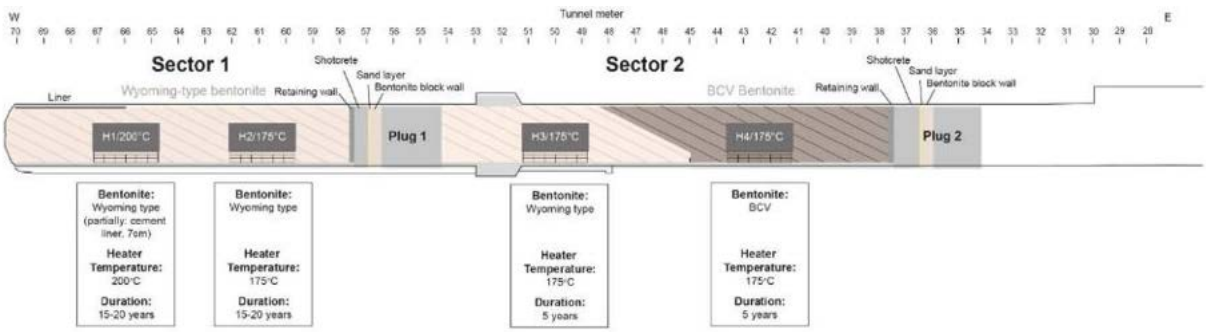

Figure 10-1 Schematic of the HotBENT heater test. Heaters are depicted in brown with the temperature indicated. BCV, Czech bentonite (figure adapted from AMBERG, 2019).

Table 10-1 Summary of the expected temperature gradient for the 200 ºC heater scenario of the HotBENT long-term (5-20 year) experiments (AMBERG, 2019)

Radial distance from heater surface (cm)	Expected max. temperature values (ºC)
10	178
20	147
30	128
40	114
50	103
60*	93
70	83

*Interface between the buffer and rock. With a heater of 1.05 m in diameter, the buffer has a thickness of 61.5 cm.

Specific objectives of the HotBENT experiment include: (1) studying the effects of high thermal loading (temperatures > 150 °C) on the performance of bentonite and/or bentonite mixtures as buffer materials at realistic scales and in-situ conditions; (2) enhancing the existing geochemical databases and the understanding of buffer performance, in particular in terms of robustness; (3) assessing the effect on the generally agreed safety functions at high temperatures; (4) evaluating the corrosion of potential canister materials and potential microbial activities; and (5) characterizing interactions between bentonite buffers with cement-based materials used for liners and/or plugs. The HotBENT experiment is emplaced in the tunnel excavated from Grimsel granodiorite that hosted the FEBEX experiment and so benefits from extensive previous characterizations (Alonso et al., 2005; Huertas & Santiago, 1997; Lanyon & Gaus, 2016; Villar, 2021). A focus of both the HotBENT study and the experiments performed at LANL is then the alteration and co-alteration behaviors of EBS materials in a crystalline host rock system.

EBS materials used in the HotBENT experiment include two types of bentonites: a Czech bentonite (BCV) and a Wyoming bentonite denoted here as full-scale experiment (FE) bentonite. Cement liner (Figure 10-1) included in the HotBENT heater test is based on low-pH cement compositions first developed as part of a 5-year project that focused on evaluating the feasibility of upscaling proposed technical approaches and materials to the industrial scales needed use in geologic repositories, the Engineering Studies and Demonstrations of Repository Designs (ESDRED) project (De Bock et al., 2008; Verstricht, 2009). The stability of ESDRED-like concrete materials in saturated repository conditions at ambient temperatures has been investigated in laboratory- and full-scale experiments. Co-alteration of bentonites in contact with both OPC and ESDRED-like low-pH cements in a clayrock URL were investigated as part of the full-scale experiments hosted in Mont Terri URL in Switzerland. Results after over two years of interaction at ambient conditions in the URL showed zoned alteration in all types of cement studied, on the scale of hundreds of microns, extending into the cement from the cement-Opalinus Clay boundary (Jenni et al., 2014). After five years of interaction, an Mg-enriched zone was observed that extended several millimeters into the cement from the cement-Opalinus Clay interface (Dauzeres et al., 2016). Increased porosity in the ESDRED-like low-pH cement also indicated increased potential for cement carbonation further into the low-pH cements than into OPC (Jenni et al., 2014).

Use of LCS is considered favorable in some repository designs for its low cost and positive long-term performance by corrosion, mechanical strength, and structural reliability metrics (King, 2012; Marsh & Taylor, 1988). Interactions between steel corrosion products and bentonite barrier materials are naturally dependent on the characteristics of the bentonite, as different mineralogical compositions may result in the availability of different components to the geochemical system that have different impacts on steel stability. For example, increased sodium chloride in the system, as through cation exchange within bentonite minerals, is expected to result in initially increased steel corrosion rates (Möller et al., 2006; Smart, 2008; You et al., 2020). In saline solutions, corrosion rates are expected to increase with increasing temperature, highlighting the importance of characterizing alteration properties of LCS at elevated temperatures. After an initial corrosion period, however, increased salinity may speed the formation of a passivating oxide layer at the steel surface that then slows corrosion rates (Cáceres et al., 2009). In addition, secondary minerals that form on steel alteration in natural systems may form a barrier to corrosion that is not well reflected in laboratory corrosion studies (Möller et al., 2006; Nogara & Zarrouk, 2018). The feedback interactions between steel, bentonite barrier minerals, and host rock formations during an elevated-temperature event in a repository may then be specific to the combination of reactants in a way not captured by simplified scenarios.

LANL completed four experiments in FY21-22 and one experiment in FY23 that were designed to complement the complexity of the HotBENT experiments by using similar materials and parameters at lab timescales to isolate transient alteration processes occurring in the early part of the heating event. The previous experiments combined a Wyoming bentonite (FE bentonite), BCV, Grimsel granodiorite, and steel in a simulated GW solution at the maximum HotBENT heater temperature (200 °C) and are

summarized in this report with new results collected in FY23. One additional experiment was completed in FY23, additionally combining the same FE bentonite as used in previous years' experiments with a low-pH cement modeled on the composition used for the shotcrete liner in HotBENT. The results of this experiment are discussed in the context of previous years' results and of applications to the HotBENT long-term experiment.

10.2 Methods

10.2.1 Hydrothermal Experiments

Experiments completed within the scope of LANL EBS International R&D were designed to characterize reaction products of barrier materials used in the ongoing HotBENT experiments. Previous years' experiments (HBT-1 through -4) focused on reactions between the FE bentonite, BCV bentonite, LCS, and Grimsel Granodiorite GW. All of HBT-1 through -4 were conducted at 200 °C for 8 weeks. The experiment completed in FY23 focused on the reaction between FE bentonite and a low-pH cement manufactured using the composition of the cement used as the liner material in HotBENT (ESDRED-like low-pH cement) and was conducted at 200 °C for 4 weeks to allow characterization of reactants during the initial stages of alteration.

Reactants in all experiments were saturated with synthetic Grimsel GW and heated isothermally using the methodology described in Section 9.2.1 and Caporuscio, et al. 2023, Appendix A. In brief, reactants (Table 10-2) were loaded into a flexible gold reaction cell and fixed into a 500 mL gasket confined closure reactor (Seyfried et al. 1987). A 1:1 mixture (by mass) of Fe_3O_4 and Fe° added at 0.07 wt.% of the total mass of reactants (solid+liquid) to buffer redox conditions: in HBT-1 through -4, the Fe buffers were mixed in with the clay reactants before the experiments, and in HBT-5, the Fe buffers were included in a gold capsule lightly crimped at the ends to allow fluid communication while preventing an interface between the Fe buffer and other reactants. Experiments were pressurized to 150 to 160 bar and were heated isothermally to 200 °C for eight weeks. Reaction liquids were extracted periodically and sampled reaction liquids from HBT-1 through -4 were split into four aliquots for pH, unfiltered anion, unfiltered cation, and filtered (0.22 µm syringe filter) cation determination. Samples from HBT-5 were split into an unfiltered aliquot for pH and aliquots for cations and anions analysis that were filtered (0.22 µm). Cation and anion aliquots from each experiment were stored in a refrigerator at 1 °C until analysis. HBT-1 and -2 were not sampled throughout the experimental durations due to COVID-19 restrictions in the lab. Parameters for all experiments are included in Table 10-2.

Table 10-2. Parameters for the HBT experiment completed in FY23 as well as those completed in FY21 and FY22. Detailed information on reactants is included in Section 10.2.2 below. All values are mass (g) except where otherwise noted.

Exp.	Components	Duration	Temp (°C)	Pressure (bars)	Synthetic GW (g)	FE (g)	BCV (g)	GG	LCS	ESD	Fe° (g)	Fe_3O_4 (g)	WWR
HBT-1	FE + LCS	8 weeks	200	150	133	21.01	-	-	5.05	-	0.55	0.55	6:1
HBT-2	BCV + LCS	8 weeks	200	150	127	-	21	-	5.03	-	0.55	0.55	5:1
HBT-3	FE + BCV + LCS	8 weeks	200	150	104	8.6	8.6	-	5.04	-	0.5	0.5	6:1
HBT-4	BCV+GG+LCS	8 weeks	200	150	127	-	15.87	7.94	5.02	-	0.75	0.75	5:1
HBT-5	FE+ESD	4 weeks	200	150	117	9.75	-	-	-	9.75	0.48	0.48	6:1

Abbreviations: GW=Grimsel groundwater; GG=Grimsel granodiorite; WB=Wyoming bentonite; BCV=Czech bentonite; OPC=ordinary Portland cement; ESD="ESDRED-like" low-pH cement; LCS=low-carbon steel; WRR=water-rock ratio (by mass)

10.2.2 Materials

10.2.2.1 Materials used in FY23

ESDRED-like low-pH cement (ESD). A low-alkali shotcrete product using a formulation developed as part of the ESDRED project (Mäder et al., 2018). The general formula includes ~60% CEM I (cement product having at least 95% OPC) with ~40% microsilica, with variable amounts of a set accelerator (Lothenbach et al., 2014).

Wyoming (FE) bentonite. The bentonite used in the present study is an unprocessed, Na-rich Wyoming bentonite that was leftover material from the FE experiment at the Mont Terri URL, which closely replicates the Wyoming-type bentonite that will be used in HotBENT. The bentonite is required to contain: > 75% smectite (Na-montmorillonite), < 1% pyrite, < 0.5% sulfur, and < 1% organic carbon as specified in Karnland et al. (2007) and Leupin and Johnson (2013). No additives to the bentonite are allowed. Granulated bentonite material and compressed block material are both used in the experiments.

Synthetic Grimsel groundwater. The synthetic GW used was identical to that of the IEBS experiments described in Section 9.2.1, selected as an approximation of the GW chemistry from the Grimsel Test Site as reported in Kersting et al. (2012). Chemistry of the synthetic fluid is presented in Table 9-2 in Section 9.2.2. The GW at the Grimsel Test Site is a Na-CO_3 type water and has a pH of ~8.6 to 8.8.

10.2.2.2 Additional Materials used in FY21 and FY22 Experiments

Czech (BCV) bentonite. BCV bentonite is an unprocessed Czech bentonite enriched in Fe. This bentonite formed from the in-situ alteration of Fe-rich tuffs and augite-biotite-type tuffites (Villar et al., 2020). The smectite content in the BCV is ~90 wt.%. BCV contains minor amounts of quartz, calcite/dolomite, apatite, goethite, kaolinite, and mica.

Grimsel granodiorite. The granodiorite used in the experiments was sourced from a drill core from the Grimsel Test Site. Major mineral phases include K-feldspar, plagioclase, and quartz. Minor phases are muscovite and biotite. Trace phases are allanite, zircon, titanite, and apatite.

Low carbon steel (LCS). LCS is mostly composed of Fe with ~0.2 wt.% C, 0.9 wt.% Mn, < 0.04 wt.% P, and < 0.05 wt.% S.

10.3 Results

10.3.1 Aqueous Geochemistry

The planned weekly sampling schedules for HBT-1 and -2 were affected by the COVID-19 health crisis and limited aqueous samples were collected from these experiments. Reaction fluids were sampled twice during the HBT-1 experiment: first, after one week of heating, and second, when the experiment was dismantled. HBT-2 was only sampled pre- and post-experiment. HBT-3 and -4 were sampled every week of the experiment duration. HBT-5 had a modified sampling schedule that included an accelerated sample schedule during the first week and was sampled once a week for the remainder of the experimental duration (four weeks). The analyzed aqueous geochemistry is summarized below and reported in Caporuscio, et al. 2023, Appendix B.

pH. All experiments started with a pH from ~8 to ~8.5, illustrated in Figure 10-2 and in Caporuscio, et al. 2023, supplementary tables B17-B26. In experiments HBT-1 through -4 that did not include cement as a reactant, the pH decreased rapidly to a relative steady-state pH of ~6. The pH as measured in samples from HBT-5 that included FE bentonite and ESD cement as reactants initially decreased in the first three days of reaction time before increasing again to greater than the initial bench pH of ~8.5 and remained at an apparent steady-state pH of ~9.

Silica. An increase in aqueous silica concentration in HBT-1 and 2 was observed (to 390–174 mg L^{-1}) between the initial sampling to the end of the experiment (Figure 10-2). The second sample and from HBT-2 and the only sample collected while the experiment was at temperature also showed an increased SiO_2 concentration relative to the initial and final samples from HBT-1 and -2. However, no trend can be unequivocally determined from the few samples from HBT-1 and -2 due to the lack of additional sampling during the experiment. SiO_2 concentrations in HBT-3 and -4 sharply increased between the initial GW solution and the first experimental sample (18 to ~180 mg L^{-1}) and continued to increase throughout the experimental duration to ~300 mg L^{-1} at experiment termination. SiO_2 concentrations in HBT-5 were observed to be substantially higher than that in HBT-1 through -4. However, we note that SiO_2 (and Fe) results may have been affected by a change in sample preparation technique for cation analysis between these experiment sets, and the increased SiO_2 concentration in HBT-5 is not interpreted to be necessarily caused by different alteration processes.

Iron. In both HBT-1 and -2, iron concentrations increased in the final samples collected after experimental termination. Increased Fe concentrations in the final samples (collected at bench conditions after experiment termination) are interpreted to be a quench effect, given the relatively low Fe concentration in the single sample collected from HBT-1 at experimental pressure and temperature (Figure 10-2). HBT-3 through -5 were sampled throughout the experimental duration and had relatively low (< 0.5 mg L^{-1}) Fe concentrations throughout the experiment. Similar to HBT-1 and -2, HBT-3 and -4 also had elevated Fe concentrations in the samples taken at bench conditions after experiment termination. The post-quench sample from HBT-5 was slightly elevated in Fe compared to the sample collected directly before quench (Figure 10-2) but was not substantially elevated compared to other samples collected during the experiment duration.

Aluminum. Aluminum concentrations in the filtered samples from HBT-1 were elevated in the sample collected after one week of reaction time and decreased again to < 0.2 mg L^{-1} in the final sample taken after experimental termination (Figure 10-2). HBT-3 and -4, sampled consistently over the entire experimental duration, also exhibited transient increases in Al concentrations: Al concentrations were elevated at weeks one and two of reaction time in HBT-3, while the Al concentration was slightly elevated (~0.2 mg L^{-1}) at week 3 of HBT-4. No samples were collected during the experimental duration of HBT-2; samples of initial and final solutions collected at bench conditions were similarly low (< 0.1 mg L^{-1}). In contrast, Al concentrations in HBT-5 increased to ~5 mg L^{-1} before decreasing to ~1.5 mg L^{-1} all within the first week of reaction time. Al concentrations then increased in a seemingly linear trend throughout the remaining experimental duration to ~2 mg L^{-1}.

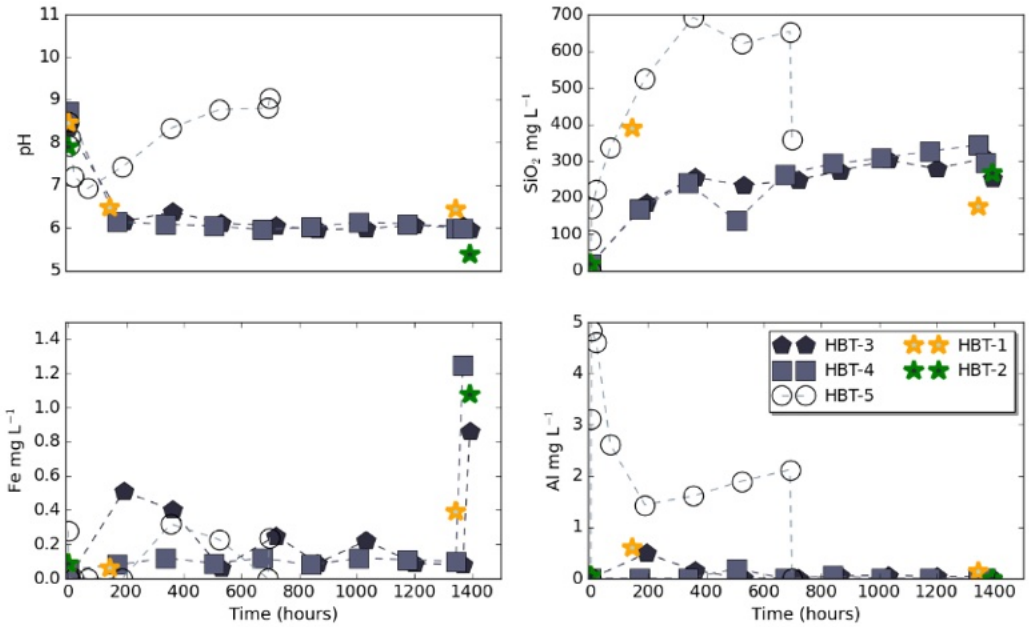

Figure 10-2. Concentration in mg L^{-1} of pH, SiO_2, Fe, and Al in HBT-1 through -5.

Alkali/alkaline earth metals. Potassium, sodium, and calcium concentrations in solution generally increased during all experiments (Figure 10-3). K and Ca increased to greater concentrations in the two experiments without FE bentonite (HBT-2 and -4). Na concentrations increased to higher values in the experiments with FE bentonite (HBT-1, -3, and 5); from the samples collected during the experimental duration of HBT-3 and -5 and the single sample collected from HBT-1 after one week of reaction time, Na appears to have increased rapidly in the first week and continue increasing throughout the experimental duration. In contrast, the samples collected during HBT-4 indicate that Na initially decreased in the experiment with BCV, before a relatively slow increase throughout the remaining experimental duration (Figure 10-3).

All samples collected at experimental conditions (from HBT-1, -3, -4, and -5) show decreased Mg concentrations (< 2 mg L^{-1}) compared to the Mg concentrations in the initial and final samples collected at bench conditions (Figure 10-3). Mg concentrations decreased throughout the durations of HBT-3 and -4 with comparatively lower concentrations throughout HBT-3. The accelerated sampling schedule of HBT-5 indicates that the Mg concentration decreased within the first day of reaction time and remained at a steady-state concentration similar to that of the two other experiments that included FE bentonite (HBT-1 and HBT-3).

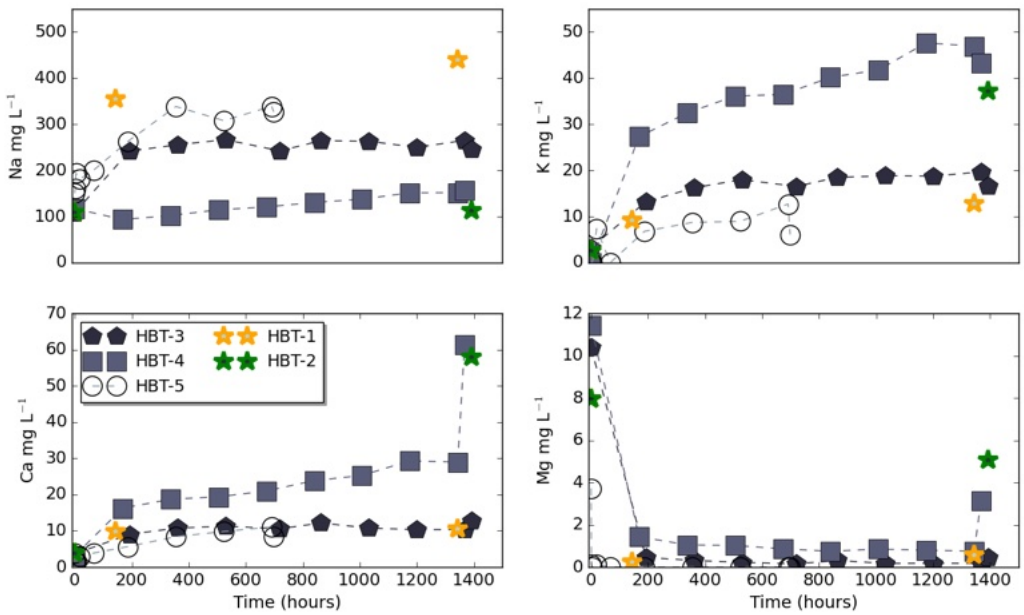

Figure 10-3. Concentration in mg L^{-1} of Na, K, Ca, and Mg in HBT-1 through -5.

Chloride. Chloride concentrations behaved relatively conservatively in most experiments, with final concentrations within ~1 mg L^{-1} of the concentration in the initial solution (Figure 10-4). Concentrations in HBT-1 were higher throughout the experimental duration (~20 mg L^{-1} compared to ~10 mg L^{-1} in HBT-2 through -4). While the final Cl concentration of HBT-3 was similar to its initial concentration, there was significant variation in the concentration over the experimental time (~10 to ~27 mg L^{-1}), while the samples collected during HBT-4 had relatively constant Cl concentrations (~10 mg L^{-1} throughout). In contrast to the preceding experiments without cement, the Cl concentration in HBT-5 rapidly increased within the first week of reaction time from ~10 mg L^{-1} to ~25 mg L^{-1}, before slowly decreasing throughout the remainder of the experiment.

Sulfate. Sulfate concentrations in the two experiments with FE bentonite generally increased. HBT-1 increased over the experiment from the initial to final sample from ~245 mg L^{-1} to ~300 mg L^{-1}. SO_4 concentrations in HBT-3 increased initially from 117 mg L^{-1} to 295 mg L^{-1} and varied over the eight weeks between ~210 mg L^{-1} and ~540 mg L^{-1} before decreasing to 138 mg L^{-1} at the end of the experiment (Figure 10-4). SO_4 trends in the two experiments without FE bentonite appeared more stable: the SO_4 concentrations in the initial and final samples collected from HBT-2 were relatively unchanged, while the SO_4 concentration in HBT-4 initially decreased (from ~150 mg L^{-1} SO_4 concentration in the initial solution) and to ~110 mg L^{-1} for the remaining experimental duration. In HBT-5 that included cement, SO_4 rapidly increased and continued increasing until the final week of the experiment, starting at ~150 mg L^{-1} and increasing to over 500 mg L^{-1}.

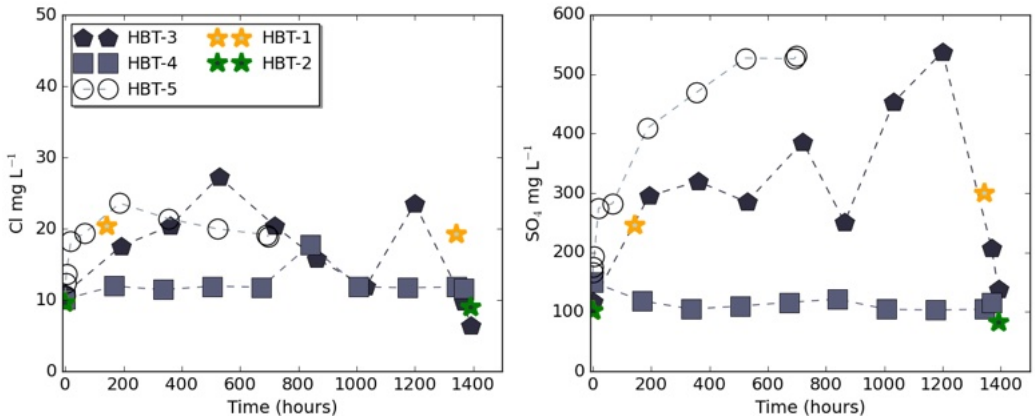

Figure 10-4. Concentration in mg L^{-1} of Cl and SO_4 in HBT-1 through -5.

10.3.2 XRD

10.3.2.1 QXRD

QXRD analyses of the starting materials and the bulk reaction products are presented in Caporuscio, et al. 2023, Table C-2 and Figure 10-5, Figure 10-6, and Figure 10-7. The results illustrate changes in the bulk mineralogy as a result of hydrothermal reactions.

FE bentonite. The unreacted FE bentonite contained 94.2 wt.% montmorillonite with minor amounts of quartz (2.1 wt.%), feldspars (1.5 wt.%), cristobalite (1.2 wt.%), and an amorphous phase (1.0 wt.%). The bentonite is slightly different from the Wyoming bentonite used in the IEBS experiment because the FE test used pure Wyoming sodium bentonite (Hansen et al., 2016).

BCV bentonite. The Czech bentonite had less montmorillonite (89.8 wt.%) than the FE bentonite and contained mica and chlorite/kaolinite. This bentonite also contained quartz, cristobalite, and an amorphous phase, along with apatite, carbonates, and goethite.

FE:BCV. A 50:50 mixture of FE and BCV bentonite was analyzed as an unreacted mixture comparable to the reactants used in HBT-3. The clay fraction accounted for 83.9 wt.% of the sample and was composed of smectite (81.2 wt.%), mica (1.6 wt.%), and chlorite/kaolinite (1.5 wt.%). The non-clay portion contained quartz, feldspars, calcite, anatase, cristobalite, and goethite. An amorphous phase accounted for ~6 wt.% of the sample. The observed totals that are different from a calculated 50:50 mix of FE and BCV likely reflect natural heterogeneity in the bentonite mineralogy.

BCV:GG. An 80:20 mixture of BCV bentonite and Grimsel granodiorite was analyzed as an unreacted counterpart to the reactants of HBT-4. The unreacted mixture was primarily smectite (83.0 wt.%) with minor mica and kaolinite. The non-clay fraction consisted of quartz (4.2 wt.%), plagioclase/feldspar (8.7 wt.%, combined) along with small amounts calcite, goethite, and cristobalite.

ESDRED-like low pH cement (ESD). The unreacted ESD cement was composed mostly of calcite (85 wt.%) with minor quartz (7.6 wt.%), plagioclase (2.7 wt.%), and mica (3.5 wt.%). Due to the heterogeneity of the cement, the QXRD analysis may not be a true representation of the sample.

HBT-1. The FE bentonite included in this experiment had a slight decrease in the smectite fraction (94.2 - 92.4 wt.%). The amorphous phase increased 1.0 wt.% to 2.0 wt.%.

HBT-2. The smectite content remained unchanged after the experiment, but the clay fraction gained the addition of illite (1.2 wt.%). Goethite was expended and magnetite is present from the added redox buffer. The amorphous phase decreased from 1.9 wt.% to 0.5 wt.%.

HBT-3. From the starting material to post-experiment, the smectite content remained unchanged. There was an increase of chlorite/kaolinite and newly formed saponite. The amorphous phase decreased (5.9–3.7 wt. %) and again goethite was no longer present.

HBT-4. The reacted BCV bentonite with Grimsel Granodiorite was generally consistent with the unreacted starting material. There was a decrease of the smectite (~6.5 wt.%) and increase of mica (2.2 wt.%) from the starting composition along with minor differences with variation in the plagioclase/feldspar content and the addition of magnetite (buffer material).

HBT-5. The FE bentonite experienced little change after four weeks of heating. There was a slight reduction (~ 3 wt.%) in smectite and a slight increase in the amorphous material (2 wt.%). However, all other changes may be attributed to natural variation between the samples (~1 wt.%).

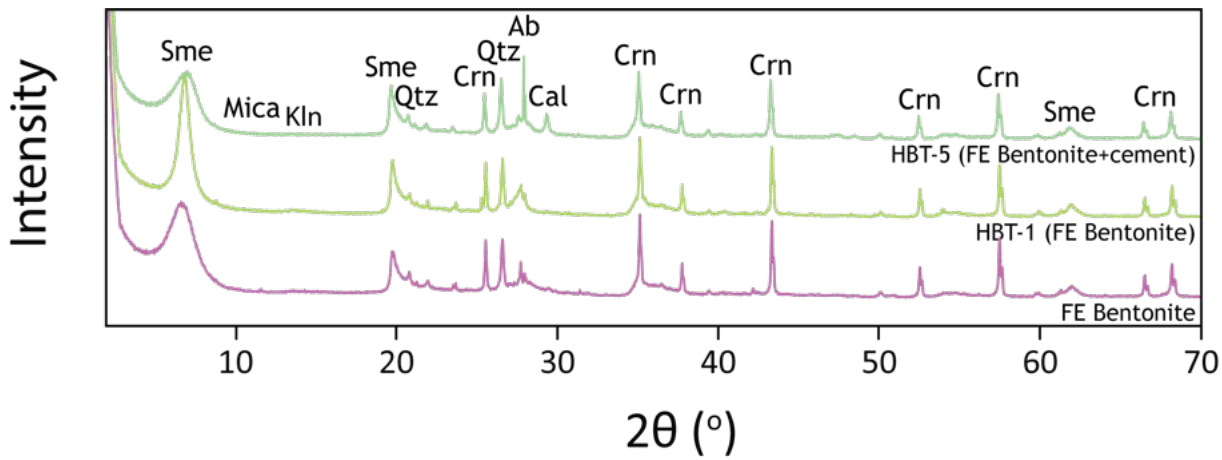

Figure 10-5. QXRD patterns of reacted bentonite from HBT-1 and -5 compared to unreacted FE bentonite. Peaks correspond to smectite (Sme), mica, kaolinite (Kln), quartz (Qtz), corundum (Crn), albite (Ab), and calcite (Cal).

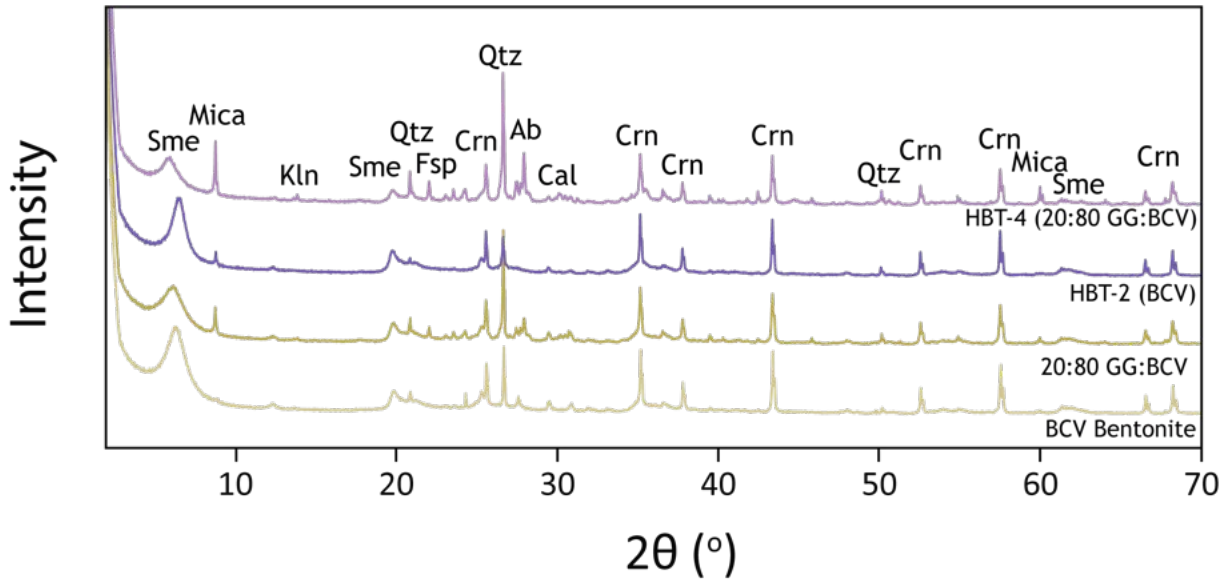

Figure 10-6 QXRD patterns of reacted bentonite from HBT-2 and -4 compared to unreacted BCV bentonite. Peaks correspond to smectite (Sme), mica, kaolinite (Kln), quartz (Qtz), feldspars (Fsp), corundum (Crn), albite (Ab), and calcite (Cal)

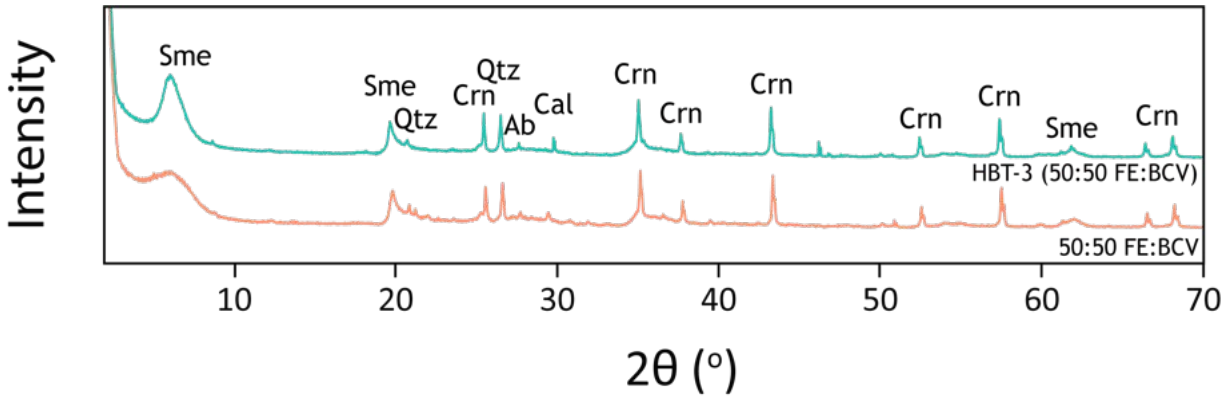

Figure 10-7. QXRD patterns of reacted bentonite from HBT-3 compared to the unreacted FE-BCV mixture. Peaks correspond to smectite (Sme), quartz (Qtz), corundum (Crn), albite (Ab), and calcite (Cal).

10.3.2.2 Cement XRD

The unreacted ESD cement contained calcium carbonate and silicon oxide phases (Figure 10-8). The ESD cement after reaction in HBT-5 also contained calcium carbonate and silicon dioxide, along with tobermorite, feldspars, and halite. The feldspar originated from the FE bentonite, whereas the halite precipitated from the aqueous fluid during the quench.

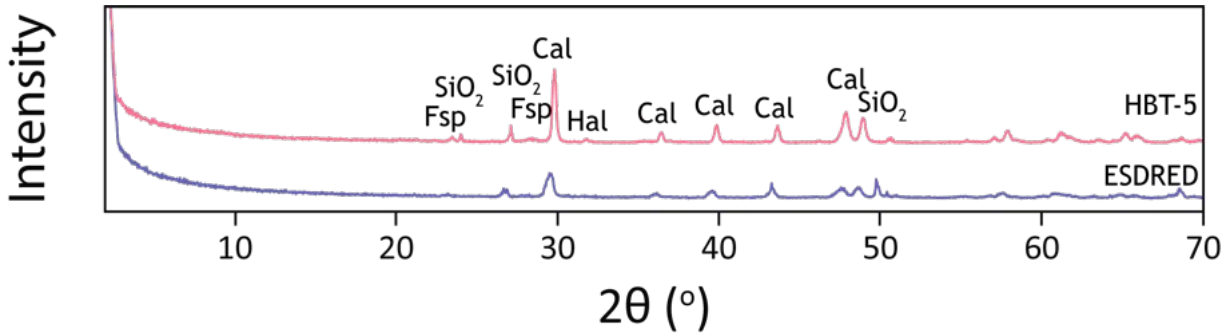

Figure 10-8. QXRD patterns of reacted ESD cement from HBT-5 compared to unreacted ESD cement. Peaks correspond to felspar (Fsp), silica (SiO_2), halite (Hal), and calcite (Cal).

10.3.2.3 Clay XRD

The clay-size fraction (< 2 µm) was separated via density separation from a gently crushed portion of the reaction products from each experiment. The XRD patterns of the ethylene glycol-saturated, oriented clay fractions can be used to determine alteration to the clay mineral structure (i.e., peak position shifts), which can be used to calculate clay mineral expandability. The ethylene glycol-saturated peak positions are presented in Table 10-3 and the XRD patterns are plotted in Figure 10-9. Using the NEWMOD calibration from Leupin et al. (2014), the illite content was estimated in the glycolated illite/smectite. In the bentonite-only experiments, there was little change in the percent illite, and a slight decrease in expandabilities (1-3%). However, in the experiments that included Grimsel granodiorite or ESD cement, the percentage of illite increased (4 and 5 wt.%, respectively) and a larger decrease in the clay expandabilities (10-13%).

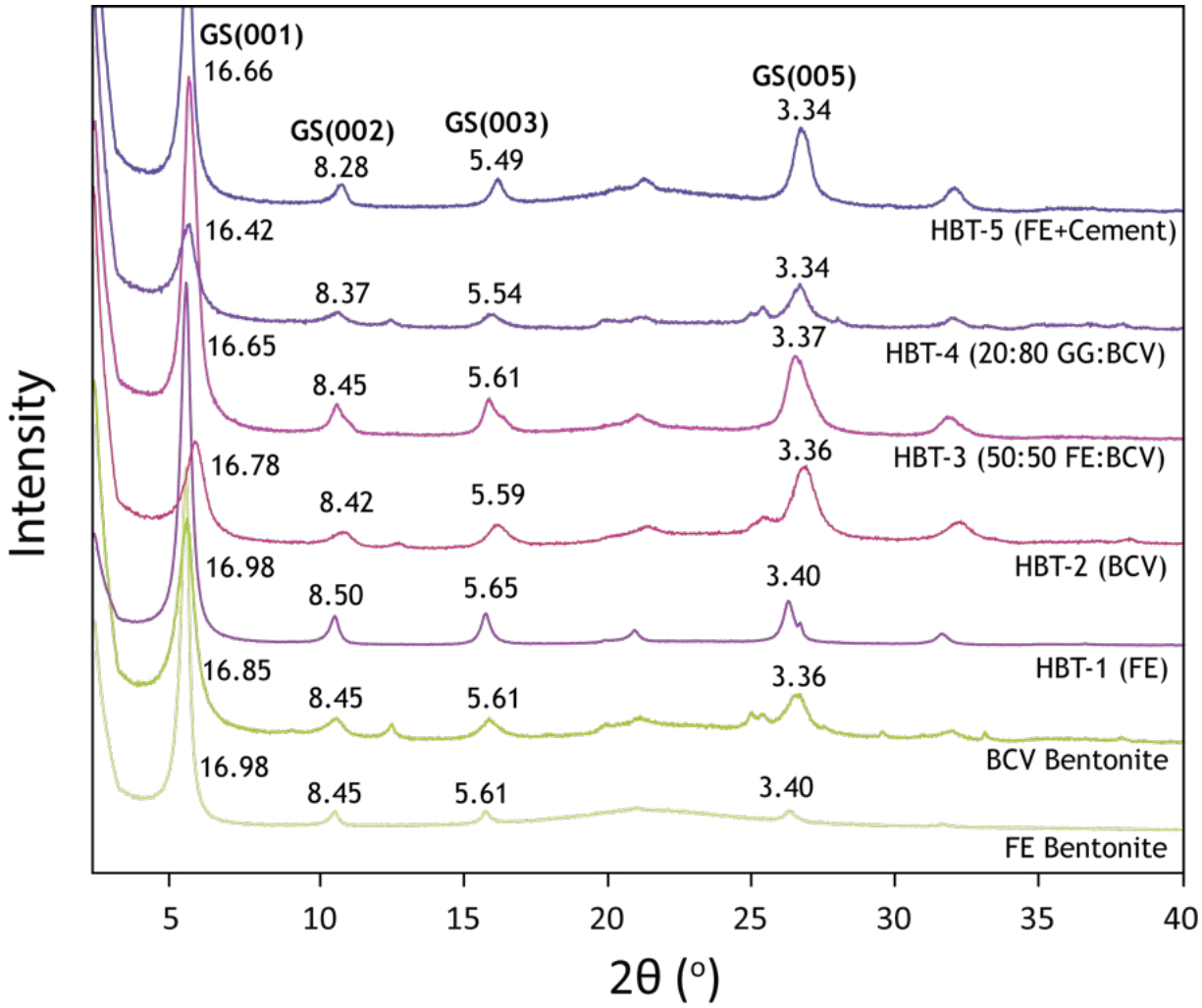

Figure 10-9. XRD patterns of the oriented, ethylene glycol-saturated, <2 µm fraction from HBT-1 through -5 compared to that of unreacted bentonite. Presented values are d-spacings for major glycolated smectite (GS) peaks.

Table 10-3. Glycolated smectite (GS) peak positions for the < 2 µm clay fraction separated from the FE and BCV bentonites. Expandability and percent illite (%I) were calculated based on the difference in position of the 002 and 003 glycolated smectite peaks.

Sample	**1**		**2**		**3**		**5**		**002/003**	**1**	**2**	**3**	
EG- Smectite	**2Θ**	**d (Å)**	**2Θ**	**d (Å)**	**2Θ**	**d (Å)**	**2Θ**	**d (Å)**	**Δ 2θ**	**%Exp**	**%Exp**	**%Exp**	**%I**
Unreacted bentonite													
FE bentonite	5.20	16.98	10.42	8.49	15.64	5.66	26.22	3.40	5.23	102	104	105	0
BCV bentonite	5.24	16.85	10.46	8.45	15.78	5.61	26.54	3.36	5.32	97	98	99	1
Bentonite + LCS													
HBT-1 (FE)	5.20	16.98	10.40	8.50	15.68	5.65	26.20	3.40	5.28	99	101	102	0
HBT-2 (BCV)	5.26	16.78	10.50	8.42	15.84	5.59	26.52	3.40	5.34	96	98	99	1
HBT-3 (FE:BCV)	5.30	16.65	10.46	8.45	15.78	5.61	26.42	3.37	5.32	97	98	99	1
Bentonite + LCS + Grimsel granodiorite													
HBT-4 (BCV)	5.38	16.42	10.68	8.37	15.98	5.54	26.70	3.34	5.42	92	91	94	5
Bentonite + ESD cement													
HBT-5 (FE)	5.30	16.66	10.68	8.28	16.12	5.49	26.70	3.34	5.44	91	90	93	5

1: $\%Exp = 973.76 - 323.45\Delta + 38.43\Delta^2 - 1.62\Delta^3$ (Eberl et al., 1993)

2: $\%Exp = 1517.8 - 548.49\Delta + 68.35\Delta^2 - 2.90\Delta^3$ (Eberl et al., 1993)

3: $\%Exp = 766.01 - 194.10\Delta + 12.924\Delta^2$ (Moore and Reynolds, 1997)

10.3.3 XRF

XRF analyses for bulk rock oxide chemistry were performed on the unreacted starting material and the bulk reaction products (Table 10-4). In experiments HBT-1 through -3, the weight percent oxide values only showed slight variations between the unreacted and reacted bentonite. All the experiments experienced a decrease in SiO_2 weight percent compared to their unreacted counterparts. HBT-2 and -3 also decreased in LOI (loss on ignition) compared to the unreacted bentonite. The weight percent of Fe_2O_3 increased for all the experiments, possibly as a result of the addition of redox buffers to the experiments or transfer of Fe from the LCS coupons added to the experiment. HBT-4, which contained BCV bentonite and Grimsel granodiorite, differed only slightly from the calculated BCV:GG XRF. HBT-4 contained higher Fe_2O_3 and Na_2O weight percentages and decreased LOI. The increase in Fe_2O_3 is likely from the addition of redox buffers and transfer of Fe from the LCS coupons.

In the experiment containing FE bentonite + ESD cement (HBT-5), the most notable difference in the bulk FE bentonite compared to the unreacted FE bentonite was an increase in CaO. This increase was due to the presence of cement in the experiment. It was notable that the Fe_2O_3 content was lower in the HBT-5 experiment due to a modification of the experimental setup which included placing the redox buffers in a crimped gold capsule versus in the bulk constituents.

Table 10-4. Weight percent oxides in unreacted and reacted solid materials.

XRF (wt. %)	HBT-1 (FE)	HBT-2 (BCV)	HBT-3 (FE:BCV)	HBT-4 (BCV+GG)	HBT-5 (FE+ESD)	FE Block	BCV Block	FE:BCV	FE+GG (Calc.)	ESD
CaO	1.34	3.89	2.54	2.94	4.28	1.39	4.17	2.86	3.64	44.72
K_2O	0.59	0.80	0.70	2.07	0.63	0.57	0.85	0.77	1.40	0.56
SiO_2	59.05	44.90	51.74	52.43	59.45	63.37	48.82	55.73	54.29	15.49
Al_2O_3	18.76	14.75	16.87	14.06	18.48	19.69	14.48	17.87	13.85	1.99
Na_2O	2.04	0.24	1.00	2.01	1.83	2.12	0.45	1.21	0.95	0.35
MgO	2.31	3.34	2.85	2.12	2.17	2.41	3.23	3.07	2.71	0.93
P_2O_5	0.06	0.56	0.28	0.35	0.04	0.05	0.58	0.33	0.49	0.13
Fe_2O_3	9.28	19.11	15.99	15.4	4.04	4.13	11.43	7.92	9.71	1.38
TiO_2	0.26	3.50	1.84	2.14	0.14	0.16	3.37	1.92	2.78	0.09
MnO	0.06	0.20	0.14	0.16	0.03	0.03	0.19	0.10	0.16	0.03
LOI	6.11	8.43	5.81	6.09	8.80	5.99	12.21	8.06	9.81	34.27
TOTAL	99.8	99.7	99.8	99.8	99.9	99.9	99.8	99.8	99.8	99.9

10.3.4 Electron Microprobe Analysis

EMP analysis for HBT-1 and -2 were completed in FY22. Analyses for HBT-3 and -4 are due to be completed in FY24. Data was collected from the clay groundmass of the two experiments and from material attached to the reacted steel surface. From the clay groundmass of the reaction products, analyzed phases included feldspar and clay. Fe-enriched clay was targeted for analysis on the steel surface. Data reduction and interpretation is ongoing for HBT-3 through -5 and will be included and discussed in the FY24 report.

Clay groundmass. The variation in the starting chemistry of the two different bentonites used in HBT-1 (FE bentonite) and HBT-2 (BCV) is reflected in the EMP analyses results. Smectite from HBT-1 is enriched in Na and smectite from HBT-2 is enriched in calcium. Future microprobe analyses of HBT-3 and HBT-4 will characterize the effect of the mixed FE-BCV bentonite system on montmorillonite cation composition and exchange.

Fe-clay. Material attached to the reacted steel coupon surface for both HBT-1 and HBT-2 included Fe-rich clay species, likely Fe-saponite. EMP results and SEM-BSE images from the steel samples are presented in Caporuscio et al. (2022). A comparison of results from HBT-1 and HBT-2 samples shows that alteration phases at the steel surface in HBT-1 have a higher weight percent value of FeO. The Fe-rich clay layer in HBT-1 is observed in a mostly continuous layer that is ~50 µm thick, and locally is observed to be > 500 µm thick. In comparison, the Fe-rich clay layer in HBT-2 is less continuous. This could be a result of sample handling and preparation. The steel surface in both coupons is observed to be cracked, with a large flake of steel separated from the steel surface in HBT-1. Small cracks were observed to extend into the steel in HBT-2.

10.3.5 SEM / EDS

HBT-1. The reacted matrix of FE bentonite was observed to have a foily, 'cornflake' texture. Minor quartz and plagioclase were also identified (Caporuscio, et al. 2023, Figure E8 [B]). A layer of Fe-oxide coated the LCS included in the experiment (Caporuscio, et al. 2023, Figure E8 [C, D]).

HBT-2. The reacted BCV clay matrix consisted mainly of smectite and was locally more Fe-rich than the FE bentonite reacted in HBT-1, consistent with the higher Fe content in the unreacted BCV bentonite (Table 10-4). Fe-carbonates were identified in the bentonite matrix and at the LCS surface (Caporuscio, et al. 2023, Figure E9): the dominant cation in the carbonate species was largely Fe with accessory Ca and Mg identified in some populations by SEM-EDS and is referred to here as siderite. As well as the siderite, minor amounts of feldspar and quartz were also observed in the matrix and are interpreted to be inherited from the unreacted material. There was honeycomb-texture Fe-saponite on the LCS along with the isolated siderite crystals (Caporuscio, et al. 2023, Figure E9 [C-E]).

HBT-3. The reacted mix of FE bentonite and BCV bentonite was dominated by smectite, with minor apatite and plagioclase (Caporuscio, et al. 2023, Figure E10 [A]). The steel was almost entirely coated with a siderite precipitate; Fe-saponite was present between siderite crystals or atop of the siderite layer (Caporuscio, et al. 2023, Figure E10 [C-D]).

HBT-4. The BCV matrix reacted in HBT-4 exhibited a less foily texture and was again identified as dominantly smectite. Fe-bearing clay minerals and siderite were found coating the LCS surface (Caporuscio, et al. 2023, Figure E11). The distal surfaces of the precipitate on the LCS were additionally coated with clay minerals more similar in structure and chemistry to the BCV bentonite matrix (Caporuscio, et al. 2023, Figure E11 [B]).

HBT-5. BSE images of the ESD cement showed that a reaction rim of ~20 µm formed at the cement-bentonite interface. After drying the cement and fixing the sample in epoxy, little of the bentonite matrix remained adhered to the cement surfaces (Figure 10-10). EDS analysis of the reaction rim showed it to be

enriched in Si and Al compared to the underlying ESD cement. ESD cement chips that were included in the experiment were intermixed with the bentonite matrix and none have been separately analyzed to date.

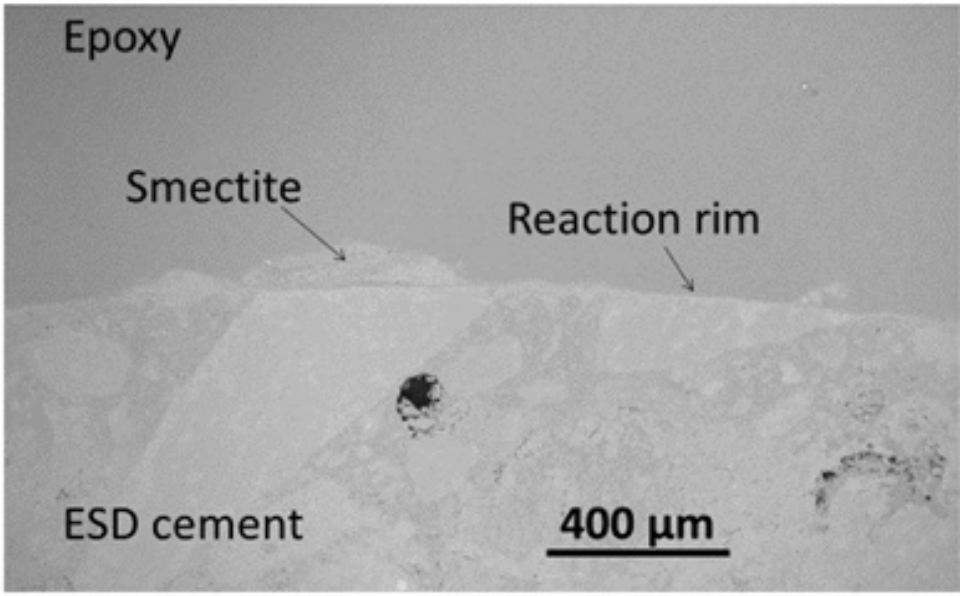

Figure 10-10. Images from BSE analysis of ESD cement reacted in HBT-5, in contact with FE-bentonite. A reaction rim was observed at the cement surface as well as isolated sections of adhered smectite.

10.4 Discussion

10.4.1 Previous FY experiments

10.4.1.1 Hydrothermal Alteration of FE and BCV Bentonite

Secondary electron SEM imaging of loose powder mounts of the reaction products shows the development of a foily texture in the fine-grained clay matrix, especially of the FE bentonite. Minor recrystallization of montmorillonite to non-swelling phases, such as muscovite, was observed in the QXRD results in experiments that included BCV bentonite. Characterization of the smectite structure using XRD analyses of ethylene glycol-saturated mounts presented a more detailed look at the alteration of the smectite during the hydrothermal experiments. The experiment with FE bentonite and no BCV (HBT-1) saw a reduction in expandability of ~4% versus ~1% in the BCV bentonite and no FE (HBT-2) experiment. The equal portions of FE:BCV in HBT-3 experienced a reduction in expandability similar to HBT-1 (FE only). The formation of illite-smectite mixed layers was not detected in the XRD patterns of the clay separations (Figure 10-9).

Steel interface mineral precipitation. Steel coupons extracted from the four experiments were characterized by SEM of the mineralized surface. Cross sections images and EMP analyses were collected for HBT-1 and -2 and are in progress for HBT-3 through -5. The SEM images from these experiments demonstrate the active environment at the bentonite-metal interface in experimental systems. The alteration mineralogy is likely controlled by the bulk chemistry as demonstrated by the differences in mineral precipitation in the four different experiments with different combinations of FE and BCV bentonite (Figure 10-5, Figure 10-6, and Figure 10-7). The steel material acted as a substrate for mineral growth in response to corrosion and allowed for the direct mineralization for new growth of surface-bound minerals in the localized environment surrounding the metal.

FE Bentonite. After HBT-1, containing FE only, the LCS was covered with black, orange, red, and white precipitants. The formation of a Fe-phyllosilicate corrosion product, Fe-saponite, was observed on the steel coupon surface during SEM analyses. These reaction products were only observed in a thin (< ~50 µm) rind on the reacted coupons. Unaltered montmorillonite was observed along with the Fe-saponite. Other observed Fe-rich corrosion products include Fe-oxides.

In the Wyoming bentonite-only experiment series described in Cheshire et al. (2018), a magnetite-like oxide layer developed at the outermost surface of the steel coupon. In addition to the crystallization of this oxide product, precipitation of Fe-rich phyllosilicates (Fe-saponite) was observed. The Fe-saponite forms a more reactive zone with a higher surface area than the original steel surface. The Fe-saponite likely precipitated directly on the steel from the solution interacting with smectite in the local environment surrounding the steel coupons. The clay matrix was not enriched in Fe like the clay observed at the steel interface. The low concentration of Fe ions in the bulk system solution (> 0.50 mg L^{-1}) and the presence of a new Fe-rich phase indicates that the reaction at the interface did not affect the chemistry of the bulk experimental system.

BCV Bentonite. In the BCV-containing experiments, HBT-2, -3, and -4, abundant rhombohedral siderite with intergrowing smectite at the LCS surfaces was apparent in SEM imaging (e.g., Caporuscio, et al. 2023, Figure E10 [D]). Previous work identified the formation of a magnetite inner layer under siderite formed at the surface of LCS during alteration in the presence of bentonite/clay-rich environments (Romaine et al., 2015; El Mendili et al., 2015; Necib et al., 2017b). Magnetite may have formed in our experiments, and future characterization of a cross section of the steel coupons will make that determination.

The transportation of the dissolved Fe species produced by the corrosion of the steel is limited to the clay-steel interface. This corrosion product forms a siderite-smectite layer, creating a transitional layer between the LCS and the bentonite groundmass. One of the suggested precipitation mechanisms to describe the corrosion of LCS to the precipitation of siderite is (El Mendili et al., 2013):

$$CO_{2\,(aq)} + H_2O_{\,(l)} \leftrightarrow 2H_2CO_{3\,(aq)} \quad (8) \qquad \textbf{Eq. (10-1)}$$

$$H_2CO_{3\,(aq)} \leftrightarrow HCO^-_{3\,(aq)} + H^+_{(aq)} \quad (9a) \qquad \textbf{Eq. (10-2)}$$

or

$$HCO^-_{3\,(aq)} \leftrightarrow CO^{2-}_{3\,(aq)} + H^+ \quad (9b) \qquad \textbf{Eq. (10-3)}$$

$$Fe_{\,(s)} \leftrightarrow Fe^{2+}_{(aq)} + 2e^-_{(aq)} \quad (10) \qquad \textbf{Eq. (10-4)}$$

$$Fe^{2+}_{(aq)} + CO^{2-}_{3\,(aq)} \leftrightarrow FeCO_{3\,(Sd)} \quad (11a) \qquad \textbf{Eq. (10-5)}$$

or

$$Fe^{2+}_{(aq)} + HCO^-_{3\,(aq)} \leftrightarrow FeCO_{3\,(Sd)} + H^+ \qquad \textbf{Eq. (10-6)}$$

The carbon species (CO_2, HCO_3^-, CO_3^{2-}) in aqueous solutions are determined primarily by pH. At 25 °C, CO_2 is prevalent at low pH, HCO_3^- at near neutral (5.9 < pH < 8.9), and CO_3^{2-} at high pH (El Mendili et al., 2014). Based on the measured pH values during the experiments, the reaction most likely followed the bicarbonate pathway, leading to the precipitation of siderite. The formation of carbonates through this pathway will increase the pH of the solution through the formation of H+ (Eq. (10-6)), consistent with the gradually decreasing pH throughout the experimental durations after the first week of reaction time, where measured (HBT-3 and -4).

SEM-EDS analyses of the precipitate at the LCS surfaces indicate that the siderite has Ca incorporated into its structure. The incorporation of Ca into the siderite structure for an Fe-Ca carbonate product ($Fe_xCa_yCO_3$) causes an in-step or spiral dislocation, similar to the manner of growth seen for calcite (Caporuscio, et al. 2023, Figure E10) and may lead to a rounded type of the siderite crystal morphology (Matamoros-Veloza et al., 2020). This rounded morphology is evident in the SEM images of the siderite crystals at the LCS surface (see Caporuscio, et al. 2023, E9-E11).

The dense Fe-mineral layer on the steel surface that forms during alteration may act as a protective corrosion product film. The formation of siderite at the steel surfaces in the HBT experiments may then have acted to limit the amount of dissolved Fe from the LCS and maintain a low Fe concentration in the bulk solution (< 0.51 mg L^{-1} observed during the HBT experiments), additionally mediated by the circumneutral pH.

10.4.2 FY23 Experiments

The EBS International experiment completed in FY23 added ESD cement as a reactant with FE bentonite and the synthesized Grimsel GW solution. This experiment was run for four weeks as opposed to the 8-week duration of previous experiments to capture the incipient mineral alteration processes in the solid reactants. The results are additionally compared to the previously completed experiments HBT-1 through -4, and to the results of experiment CEM-3 completed as part of the EBS R&D FY23 work package discussed previously.

10.4.2.1 Aqueous Chemistry

The pH (as measured at 25 °C) increased in HBT-5 as compared to the other FE bentonite experiments (HBT-1, -2 and -4). During the first week of reaction time, however, in HBT-5 the pH initially decreased by 1.5 pH units (from 8.5 to ~7, as measured at bench) before increasing again to pH >9. The buffering capacity of montmorillonite through (de)protonation reactions at edge sites has some capacity to control pH, as seen in all of HBT-1 through -5 that have very similar steady-state pH values of ~6. However, this capacity for pH buffering is quickly overwhelmed by the release of OH- from ESD cement alteration, as evidenced by the increased pH after the first week of reaction time. Continued exposure to highly alkaline fluids may have some effect on bentonite through alteration to non-swelling clays. QXRD confirmed a ~3% loss of smectite minerals in the bentonite mineral assemblage after reaction (Section 10.3.1).

Increases in Al and Si observed in HBT-5 were also substantially greater than those in HBT-1 through -4 (Figure 10-2). The increased concentrations are not solely attributable to the addition of cement, since while Al trends in HBT-5 are similar to those of the CEM-series experiments discussed in Section **Error! Reference source not found.** that included ESD cement with no bentonite reactants, the Si concentrations in HBT-5 are substantially higher. This suggests another mechanism of increasing Si and Al concentrations in HBT-5. At a given temperature, increasing pH above circumneutral results in increased silicate solubility. At the conditions of the experiments, however, the in-situ pH in any of the experiments are not substantially above circumneutral: in-situ pH at 200 °C may range from ~5 in HBT-1 through -4, to ~6.5 in HBT-5. The cause of the elevated Si concentrations in HBT-5 is then currently not identified. Future work will focus on ongoing microscale and bulk characterizations of the solid reacted products (FE bentonite and ESD cement), including EMP analyses of the major and minor mineral phases to evaluate preferential dissolution or alteration of the materials in HBT-5.

The lack of sampling during experiments HBT-1 and -2 means that aqueous chemistry trends over the course of the experiments were not recorded. For this reason, the aqueous chemistry results of HBT-2 and -3 are not included in depth in the comparisons made in this discussion. The first and final samples of each of these experiments give some insight into the aqueous processes, however, and it is worth briefly noting here that the few collected samples from show that most elements analyzed HBT-1 appear to similar in trends if not in values to samples collected from HBT-3 and -5, that also included FE bentonite.

Similarly, the few samples collected from HBT-2 appear to follow trends analogous to those observed in HBT-4 that also reacted BCV bentonite and no FE bentonite. These initial results show reproducible impacts of each of the reacted barrier materials, especially the type of bentonite used (here, FE or BCV). Future work will focus on applying these results to model predictable outcomes for EBS stability based on the contributions of and interactions between different barrier materials.

10.4.2.2 Cement-FE bentonite co-alteration

The cylinder of ESD cement that was reacted in HBT-5 formed a reaction rim at the cement-solution interface during the four-week experiment. Chemical mapping showed most of the rim to be enriched in Si and Al (Figure 10-11): isolated locations of Ca-rich products in the reaction rim were also identified. This result is similar to that observed in the reaction rim formed in ESD cement reacted at 200 °C in CEM-1 (Section 9.4.3.4). The potential mechanisms for this alteration processes are discussed above: in brief, elevated temperature may result in higher Si to Ca ratios responsive to cement mineral dissolution as well as lower CO_2 solubility in solution, increasing the potential for silicate precipitation as opposed to calcite formation through cement carbonatation processes. In HBT-5, the impact of co-alteration with FE bentonite is apparent in the appearance of Al in the reaction rim, which was not observed in the cement reacted without bentonite in CEM-3. The identification of the secondary minerals is the focus of ongoing work characterizing the surface of the cement and reacted chips through Raman spectroscopy and SEM, as well as analysis of the reaction rim by EMP. Based on the CSH phases that formed abundantly in other cement experiments conducted at 200 °C and the chemical analyses to date, the reaction rim here is expected to be at least in part composed of CSH and C(A)SH minerals.

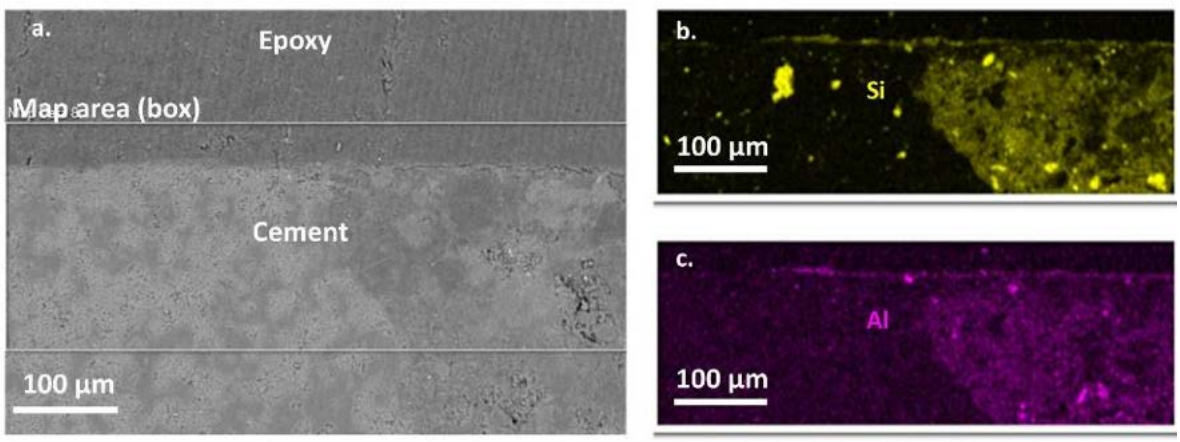

Figure 10-11. ESD cement round post-reaction in HBT-5. (a). BSE image of the cement mount in cross section, showing an area mapped for chemical analysis in the inset box. (b). EDS map of Si counts mapped in the area of the inset box. (c). EDS map of Al counts from the same area. (Fig 35)

Alkali elements in HBT-5 followed similar trends to those of the other experiments with FE bentonite as a reactant (HBT-1 and -3). Na increased during the experiments to higher concentrations than in HBT-4 (or in the quench sample of HBT-2), to slightly higher than the Na concentrations in samples collected from HBT-3 after the same amount of reaction time (Figure 10-12). K increased throughout the experiment duration, at slower rates and to lower concentrations than observed in the other HBT experiments. Ca increased over the entire experimental duration at rates and concentrations similar to HBT-4, and Mg quickly decreased to below detection limits (0.1 mg L^{-1}) within the first week of reaction time. From these results it appears that the concentrations of alkali elements are largely controlled by the type of bentonite included as a reactant rather than the added cement at the experimental conditions, where K and Ca concentrations are greater in solutions reacting with BCV bentonite, while Na concentrations are greater

in solutions reacting with FE bentonite. The contribution from the ESD cement appears to be elevated Na and decreased K concentrations compared to the other experiments that reacted FE-bentonite.

Comparing trends in K and Na concentrations in HBT-5 to in CEM-3, that reacted ESD cement with no bentonite, suggests cement-driven alteration processes occurred in the bentonite matrix. In CEM-3, the K concentration increased rapidly to > 40 mg L^{-1} within the first week of reaction time, while Na remained relatively conservative after a slight increase (to ~150 mg L^{-1}) in the first few days. This indicates that the ESD cement acted as a source of K in the system at 200 ºC. In HBT-5 the trends are reversed: K increased slowly over the experimental duration to ~10 mg L^{-1}, while Na increased rapidly to ~350 mg L^{-1} before concentration stopped increasing after ~2 weeks. Na additionally increased to greater concentrations than observed in the HBT experiments that reacted FE bentonite without cement. The observed increase in Na concentrations paired with the evidence that K was released from the ESD cement suggests that Na/K ion exchange occurred in the clays of the bentonite matrix reacted in HBT-5. This process potentially contributed to the alteration of the montmorillonite, observed in the decreased post-reaction smectite content identified by QXRD (Section 10.3.2.1, Figure 10-5).

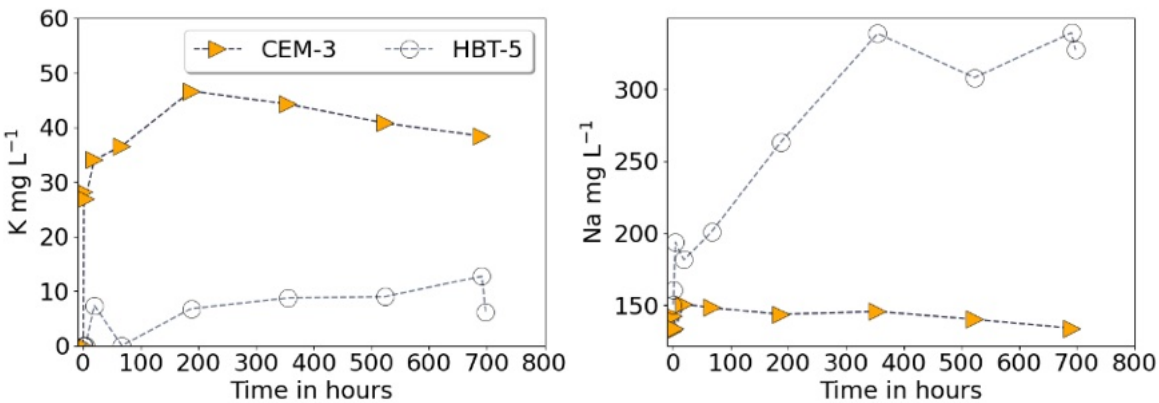

Figure 10-12. K and Na concentrations from CEM-3, that reacted ESD cement with synthetic Grimsel groundwater at 200 ºC; and HBT-5, that reacted the same ESD cement with FE bentonite in synthetic Grimsel groundwater.

The comparison between experimental results from HBT-5 to CEM-1 also highlights the potential for Na/K exchange in smectite minerals during interaction between different bentonites. The BCV bentonite reacted in HBT-4 resulted in K concentrations that increased throughout the experimental duration to relatively high concentrations (> 35 mg L^{-1}), and modest increases in Na (from ~100 to ~150 mg L^{-1}). The comparatively lower K concentrations from HBT-3 (< 20 mg L^{-1}) were also paired with an increase in Na that was not observed in HBT-4 (to >300 mg L^{-1}). This suggests the potential for the FE bentonite to act as a sink for K and source for Na through cation exchange between clays as well as to the bulk solution. Future work evaluating mass balance in each of these experiments can then be used to compare to predictive models of EBS interaction. The results may also be applied to understanding the effect of aqueous phase equilibration on the EBS materials used in the HotBENT full-scale experiment, where BCV and FE bentonite will have had long-term interactions.

10.5 Conclusions

The completed experiments document the potential mineralogical and geochemical changes in the FE and BCV bentonite at 200 ºC and water saturated conditions. The main observed effects of heating for the eight-week period were the slight reduction in montmorillonite swelling, the formation of carbonate minerals in experiments that contained BCV, and the lack of formation of silicate minerals such as zeolites. LCS coupons included in the experiments were variably corroded and provided a substrate for

Fe-rich mineral precipitation. Fe-oxides and phyllosilicates were observed in the experiment with FE bentonite only. In experiments with BCV, Fe-rich carbonates (siderite) were observed on the reacted steel surface in addition to oxides and Fe-saponite.

Completed analyses for these and future experiments using BCV bentonite will focus on the mechanisms that drive $FeCO_3$ formation at the steel surfaces. Future experiments may focus additionally on how the pH effects caused by the addition of cement products affect this and other reactions in the FE-BCV bentonite mixture in a crystalline environment. Completing experiment sets at lower temperatures (90 ºC, the predicted temperature at the buffer/rock interface) will also allow insight into any threshold behaviors for the reactions interpreted to occur in our experiments, especially considering the lower stability of carbonate minerals with decreasing temperature.

The results of the experiment in FY23 (HBT-5) additionally reacting FE bentonite with a low-alkali cement (ESD cement) resulted in a bulk solution pH of ~9 (as measured at 25 ºC), elevated from bulk solution pH values of ~6 in previous HBT experiments that did not react cement. Increased Na concentrations and depressed K concentrations compared to the anticipated contribution from the ESD cement also suggested cation exchange in the smectite phases. The reacted FE bentonite additionally had a smectite content that decreased by ~3% after hydrothermal interaction with the ESD cement. The reacted ESD cement after co-alteration with bentonite was observed to have formed a thin (~20 µm) Si-Al enriched reaction rim apparently comprising C(A)SH minerals at the cement-solution boundary.

Future work will focus on extracting geochemical effects driven by each of the reactants (FE bentonite, BCV bentonite, steel, host rock, and cement) on the hydrothermal chemistry of EBS systems over time. Isolating the effect of each reactant will facilitate predictive modelling that can be validated by comparison to the short-term results of the HBT experiments discussed here, as well as with future results from the long-term HotBENT experiment. Future experiments will be designed to isolate any ambiguous processes with the goal of contributing constraints on reaction rates and products to geochemical databases characterizing in-situ EBS alteration over repository timescales.

This page intentionally left blank.

11. CALIBRATED SIMULATIONS OF A FULL-SCALE HEATER EXPERIMENT IN OPALINUS CLAY

11.1 Introduction

The full-scale emplacement experiment at the Mont Terri Underground Rock Laboratory, Switzerland has been used for process model development and modeling analysis, as part of the DECOVALEX-2023, Task C study (Figure 11-1). The experiment was designed in part to investigate thermal-hydrological-mechanical (THM) processes resulting from emplacement of spent fuel and high-level nuclear waste in a geological repository in opalinus clay host rock (Nagra, 2019). In DECOVALEX-2023, Task C numerical models were built to study the various processes such as bentonite thermal conditions and pore pressure changes in the opalinus clay because of heating using experimental dataset.

This report summarizes progress in coupled Thermal-Hydrologic (TH) modeling of Step 1c, with calibration modeling and the addition of shotcrete to the model geometry. Step 1 is on modeling the heating phase of the FE experiment with changes in pore pressure in the opalinus clay, because of heating. Step 1c is on calibration of models using available data.

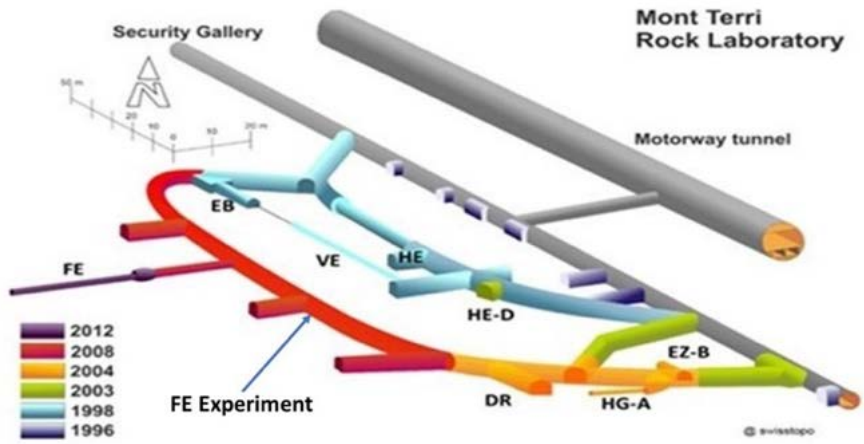

Figure 11-1. The FE experiment at the Mont Terri underground laboratory

11.2 Step 1c Modeling

The Step 1c TH simulations started using properties developed in Step 0. Properties were then varied during model calibration using experimental data. For the TH simulations the numerical code PFLOTRAN (Hammond et al., 2014) was used. Simulations were run for five years from the start of heating.

11.2.1 Step 1c Model Geometry

Figure 11-2 shows a representation of the experimental setup, with the experiment tunnel represented as a cylinder, and heaters placed in the tunnel with the centerline of the heater aligned to the centerline of the tunnel. The opalinus clay is bedded and has anisotropic properties in directions parallel and perpendicular to bedding. The bedding dips at 34˚ from the horizontal as shown in Figure 11-3. To include shotcrete around the walls of the experimental tunnel and to add mesh refinements, a new 50 m x 50 m x 50 m mesh was generated. The new mesh size has 1,497,366 elements (Figure 11-4). A 30 cm thick shotcrete was included, represented with two elements in the radial direction, as shown in Figure 11-5. Solving the coupled flow and energy multiphase equations and the large mesh size required use of high-performance computing.

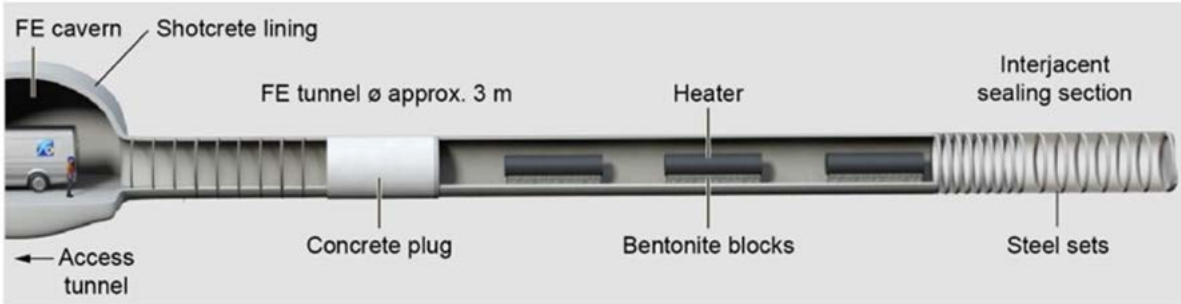

Figure 11-2. Schematic diagram of model geometry for Step 1 simulations.

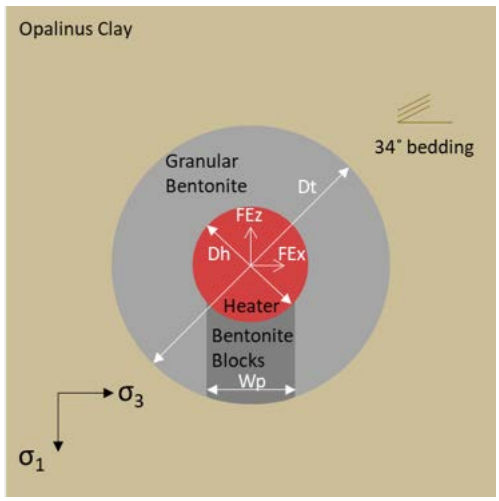

Figure 11-3. Model geometry for Step 0 (cross-section view of tunnel).

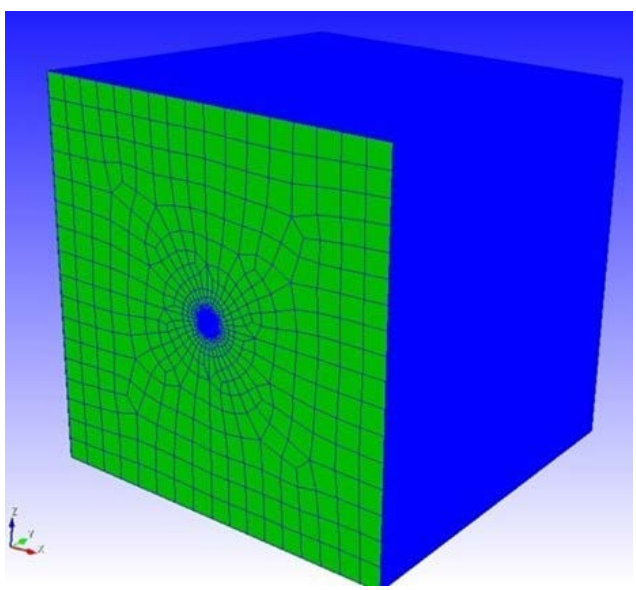

Figure 11-4. Geometry and meshing used for Step 1c simulations.

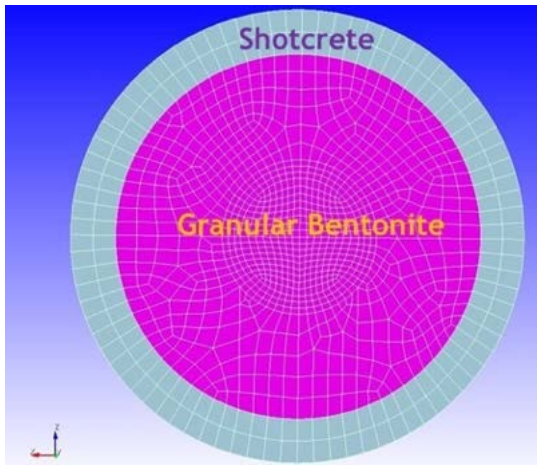

Figure 11-5. Representation of shotcrete used for Step 1c simulations.

11.2.2 Simulation Model Setup

For Step1c, simulations start with the heating phase using the heating schedule given in Table 11-1. Representation of the experimental tunnel for the simulations is shown in Figure 11-6. Activities prior to the heating phase such as the ventilation phase have not yet been considered. Thus, the initial condition used for simulations is not the undisturbed state. Approximations were made to capture an initial condition that closely fits the condition at the beginning of heating. The following initial and boundary conditions were assumed:

- The opalinus clay was assumed to be initially at a temperature of 16.5 °C and pore water pressure of 2 MPa. Hydrostatic pressure was applied. Anisotropy in permeability and thermal conductivity was applied because of the bedding.
- The granular bentonite and the bentonite blocks were assumed to be initially at a temperature of 18 °C and different saturation conditions. They were assumed to be at liquid saturation of 0.65 and 0.18, respectively. Those conditions match the initial relative humidity at each material.
- The concrete was assumed to be at an initial liquid saturation of 0.1
- Diffusion Coefficient values of 2.0×10^{-9} m^2/s for the liquid phase and 2.0×10^{-5} m^2/s for the gas phase were used.
- Boundary Condition: heater power schedule is given in Table 11-1. Heating was started with Heater 1 only, with stepped increase to the maximum amount. Heaters 2 and 3 were then added at Days 64 and 65, respectively.

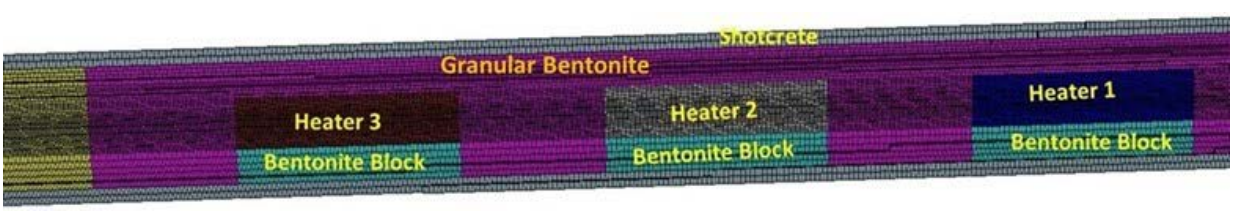

Figure 11-6. Representation of the experimental tunnel, Step 1c simulations.

Table 11-1. Heating schedule for the three heaters (Task C Specifications)

	Date	Power (W)
Heater 1	12/15/2014 01/13/2015 02/16/2015	500 1000 1350
Heater 2	02/17/2015	1350
Heater 3	02/18/2015	1350

For Step 1c simulations material and fluid properties that are part of the PFLOTRAN code (Hammond et al., 2014) were mainly used. For TH simulations water and steam properties Equation-of-State (EOS) from the International Formulating Committee (IF97, 1997) were used. Water density, steam density and enthalpy are calculated as a function of temperature and pressure. Viscosity is calculated as a function of temperature, pressure, and saturation pressure. Vapor diffusion is a function of pressure and temperature. The diffusion coefficient is calculated using the equation by Vargaftik (1957) and Walker et al. (1981).

In PFLOTRAN heat capacity is represented as a constant value. The Task C provided relation for thermal conductivity as a function of saturation as well as the default function in PFLOTRAN were used. The default thermal conductivity equation in PFLOTRAN (Somerton et al., 1974) is given as:

$$\lambda_{th} = \lambda_{dry} + \sqrt{s}(\lambda_{sat} - \lambda_{dry}) \quad \textbf{(Eq. 11-1)}$$

Where:

- λ_{th} = thermal conductivity
- λ_{dry} = dry thermal conductivity
- λ_{sat} = fully saturated thermal conductivity

11.3 Step 1c Simulation Results

Updated TH simulations were made for Step 1c. As described above, parameter values were varied to calibrate the model using experimental data. Selected calibration simulation results are presented below. The calibrated properties for granular bentonite, bentonite blocks, and opalinus clay are shown in Table 11-2. The calibrated shotcrete properties were permeability of 2.0E-21 m^2, thermal conductivity of 0.3 (dry)/0.5 (wet) W/m K and pore compressibility of 3.5E-12 1/Pa. Figure 11-7 shows predicted distribution of temperature after 1800 days of simulation. The figure on the left is a cross-section along the tunnel axis. The figure on the right is a cross-section perpendicular to tunnel axis, showing the effect of the anisotropy in the opalinus clay. In addition, mesh refinement and the presence of the shotcrete with the selected properties has affected results. Figure 11-7 and figures of distribution of pressure and saturation show that the selected domain size for TH simulations minimizes boundary effects.

Table 11-2. Calibrated properties.

Input Parameter	Value
Granular bentonite permeability (m^2)	3.5E-21
Granular bentonite thermal Conductivity (W/m K)	0.3/1.0
Granular bentonite pore compressibility (1/Pa)	6.95E-7
Bentonite blocks permeability (m^2)	1.0E-22
Bentonite blocks thermal Conductivity (W/m K)	0.8/1.1
Bentonite blocks pore compressibility (1/Pa)	3.74E-7
Opalinus clay permeability (Parallel) (m^2)	1.5E-20
Opalinus clay permeability (Perpendicular) (m^2) Opalinus clay thermal Conductivity (Parallel) (W/m K)	3.0E-21 1.8
Opalinus clay thermal Conductivity (Perpendicular) (W/m K)	1.29
Opalinus clay pore compressibility (1/Pa)	5.13E-10

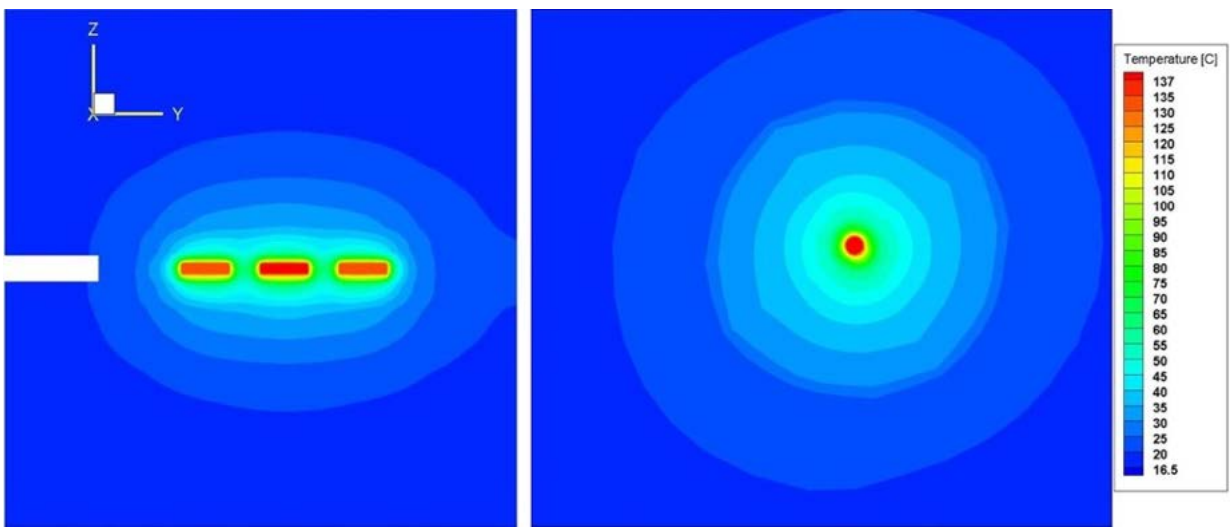

Figure 11-7. Prediction of temperature distribution at 1800 days.

Predictions of temperature, relative humidity, and pressure evolution at selected observation points in the bentonite units and opalinus clay were also conducted. The predicted results were compared to experimental results as shown below.

11.3.1 Results in the Bentonite

Figure 11-8 shows locations of observation points in the granular bentonite where results are to be shown. Figure 11-9 and Figure 11-10 show early time evolution of temperature and pressure, respectively. The plots illustrate processes dominant at early time at different locations close to Heater 2. Heating starts at Heater 2 after 64 days of simulation time (Table 11-1). Thus, temperatures are near constant during this period. Once heating is started temperatures rise at the observation points according to their proximity to the heater and their position with respect to the opalinus clay bedding (anisotropy). Figure 11-10 shows the respective gas saturation evolutions. The period before the start of heating is marked by gradual

saturation of the granular bentonite due to flow from the opalinus clay. At the start of heating, points close to the heater see immediate drying up due to conduction and vapor diffusion. Points further from the heater show a sharp drop of gas saturation before rising. As with temperature, gas saturation is also affected due to position with respect to the opalinus clay bedding.

Predictions of temperature and relative humidity, along with experimental data, are shown in Figure 11-11 and Figure 11-12, respectively. The predicted results using calibrated properties are close to the experimental. Figure 11-13 shows effect of shotcrete thermal conductivity on temperature at point 7. Matching was better when shotcrete lower thermal conductivity values were used.

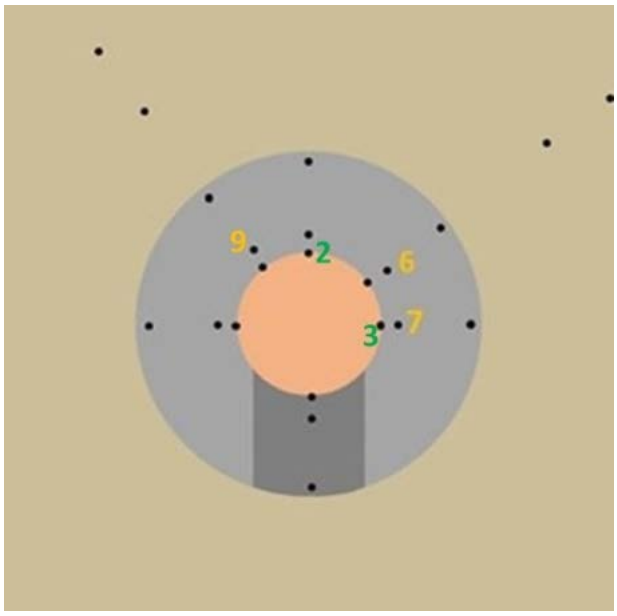

Figure 11-8. Location of observation points in the granular bentonite near Heater 2 (Points 2, 3) and, 20 cm away from Heater 2 (Points 6, 7 and 9)

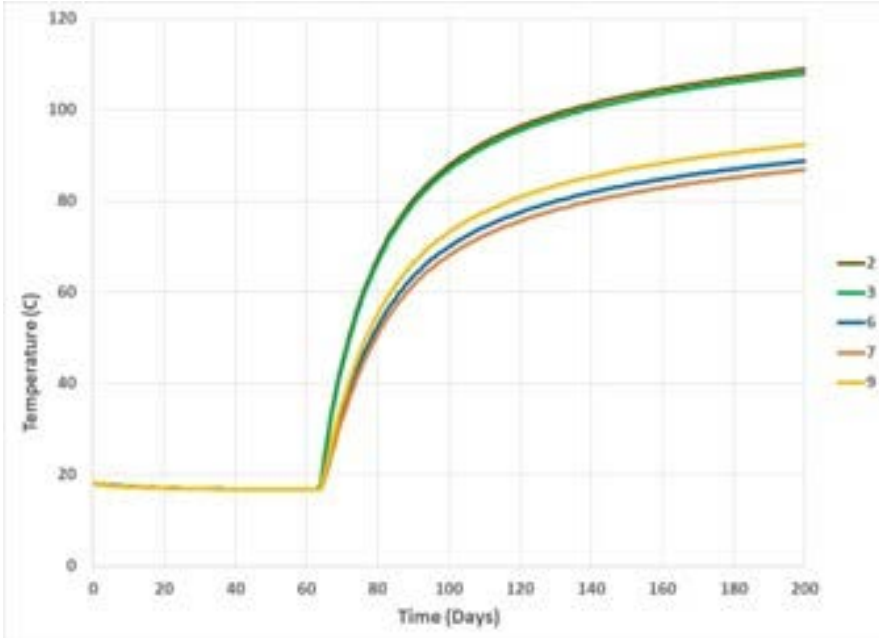

Figure 11-9. Model temperature prediction at early time at selected observation points in the granular bentonite

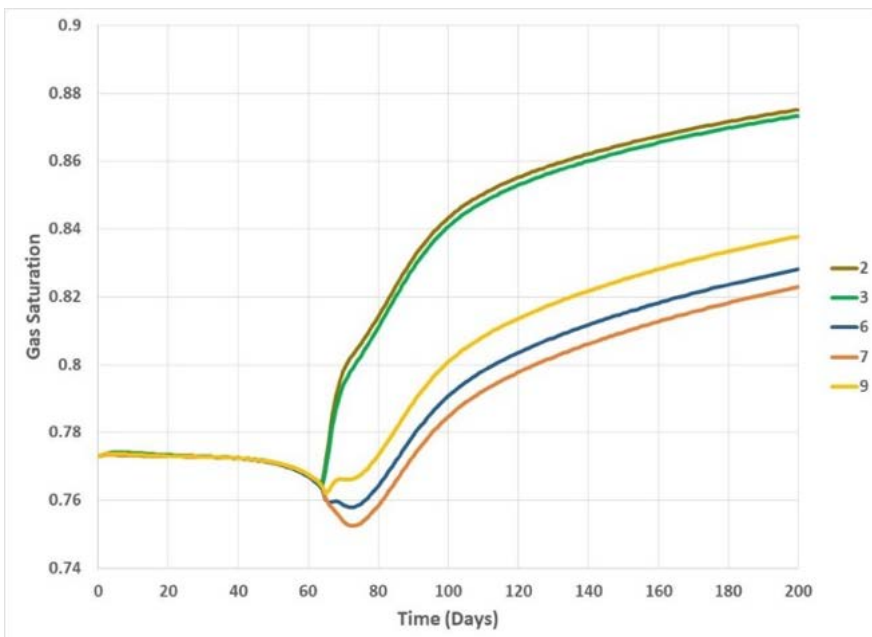

Figure 11-10. Model gas saturation prediction at early time at selected observation points in the granular bentonite

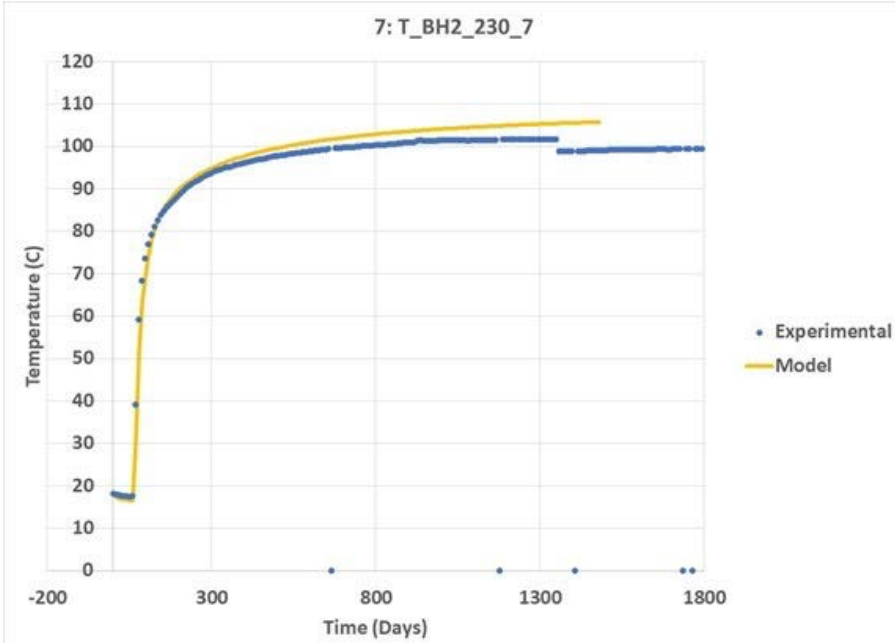

Figure 11-11. Temperature comparison at observation point 7 (Model and Experimental).

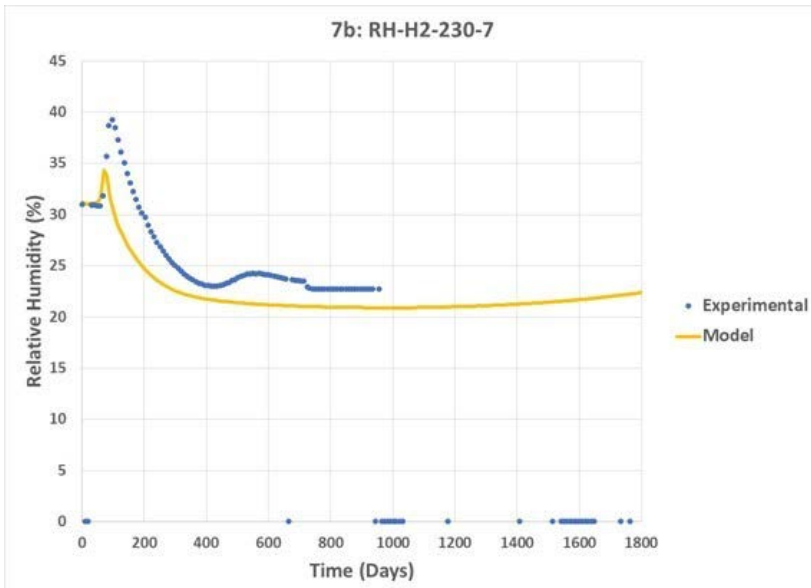

Figure 11-12. Relative humidity comparison at observation point 7 (Model and Experimental).

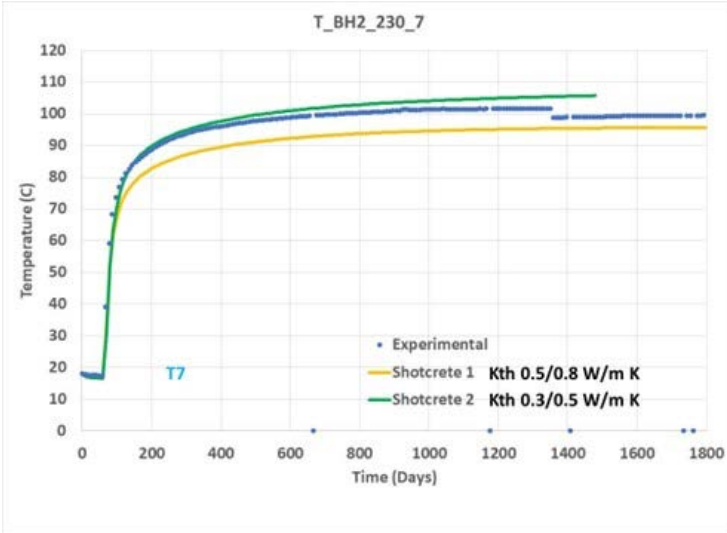

Figure 11-13. Temperature comparison at observation point 7, effect of shotcrete thermal conductivity.

The calibration simulations also included the opalinus clay. For this report results are shown for observation point 02 in the opalinus clay (Figure 11-14), which is the closest observation point to the experiment tunnel. Predictions of pressure and temperature, along with experimental data, are shown in Figure 11-15 and Figure 11-16, respectively. The predicted results are generally close to the experimental. Further calibrations will be conducted to improve pressure predictions at earlier time. Figure 11-17 shows effect of shotcrete permeability on pressure at observation point 02. Selecting high shotcrete permeability results in faster drainage into the tunnel, and thus lower pressures. This was also observed with opalinus clay permeability.

Figure 11-14. Location of observation point 2 in the opalinus clay, close to the experimental tunnel.

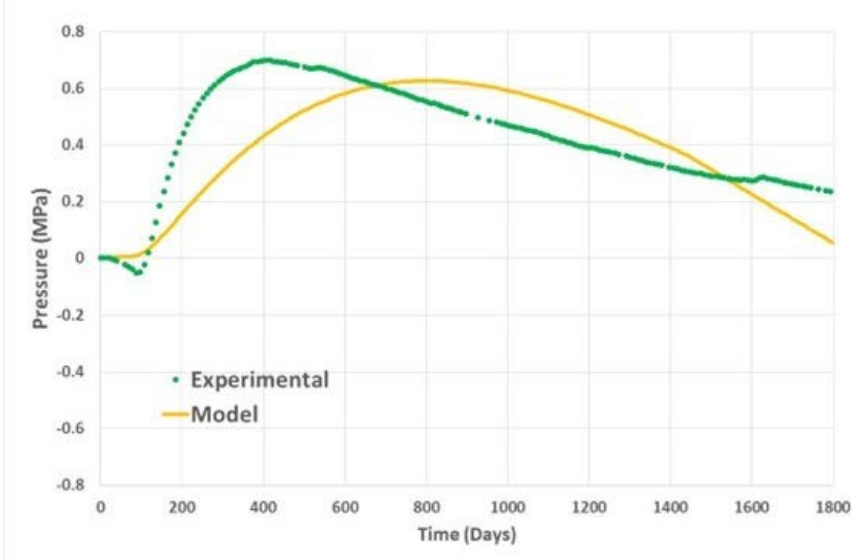

Figure 11-15. Pressure comparison at observation point 2 in the opalinus clay (Model and Experimental)

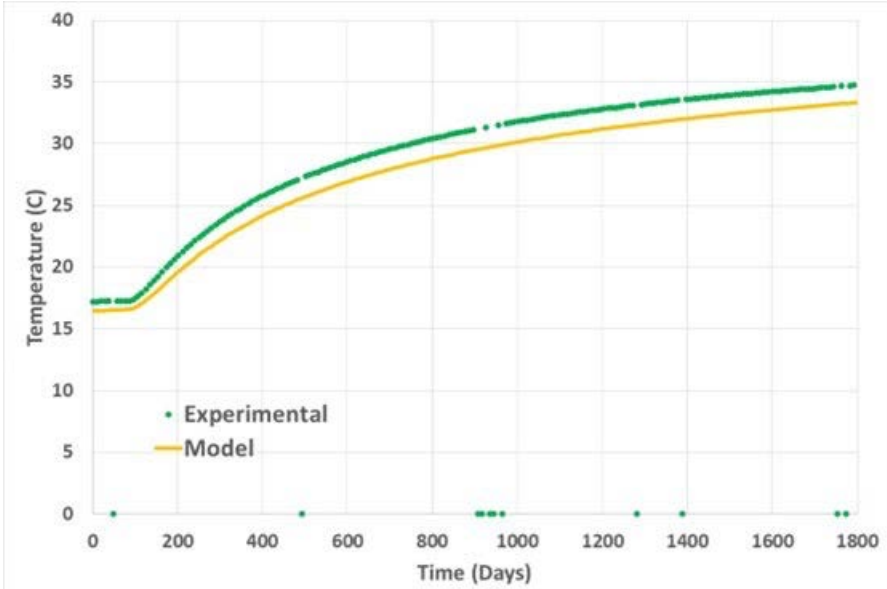

Figure 11-16. Temperature comparison at observation point 2 in the opalinus clay (Model and Experimental).

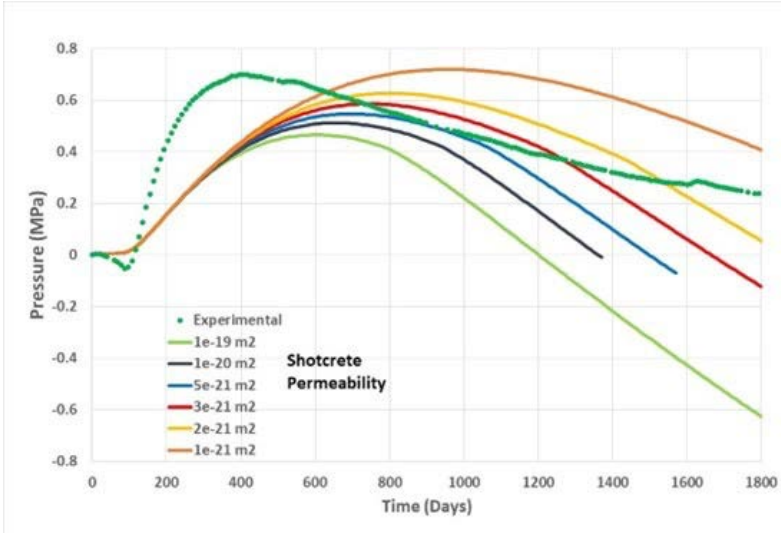

Figure 11-17. Comparison of pressure predictions at observation point 2 in the opalinus clay, effect of shotcrete permeability.

11.4 Summary and Future Work

Calibration TH simulations of Task C, Step 1c were conducted using PFLOTRAN numerical code and a refined 3-D mesh. The new mesh also includes a 30 cm thick shotcrete. Comparison of predicted temperature evolution at selected observation points in the bentonite blocks and opalinus clay with experimental data were very close. The presence of the shotcrete affects both fluid flow and heat transport between the opalinus clay and the tunnel. Results also show that the selected domain size is adequate for TH simulations due to the minimal boundary effects. Predictive simulations will continue with Step 2, which includes modeling of the ventilation phase. New modeling of the heating phase will follow to update simulations using parameters developed during the ventilation phase. The simulations described in this report assumed that the FE experiment can be represented using TH processes. There is a need to quantify the effect of neglecting rock mechanics on simulation results. Note also that results from intermediate simulations such as presented here are preliminary, and thus may not be representative.

This page intentionally left blank.

12. SYNTHESIS, CHARACTERIZATION, AND EVALUATION OF MODIFIED BOEHMITE MATERIALS AS ANION SORBENT ADDITIVE IN EBS DESIGN

12.1 Introduction

The design of engineered barrier systems for deep geologic nuclear waste repositories includes materials that have a high adsorption selectivity for specific radionuclides. Readily available natural materials, such as bentonites, serve to trap a broad range of cationic radionuclides, but sorbents are also needed for selective adsorption of anionic radionuclides (*e.g.,* iodine). Our R&D effort has focused on modifying layered AlOOH (boehmite) to develop hybrid materials whose internal and external surfaces can be altered for high selectivity for specific radionuclides. This report highlights results from recent efforts to better understand and characterize organically modified boehmite (glycoboehmite, GB), which contains intercalated butanediol molecules (Bell et al., 2021). Molecular modeling was used to evaluate GB structural and spectroscopic properties of GB as a function of butanediol loading, and batch sorption experiments were used to evaluate iodide uptake capacity of ion-exchanged GB.

12.2 Structural and Spectroscopic Properties of Glycoboehmite from Molecular Modeling

Classical molecular dynamics (CMD) simulations were combined with quantum calculations (density functional theory, DFT) to determine GB properties as a function of butanediol loading. Figure 12-1 shows the layer spacing of GB as a function of butanediol content per unit cell (u.c.) from CMD simulations. Note that a loading of 2.0 diols/u.c. corresponds to a 1:1 aluminol:diol ratio on the boehmite basal surface. The CMD results are in good agreement with DFT geometry optimization at low and high loadings, and with experimental X-ray diffraction (XRD) (Inoue et al., 1989). The CMD layer spacings are consistently lower than DFT results, which is discussed below.

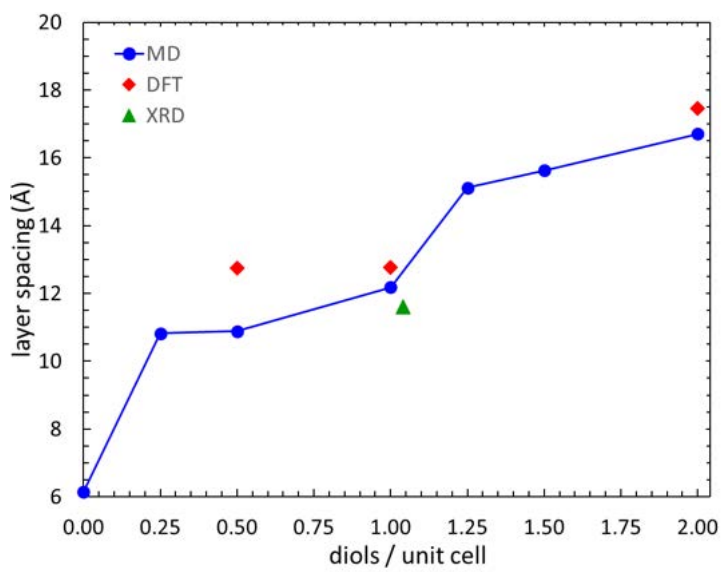

Figure 12-1. Results from MD simulations showing average layer spacing of glycoboehmite as a function of butanediol loading. Results from DFT calculations measurements and XRD (Inoue et al., 1989) are shown for comparison.

Snapshots from CMD simulations and DFT geometry optimization are shown in Figure 12-2. At low loading (0.5 diols/u.c.), butanediol molecules are able to cross link between adjacent AlOOH layers via hydrogen bonding. The CMD layer spacing is smaller than DFT by 1.75 Å because the alkyl chains are not fully extended in the former. In addition, the functional used in the present DFT calculations has a well-known, systematic tendency to slightly overestimate bond length distances compared to XRD data. Thermal effects in the CMD simulations allow mixing of the alkyl chains, resulting in small layer spacings. At higher loading (2.0 diols/u.c.), individual boehmite layers become separated, resulting in higher layer spacings. The CMD and DFT layer spacings are in much better agreement because there is less conformational flexibility within the butanediol monolayers. The arrangement of butanediol monolayers at high loading results in a hydrophilic midplane region that is coated with alcohol groups, which should be accessible to aqueous ions.

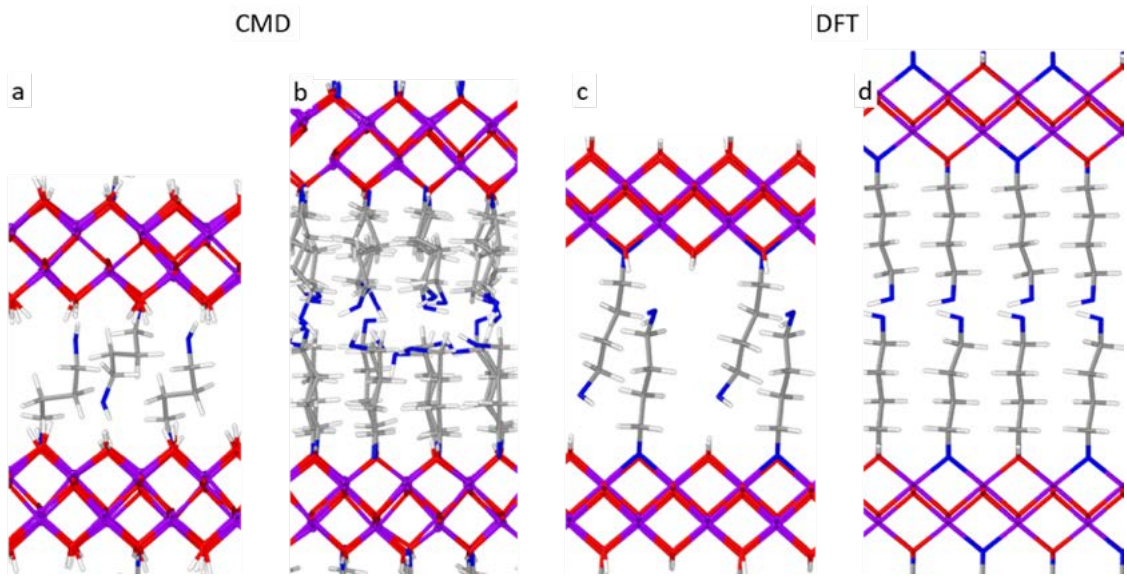

Figure 12-2. Snapshot of GB from CMD simulations at a) 0.5 diols/u.c and b) 2.0 diols/u.c.; corresponding DFT-optimized structures c) 0.5 diols/u.c and d) 2.0 diols/u.c. (Al=purple, O_boehmite=red, C=gray, H=white, O_alcohol=blue).

The thermal stability of GB models up to 300 °C (573 K) were also simulated using CMD. As seen in Figure 12-3, models with a partially filled interlayer and a full monolayer show limited thermal expansion over this temperature range. These results agree with experimental thermal analysis of synthesized GB, which showed minor mass loss up to 200 °C attributed to adsorbed water (Bell et al., 2021). These preliminary results suggest that this material, in its pristine state, is expected to be stable in repository settings.

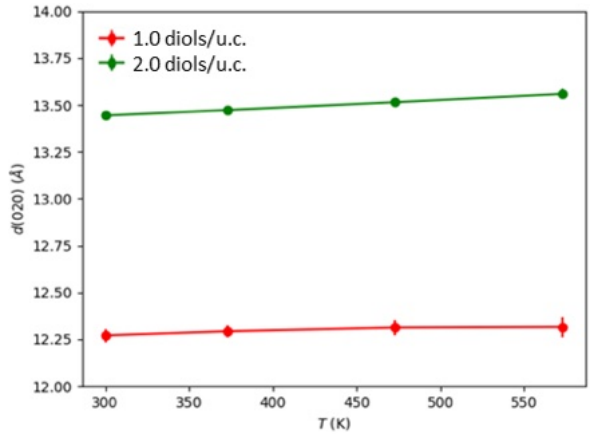

Figure 12-3. Results from CMD simulations of GB showing the layer spacing as a function of temperature for loadings of 1.0 and 2.0 diols/u.c. Error bars are shown as lines.

To further confirm the thermal stability of the GB models used in CMD simulations, ab initio molecular dynamics (AIMD) simulations were conducted at several temperatures between 300 and 573 K for smaller supercells at the same butanediol loadings. CMD snapshots were used as initial structures for AIMD. Consistent with results from CMD simulations, analysis of the AIMD simulations for temperatures up to 573 K did not show any decomposition of diols or OH/CH dissociation. Calculated radial distribution functions, g(r), with fixed cell volumes also indicate that the chemisorbed GB structures are stable at high temperature (Figure 12-4).

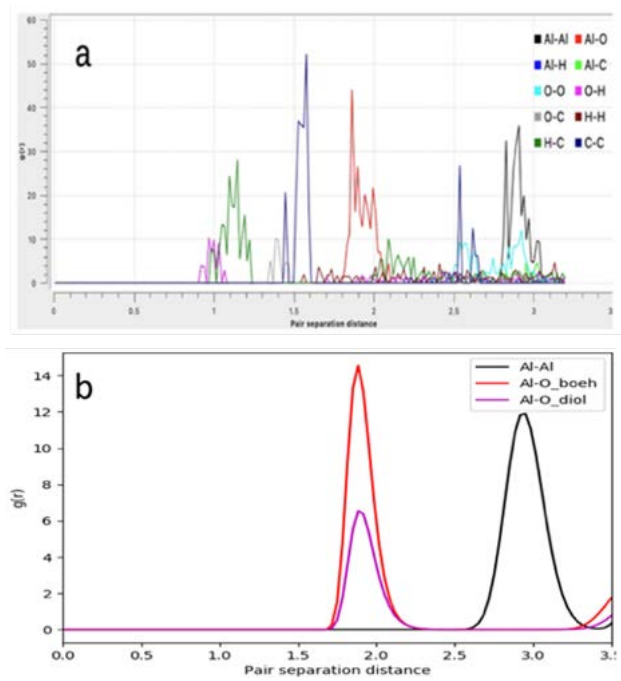

Figure 12-4. Radial distribution functions, g(r), as functions of pair separation distance (Å) for various atom pairs in the (a) AIMD and (b) CMD simulations at 573 K of the chemisorbed GB models corresponding to low loading (1.0 diols/u.c.).

12.3 Experimental Evaluation of Glycoboehmite Materials for Anion Sorption

The synthesis and characterization of GB was detailed in a previous publication (Bell et al., 2021). Previous zeta potential results showed that glycol modification of boehmite lowered the isoelectric point (IEP) from 8.6 (aqueous boehmite) to 5.2–6.0 (GB), suggesting that GB surface charge could be used to modify this material for high anion sorption capacity. Because GB contains adsorbed K^+ resulting from the use of KOH as a mineralizer, we explored the possibility of post-synthetic modification in the form of cation exchange. Specifically, we produced modified GB using chloride solutions containing divalent metal cations (Mg^{2+} and Ni^{2+}) to provide sites for enhanced anion binding. The isoelectric point is shifted to a pH of 6.5 in the Ni-treated material (Figure 12-5). The shape of the curve is also altered from the linear charging profile in GB. At pH above the IEP, there is a more rapid development of negative surface charge between pH 7 to 8.5, with a higher magnitude of negative charging up to pH 10. It follows that the addition of the positive Ni^{2+} cations raises the IEP as would be expected for surface adsorption.

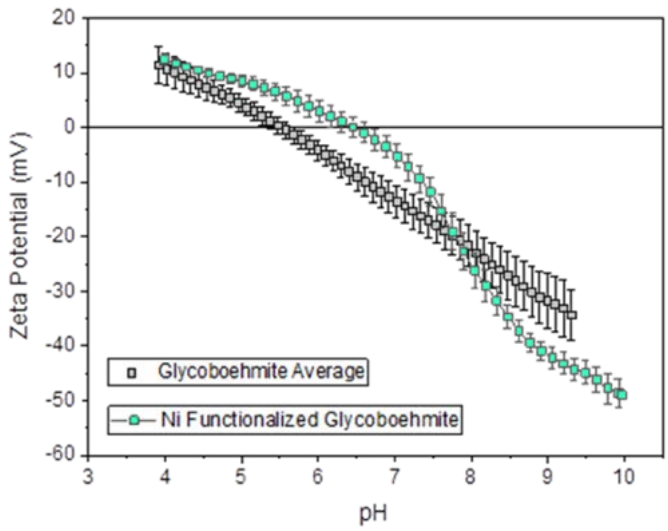

Figure 12-5. Average value and standard deviation of glycoboehmite zeta potential as a function of pH.

To further investigate the cation exchange in the material, inductively coupled plasma optical emission spectroscopy (ICP-OES) was used to measure the cations in $MgCl_2$, $CaCl_2$, and $NiCl_2$ solutions after reaction with GB. Results in Figure 12-6 show reduced uptake of the alkaline earth cations compared with Ni^{2+}, even though a similar amount of K^+ was released in each case. Additional experiments are planned to further evaluate the surface charging behavior of GB with ion exchange, including the possibility of Ni^{2+} incorporation into the AlOOH framework.

Figure 12-6. ICP-OES results from GB cation exchange experiments showing uptake of Mg^{2+}, Ca^{2+}, and Ni^{2+} along with release of K^{+}

Subsequent batch I^{-} sorption experiments (Figure 12-7) show impressive I^{-} uptake by Ni-GB compared to as-synthesized GB or Mg-GB. Iodide uptake by Ni-GB is an order of magnitude greater than the other materials, which cannot be explained by the greater Ni^{2+} loading seen in the cation exchange results. Figure 12-7 also shows that I^{-} uptake by Ni-GB is reduced when the pH is held fixed at 7.0. Based on the zeta potential results, the surface charge is more negative at pH 7 compared to pH 6, suggesting an electrostatic component to I^{-} uptake.

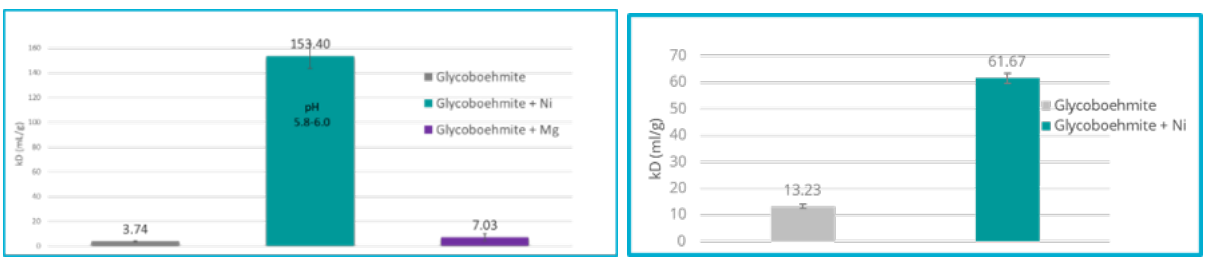

Figure 12-7. Results from batch sorption experiments showing I^{-} adsorption coefficient (kD) for (left) as-synthesized and cation-exchanged GB at natural pH of the material (5.8–6.0), and (right) as-synthesized and Ni-exchanged GB while adjusting the pH to 7.0.

12.4 Summary and Future Work

We have combined molecular modeling with experiment to develop modified boehmite materials for the adsorption of anionic radionuclides such as I^{-} in EBS environments. Molecular modeling results revealed the interlayer expansion and structure as a function of butanediol loading. Importantly, the interlayer region at higher loading contains a hydrophilic region coated with alcohol groups, providing a possible region for ion adsorption. Future modeling efforts will examine in detail the interaction between adsorbed ions and GB. Experimental results showed that GB can be modified via cation exchange, producing a material rich in divalent cation sites for subsequent anion binding. In particular, batch sorption experiments showed that Ni-modified GB has an impressive sorption capacity for I^{-}. Future experimental efforts will focus on identifying the mechanisms for both cation exchange and anion uptake and evaluating the material's stability under repository conditions.

This page intentionally left blank.

13. CHEMO-MECHANICAL CHARACTERIZATION OF CEMENT-ROCK INTERFACES

13.1 Overview

The long-term performance of cementitious materials at interfaces between cements and geologic strata (e.g., rock formations) is a critical safety component in many applications, including deep well storage (Newell & Carey, 2012; Hangx et at., 2016), boreholes for oil and gas extraction (Mangadlao et al., 2015), nuclear waste disposal (Ewing et al., 2016), and a broad spectrum of engineered barrier materials and structures (Ingraffea et al., 2014; Gaucher & Blanc, 2006). Cement mix designs and additives are chosen to achieve safety functions of structural performance, hydraulic containment, and contaminant retention at the interface with host rock. Failure of cements in this region can result from chemo-mechanical transformations at the cement-rock interface, induced by natural gradients in mineral assemblage, pore water pH, and porosity that promote mass transport and chemical reactions across the boundary. The important characteristics that may change spatially and temporally during long-term interactions are porosity, solid volume, mineralogy, porewater pH and composition, hydration, mechanical properties (e.g., elastic modulus, ductility), and mass transport properties. For the proposed use of cement in potential borehole and mined disposal configurations, the long-term performance of the cements at the interface with host rock is uncertain. The characterization of chemo-mechanical changes at interfaces is needed: (i) for selecting appropriate formulation and construction of the cementitious materials for stable, long-term nuclear waste disposal (Gruber et al., 2022), and, (ii) to validate the mechanisms incorporated into models that are used to provide long-term performance estimates.

Without a consistent way to characterize cement-host rock interfaces, it is difficult to compare cement characteristics on the micro and nanoscale and have a basis for comparison with simulation results. Thus, a methodology was developed to compare interface evolution under varying conditions with several different host rocks. The resulting data collected could then be used to calibrate model predictions of alteration zones, increasing the reliability of long-term estimates.

A draft journal manuscript has been completed for a case study on oil shale-OPC Paste interfaces and will be submitted later this year. The discussion below will briefly discuss these findings and outline the process for data analysis going forward for other interface studies.

13.2 Objectives

The overall objective for this project is to provide and demonstrate methodology for determining mechanistically based estimates of long-term changes in the chemo-mechanical properties of cementitious materials interfacing with host rocks relevant to potential nuclear waste disposal sites.

This research (i) characterizes chemical and mechanical changes within the alteration zones of both the cements and the host rocks after controlled aging processes; (ii) identifies structural and chemical features that affect the fate of radionuclides at the interface of dissimilar materials; and (iii) provides a basis to verify predicted changes in major mineral phase composition and distribution that affect the diffusion-controlled transport of tracer constituents using reactive transport modeling.

13.3 Methods

13.3.1 Workflows

An approach for rock/cement interface characterization workflow was developed that facilitates comparison of geochemical-reactive transport simulations with experimental results. Experimental data is

collected using a variety of instruments that characterize chemical and mechanical properties (Figure 13-1).

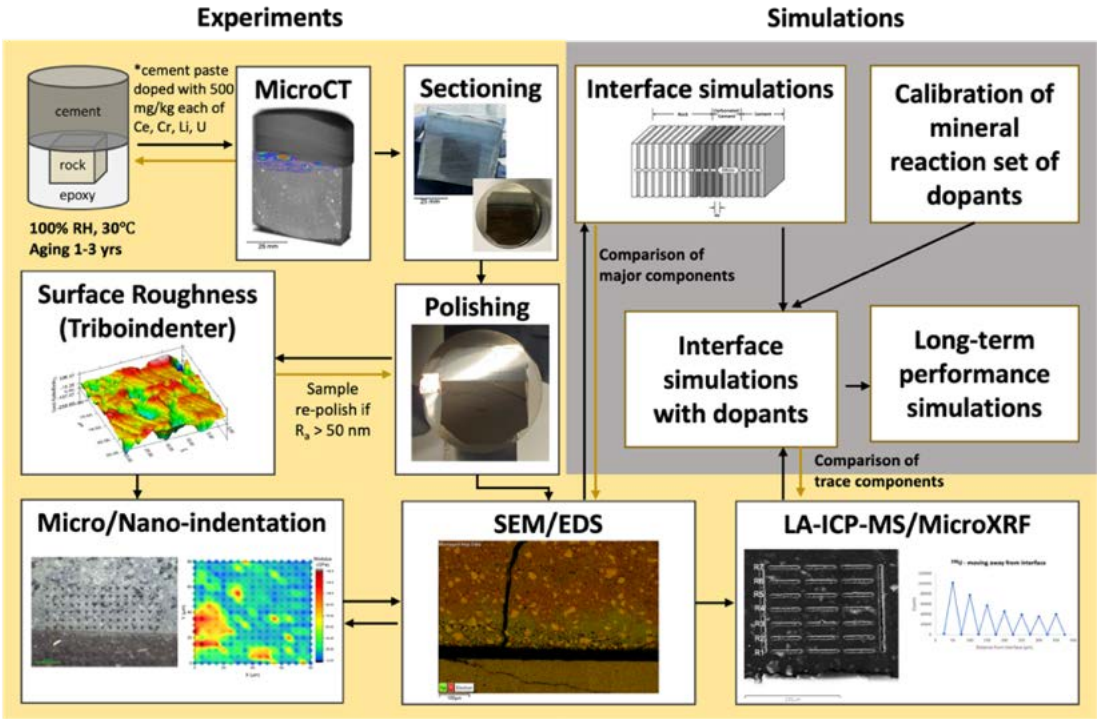

Figure 13-1. Project workflow combining a variety of characterization equipment; outlines how simulation results can be compared to experimental data.

For each step in the workflow, Table 13-1 summarizes the characterization techniques utilized and the corresponding information obtained at each step. Optical Microscopy has since been added to the workflow, and an updated version of Figure 13-1 will be published in the next few months.

Table 13-1. Characterization Summary

Instrument	Application Summary	Purpose of Results
MicroCT	Uses x-rays to non-destructively capture 3D images of materials. X-ray intensity is correlated to the density of the material imaged. Non-destructive.	Observe relative density changes near the interface; identify large features of interest for priority sectioning (interfacial deposits, large cracks, etc.)
Optical Microscopy	Uses visible light to illuminate a sample both through (brightfield) and around (darkfield) an objective lens. An attached camera allows capture of the reflected light for processing purposes. Non-destructive.	Observe surface features (e.g., unhydrated cement particles, pores, layering) and compare them to intensity changes observed in microCT; select areas for precise BSE and EDS imaging
SEM/EDS	Uses an energized electron beam in tandem with a variety of detectors to measure backscattered electrons, secondary electrons, and x-rays emitted from the sample. Non-destructive.	Measure quantitative elemental composition of major constituents, characterize surface features of polished sample, select areas for mechanical testing
Micro-indentation	Uses a large Berkovich tip to perform micro-mechanical indentation tests. Micro-indentation measures phase-averaged mechanical responses (> 10 µm spot size).	Measure reduced modulus and hardness of average phases in a region; identify gradients in mechanical properties over large areas
Nano-indentation	Uses a small Berkovich tip to perform a variety of nano-scale mechanical tests. Nano-indentation looks at the single-phase mechanical response of materials (< 1 µm spot size).	Measure reduced modulus and hardness of single phases in a region; identify mechanically distinct phases that can be correlated with SEM/EDS data for phase deconvolution
Laser Ablation Inductively Coupled Plasma Mass Spectroscopy (LA-ICP-MS)	Uses a laser ablation system in tandem with an ICP-MS to quantify spatial distribution of constituents at low concentration.	Measure elemental composition of constituents at low concentrations (dopants added at 500 mg/kg) - can be used qualitatively or quantitatively
MicroXRF	Uses characteristic x-ray florescence to spatially quantify the elemental composition near a material's surface. Non-destructive.	Measures quantitative phase composition of constituents at low concentration (dopants added at 500 mg/kg)

To process the data collected from the instrument analysis, an analytical workflow has also been developed. This workflow incorporates technology provided on the instrument software, a machine learning program called AIVIA (Leica Microsystems, Germany), and other MatLab developed codes.

13.3.2 Sample Casting/Aging

Carbonate dominant rocks were obtained for this experiment from the Yamin Plateau in Northern Negev, Israel. The rocks (oil shale, marl, and chalk) were analyzed for mineralogical composition via X-ray diffraction (XRD) analysis using the methodology in Gruber et al. (2022). Rock samples were sectioned in 1" cubes using a low speed saw with diamond blades and embedded in epoxy using 2" x 2" PVC cylinder molds, exposing only the top surface. After saturating samples, an ordinary Portland cement (OPC) paste was cast on top. The OPC cement paste was mixed using a w/b of 0.4 and a 1% addition of MasterGlenium 7700 (BASF, Germany). The water included in the mix design was doped with heavy

metal salts (lithium, cerium, chromium, and uranium) at 500 mg/kg each as analogue tracers for radionuclides. Samples were cured for 1 year at >95%RH and 30°C.

The same rock material and doped cement samples also were processed and tested independently using standard EPA protocols. The purpose of these experiments was twofold: (1) examine the pH-dependent available content of major constituents at near-equilibrium conditions (EPA, 2012) and (2) measure the effective diffusivity of conservative and major reactive constituents (EPA, 2017). For both experiments, elemental analysis was performed using inductively coupled plasma mass spectrometry (ICP-MS) and inductively coupled plasma optical emission spectroscopy (ICP-OES) (EPA, 2014). The results of these Methods for limestone and marl were previously reported by Gruber et al. (2022).

13.3.3 MicroCT

Aged samples were sent to Purdue University for MicroCT scanning and analysis. The goal of these preliminary scans was to identify a potential alteration zone depth (via grayscale density changes) and key features (large cracks, interfacial deposits) indicative of interfacial reactions. From this information, appropriate cutting planes for characterization were established.

13.3.4 Sample Preparation – Sectioning

After selecting a region of interest for characterization, samples were demolded and sectioned using a low speed saw with a diamond blade. The interface for characterization was stabilized with an epoxy-attached stainless-steel plate, segmented from the thin section slide, and embedded in a 1.5” round silicon mold with epoxy. Then, samples were polished to specification for characterization.

13.3.5 Sample Preparation – Polishing

Samples were polished to achieve average surface roughness over three 50 μm^2 area of <50 nm to meet requirements for subsequent nano-indentation. Polishing was carried out using a NANO-1000S benchtop polisher (PACE Technologies, USA) and ethanol as the lubricant. First, four grinding steps using progressively finer silicon carbide paper (320, 400, 600, and 1200 grit) were used in increasing intervals from *ca*. 30 seconds to 4 minutes, then three polishing steps using 9-, 6-, and 1-micron polycrystalline diamond pastes were applied in increasing intervals from ca. 6 to 10 minutes each. The success of this process was verified using surface probe microscopy (SPM) imaging on a Hysitron TI980 Triboindenter (Bruker, USA).

13.3.6 SEM-EDS

An FEI Quanta FEG 650 environmental scanning electron microscope (ESEM) (FEI Company, USA) fit with a Schottky field emission gun was used to collect backscatter electron (BSE) images and large area maps of major element composition using energy dispersive x-ray spectroscopy (EDS) across the sample surface.

First, BSE was used to image the entire interface and select areas of interest for characterization. After performing Nanoindentation on the TI980 Triboindenter, the same areas were reimaged using the identical image collection specifications to capture chemical composition over precise indent locations.

13.3.7 Micro/Nano-indentation

A Hystitron TI980 (Bruker, USA) was used to perform nanoindentation and microindentation on the cement in the interface sample. Areas of interest were selected and analyzed via SEM-EDS before and after indentation.

For tribological (SPM) imaging and nanomechanical (nano-indentation) testing, a standard transducer with a diamond Berkovich tip was used. Nano-indentation was used to identify mechanically distinct phases and correlate the results with chemical phases identified using EDS. Specifically, grid nanoindentation was performed below the alteration zone and above the alteration zone.

Reduced modulus and hardness were calculated through instrument analysis of the load vs. displacement curve using the Oliver and Pharr Method (Oliver & Pharr, 2004). The reduced modulus measures the combined elastic deformation of the sample and the tip and can be converted to elastic modulus (Shuman et al., 2007). Each indent curve is then visually evaluated, and malformed curves- indicating pore indentation, improper tip-to-sample contact, or sample cracking- were discarded.

13.3.8 LA-ICP-MS & MicroXRF

Laser Ablation Inductively Coupled Plasma Mass Spectroscopy (LA-ICP-MS) (NWR 213 (Elemental Scientific Lasers, Bozeman,MT) coupled with NexION 2000B (Perkin Elmer Corporation, Waltham, MA)) and MicroXRF analysis for spatial gradients of trace species (e.g., dopants used as radionuclide surrogates) is under development.

13.3.9 Image Segmentation & Analysis Programs

Machine learning software AIVIA was used to perform object segmentation on BSE images. Programs provided with the previously described characterization equipment also were used in tandem with in-lab developed code (MatLab) to further analyze the collected instrument data.

13.4 Results and Discussion

13.4.1 Oil Shale-OPC Paste Interface

Last year it was reported that chemical changes in Ca, S, Si and C were seen in the cement at the interface with oil shale. These chemical changes were also measured in conjunction with mechanical changes in the properties of reduced modulus and hardness in the first 300 µm (Matteo et al., 2022). Though the preliminary results discussed remain accurate, the added machine learning capabilities enhanced the data analysis process and helped expand the understanding of alteration mechanisms occurring at the oil shale-OPC paste interface. Last year, the discussion focused primarily on changes in raw EDS data and a shift in mechanical properties measured within the first 300 µm of the cement at the interface. With the added segmentation capabilities, we were able to quantify changes in micro-scale porosity and unhydrated cement particles and use this information to identify distinct layers near the interface. An example of this workflow is shown in Figure 13-2.

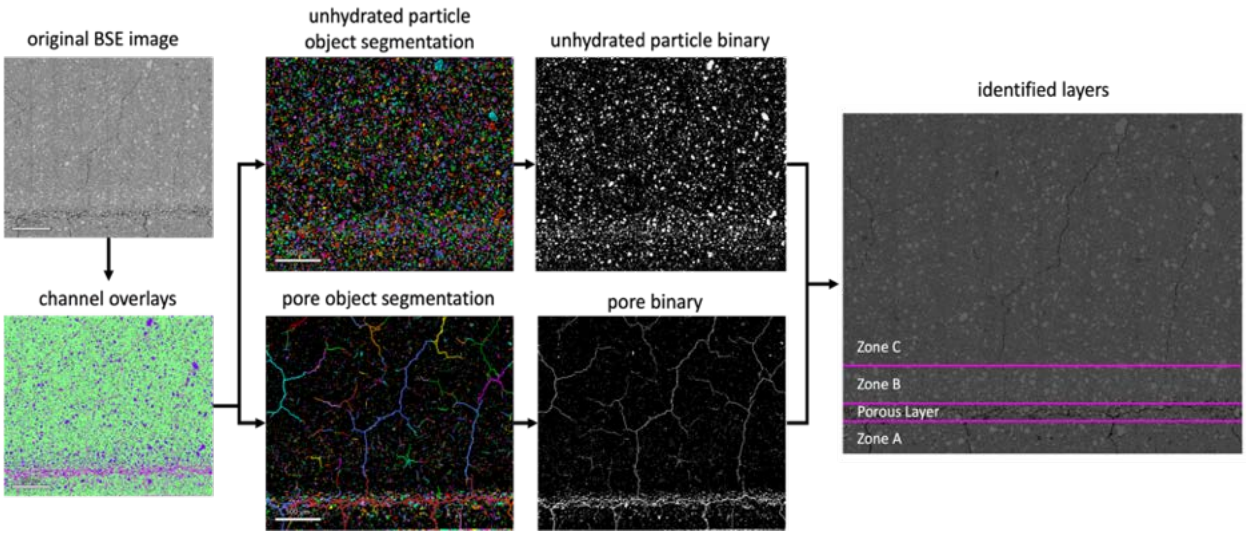

Figure 13-2. AIVIA software segmentation workflow, with final layer segments within the cement shown on the far right.

Each of the identified layers shown in Figure 13-2 were established based on changes in the area coverage of their porosity and unhydrated cement particles. From there, changes in their chemical and mechanical properties were more accurately analyzed. Table 13-2 lists these properties.

Table 13-2. Layer Property Summary

Zone Label	Distance from Interface	Layer Thickness	Unhydrated Particle Area Coverage	Pore Area Coverage *pores measuring 0.6 μm² to 8000 μm²
Zone A	0 μm – 205 μm	205 μm	9.5%	3.8%
Porous Layer	205 μm – 315 μm	110 μm	13.7%	17.9%
Zone B	315 μm – 545 μm	230 μm	18.5%	2.2%
Zone C	545 μm – 2000 μm	1.5 mm	9.9%	1.2%

First, changes in the elemental distribution in the cement layers (zones) were re-evaluated by removing both the pores and unhydrated cement particles to see if the chemical gradients visible in only the hydrated regions. Once again, changes in Ca, S, Si, and C were observed. For Zone A there was a depletion in Ca, and an enrichment of S, Si, and C measured. In the Porous Layer, all of the same changes were observed with the exception of the silicon.

Then, mechanical changes remain the same as reported last year, but an additional region was measured to ensure that the unaltered region was accurately captured. An example of this is shown in Figure 13-3.

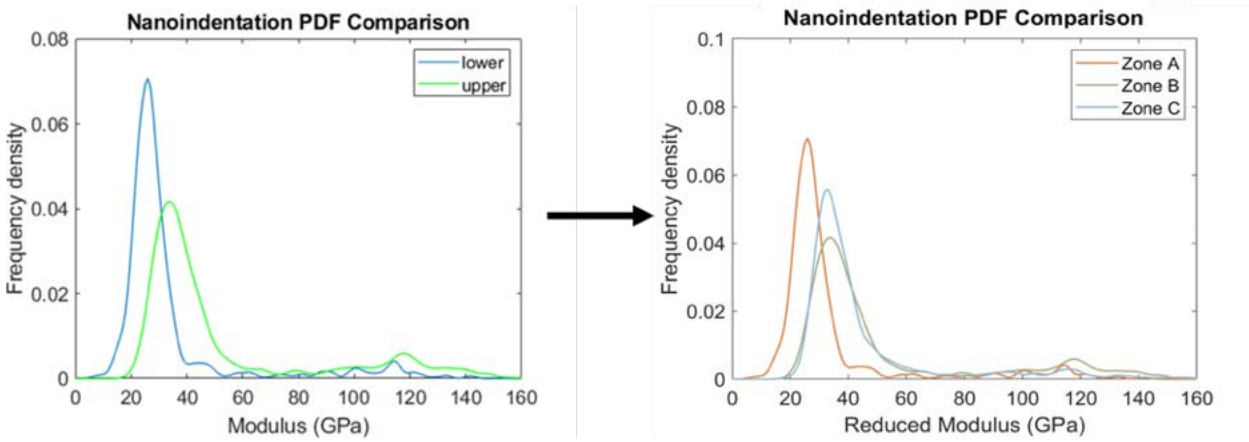

Figure 13-3. Previously reported nanoindentation results are shown on the left, with the updated results that include an additional region are shown on the right.

These results ultimately showed that Zone A was the only region impacted by mechanical changes. By identifying these mechanically distinct phases, correlation with local element distributions can be used to determine changes in which cementitious phases are causing the decrease in mechanical properties. Chemical composition of the indents on hydrated phases were analyzed using SEM/EDS and the results are shown in Figure 13-4.

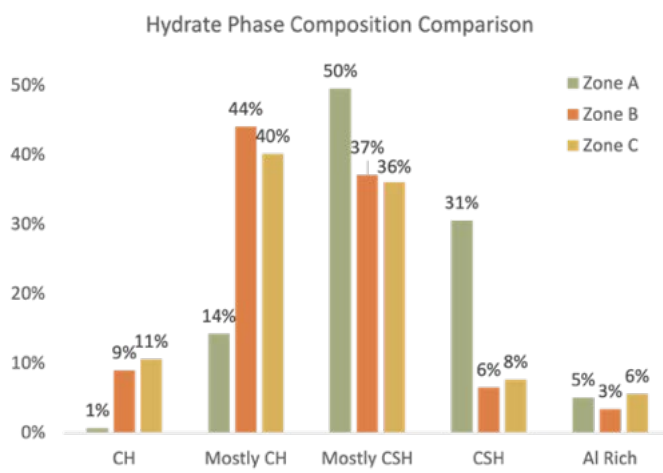

Figure 13-4. Comparison of the cement phases on indented hydrates in cement Zones A B and C.

As shown in the above figure, Zone A shows a shift in hydrates towards CSH phases, with near-complete dissolution of pure CH phases, while Zones B and C show majority blended CSH and CH phases. The next step was to compare the changes in cementitious phases to the shift in mechanically distinct phases, to determine if there was a single phase influencing the decrease in hardness and reduced modulus, or if all phases were showing this decrease. Zone A's results are shown in Figure 13-5.

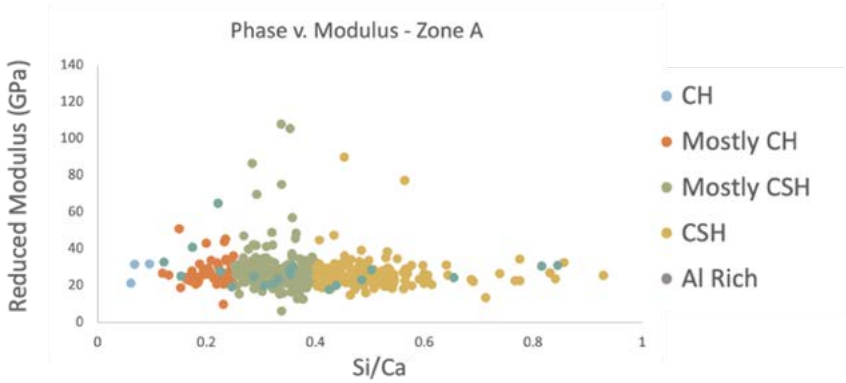

Figure 13-5. Comparison of the reduced modulus values to the Si/Ca ratio of indents on hydrates in Zone A

As shown in the figure, there was no single phase that contributed to the reduction in mechanical properties for Zone A. This indicates that the mechanism of alteration observed at the interface of this sample causes reduced stiffness of all chemical phases present.

After 1.5 years of aging, the alteration of the oil shale-OPC paste interface can be characterized by a 200 µm alteration zone adjacent to the interface, with a 100 µm dissolution front leading further into the cement. The mechanism of alteration can be attributed to many things, but the seemingly primary mechanism is sulfate-attack with calcium leaching. The upcoming paper will discuss all the possible alteration mechanisms in detail and will provide more context to these conclusions. Ultimately, the comparison of the provided results with predictive models will help improve simulation precision and accuracy moving forward.

13.4.2 Other Rock-Cement Interfaces

With the updated experimental and analysis workflows, the other rock-cement interfaces will be studied further to determine the depth of reaction across different interface types. In last year's report, marl and chalk at an interface with OPC paste were discussed, with reaction depths of 50 µm and 20µm, respectively. These interfaces, and others, will be investigated in greater detail during the next phase of analysis.

13.5 Experimental Comparison to Models

As previously reported, Gruber et al., showed that when comparing these different carbonate rocks interfacing with OPC paste, oil shale was the most reactive, followed by marl, then limestone (Gruber et al., 2022). These long-term alteration estimates assuming saturated conditions are shown in Figure 13-6.

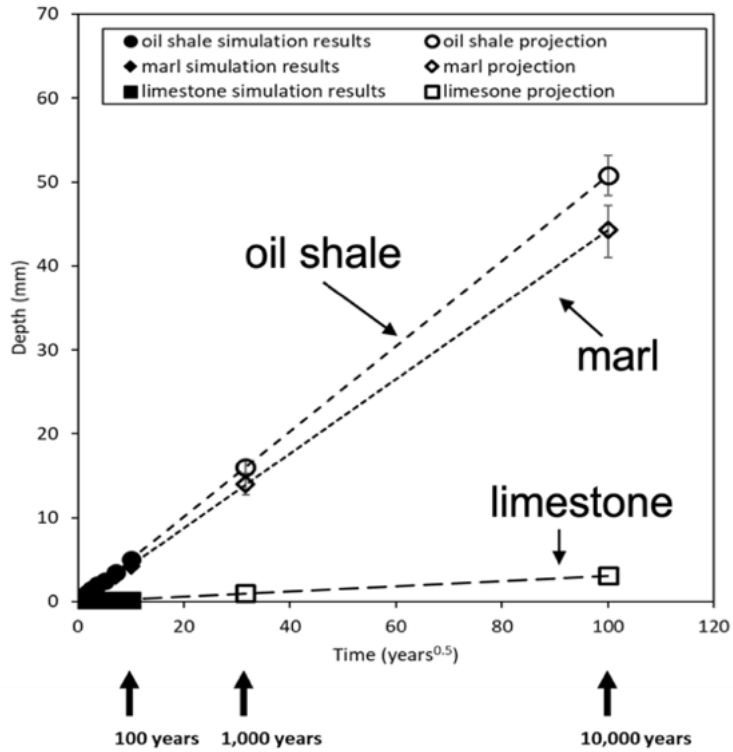

Figure 13-6. Model carbonation front predictions (from Gruber et. al. 2022).

Based on these long-term scenarios, after 1,000 years, oil shale-OPC paste and marl-OPC paste interfaces predict 16- and 14-mm carbonation front, respectively. However, the long-term estimates shown do not account for changes in porosity as a result of mineral phase changes. These same reactivity models were resolved to a 1.5-year time frame and are summarized in Table 13-3 below.

Table 13-3. Result Summary – Modeling vs. Experimental.

Rock Type	Modeling	SEM-EDS	Indentation
Oil Shale	Within ca. 500 µm of interface: • Depleted portlandite • C-S-H/HG mixed changes (e.g., CNASH increase) • Ettringite increase	200 µm alteration zone: depletion of Ca, enrichment of Si, S, and C. 100 µm porous zone: depletion of Ca, enrichment of S and C	200 µm alteration zone: decrease in both hardness and reduced modulus; fewer high-stiffness phases such as CH, and formation of a lower-stiffness CSH phase

The models have accurately predicted, within experimental uncertainty, alteration front depths after 1.5 years of aging for an oil shale-OPC paste interface. The results of this experimental work are being used to improve model parameters and available reactions sets for future predictions. As of now, updated models are in development which will include porosity changes that result from the dissolution and precipitation of different minerals in the materials.

13.6 Summary and Future Work

The most important work completed in the last year has been updating and applying the workflows discussed in Section 13.3.1. The streamlined workflows with flexible-parameter data analysis programs

provides the tools to analyze any interface of interest relevant to specific disposal conditions. These methods have allowed us to understand and compare the changes in both chemical and mechanical properties on a micro-scale, and eventually should be integrated to understand changes occurring on a macro-scale. The addition of porosity evolution to the models will significantly increase their reliability by providing more complete and accurate long-term durability predictions across all interface types.

Over the next year, these workflows will be applied to the other interfaces prepared for this project and will also be used to analyze the alterations that occur at a cement-bentonite interface under high temperature and pressure scenarios in a collaboration with Los Alamos National Laboratory.

REFERENCES

Abe, T., & Iida, Y. (2022). Review of Performance Assessment for Engineered Barrier Systems to Support Future RD&D of Radioactive Waste Management in Japan. *Journal of Advanced Concrete Technology*, *20*(3), 236–253. https://doi.org/10.3151/jact.20.236

Abdullah, W. S., Alshibli, K. A., & Al-Zoubi, M. S. (1999). Influence of pore water chemistry on the swelling behavior of compacted clays. *Applied Clay Science*, *15*(5–6), 447–462. https://doi.org/10.1016/s0169-1317(99)00034-4

Aldaba, D., Glaus, M., Leupin, O., van Loon, L., Vidal, M., & Rigol, A. (2014). Suitability of various materials for porous filters in diffusion experiments. *Radiochimica Acta*, *102*(8), 723–730. https://doi.org/10.1515/ract-2013-2176

Alonso, E. E., Alcoverro, J., Coste, F., Malinsky, L., Merrien-Soukatchoff, V., Kadiri, I., Nowak, T., Shao, H., Nguyen, T. S., Selvadurai, A. P. S., Armand, G., Sobolik, S. R., Itamura, M. T., Stone, C., Webb, S. W., Rejeb, A. B., Tijani, M., Maouche, Z., Kobayashi, A., . . . Jussila, P. (2005). The FEBEX benchmark test: case definition and comparison of modelling approaches. *International Journal of Rock Mechanics and Mining Sciences*, *42*(5–6), 611–638. https://doi.org/10.1016/j.ijrmms.2005.03.004

Alonso, M. C., García Calvo, J. L., Cuevas, J., Turrero, M. J., Fernández, R., Torres, E., & Ruiz, A. I. (2017). Interaction processes at the concrete-bentonite interface after 13 years of FEBEX-Plug operation. Part I: Concrete alteration. *Physics and Chemistry of the Earth, Parts A/B/C*, *99*, 38–48. https://doi.org/10.1016/j.pce.2017.03.008

Altmann, S. (2008). 'Geochemical research: A key building block for nuclear waste disposal safety cases. *Journal of Contaminant Hydrology*, *102*(3–4), 174–179. https://doi.org/10.1016/j.jconhyd.2008.09.012

Altmann, S., Tournassat, C., Goutelard, F., Parneix, J. C., Gimmi, T., & Maes, N. (2012). Diffusion-driven transport in clayrock formations. *Applied Geochemistry*, *27*(2), 463–478. https://doi.org/10.1016/j.apgeochem.2011.09.015

Álvarez, M., Lapitz, P., & Ruzzante, J. (2008). AE response of type 304 stainless steel during stress corrosion crack propagation. *Corrosion Science*, *50*(12), 3382–3388. https://doi.org/10.1016/j.corsci.2008.08.028

AMBERG. (2019). HotBENT: Experiment Plan (Draft 20190927 v2.docx). Distributors: Florian Kober (NAGRA) & Stratis Vomvoris (NAGRA).

Andersson, J., Skagius, K., Winberg, A., Lindborg, T., & Ström, A. (2013). Site-descriptive modelling for a final repository for spent nuclear fuel in Sweden. *Environmental Earth Sciences*, *69*(3), 1045–1060. https://doi.org/10.1007/s12665-013-2226-1

ANDRA. (2005). Dosier 2005 Argile-Architecture and management of a geological repository, C.RP.ADP.04.0001

Balistrieri, L. S., & Chao, T. T. (1987). Selenium Adsorption by Goethite. *Soil Science Society of America Journal*, *51*(5), 1145–1151. https://doi.org/10.2136/sssaj1987.03615995005100050009x

Balistrieri, L. S., & Chao, T. (1990). Adsorption of selenium by amorphous iron oxyhydroxide and manganese dioxide. *Geochimica et Cosmochimica Acta*, *54*(3), 739–751. https://doi.org/10.1016/0016-7037(90)90369-v

Bar-Yosef, B., and Meek, D. (1987) Selenium Sorption by Kaolinite and Montmorillonite. *Soil Science*, *144*(1), 11–19. https://doi.org/10.1097/00010694-198707000-00003

Beaver, R. C., Engel, K., Binns, W. J., & Neufeld, J. D. (2022). Microbiology of barrier component analogues of a deep geological repository. *Canadian Journal of Microbiology*, *68*(2), 73–90. https://doi.org/10.1139/cjm-2021-0225

Bell, N. S., Rodriguez, M. A., Kotula, P. G., Kruichak, J. N., Hernandez-Sanchez, B. A., Casillas, M., Kolesnichenko, I. V., & Matteo, E. N. (2021). Polymer intercalation synthesis of glycoboehmite nanosheets. *Applied Clay Science*, *214*, 106273. https://doi.org/10.1016/j.clay.2021.106273

Birkholzer, J. Zheng, L., and Faybishenko, B. (2022). International Collaboration Activities in Geologic Disposal Research: FY22 Progress, Milestone Report M2SF-22LB01307022

Blechschmidt, I., Martin, A. J., Kober, F., and Vomvoris, S. (2020). Grimsel Test Site-A Successful International Underground Research Laboratory for Many Decades-204292020 2020, WM Symposia, Inc., PO Box 27646, 85285-7646 Tempe, AZ (United States).

Bolt, G. H. and Van Riemsdijk, W. H. (1982). "Ion Adsorption on Inorganic Variable Charge Constituents". Soil Chemistry, Part B Physico-chemical Models. B. G. H. Amsterdam Elsevier: 459-504.

Börjesson, L., Gunnarsson, D., Johannesson, L-E., and Jonsson, E. (2010). Design, production and initial state of the buffer. Svensk Kärnbränslehantering Technical Report, TR-10-15, 89.

Bourdelle, F., Mosser-Ruck, R., Truche, L., Lorgeoux, C., Pignatelli, I., & Michau, N. (2017). A new view on iron-claystone interactions under hydrothermal conditions (90 °C) by monitoring in situ pH evolution and H2 generation. *Chemical Geology*, *466*, 600–607. https://doi.org/10.1016/j.chemgeo.2017.07.009

Bourdelle, F., Truche, L., Pignatelli, I., Mosser-Ruck, R., Lorgeoux, C., Roszypal, C., & Michau, N. (2014). Iron–clay interactions under hydrothermal conditions: Impact of specific surface area of metallic iron on reaction pathway. *Chemical Geology*, *381*, 194–205. https://doi.org/10.1016/j.chemgeo.2014.05.013

Bourg, I. C., & Tournassat, C. (2015). Chapter 6 - Self-Diffusion of Water and Ions in Clay Barriers. In *Developments in Clay Science* (Vol. 6, pp. 189–226). Elsevier.

Bourg, I. C., Sposito, G., & Bourg, A. C. M. (2006). Tracer diffusion in compacted, water-saturated bentonite. *Clays and Clay Minerals*, *54*(3), 363–374. https://doi.org/10.1346/ccmn.2006.0540307

Bradbury, M. H., & Baeyens, B. (2003). Porewater chemistry in compacted re-saturated MX-80 bentonite. *Journal of Contaminant Hydrology*, *61*(1–4), 329–338. https://doi.org/10.1016/s0169-7722(02)00125-0

Bradbury, M. H., Berner, U., Curti, E., Hummel, W., Kosakowski, G., and Thoenen, T. (2014). The long term geochemical evolution of the nearfield of the HLW repository (No. NTB-- 12-01). Paul Scherrer Institute (PSI).

Breiman, L. (2001). Random forests. *Machine Learning*, *45*(1), 5–32. https://doi.org/10.1023/a:1010933404324

Brown, G. E., Henrich, V. E., Casey, W. H., Clark, D. L., Eggleston, C., Felmy, A., Goodman, D. W., Grätzel, M., Maciel, G., McCarthy, M. I., Nealson, K. H., Sverjensky, D. A., Toney, M. F., & Zachara, J. M. (1999). Metal Oxide Surfaces and Their Interactions with Aqueous Solutions and Microbial Organisms. *Chemical Reviews*, *99*(1), 77–174. https://doi.org/10.1021/cr980011z

Cáceres, L., Vargas, T., & Herrera, L. a. P. (2009). Influence of pitting and iron oxide formation during corrosion of carbon steel in unbuffered NaCl solutions. *Corrosion Science*, *51*(5), 971–978. https://doi.org/10.1016/j.corsci.2009.02.021

Calvo, J. G., Hidalgo, A., Alonso, C. and Luco, L. F. (2010). Development of low-pH cementitious materials for HLRW repositories: Resistance against ground waters aggression. *Cement and Concrete Research*, 40(8), 1290-1297.

Caporuscio, F.A., Sauer, K.B., Rock, M.J., and Houser, L.M., (2018). Engineered System R&D and International Collaborations – Los Alamos National Laboratory (FY18). Deliverable. SF&WD R&D Work package # SF18LA01030801/SF-18LA01030805, LA-UR-18- 27601.

Caporuscio, F. A., Migdissov, A., Rock, M. J., Sauer, K. B., and van Hartesveldt, N. F. (2019). Engineered Barrier System R&D and International Collaborations–LANL (FY19) (No. LA-UR-19-24222). Los Alamos National Lab. (LANL), Los Alamos, NM (United States).

Caporuscio, F. A., Sauer, K. B., Rock, M. J., Kalintsev, A., Migdissov, A., & Alcorn, C. D. (2020). Engineered Barrier System R&D and International Collaborations–LANL (FY20): Spent Fuel and Waste Disposition: Los Alamos National Lab (LANL), Los Alamos, NM.

Caporuscio, F.A., Sauer, K.B., and Rock, M.J. (2021), Engineered System R&D and International Collaborations. LA-UR-21-26538. Los Alamos National Laboratory (FY21).

Caporuscio, F. A., Zandanel, A. E., Rock, M. J., and Sauer, K. B. (2022). Engineered Barrier System R&D and International Collaborations, LANL (FY22) Deliverable. SF&WD R&D Work package # SF-22LA01030801, SF-22LA01030802, LA-UR-22-29024.

Caporuscio, F. A., Zandanel, A. E., Rock, M. J., and McKanna, A. J. (2023). Engineered Barrier System R&D and International Collaborations, LANL (FY23) Deliverable. SF&WD R&D Work package # SF-22LA01030801, SF-22LA01030802, LA-UR-23-29675.

Cathelineau, M., Guillaume, D., Mosser-Ruck, R., Dubessy, J., Charpentier, D., Villiéras, F., Michau, N., (2005). Dissolution–crystallization processes affecting di-octahedral smectite in presence of iron metal: implication on mineral distribution in clay barriers. *Clays in Natural and Engineered Barriers for Radioactive Waste Confinement*. ANDRA, France, p. 35.

Castellanos, E., Villar, M. V., Romero, E., Lloret, A., & Gens, A. (2008). Chemical impact on the hydro-mechanical behaviour of high-density FEBEX bentonite. *Physics and Chemistry of the Earth, Parts a/B/C*, *33*, S516–S526. https://doi.org/10.1016/j.pce.2008.10.056

Chang, C. Y., Borglin, S., Chou, C., Zheng, L., Wu, Y., Kneafsey, T. J., Nakagawa, S., Voltolini, M., & Birkhölzer, J. (2023). Hydro-mechanical behavior of heated bentonite buffer for geologic disposal of high-level radioactive waste: A bench-scale X-ray computed tomography investigation. *Applied Clay Science*, *232*, 106792. https://doi.org/10.1016/j.clay.2022.106792

Chaparro, M. C., Finck, N., Metz, V., & Geckeis, H. (2021). Reactive Transport Modelling of the Long-Term Interaction between Carbon Steel and MX-80 Bentonite at 25 °C. *Minerals*, *11*(11), 1272. https://doi.org/10.3390/min11111272

Charlet, L., Scheinost, A., Tournassat, C., Greneche, J., Géhin, A., Fernández-Martı´nez, A., Coudert, S., Tisserand, D., & Brendle, J. (2007). Electron transfer at the mineral/water interface: Selenium reduction by ferrous iron sorbed on clay. *Geochimica et Cosmochimica Acta*, *71*(23), 5731–5749. https://doi.org/10.1016/j.gca.2007.08.024

Charlet, L., Kang, M., Bardelli, F., Kirsch, R., Géhin, A., Grenèche, J. M., & Chen, F. (2012). Nanocomposite Pyrite–Greigite Reactivity toward Se(IV)/Se(VI). *Environmental Science & Technology*, *46*(9), 4869–4876. https://doi.org/10.1021/es204181q

Chen, C., & Wang, T. (2017). An innovative method for determining the diffusion coefficient of product nuclide. *Nuclear Engineering and Technology*, *49*(5), 1019–1030. https://doi.org/10.1016/j.net.2017.03.011

Chen, W., Grabowski, R., & Goel, S. (2022). Clay Swelling: Role of Cations in Stabilizing/Destabilizing Mechanisms. *ACS Omega*, *7*(4), 3185–3191. https://doi.org/10.1021/acsomega.1c04384

Chermak, J. A. (1992). Low Temperature Experimental Investigation of the Effect of High pH NaOH Solutions on the Opalinus Shale, Switzerland. *Clays and Clay Minerals*, *40*(6), 650–658. https://doi.org/10.1346/ccmn.1992.0400604

Cheshire, M. C., Caporuscio, F. A., Rearick, M. S., Jove-Colon, C., & McCarney, M. K. (2014). Bentonite evolution at elevated pressures and temperatures: An experimental study for generic nuclear repository designs. *American Mineralogist*, *99*(8–9), 1662–1675. https://doi.org/10.2138/am.2014.4673

Cheshire, M. C., Caporuscio, F. A., Jove Colón, C. F., Norskog, K. E. (2018). Fe-saponite growth on low-carbon and stainless steel in hydrothermal-bentonite experiments. *Journal of Nuclear Materials*, 511, 353-366.

COMSOL Multiphysics® v. 5.6. www.comsol.com. COMSOL AB, Stockholm, Sweden.

Corey, A. (1954). The interrelation between gas and oil relative permeabilities. Producers Monthly, 38-41.

Crerar, D. A., Susak, N., Borcsik, M., & Schwartz, S. (1978). Solubility of the buffer assemblage pyrite + pyrrhotite + magnetite in NaCl solutions from 200 to 350°C. *Geochimica et Cosmochimica Acta*, *42*(9), 1427–1437. https://doi.org/10.1016/0016-7037(78)90048-0

Dauzères, A., Achiedo, G., Nied, D., Bernard, E., Alahrache, S., & Lothenbach, B. (2016). Magnesium perturbation in low-pH concretes placed in clayey environment—solid characterizations and modeling. *Cement and Concrete Research*, *79*, 137–150. https://doi.org/10.1016/j.cemconres.2015.09.002

Davis, J. A., James, R. O., and Leckie, J. O. (1978). "Surface Ionization and Complexation at Oxide-Water Interface .1. Computation of Electrical Double-Layer Properties in Simple Electrolytes." *Journal of Colloid and Interface Science* 63(3): 480-499.

Davis, J. A., Meece, D. E., Köhler, M., & Curtis, G. P. (2004). Approaches to surface complexation modeling of Uranium(VI) adsorption on aquifer sediments. *Geochimica Et Cosmochimica Acta*, *68*(18), 3621–3641. https://doi.org/10.1016/j.gca.2004.03.003

De Bock, C., Bosgiraud, J.-M., Weber, H., Rothfuchs, T., Verstricht, J., Breen, B., Johnson, M., and Andra, F. (2008). Achievements of the ESDRED project in buffer construction technology, *in* Proceedings of Euradwaste'08 Conference, Luxembourg. p. 20-22.

Delay, J., Vinsot, A., Krieguer, J.-M., Rebours, H., and Armand, G. (2007) Making of the underground scientific experimental programme at the Meuse/Haute-Marne underground research laboratory, North Eastern France. Physics and Chemistry of the Earth, Parts A/B/C 32, 2-18.

Dzombak, D. A., & Morel, F. M. M. (1990). *Surface complexation modeling: Hydrous Ferric Oxide*. John Wiley & Sons.

Dohrmann, R., Kaufhold, S., & Lundqvist, B. (2013). Chapter 5.4: The role of clays for safe storage of nuclear waste. In *Developments in Clay Science* (Vol. 5, pp. 677–710). https://doi.org/10.1016/b978-0-08-098259-5.00024-x

Dohrmann, R., & Kaufhold, S. (2014). Cation Exchange and Mineral Reactions Observed in Mx 80 Buffer Samples of the Prototype Repository <I>in Situ</I> Experiment in Äspö, Sweden. *Clays and Clay Minerals*, *62*(5), 357–373. https://doi.org/10.1346/ccmn.2014.0620501

Dzombak, A. and Morel, F. M. M. (1990). *Surface Complexation Modeling: Hydrous Ferric Oxide*. New York, Wiley.

Eberl, D. D., Velde, B., & McCormick, T. C. (1993). Synthesis of illite-smectite from smectite at Earth surface temperatures and high pH. *Clay Minerals*, *28*(1), 49–60. https://doi.org/10.1180/claymin.1993.028.1.06

El Mendili, Y. E., Abdelouas, A., & Bardeau, J. (2013). Insight into the mechanism of carbon steel corrosion under aerobic and anaerobic conditions. *Physical Chemistry Chemical Physics*, *15*(23), 9197. https://doi.org/10.1039/c3cp50853f

el Mendili, Y., Abdelouas, A., Ait Chaou, A., Bardeau, J. F., & Schlegel, M. (2014). Carbon steel corrosion in clay-rich environment. *Corrosion Science*, *88*, 56–65. https://doi.org/10.1016/j.corsci.2014.07.020

el Mendili, Y. E., Abdelouas, A., Karakurt, G., Chaou, A. A., Essehli, R., Bardeau, J., & Greneche, J. (2015). The effect of temperature on carbon steel corrosion under geological conditions. *Applied Geochemistry*, *52*, 76–85. https://doi.org/10.1016/j.apgeochem.2014.11.008

Engel, K., Coyotzi, S., Vachon, M. A., McKelvie, J., & Neufeld, J. D. (2019). Validating DNA extraction protocols for bentonite clay. *mSphere*, *4*(5). https://doi.org/10.1128/msphere.00334-19

ENRESA. (2006). Full-scale engineered barriers experiment updated final report 1994–2004. ENRESA Tech. Publ (05-0/2006, P590).

EPA, U.S. (2012). SW-846 Test Method 1313: *Liquid-solid partitioning as a function of extract pH using a parallel batch extraction procedure*. EPA publication SW-846.

EPA, U.S. (2014). SW-846 Test Method*6010D:* Inductively Coupled Plasma-Optical Emission Spectrometry (ICP-OES). EPA publication SW-846.

EPA, U.S. (2017). SW-846 Test Method 1315*: Mass Transfer Rates of Constituents in Monolithic or Compacted Granular Materials Using a Semi-Dynamic Tank Leaching Procedure*. EPA publication SW-846.

Ewing, R. C., Whittleston, R. A., & Yardley, B. W. (2016). Geological Disposal of Nuclear Waste: a Primer. *Elements*, *12*(4), 233–237. https://doi.org/10.2113/gselements.12.4.233

Fernández, R., Cuevas, J., and Mäder, U. K. (2009). Modelling concrete interaction with a bentonite barrier. *European Journal of Mineralogy*, 21(1), 177-191.

Fernández, R., Torres, E., Ruiz, A. I., Cuevas, J., Alonso, M. C., Calvo, J. L. G., and Turrero, M. J. (2017). Interaction processes at the concrete-bentonite interface after 13 years of FEBEX-Plug operation. Part II: Bentonite contact. *Physics and Chemistry of the Earth*, Parts A/B/C, 99, 49-63.

Fernández, A. M., Kaufhold, S., Sánchez-Ledesma, D., Rey, J. J., Melón, A., Robredo, L., Fernandez, S., Labajo, M., & Clavero, M. A. (2018). Evolution of the THC conditions in the FEBEX in situ test after 18 years of experiment: Smectite crystallochemical modifications after interactions of the bentonite with a C-steel heater at 100 °C. *Applied Geochemistry*, *98*, 152–171. https://doi.org/10.1016/j.apgeochem.2018.09.008

Figueiredo, B., Tsang, C. F., Niemi, A., and Lindgren, G. (2016). The state-of-art of sparse channel models and their applicability to performance assessment of radioactive waste repositories in fractured crystalline formations. *Hydrogeology Journal*, 24(7), 1607-1622.

García-Gutiérrez, M., Missana, T., Mingarro, M., Samper, J., Dai, Z., & Molinero, J. (2001). Solute transport properties of compacted Ca-bentonite used in FEBEX project. *Journal of Contaminant Hydrology*, *47*(2–4), 127–137. https://doi.org/10.1016/s0169-7722(00)00143-1

García-Siñeriz and Tuñón, S. (1997-2020). Hotbent: Experiment plan. NAGRA technical report, 185:105360.

Gaucher, E., & Blanc, P. (2006). Cement/clay interactions – A review: Experiments, natural analogues, and modeling. *Waste Management*, *26*(7), 776–788. https://doi.org/10.1016/j.wasman.2006.01.027

Gaudin, A., Bartier, D., Truche, L., Tinseau, E., Foct, F., Dyja, V., Maillet, A. and Beaufort, D. (2013). First corrosion stages in Tournemire claystone/steel interaction: In situ experiment and modelling approach. *Applied clay science*, 83, 457-468.

Gaus I., Garitte, B., Senger, R., Gens, A., Vasconcelos, R., Garcia-Sineriz, J-L., Trick, T., Wieczorek, K., Czaikowski, O., Schuster, K., Mayor, J. C., Velasco, M., Kuhlmann U., and Villar, M.V. (2014). The HE-E Experiment: Lay-out, Interpretation and THM Modelling. Nagra Arbeitsbericht. NAB 14-053. Nagra, Wettingen. PEBS deliverable D2.2-11 and D3.2-2.

Ge, H., Cai, X. J., Tyson, J. F., Uden, P. C., Denoyer, E. R., & Block, E. (1996). Identification of selenium species in selenium-enriched garlic, onion and broccoli using high-performance ion chromatography with inductively coupled plasma mass spectrometry detection. *Analytical Communications*, *33*(8), 279. https://doi.org/10.1039/ac9963300279

Giguere, A. T., Eichorst, S. A., Meier, D. V., Herbold, C. W., Richter, A., Greening, C., & Woebken, D. (2020). Acidobacteria are active and abundant members of diverse atmospheric H2-oxidizing communities detected in temperate soils. *The ISME Journal*, *15*(2), 363–376. https://doi.org/10.1038/s41396-020-00750-8

Gilmour, K., Davie, C., & Gray, N. (2021). An indigenous iron-reducing microbial community from MX80 bentonite - A study in the framework of nuclear waste disposal. *Applied Clay Science*, *205*, 106039. https://doi.org/10.1016/j.clay.2021.106039

Glaus, M. A., Rossé, R., Van Loon, L. R., & Yaroshchuk, A. (2008). Tracer diffusion in sintered stainless steel filters: measurement of effective diffusion coefficients and implications for diffusion studies with compacted clays. *Clays and Clay Minerals*, *56*(6), 677–685. https://doi.org/10.1346/ccmn.2008.0560608

González-Santamaría, D., Angulo, M., Ruiz, A., Fernández, R., Ortega, A., & Cuevas, J. (2018). Low-pH cement mortar-bentonite perturbations in a small-scale pilot laboratory experiment. *Clay Minerals*, *53*(2), 237–254. https://doi.org/10.1180/clm.2018.16

González-Santamaría, D. E., Fernández, R., Ruiz, A., Ortega, A., & Cuevas, J. (2020). High-pH/low pH ordinary Portland cement mortars impacts on compacted bentonite surfaces: Application to clay barriers performance. *Applied Clay Science*, *193*, 105672. https://doi.org/10.1016/j.clay.2020.105672

Greening, C., Berney, M., Hards, K., Cook, G. M., & Conrad, R. (2014). A soil actinobacterium scavenges atmospheric H_2 using two membrane-associated, oxygen-dependent [NiFe] hydrogenases. *Proceedings of the National Academy of Sciences of the United States of America*, *111*(11), 4257–4261. https://doi.org/10.1073/pnas.1320586111

Grimsel Test, S., (2023). High Temperature Effects on Bentonite Buffers (HotBENT) - Aims & Objectives: GTS Grimsel Test Site.

Gruber, C., Steen, M., Brown, K. G., Delapp, R., Matteo, E. N., Klein-BenDavid, O., Bar-Nes, G., Meeussen, J. C., Ayers, J. C., & Kosson, D. S. (2022). Cement-carbonate rock interaction under saturated conditions: From laboratory to modeling. *Cement and Concrete Research*, *160*, 106899. https://doi.org/10.1016/j.cemconres.2022.106899

Gueven, N., and Huang, W. L. (1990). Effects of Mg^{2+} and Fe^{3+} substitutions on the crystallization of discrete illite and illite/smectite mixed layers. Int. rep. Dept. Geosciences Texas Tech University, Exxon Production research Co, Houston, Texas.

Guillaume, D., Neaman, A., Cathelineau, M., Mosser-Ruck, R., Peiffert, C., Abdelmoula, M., Dubessy, J., Villiéras, F., Baronnet, A., & Michau, N. (2003). Experimental synthesis of chlorite from smectite at 300°C in the presence of metallic Fe. *Clay Minerals*, *38*(3), 281–302. https://doi.org/10.1180/0009855033830096

Guillaume, D., Neaman, A., Cathelineau, M., Mosser-Ruck, R., Peiffert, C., Abdelmoula, M., Dubessy, J., Villieras, F., and Michau, N. (2004). Experimental study of the transformation of smectite at 80 to 300 °C in the presence of Fe oxides. *Clay Minerals*, 39, 17-34.

Günther, Thomas & Rücker, Carsten. (2012). Boundless Electrical Resistivity Tomography (BERT) v. 2.0 - Open Access Software for Advanced and Flexible Imaging.

Guyonnet, D., Touze-Foltz, N., Norotte, V., Pothier, C., Didier, G., Gailhanou, H., Blanc, P., & Warmont, F. (2009). Performance-based indicators for controlling geosynthetic clay liners in landfill applications. *Geotextiles and Geomembranes*, *27*(5), 321–331. https://doi.org/10.1016/j.geotexmem.2009.02.002

Hadi, J., Wersin, P., Serneels, V., & Greneche, J. (2019). Eighteen years of steel–bentonite interaction in the FEBEX in situ test at the Grimsel Test Site in Switzerland. *Clays and Clay Minerals*, *67*(2), 111–131. https://doi.org/10.1007/s42860-019-00012-5

Hammond, G. E., Lichtner, P. C., & Mills, R. T. (2014). Evaluating the performance of parallel subsurface simulators: An illustrative example with PFLOTRAN. *Water Resources Research*, *50*(1), 208–228. https://doi.org/10.1002/2012wr013483

Hangx, S. J. T., Linden, A. V. D., Marcelis, F., & Liteanu, E. (2016). Defining the Brittle Failure Envelopes of Individual Reaction Zones Observed in CO_2-Exposed Wellbore Cement. *Environmental Science &Amp; Technology*, *50*(2), 1031–1038. https://doi.org/10.1021/acs.est.5b03097

Hansen, J., Doudou, S., Palmu, M., and White, M. (2016). DOPAS Work Package 6 Deliverable D6. 4: DOPAS Project Final Summary Report.

Hardin, E., Hadgu, T., & Clayton, D. J. (2015). *Cavern/Vault disposal concepts and thermal calculations for direct disposal of 37-PWR size DPCs*. Prepared for U.S. Department of Energy Used Fuel Disposition Campaign Revision History. https://doi.org/10.2172/1172177

Hedin, A., & Olsson, O. (2016). Crystalline rock as a repository for Swedish spent nuclear fuel. *Elements*, *12*(4), 247–252. https://doi.org/10.2113/gselements.12.4.247

Hiemstra, T., & Van Riemsdijk, W. (1991). Physical chemical interpretation of primary charging behaviour of metal (hydr) oxides. *Colloids and Surfaces*, *59*, 7–25. https://doi.org/10.1016/0166-6622(91)80233-e

Hiemstra, T., & Van Riemsdijk, W. (1996). A Surface Structural Approach to Ion Adsorption: The Charge Distribution (CD) Model. *Journal of Colloid and Interface Science*, *179*(2), 488–508. https://doi.org/10.1006/jcis.1996.0242

Hiemstra, T., Van Riemsdijk, W., & Bolt, G. (1989). Multisite proton adsorption modeling at the solid/solution interface of (hydr)oxides: A new approach. *Journal of Colloid and Interface Science*, *133*(1), 91–104. https://doi.org/10.1016/0021-9797(89)90284-1

Hiemstra, T., Venema, P., & Riemsdijk, W. (1996). Intrinsic Proton Affinity of Reactive Surface Groups of Metal (Hydr)oxides: The Bond Valence Principle. *Journal of Colloid and Interface Science*, *184*(2), 680–692. https://doi.org/10.1006/jcis.1996.0666

Huertas, F., & Santiago, J. L. (1997). The FEBEX Project. General Overview: MRS Online Proceedings Library (OPL), v. 506, p. 343-349.

Idemitsu, K., Kozaki, H., Yuhara, M., Arima, T., & Inagaki, Y. (2016). Diffusion behavior of selenite in purified bentonite. *Progress in Nuclear Energy*, *92*, 279–285. https://doi.org/10.1016/j.pnucene.2015.08.012

Idiart, A., Laviña, M., Grandia, F., and Pont, A. (2020). Reactive transport modelling of montmorillonite dissolution. Report for the safety evaluation. SE-SFL. SKB R-19-15. Svensk Kärnbränslehantering AB.

International Formulating Committee (IF97, 1997): International Association for the Properties of Water and Steam Revised Release on the IAPWS Industrial Formulation 1997 for the Thermodynamic Properties of Water and Steam, Lucerne, Switzerland August 2007.

Ingraffea, A. R., Wells, M. T., Santoro, R., & Shonkoff, S. B. (2014). Assessment and risk analysis of casing and cement impairment in oil and gas wells in Pennsylvania, 2000–2012. *Proceedings of the National Academy of Sciences of the United States of America*, *111*(30), 10955–10960. https://doi.org/10.1073/pnas.1323422111

Inoue, M. (1989). Alcohothermal Treatments of Gibbsite: Mechanisms for the formation of boehmite. *Clays and Clay Minerals*, *37*(1), 71–80. https://doi.org/10.1346/ccmn.1989.0370109

Jenni, A., Mäder, U., Lerouge, C., Gaboreau, S., & Schwyn, B. (2014). In situ interaction between different concretes and Opalinus Clay. *Physics and Chemistry of the Earth, Parts a/B/C*, *70–71*, 71–83. https://doi.org/10.1016/j.pce.2013.11.004

Jové Colón, C. F., Caporuscio, F. A, Sauer, K., and Cheshire, M. C. (2019). Engineered Barrier Material Interactions at Elevated Temperatures: Bentonite-metal interactions under elevated temperature conditions. SAND2019-0714C. Sandia National Laboratories. Albuquerque, NM. https://www.osti.gov/servlets/purl/1595898.

Kalam, S., Basu, A., Ahmad, I., Sayyed, R. Z., El-Enshasy, H. A., Dailin, D. J., & Suriani, N. L. (2020). Recent understanding of soil acidobacteria and their ecological significance: A Critical review. *Frontiers in Microbiology*, *11*. https://doi.org/10.3389/fmicb.2020.580024

Karnland, O., Olsson, S. and Nilsson, U. (2006). Mineralogy and Sealing Properties of Various Bentonites and Smectite-Rich Clay Materials. Technical Report TR-06-30. Clay Technology AB, Stockholm, 112 p.

Karnland, O., Olsson, S., Nilsson, U. J., & Sellin, P. (2007). Experimentally determined swelling pressures and geochemical interactions of compacted Wyoming bentonite with highly alkaline solutions. *Physics and Chemistry of the Earth, Parts a/B/C*, *32*(1–7), 275–286. https://doi.org/10.1016/j.pce.2006.01.012

Kaufhold, S., Hassel, A. W., Sanders, D., & Dohrmann, R. (2015). Corrosion of high-level radioactive waste iron-canisters in contact with bentonite. *Journal of Hazardous Materials*, 285, 464-473.

Kersting, A., Zavarin, M., Zhao, P., Dai, Z., Carroll, S., Wang, Y., Miller, A., James, S., Reimus P., Zheng, L., Li, L., Rutqvist, J., Liu, H., & Birkholzer, J. (2012). Radionuclide Interaction and Transport in Representative Geologic Media. FCRD-UFD-2012-000154. Lawerence-Livermore National Lab.

King, F. (2012). Factors in the Selection of Container Materials for the Disposal of HLW/SF: MRS Online Proceedings Library (OPL), v. 1475, p. imrc11-1475.

Kober, F., & Schneeberger, R. (2022). Presentation on 9th HotBENT. Partner Meeting, 01/02 November 2022. Wettingen, Switerzland.

Kober, F., Schneeberger, R. & Manukyan, E. (2022). "Updates on the HotBENT project", Presentation on 8th HotBENT Partner Meeting, 17/19 May 2022, online.

Kukkonen, I., Kivekäs, L., Vuoriainen, S., and Kääriä, M. (2011). Thermal Properties of Rocks in Olkiluoto. Results of laboratory measurements 1994-2010. (POSIVA-WR-11-17). Finland.

Kursten, B., Cornelis, B., Labat, S. and Van Iseghem, P. (1997). Completion of the Corrosion Programme in Boom Clay – in situ experiments, Report EUR-17105, SCK•CEN (Mol, Belgium).

Kursten, B., Smailos, E., Azkarate, I., Werme, L., Smart, N. R., Marx, G., Cuñado, M. A., and Santarini, G. (2004). "Corrosion evaluation of metallic HLW/spent fuel disposal containers. Review". Conference: Prediction of Long-Term Corrosion Behaviour in Nuclear Waste Systems. Eurocorr.

Lanson, B., Lantenois, S., Van Aken, P. A., Bauer, A., & Plançon, A. (2012). Experimental investigation of smectite interaction with metal iron at 80 C: Structural characterization of newly formed Fe-rich phyllosilicates. *American Mineralogist*, *97*(5–6), 864–871. https://doi.org/10.2138/am.2012.4062

Lantenois, S., Lanson, B., Muller, F., Bauer, A., Jullien, M., & Plançon, A. (2005). Experimental study of smectite interaction with metal Fe at low temperature: 1. Smectite destabilization. *Clays and Clay Minerals*, 53(6), 597-612.

Lanyon, G. W., & Gaus, I. (2016). Main outcomes and review of the FEBEX in situ test (GTS) and mock-up after 15 years of operation: Fracture Systems Ltd.

Lasaga, A. C., Soler, J. M., Ganor, J., Burch, T., & Nagy, K. L. (1994). Chemical weathering rate laws and global geochemical cycles. *Geochimica Et Cosmochimica Acta*, *58*(10), 2361–2386. https://doi.org/10.1016/0016-7037(94)90016-7

Leupin, O. X., & Johnson, L. H. (2013). Buffer requirements for a SF/HLW repository in Opalinus Clay. Nagra working report, NAB 13-46, Nagra, Wettingen, Switzerland. www.nagra.ch.

Leupin, O. X., Birgersson, M., Karnland, O., Korkeakoski, P., Sellin, P., Mäder, U., and Wersin, P. (2014). Montmorillonite stability under near-field conditions. (NTB-14-12). 1015-2636. Switzerland.

Leupin, O. X., Bernier-Latmani, R., Bagnoud, A., Moors, H., Leys, N., Wouters, K., & Stroes-Gascoyne, S. (2017). Fifteen years of microbiological investigation in Opalinus Clay at the Mont Terri rock laboratory (Switzerland). *Swiss Journal of Geosciences*, *110*(1), 343–354. https://doi.org/10.1007/s00015-016-0255-y

Li, C., & Zarzycki, P. (2022). A computational pipeline to generate a synthetic dataset of metal ion sorption to oxides for AI/ML exploration. *Frontiers in Nuclear Engineering*, *1*. https://doi.org/10.3389/fnuen.2022.977743

Li, C., Adeniyi, E. O., and Zarzycki, P. (2023). Random Forest Surrogate for Surface Complexation Model of U(VI) Sorption to Oxides, Nature Scientific Reports (under review)

Liu, L. (2013). Prediction of swelling pressures of different types of bentonite in dilute solutions. *Colloids and Surfaces A: Physicochemical and Engineering Aspects*, *434*, 303–318. https://doi.org/10.1016/j.colsurfa.2013.05.068

Liu, H.H., Houseworth, J., Rutqvist, J., Zheng, L., Asahina, D., Li, L., Vilarrasa, V., Chen, F., Nakagawa, S., Finsterle, S., Doughty, C., Kneafsey, T. and Birkholzer, J. (2013). Report on THMC modeling of the near field evolution of a generic clay repository: Model validation and demonstration, Lawrence Berkeley National Laboratory, August, 2013, FCRD-UFD-2013-0000244.

Liu, X., Tournassat, C., Grangeon, S., Kalinichev, A. G., Takahashi, Y., & Fernandes, M. M. (2022). Molecular-level understanding of metal ion retention in clay-rich materials. *Nature Reviews Earth & Environment*, *3*(7), 461–476. https://doi.org/10.1038/s43017-022-00301-z

López-Fernández, M., Cherkouk, A., Vílchez-Vargas, R., Jáuregui, R., Pieper, D. H., Boon, N., Sánchez-Castro, I., & Merroun, M. L. (2015). Bacterial diversity in bentonites, engineered barrier for deep geological disposal of radioactive wastes. *Microbial Ecology*, *70*(4), 922–935. https://doi.org/10.1007/s00248-015-0630-7

Lothenbach, B., Scrivener, K. and Hooton, R. D. (2011). Supplementary cementitious materials. *Cement and Concrete Research*, 41(12), 1244-1256.

Lothenbach, B., Rentsch, D., & Wieland, E. (2014). "Hydration of a silica fume blended low-alkali shotcrete cement". *Physics and Chemistry of the Earth, Parts A/B/C*, v. 70, p. 3-16. ISSN 1474-7065/

Lu, N., & Dong, Y. (2015). Closed-Form Equation for Thermal Conductivity of Unsaturated Soils at Room Temperature. *Journal of Geotechnical and Geoenvironmental Engineering*, *141*(6). https://doi.org/10.1061/(asce)gt.1943-5606.0001295

Lützenkirchen, J., Marsac, R., Kulik, D. A., Payne, T. E., Xue, Z., Orsetti, S., & Haderlein, S. B. (2015). Treatment of multi-dentate surface complexes and diffuse layer implementation in various speciation codes. *Applied Geochemistry*, *55*, 128–137. https://doi.org/10.1016/j.apgeochem.2014.07.006

Ma, B., Charlet, L., Fernandez-Martinez, A., Kang, M., & Madé, B. (2019). A review of the retention mechanisms of redox-sensitive radionuclides in multi-barrier systems. *Applied Geochemistry*, *100*, 414–431. https://doi.org/10.1016/j.apgeochem.2018.12.001

Mäder, U., Jenni, A., Lerouge, C., Gaboreau, S., Miyoshi, S., Kimura, Y., Cloet, V., Fukaya, M., Claret, F., Otake, T., Shibata, M., & Lothenbach, B. (2017). 5-year chemico-physical evolution of concrete–claystone interfaces, Mont Terri rock laboratory (Switzerland). *Swiss Journal of Geosciences*, *110*(1), 307–327. https://doi.org/10.1007/s00015-016-0240-5

Mäder, U., Jenni, A., Lerouge, C., Gaboreau, S., Miyoshi, S., Kimura, Y., Cloet, V., Fukaya, M., Claret, F., Otake, T., Shibata, M., & Lothenbach, B. (2017). 5-year chemico-physical evolution of concrete–claystone interfaces, Mont Terri rock laboratory (Switzerland). In *Springer eBooks* (pp. 309–329). https://doi.org/10.1007/978-3-319-70458-6_16

Mangadlao, J. D., Cao, P., & Advincula, R. C. (2015). Smart cements and cement additives for oil and gas operations. *Journal of Petroleum Science and Engineering*, *129*, 63–76. https://doi.org/10.1016/j.petrol.2015.02.009

Mariner, P. E., Lee, J. H., Hardin, E. L., Hansen, F. D., Freeze, G. A., Lord, A. S., and Price, R. H. (2011). Granite disposal of US high-level radioactive waste. SAND2011-6203, Sandia, California.

Marsh, G. P., & Taylor, K. (1988). An assessment of carbon steel containers for radioactive waste disposal. *Corrosion Science*, *28*(3), 289–320. https://doi.org/10.1016/0010-938x(88)90111-4

Martin, P. L., Barcala, J. M. and Huertas, F. (2006). Large-scale and long-term coupled thermo- hydro-mechanic experiments with bentonite: the FEBEX mock-up test. *Journal of Iberian Geology*, 32, 259–282.

Martinez, V., Abós, H. and García-Siñeriz, J. L. (2016). FEBEXe: Final Sensor Data Report (FEBEX "in situ" Experiment) - Arbeitsbericht NAB 16-19, National Cooperative for the Disposal of Radioactive Waste (NAGRA), Wettingen, Switzerland.

Marty, N. C. M., Bildstein, O., Blanc, P., Claret, F., Cochepin, B., Gaucher, E. C., Jacques, D., Lartigue, J. E., Liu, S., Mayer, K. U., Meeussen, J. C. L., Munier, I., Pointeau, I., Su, D., & Steefel, C. I. (2015). Benchmarks for multicomponent reactive transport across a cement/clay interface. *Computational Geosciences*, *19*(3), 635–653. https://doi.org/10.1007/s10596-014-9463-6

Marx, A., Dusek, J., Jankovec, J., Šanda, M., Vogel, T., Van Geldern, R., Hartmann, J., & Barth, J. a. C. (2017). A review of $CO_2$and associated carbon dynamics in headwater streams: A global perspective. *Reviews of Geophysics*, *55*(2), 560–585. https://doi.org/10.1002/2016rg000547

Matamoros-Veloza, A., Barker, R., Vargas, S., & Neville, A. (2020). Iron Calcium Carbonate Instability: Structural Modification of Siderite Corrosion Films. *ACS Applied Materials & Interfaces*, *12*(43), 49237–49244. https://doi.org/10.1021/acsami.0c14513

Matteo, E., Hardin, E., Hadgu T., Park, H., Rigali, M., and Jove-Colon, C. F. (2016). Status of Progress Made Toward Preliminary Design Concepts for the Inventory in Select Media for DOE-Managed HLW/SNF. SAND2016-9823 R. Sandia National Laboratories, Albuquerque, NM.

Matteo, E. N., Hadgu, T., Zheng, L., Xu, H., Fox, P., Nico, P., Birkholzer, J., Caporuscio, F. A., Sauer, K. B., and Rock, M. J. (2018). Evaluation of Engineered Barrier Systems in the Disposition of Spent Nuclear Fuel: Sandia National Laboratory. Albuquerque, NM.

Matteo, E.N., et al. (2022). *Evaluation of Engineered Barrier Systems FY22 Report*. Sandia National Lab.(SNL-NM), Albuquerque, NM (United States).

Meleshyn, A. (2014). Microbial processes relevant for the long-term performance of high-level radioactive waste repositories in clays. *Geological Society, London, Special Publications*, *400*(1), 179–194. https://doi.org/10.1144/sp400.6

Mills, M., Sanchez, A. C., Boisvert, L., Payne, C. B., Ho, T. A., & Wang, Y. (2023). Understanding smectite to illite transformation at elevated (>100 °C) temperature: Effects of liquid/solid ratio, interlayer cation, solution chemistry and reaction time. *Chemical Geology*, *615*, 121214. https://doi.org/10.1016/j.chemgeo.2022.121214

Mindess, S., Young, J. F., & Darwin, D. (2003). *Concrete*. 2nd Edition. Pearson. P.644

Missana, T., & Geckeis, H. (2006) The CRR final project report series II: Supporting laboratory experiments with radionuclides and bentonite colloids: National Cooperative for the Disposal of Radioactive Waste (NAGRA). Switerzland.

Missana, T., Alonso, U., & García-Gutiérrez, M. (2009). Experimental study and modelling of selenite sorption onto illite and smectite clays. *Journal of Colloid and Interface Science*, *334*(2), 132–138. https://doi.org/10.1016/j.jcis.2009.02.059

Mohammed, M. H., Pusch, R., Warr, L. N., Kasbohm, J., & Knutsson, S. (2015). Interaction of clay and concrete relevant to the deep disposal of high-level radioactive waste. *Applied Clay Science*, *118*, 178–187. https://doi.org/10.1016/j.clay.2015.08.008

Mohammed, M. H., Pusch, R., Knutsson, S., & Warr, L. N. (2016). Hydrothermal alteration of clay and low pH concrete applicable to deep borehole disposal of high-level radioactive waste – A pilot study. *Construction and Building Materials*, *104*, 1–8. https://doi.org/10.1016/j.conbuildmat.2015.12.003

Möller, H., Boshoff, H. T., & Froneman, H. (2006). The corrosion behaviour of a low carbon steel in natural and synthetic seawaters. *Journal of the Southern African Institute of mining and Metallurgy*, v. 106, no. 8, p. 585-592.

Mon, A., Samper, J., Montenegro, L., Naves, A., & Fernández, J. (2017). Long-term non-isothermal reactive transport model of compacted bentonite, concrete and corrosion products in a HLW

repository in clay. *Journal of Contaminant Hydrology*, *197*, 1–16. https://doi.org/10.1016/j.jconhyd.2016.12.006

Montavon, G., Guo, Z., Lützenkirchen, J., Alhajji, E., Kedziorek, M., Bourg, A., & Grambow, B. (2009). Interaction of selenite with MX-80 bentonite: Effect of minor phases, pH, selenite loading, solution composition and compaction. *Colloids and Surfaces A: Physicochemical and Engineering Aspects*, *332*(2–3), 71–77. https://doi.org/10.1016/j.colsurfa.2008.09.014

Moore, D. M. & Reynolds, R.C. (1997). X-ray Diffraction and the identification and analysis of clay minerals. Oxford University Press, New York, New York, 377.

Mori, H., Maruyama, F., Kato, H., Toyoda, A., Dozono, A., Ohtsubo, Y., Nagata, Y., Fujiyama, A., Tsuda, M., & Kurokawa, K. (2013). Design and Experimental Application of a Novel Non-Degenerate Universal Primer Set that Amplifies Prokaryotic 16S rRNA Genes with a Low Possibility to Amplify Eukaryotic rRNA Genes. *DNA Research*, *21*(2), 217–227. https://doi.org/10.1093/dnares/dst052

Moridis, G. J. (1999). Semianalytical solutions for parameter estimation in diffusion cell experiments. *Water Resources Research*, *35*(6), 1729–1740. https://doi.org/10.1029/1999wr900084

Morodome, S., & Kawamura, K. (2011). In Situ X-ray Diffraction Study of the Swelling of Montmorillonite as Affected by Exchangeable Cations and Temperature. *Clays and Clay Minerals*, *59*(2), 165–175. https://doi.org/10.1346/ccmn.2011.0590205

Mosser-Ruck, R., Cathelineau, M., Guillaume, D., Charpentier, D., Rousset, D., Barres, O., and Michau, N. (2010). Effects of temperature, pH, and iron/clay and liquid/clay ratios on experimental conversion of dioctahedral smectite to berthierine, chlorite, vermiculite, or saponite. *Clays and Clay Minerals*, 58, 280-291.

Mosser-Ruck, R., Pignatelli, I., Bourdelle, F., Abdelmoula, M., Barres, O., Guillaume, D., Charpentier, D., Rousset, D., Cathelineau, M., & Michau, N. (2016). Contribution of long-term hydrothermal experiments for understanding the smectite-to-chlorite conversion in geological environments. *Contributions to Mineralogy and Petrology*, *171*(11). https://doi.org/10.1007/s00410-016-1307-z

Mull, R. (1984). Mass estimates by computed tomography: physical density from CT numbers. *American Journal of Roentgenology*, *143*(5), 1101–1104. https://doi.org/10.2214/ajr.143.5.1101

NAGRA. (2017). Agreement between U.S. Department of Energy and National Cooperative for the Disposal of Radioactive Waste (NAGRA), Switzerland on the Phase VI International Experiment HOTBENT (High Temperature Effects on Bentonite), Wettingen, Switzerland.

NAGRA, 2019. Implementation of the Full-scale Emplacement Experiment at Mont Terri: Design, Construction and Preliminary Results. Nagra Technical Report 15-02.

Necib, S., Diomidis, N., Keech, P., & Nakayama, M. (2017a). Corrosion of carbon steel in clay environments relevant to radioactive waste geological disposals, Mont Terri rock laboratory (Switzerland). *Swiss Journal of Geosciences*, *110*(1), 329–342. https://doi.org/10.1007/s00015-016-0259-7

Necib, S., Linard, Y., Crusset, D., Schlegel, M. L., Daumas, S., & Michau, N. (2017b). Corrosion processes of C-steel in long-term repository conditions. *Corrosion Engineering Science and Technology*, *52*(sup1), 127–130. https://doi.org/10.1080/1478422x.2017.1320155

Nelder, J. A., & Mead, R. (1965). A simplex method for function minimization. *The Computer Journal*, *7*(4), 308–313. https://doi.org/10.1093/comjnl/7.4.308

Newell, D. L., & Carey, J. W. (2012). Experimental Evaluation of Wellbore Integrity Along the Cement-rock Boundary. *Environmental Science &Amp; Technology*, *47*(1), 276–282. https://doi.org/10.1021/es3011404

Nguyen-Thanh, L., Hoang-Minh, T., Kasbohm, J., Herbert, H. J., Thuy, D. N., & Le Thi, L. (2014). Characterization of Fe-smectites and their alteration potential in relation to engineered barriers for HLW repositories: The Nui Nua clay, Thanh Hoa province, Vietnam. *Applied Clay Science*, 101, 168-176.

Nogara, J., & Zarrouk, S. J. (2018). Corrosion in geothermal environment Part 2: Metals and alloys. *Renewable & Sustainable Energy Reviews*, *82*, 1347–1363. https://doi.org/10.1016/j.rser.2017.06.091

Nutt, M., Morris, E., Puig Joe Carter, F., Rodwell, P., Delley Rob Howard, A., Giuliano, D., Puig Carter, F., and Delley, A. (2012). Used Fuel Management System Architecture Evaluation, Fiscal Year 2012. FCRD-NFST-2013-000020 REV. 0. Argonne National Laboratory.

Ohmoto, H., Hayashi, K. I., & Kajisa, Y. (1994). Experimental study of the solubilities of pyrite in NaCl-bearing aqueous solutions at 250–350°C. *Geochimica et Cosmochimica Acta*, *58*(10), 2169–2185. https://doi.org/10.1016/0016-7037(94)90003-5

Oliver, W., & Pharr, G. (2004). Measurement of hardness and elastic modulus by instrumented indentation: Advances in understanding and refinements to methodology. *Journal of Materials Research*, *19*(1), 3–20. https://doi.org/10.1557/jmr.2004.19.1.3

Olsson, S., & Karnland, O. (2011). Mineralogical and chemical characteristics of the bentonite in the A2 test parcel of the LOT field experiments at Äspö HRL, Sweden. *Physics and Chemistry of the Earth, Parts a/B/C*, *36*(17–18), 1545–1553. https://doi.org/10.1016/j.pce.2011.10.011

Oy, P. (2012). *Safety case for the disposal of spent nuclear fuel at Olkiluoto: Synthesis 2012*.

Pedersen, K. (1996). Investigations of subterranean bacteria in deep crystalline bedrock and their importance for the disposal of nuclear waste. *Canadian Journal of Microbiology*, *42*(4), 382–391. https://doi.org/10.1139/m96-054

Pedersen, K. (1999). Subterranean microorganisms and radioactive waste disposal in Sweden. *Engineering Geology*, *52*(3–4), 163–176. https://doi.org/10.1016/s0013-7952(99)00004-6

Pedersen, Karsten (2000). Microbial processes in radioactive waste disposal (SKB-TR--00-04). Sweden

Pedregosa, F., Varoquaux, G., Gramfort, A., Michel, V., Thirion, B., Grisel, O., Blondel, M., Prettenhofer, P., Weiss, R., Dubourg, V., Vanderplas, J., Passos, A., Cournapeau, D., Brucher, M., Perrot, M., & Duchesnay, É. (2011). SciKit-Learn: Machine Learning in Python. *Journal of Machine Learning Research*. 12, 2825–2830. https://doi.org/10.5555/1953048.2078195

Piché-Choquette, S., & Constant, P. (2019). Molecular hydrogen, a neglected key driver of soil biogeochemical processes. *Applied and Environmental Microbiology*, *85*(6). https://doi.org/10.1128/aem.02418-18

Pignatelli, I., Bourdelle, F., Bartier, D., Mosser-Ruck, R., Truche, L., Mugnaioli, E., & Michau, N. (2014). Iron–clay interactions: Detailed study of the mineralogical transformation of claystone with emphasis on the formation of iron-rich T–O phyllosilicates in a step-by- step cooling experiment from 90° C to 40° C. Chemical Geology, 387, 1-11.

Pruess, K., Oldenburg, C., & Moridis, G. (1999). TOUGH2 User's Guide, Version 2.0. LBNL-43134. Lawrence Berkeley National Laboratory, Berkeley, California.

Pusch, R. & Madsen, F.T. (1995). Aspects on the Illitization of the Kinnekulle Bentonites. *Clays and Clay Minerals*, *43*(3), 261–270. https://doi.org/10.1346/ccmn.1995.0430301

Pusch, R., Zwahr, H., Gerber, R., & Schomburg, J. (2003). Interaction of cement and smectitic clay—theory and practice. *Applied Clay Science*, *23*(1-4), 203-210

Pusch, R., Prikryl, R., Weishauptová, Z., Xiaodong, L., & Knutsson, S. (2012). Role of clay microstructure in expandable buffer clay. *Journal of Purity, Utility Reaction and Environment*, 1(6), 267-292.

Pusch, R., Kasbohm, J., Knutsson, S., Yang, T., & Nguyen-Thanh, L. (2015). The role of smectite clay barriers for isolating high-level radioactive waste (HLW) in shallow and deep repositories. *Procedia Earth and Planetary Science*, 15, 680-687.

Rao, S. M., Thyagaraj, T., & Rao, P. R. (2013). Crystalline and Osmotic Swelling of an Expansive Clay Inundated with Sodium Chloride Solutions. *Geotechnical and Geological Engineering*, *31*(4), 1399–1404. https://doi.org/10.1007/s10706-013-9629-3

Rasband, W.S. ImageJ, U. S. National Institutes of Health, Bethesda, Maryland, USA, https://imagej.nih.gov/ij/, 1997-2022.

Rasmusson M. (2022). Description of TASK 12 – Subtask A, B & C Specification of Benchmarking test Cement-clay interaction, Personal communication

Rimmelé, G., Barlet-Gouédard, V., Porcherie, O., Goffé, B., & Brunet, F. (2008). Heterogeneous porosity distribution in Portland cement exposed to CO2-rich fluids. *Cement and Concrete Research*, *38*(8–9), 1038–1048. https://doi.org/10.1016/j.cemconres.2008.03.022

Romaine, A., Jeannin, M., Sabot, R., Necib, S., & Refait, P. (2015). Corrosion processes of carbon steel in argillite: Galvanic effects associated with the heterogeneity of the corrosion product layer. *Electrochimica Acta*, *182*, 1019–1028. https://doi.org/10.1016/j.electacta.2015.10.010

Ross D. S. & Ketterings Q. (1986) Chapter 9: Recommended Methods for Determining Soil Cation Exchange Capacity.

Samper, J., Zheng, L., Fernández, A. M., & Montenegro, L. (2008). Inverse modeling of multicomponent reactive transport through single and dual porosity media. *Journal of Contaminant Hydrology*, *98*(3–4), 115–127. https://doi.org/10.1016/j.jconhyd.2008.03.008

Sato, H., Yui, M., & Yoshikawa, H. (1994). Diffusion behavior for SE and ZR in Sodium-Bentonite. *MRS Proceedings*, *353*. https://doi.org/10.1557/proc-353-269

Sauer, K., Caporuscio, F., Rock, M., Cheshire, M., & Jové-Colón, C. (2020). Hydrothermal Interaction of Wyoming Bentonite and Opalinus Clay. *Clays and Clay Minerals*, *68*(2), 144–160. https://doi.org/10.1007/s42860-020-00068-8

Savage, D. (1997). Review of the potential effects of alkaline plume migration from a cementitious repository for radioactive waste. Research & Development Technical Report P60, UK Environment Agency, Bristol, UK.

Savage, D., & Benbow, S. (2007) Low pH cements (SKI-R-07-32). Swedish Nuclear Power Inspectorate. Sweden.

Savage, D., Noy, D., & Mihara, M. (2002). Modelling the interaction of bentonite with hyperalkaline fluids. *Applied Geochemistry*, *17*(3), 207–223. https://doi.org/10.1016/s0883-2927(01)00078-6

Savage, D., Walker, C., Arthur, R., Rochelle, C., Oda, C., & Takase, H. (2007). Alteration of bentonite by hyperalkaline fluids: A review of the role of secondary minerals. *Physics and Chemistry of the Earth*, Parts A/B/C, 32(1-7), 287-297.

Savage, D., Benbow, S., Watson, C., Takase, H., Ono, K., Oda, C., & Honda, A. (2010). Natural systems evidence for the alteration of clay under alkaline conditions: An example from Searles Lake, California. *Applied Clay Science*, *47*(1–2), 72–81. https://doi.org/10.1016/j.clay.2009.08.024

Šavija, B., & Luković, M. (2016). Carbonation of cement paste: Understanding, challenges, and opportunities. *Construction and Building Materials*, *117*, 285–301. https://doi.org/10.1016/j.conbuildmat.2016.04.138

Savoye, S., Beaucaire, C., Fayette, A., Herbette, M., & Coelho, D. (2012). Mobility of Cesium through the Callovo-Oxfordian Claystones under Partially Saturated Conditions. *Environmental Science & Technology*, *46*(5), 2633–2641. https://doi.org/10.1021/es2037433

Segad, M., Jönsson, B., & Cabane, B. (2012a). Tactoid formation in Montmorillonite. *Journal of Physical Chemistry C*, *116*(48), 25425–25433. https://doi.org/10.1021/jp3094929

Segad, M., Hanski, S., Olsson, U., Ruokolainen, J., Åkesson, T., & Jönsson, B. (2012b). Microstructural and Swelling Properties of Ca and Na Montmorillonite: (In Situ) Observations with Cryo-TEM and SAXS. *Journal of Physical Chemistry C*, *116*(13), 7596–7601. https://doi.org/10.1021/jp300531y

Seiphoori, A. (2015). Thermo-hydro-mechanical characterisation and modelling of Wyoming granular bentonite. Technical Report 15-05, Nagra, Wettingen, Switzerland.

Sellin, P., & Leupin, O. X. (2013). The Use of Clay as an Engineered Barrier in Radioactive-Waste Management – A Review. *Clays and Clay Minerals*, *61*(6), 477–498. https://doi.org/10.1346/ccmn.2013.0610601

Seyfried, J.R., Janecky, D.R., and Berndt, M.E. (1987). Rocking autoclaves for hydrothermal experiments II. The flexible reaction-cell system. Hydrothermal Experimental Techniques, Eds. Ulmer, G.C. and Barnes, H.L. John Wiley & Sons, pp. 216 – 239.

Sevcu, Alena, Steinova, J., Burkartova, K., & Cerna, K. (2018). "MIND: Microbial Diversity in Aged Bentonites"

Shuman, D. J., Costa, A. L., & Andrade, M. S. (2007). Calculating the elastic modulus from nanoindentation and microindentation reload curves. *Materials Characterization*, *58*(4), 380–389. https://doi.org/10.1016/j.matchar.2006.06.005

SKB, (2011a). Long-term safety for the final repository for spent nuclear fuel at Forsmark. Main report of the SR-Site project. Swedish Nuclear Fuel and Waste Management Co.

SKB. (2011b). Application for License under the Nuclear Activities Act. Submitted to: Swedish Radiation Safety Authority. Stockholm, Sweden.

Smailos, E., Cuñado, M. A., Azkarate, I., Kursten, B. and Marx, G. (2002). Long-Term Performance of Candidate Materials for HLW/Spent Fuel Disposal Containers, Report FZKA 6706, FZK.INE (Karlsruhe, Germany).

Smart, N. R. (2008). The corrosion behavior of carbon steel radioactive waste packages: A summary review of Swedish and UK research: NACE CORROSION, p. NACE-P3013.

Somerton W.H., El-Shaarani A. H. and Mobarak S. M., 1974. High temperature behavior of rocks associated with geothermal-type reservoirs. Paper SPE-4897. Proceedings of the 44th Annual California Regional Meeting of the Society of Petroleum Engineers. Richardson, TX: Society of Petroleum Engineers.

Sverjensky, D. A. (2005). Prediction of surface charge on oxides in salt solutions: Revisions for 1:1 (M+L−) electrolytes. *Geochimica Et Cosmochimica Acta*, *69*(2), 225–257. https://doi.org/10.1016/j.gca.2004.05.040

Svemar, C., (2005). Cluster Repository Project (CROP). Final Report of European Commission Contract FIR1-CT-2000-2003, Brussels, Belgium.

Svemar, C., Johannesson, L-E., Grahm, P., Svensson, D., Kristensson, O., Lönnqvist, M., and Nilsson, U. (2016). Prototype Repository. Opening and retrieval of outer section of Prototype Repository at Äspö Hard Rock Laboratory. Summary report. SKB TR-13-22, Svensk Kärnbränslehantering AB.

Taborowski, T., Bengtsson, A., Chukharkina, A., & Blom, A. (2019). Bacterial presence and activity in compacted bentonites.

Takahashi, Y., Kawamura, K., Sato, T., Kobayashi, I., & Ichikawa, Y. (2015). *In situ*X-ray diffraction observation of smectite hydration under constant volume. *Journal of Nuclear Science and Technology*, *52*(12), 1470–1479. https://doi.org/10.1080/00223131.2015.1009955

Takase, H. (2004). Discussion on PA model development for bentonite barriers affected by chemical interaction with concrete, do we have enough evidence to support bentonite stability?, *in* Proceedings Proc. Int. Workshop on Bentonite-Cement Interaction in Repository Environments, Tokyo, Japan, Apr. 14-16, 20042004.

Tinnacher, R. M., Holmboe, M., Tournassat, C., Bourg, I. C., & Davis, J. A. (2016). Ion adsorption and diffusion in smectite: Molecular, pore, and continuum scale views. *Geochimica et Cosmochimica Acta*, *177*, 130–149. https://doi.org/10.1016/j.gca.2015.12.010

Tournassat, C., & Appelo, C. (2011). Modelling approaches for anion-exclusion in compacted Na-bentonite. *Geochimica et Cosmochimica Acta*, *75*(13), 3698–3710. https://doi.org/10.1016/j.gca.2011.04.001

Tournassat, C., & Steefel, C. I. (2021). Modeling diffusion processes in the presence of a diffuse layer at charged mineral surfaces: a benchmark exercise. *Computational Geosciences*, *25*(4), 1319–1336. https://doi.org/10.1007/s10596-019-09845-4

Tournassat, C., Steefel, C. I., Bourg, I. C., & Bergaya, F. (2015). *Natural and engineered clay barriers*. Elsevier Science Limited.

Tournassat, C., Tinnacher, R., Grangeon, S., & Davis, J. (2018). Modeling uranium(VI) adsorption onto montmorillonite under varying carbonate concentrations: A surface complexation model accounting for the spillover effect on surface potential. *Geochimica et Cosmochimica Acta*, *220*, 291–308. https://doi.org/10.1016/j.gca.2017.09.049

Tournassat, C., Steefel, C. I., Fox, P., & Tinnacher, R. M. (2023). Resolving experimental biases in the interpretation of diffusion experiments with a user-friendly numerical reactive transport approach. *Scientific Reports*, *13*(1). https://doi.org/10.1038/s41598-023-42260-5

Van Genuchten, M. T. (1980). A closed-form equation for predicting the hydraulic conductivity of unsaturated soils. *Soil Science Society of America Journal*, *44*(5), 892–898. https://doi.org/10.2136/sssaj1980.03615995004400050002x

Vargaftik, N.B. Tables on the Thermophysical Properties of Liquids and Gases, 2nd Ed., John Wiley & Sons, New York, NY, 1975.

Verstricht, J. (2009). The ESDRED project: Engineering studies and demonstration of repository designs.

Villar, M. (2017). NAGRA FEBEX-DP Post-mortem THM-THG Analysis Report. http://documenta.ciemat.es/handle/123456789/1122

Villar, M. V. (2021). FEBEX-DP Postmortem THM/THC Analysis Report. NAGRA technical report. NAB 16-17.

Villar, M. V., Cuevas, J., Fernandez-Llamosas, H., & Garcia-Mina, J. M. (2008). Microbial diversity in clayey samples from a geological repository for radioactive waste. *FEMS Microbiology Ecology*, 63(1), 50-64.

Villar, M. V., Iglesias, R. J., Gutiérrez-Álvarez, C., & Carbonell, B. (2018). Hydraulic and mechanical properties of compacted bentonite after 18 years in barrier conditions. *Applied Clay Science*, *160*, 49–57. https://doi.org/10.1016/j.clay.2017.12.045

Villar, M. V., Iglesias, R. J., García-Siñeriz, J. L., Lloret, A., & Huertas, F. (2020). Physical evolution of a bentonite buffer during 18 years of heating and hydration. *Engineering Geology*, *264*, 105408. https://doi.org/10.1016/j.enggeo.2019.105408

Vomvoris, S., Birkholzer, J., Zheng, L., Gaus, I., Blechschmidt, I. (2015). THMC behavior of clay-based barriers under high temperature- from laboratory to URL scale. 678-687. Proceedings of the International High Level Radioactive Waste Management meeting. Charleston, NC.

Wakim, J., Hadj–Hassen, F., & De Windt, L. (2009). Effect of aqueous solution chemistry on the swelling and shrinkage of the Tournemire shale. *International Journal of Rock Mechanics and Mining Sciences*, *46*(8), 1378–1382. https://doi.org/10.1016/j.ijrmms.2009.08.002

Walker, W.R., J.D. Sabey, and D.R. Hampton. Studies of Heat Transfer and Water Migration in Soils, Final Report, Department of Agricultural and Chemical Engineering, Colorado State University, Fort Collins, CO, 80523, April 1981.

Wang, Z., Wang, H., Li, Q., Xu, M., Guo, Y., Li, J., & Wu, T. (2016). pH effect on Re(VII) and Se(IV) diffusion in compacted GMZ bentonite. *Applied Geochemistry*, *73*, 1–7. https://doi.org/10.1016/j.apgeochem.2016.07.015

Wersin, P., & Kober, F. (2017). FEBEX-DP-Metal corrosion and iron-bentonite interaction studies. (Nagra Arbeitsberichte NAB 16-16). Wettingen, Switzerland: Nagra.

Wersin, P., Johnson, L., & McKinley, I. (2007). Performance of the bentonite barrier at temperatures beyond 100°C: A critical review. *Physics and Chemistry of the Earth, Parts A/B/C*, *32*(8–14), 780–788. https://doi.org/10.1016/j.pce.2006.02.051

Westall, J., & Hohl, H. (1980). A comparison of electrostatic models for the oxide/solution interface. *Advances in Colloid and Interface Science*, *12*(4), 265–294. https://doi.org/10.1016/0001-8686(80)80012-1

Whittaker, M. L., Lammers, L. N., Carrero, S., Gilbert, B., & Banfield, J. F. (2019). *Ion exchange selectivity in clay is controlled by nanoscale chemical–mechanical coupling* (Vol. 116, Issue 44). Proceedings of the National Academy of Sciences. https://doi.org/10.1073/pnas.1908086116

Wilson, J., Savage, D., Cuadros, J., Shibata, M., & Ragnarsdottir, K. V. (2006a). The effect of iron on montmorillonite stability.(I) Background and thermodynamic considerations. *Geochimica et Cosmochimica Acta*, 70(2), 306-322.

Wilson, J., Cressey, G., Cressey, B., Cuadros, J., Ragnarsdottir, K. V., Savage, D., and Shibata, M. (2006b). The effect of iron on montmorillonite stability.(II) Experimental investigation. *Geochimica et Cosmochimica Acta*, 70(2).

Wu, T., Wang, H., Zheng, Q., Zhao, Y., & Van Loon, L. R. (2014). Diffusion behavior of Se(IV) and Re(VII) in GMZ bentonite. *Applied Clay Science*, *101*, 136–140. https://doi.org/10.1016/j.clay.2014.07.028

Wu, T., Wang, Z., Wang, H., Zhang, Z., & van Loon, L. R. (2017). Salt effects on Re(VII) and Se(IV) diffusion in bentonite. *Applied Clay Science*, *141*, 104–110. https://doi.org/10.1016/j.clay.2017.02.021

Xu, T., Spycher, N., Sonnenthal, E., Zhang, G., Zheng, L., & Pruess, K. (2011). TOUGHREACT Version 2.0: A simulator for subsurface reactive transport under non-isothermal multiphase flow conditions. *Computers & Geosciences*, *37*(6), 763–774. https://doi.org/10.1016/j.cageo.2010.10.007

Xu, D., Tang, Z., & Zhang, L. (2019). Interpretation of coarse effect in simple shear behavior of binary sand-gravel mixture by DEM with authentic particle shape. *Construction and Building Materials*, *195*, 292–304. https://doi.org/10.1016/j.conbuildmat.2018.11.059

Yates, D. E., Levine, S., & Healy, T. W. (1974). Site-binding model of the electrical double layer at the oxide/water interface. *Journal of the Chemical Society, Faraday Transactions 1: Physical Chemistry in Condensed Phases*, *70*(0), 1807. https://doi.org/10.1039/f19747001807

You, Z., Lai, Y., Zeng, H., & Yang, Y. (2020). Influence of water and sodium chloride content on corrosion behavior of cast iron in silty clay. *Construction and Building Materials*, *238*, 117762. https://doi.org/10.1016/j.conbuildmat.2019.117762

Zandanel, A., Sauer, K., Rock, M., Caporuscio, F., Telfeyan, K., & Matteo, E. N. (2022). Impacts of crystalline host rock on repository barrier materials at 250 °C: Hydrothermal Co-Alteration of Wyoming bentonite and steel in the presence of grimsel granodiorite. *Minerals*, *12*(12), 1556. https://doi.org/10.3390/min12121556

Zhang, C. (2018). Thermo-hydro-mechanical behavior of clay rock for deep geological disposal of high-level radioactive waste. *Journal of Rock Mechanics and Geotechnical Engineering*, *10*(5), 992–1008. https://doi.org/10.1016/j.jrmge.2018.03.006

Zhang, D., Ghouleh, Z., & Shao, Y. (2017). Review on carbonation curing of cement-based materials. *Journal of CO2 Utilization*, *21*, 119–131. https://doi.org/10.1016/j.jcou.2017.07.003

Zheng, L., Samper, J., Montenegro, L., & Fernández, A. M. (2010). A coupled THMC model of a heating and hydration laboratory experiment in unsaturated compacted FEBEX bentonite. *Journal of Hydrology*, *386*(1–4), 80–94. https://doi.org/10.1016/j.jhydrol.2010.03.009

Zheng, L., Rutqvist, J., Liu, H. H., Birkholzer, J. T., & Sonnenthal, E. (2014). Model evaluation of geochemically induced swelling/shrinkage in argillaceous formations for nuclear waste disposal. *Applied Clay Science*, *97–98*, 24–32. https://doi.org/10.1016/j.clay.2014.05.019

Zheng, L., Rutqvist, J., Birkholzer, J. T., & Liu, H. H. (2015a). On the impact of temperatures up to 200 °C in clay repositories with bentonite engineer barrier systems: A study with coupled thermal, hydrological, chemical, and mechanical modeling. *Engineering Geology*, *197*, 278–295. https://doi.org/10.1016/j.enggeo.2015.08.026

Zheng, L., Rutqvist, J., Xu, H., & Birkholzer, J. T. (**2017b**). Coupled THMC models for bentonite in an argillite repository for nuclear waste: Illitization and its effect on swelling stress under high temperature. *Engineering Geology*, *230*, 118–129. https://doi.org/10.1016/j.enggeo.2017.10.002

Zheng, L., Xu, H., and Birkholzer, J.T. (2018), THMC Modeling in Support of HotBENT, an Experiment Studying the Effects of High Temperatures on Clay Buffers/Near-field, NAGRA Working Report, NAB 18-032, 2018, Switzerland

Zheng, L., H. Xu, B. Gilbert, N. Subramanian, L. Lammers, P. Nico, P. Fox, C. Tournassat, M. Whittaker, S. Borglin, Y. Wu, C. Chang, C. Chou, T. Kneafsey (2020a) Engineered Barrier System Research Activities at LBNL: FY20 Progress Report, Lawrence Berkeley National Laboratory, LBNL- 2001331

Zheng, L., Xu, H., Rutqvist, J., Reagan, M., Birkholzer, J., Villar, M. V., & Fernández, A. M. (2020b). The hydration of bentonite buffer material revealed by modeling analysis of a long-term in situ test. *Applied Clay Science*, *185*, 105360. https://doi.org/10.1016/j.clay.2019.105360

Zheng, L., Borglin, S., Zarzycki, P., Chang, C., Fox, P., Yoon, S., Dong, W., Nico, P., Tournassat, C., Chou, C., Steefel, C., Peruzzo, L., Farrell, S., Gilbert, B., and Wu, Y. (2022) LBNL Engineered Barrier System R&D Activities in FY 22. Lawrence Berkely National Laboratory.

Zhou, X., Li, J., & Xu, Y. (2021a). A new thermal analysis model with three heat conduction layers in the nuclear waste repository. *Nuclear Engineering and Design*, *371*, 110929. https://doi.org/10.1016/j.nucengdes.2020.110929

Zhou, X., Xu, Y., Sun, D., Tan, Y., & Xu, Y. (2021b). Three-dimensional thermal–hydraulic coupled analysis in the nuclear waste repository. *Annals of Nuclear Energy*, *151*, 107866. https://doi.org/10.1016/j.anucene.2020.107866

Zhu, C. (2005). In situ feldspar dissolution rates in an aquifer. *Geochimica Et Cosmochimica Acta*, *69*(6), 1435–1453. https://doi.org/10.1016/j.gca.2004.09.005

APPENDIX A - EVALUATION OF PROGRESS TOWARDS EBS-RELATED 2019 SFWST ROADMAP PRIORITIES

R&D Task ID	R&D Activity/Task Name	Importance to the Safety Case (ISC)	R&D Needed	Status
A-08	**Evaluation of Ordinary Portland Cement (OPC)**	**High**	Evaluation of ordinary Portland cement (OPC) interactions with engineered barrier materials. Geochemical and mineralogical evaluation of cementitious material interaction with barrier materials (steel, bentonite, clay rock) at elevated pressures and temperatures. Baseline the chemical reactions of a shotcrete liner in contact with engineered barrier materials. The emphasis will be on the characterization of (secondary) cementitious phases in response to hydrothermal alteration. This will include steel corrosion measurements, which will provide data revealing if corrosion is inhibited in the presence of cement.	Task 12 of the SKB Task Force is focused on modelling cement/bentonite interfaces. This includes mineralogic, chemical, and textural changes at the interface. (Section 7) Hydrothermal testing that has provided datasets to understand cement-metal-rock interactions. (Section 10 and 11) Experimental and modeling capabilities have been developed to understand cement-rock interfaces. This includes characterization of interface mineralogic alteration, pore alteration, and micromechanical properties alteration (Section 12).

E-09	**Cement plug/liner degradation**	**High**	High importance for design/construction arguments affecting disposal system design that utilize backfill/buffer as an engineered barrier and potential generation of preferential pathways through the EDZ Methods for characterizing groundwater chemistry and models to predict water chemistry evolution in the near field need to be further improved. Need to define a generic chemistry for each geologic environment. Need to identify interactions with EBS materials (e.g., introduced fluids, alkaline plume from the near field).	Task 12 of the SKB Task Force is focused on modelling cement/bentonite interfaces. This includes mineralogic, chemical, and textural changes at the interface. (Section 7) Hydrothermal testing that has provided datasets to understand cement-metal-rock interactions. (Section 10 and 11). Experimental and modeling capabilities have been developed to understand cement-rock interfaces. This includes characterization of interface mineralogic alteration, pore alteration, and micromechanical properties alteration (Section 12)
E-11	EBS High Temp experimental data collection- To evaluate high temperature mineralogy /geochemistry changes.	**High**	Need to know the evolution of the characteristics of the EDZ. Need to understand the coupled evolution of near-field host rock (EDZ) and backfill. R&D (e.g., FEBEX) needs to take more data during the cooldown period (re-saturation and other property changes).	h-scale Column Tests in support of the HotBENT. In FY22, the first set of columns, HotBENT-Lab #1, was completed and extensive data sets were collected during the test and after the column dismantling. In FY23, we conducted the HotBENT-Lab #2 test, which differed from the HotBENT-Lab #1 in the following features: (1) bentonite type, (2) initial bentonite density and water content, (3) water chemistry, and (4) hydration pressure. Both columns were then dismantled to measure chemical and physical changes within the column materials. (Section 6) Developing methods to use the large-scale field experiment HotBENT to understand the THMC evolution of bentonite under high temperature. (Section 8)

E-17	Buffer Material by Design	**High**	Development of new generation buffer materials (thermal management, resistance to erosion, limitation of chemical gradients/interactions) Impact of new materials on source term Sorption capacity for anionic species	There are several NEUP projects exploring the topic for thermal conductivity enhancing additives, both in compacted and pelletized bentonite. Several SFWST personnel serve as POC on these projects. Novel materials have been developed for anionic sorption, specifically targeting Iodine-129. Progress is being made towards understanding the Sorption mechanisms for these materials (Section 13). Next steps include testing these materials within a bentonite column to understand their durability and sorption capacity under more realistic repository conditions.
I-04	Experiment of bentonite EBS under High Temperature: HotBENT	**High**	• Thermal limit of crystalline and argillite repository with bentonite EBS. • Hydrological, mechanical and chemical alteration of various types of bentonite that backfilled EBS under high temperature (200 °C) • Validation of coupled THMC model • Supply GDSA with the porosity, permeability, swelling pressure, vapor pressure evolution and clay mineral alteration under high temperature • Cross-fertilize with THC processes in EBS and thermodynamic DB development	Bench-scale Column Tests in support of the HotBENT. In FY22, the first set of columns, HotBENT-Lab #1, was completed and extensive data sets were collected during the test and after the column dismantling. In FY23, we conducted the HotBENT-Lab #2 test, which differed from the HotBENT-Lab #1 in the following features: (1) bentonite type, (2) initial bentonite density and water content, (3) water chemistry, and (4) hydration pressure. Both columns were then dismantled to measure chemical and physical changes within the column materials. (Section 6) Hydrothermal experiments were designed to understand geochemical and mineralogical changes that may occur in the EBS at the HotBENT conditions. Experiments completed in FY23 included different combinations of the two bentonites (FE and BCV) plus cement with groundwater (synthetic Grimsel granodiorite groundwater). In FY22, an experiment was completed that included Grimsel granodiorite wall rock as a reactant in addition to BCV bentonite and LCS. (Section 10).

E-03	THC Processes in EBS	**Medium-High**	Engineered barrier (metal-clay-rock) material interactions & experimental data Modeling (thermodynamic & reactive transport) Includes temperatures relevant to DPC. Provide chemical constraints for SNF degradation andradionuclide transport. May be of high importance for performance in certain environments and disposal concepts that utilize backfill/buffer as a engineered barrier - governs "source term" release upon failure of waste packages for certain designs in certain environments. High importance for design/construction - could affect disposal system design that utilize backfill/buffer as an engineered barrier, how it is constructed, and emplacement of waste and backfill/buffer (i.e., size of waste packages and spacing). High importance for overall confidence - secondary isolation barrier and long-term barrier performance.	Modelling tools to improve the parametrization and performance of meso- and macroscopic models (such as surface complexation model, SCM) of radionuclide migration in the bentonite barrier via molecular modeling and Artificial Intelligence/Machine Learning methods. In FY23, we developed a computational pipeline to generate synthetic datasets, train AI/ML models, and used these trained models as the SCM surrogate for the case of uranium sorption to oxides at varying environmental conditions. (Section 3) Developing experimental and modeling tolls to understand the diffusion and adsorption of Se. FY23 work includes: (1) diffusion experiments conducted on the filters, which will allow better modeling interpretation of the diffusion data for 3H and Se(VI) in the through-diffusion experiments; (2) a new set of ongoing diffusion experiments conducted with Se(IV) under the same conditions as the experiment with Se(VI) and Se batch adsorption experiments on montmorillonite; and (3) a newly released graphical user interface, CrunchEase, which is based on the reactive transport code CrunchClay.. (Section 4) Experiments on potential microbial activity in materials collected from the FEBEX experiment were conducted to understand the change of microbial activity for samples after long-term heating and hydration. Samples were incubated in non-enriched minimal conditions and experiments were designed to determine if these materials possess microbial communities with the ability to metabolize H2 or other substrates, and to assess how the FEBEX test impacted those capabilities. The findings indicate that there is still a considerable metabolic potential within the microbial communities, underscoring the significant role of microbial metabolism in long-term

				nuclear waste disposal repositories employing clay as a barrier material. (Section 5) DECOVALEX Task C activities are wrapping in FY24. This developed tools and capabilities for analyzing URL test results for EBS focused field tests. These tools will continue to be refined in application to HotBENT and other emerging URL tests. (Section 11).
E-10	High-Temperature Behavior	**Medium-High**	Need to know the evolution of the characteristics of the EDZ. Need to understand the coupled evolution of near-field host rock (EDZ) and backfill. Need to address multiple or longer thermal pulse case.	Bench-scale Column Tests in support of the HotBENT. In FY22, the first set of columns, HotBENT-Lab #1, was completed and extensive data sets were collected during the test and after the column dismantling. In FY23, we conducted the HotBENT-Lab #2 test, which differed from the HotBENT-Lab #1 in the following features: (1) bentonite type, (2) initial bentonite density and water content, (3) water chemistry, and (4) hydration pressure. Both columns were then dismantled to measure chemical and physical changes within the column materials. (Section 6) Developing methods to use the large-scale field experiment HotBENT to understand the THMC evolution of bentonite under high temperature. (Section 8) Hydrothermal experiments were designed to understand geochemical and mineralogical changes that may occur in the EBS at the HotBENT conditions. Experiments completed in FY23 included different combinations of the two bentonites (FE and BCV) plus cement with groundwater (synthetic Grimsel granodiorite groundwater). In FY22, an experiment was completed that included Grimsel granodiorite wall rock as a reactant in addition to BCV bentonite and LCS. (Section 10).